

**AFRL-PR-WP-TR-2004-2047**

**INVESTIGATION OF JET  
IMPINGEMENT COOLING USING  
HIGH PRANDTL NUMBER FLUIDS  
AND AMMONIA FOR MILITARY  
APPLICATIONS**



**Dr. Muhammad Mustafizur Rahman**

**University of South Florida  
Department of Mechanical Engineering  
4202 E. Fowler Avenue, ENB 118  
Tampa, FL 33620**

**MARCH 2004**

**Final Report for 16 September 1998 – 15 October 2003**

**Approved for public release; distribution is unlimited.**

**STINFO FINAL REPORT**

**PROPULSION DIRECTORATE  
AIR FORCE MATERIEL COMMAND  
AIR FORCE RESEARCH LABORATORY  
WRIGHT-PATTERSON AIR FORCE BASE, OH 45433-7251**

## NOTICE

USING GOVERNMENT DRAWINGS, SPECIFICATIONS, OR OTHER DATA INCLUDED IN THIS DOCUMENT FOR ANY PURPOSE OTHER THAN GOVERNMENT PROCUREMENT DOES NOT IN ANY WAY OBLIGATE THE U.S. GOVERNMENT. THE FACT THAT THE GOVERNMENT FORMULATED OR SUPPLIED THE DRAWINGS, SPECIFICATIONS, OR OTHER DATA DOES NOT LICENSE THE HOLDER OR ANY OTHER PERSON OR CORPORATION; OR CONVEY ANY RIGHTS OR PERMISSION TO MANUFACTURE, USE, OR SELL ANY PATENTED INVENTION THAT MAY RELATE TO THEM.

THIS REPORT IS RELEASABLE TO THE NATIONAL TECHNICAL INFORMATION SERVICE (NTIS). AT NTIS, IT WILL BE AVAILABLE TO THE GENERAL PUBLIC, INCLUDING FOREIGN NATIONS.

THIS TECHNICAL REPORT HAS BEEN REVIEWED AND IS APPROVED FOR PUBLICATION.

/s/

---

KIRK L. YERKES  
Project Engineer  
Energy Storage & Thermal Sciences Branch

/s/

---

JOHN G. NAIRUS  
Chief  
Energy Storage & Thermal Sciences Branch

/s/

---

CYNTHIA A. OBRINGER  
Deputy Chief  
Power Division  
Propulsion Directorate

Do not return copies of this report unless contractual obligations or notice on a specific document require its return.

REPORT DOCUMENTATION PAGE					Form Approved OMB No. 0704-0188	
<p>The public reporting burden for this collection of information is estimated to average 1 hour per response, including the time for reviewing instructions, searching existing data sources, gathering and maintaining the data needed, and completing and reviewing the collection of information. Send comments regarding this burden estimate or any other aspect of this collection of information, including suggestions for reducing this burden, to Department of Defense, Washington Headquarters Services, Directorate for Information Operations and Reports (0704-0188), 1215 Jefferson Davis Highway, Suite 1204, Arlington, VA 22202-4302. Respondents should be aware that notwithstanding any other provision of law, no person shall be subject to any penalty for failing to comply with a collection of information if it does not display a currently valid OMB control number. <b>PLEASE DO NOT RETURN YOUR FORM TO THE ABOVE ADDRESS.</b></p>						
1. REPORT DATE (DD-MM-YY) March 2004		2. REPORT TYPE Final		3. DATES COVERED (From - To) 09/16/1998 – 10/15/2003		
4. TITLE AND SUBTITLE INVESTIGATION OF JET IMPINGEMENT COOLING USING HIGH PRANDTL NUMBER FLUIDS AND AMMONIA FOR MILITARY APPLICATIONS				5a. CONTRACT NUMBER F33615-98-1-2923		
				5b. GRANT NUMBER		
				5c. PROGRAM ELEMENT NUMBER 62203F		
6. AUTHOR(S) Dr. Muhammad Mustafizur Rahman				5d. PROJECT NUMBER 3145		
				5e. TASK NUMBER 20		
				5f. WORK UNIT NUMBER C7		
7. PERFORMING ORGANIZATION NAME(S) AND ADDRESS(ES)  University of South Florida Department of Mechanical Engineering 4202 E. Fowler Avenue, ENB 118 Tampa, FL 33620				8. PERFORMING ORGANIZATION REPORT NUMBER		
9. SPONSORING/MONITORING AGENCY NAME(S) AND ADDRESS(ES)  Propulsion Directorate Air Force Research Laboratory Air Force Materiel Command Wright-Patterson AFB, OH 45433-7251				10. SPONSORING/MONITORING AGENCY ACRONYM(S) AFRL/PRPS		
				11. SPONSORING/MONITORING AGENCY REPORT NUMBER(S) AFRL-PR-WP-TR-2004-2047		
12. DISTRIBUTION/AVAILABILITY STATEMENT Approved for public release; distribution is unlimited.						
13. SUPPLEMENTARY NOTES Report contains color.						
14. ABSTRACT <p>The objective of this project was to perform a comprehensive numerical study for the prediction of conjugate heat transfer during jet impingement cooling. Calculations were done primarily for two working fluids: MIL-7808 and ammonia. A number of substrate materials were studied. The investigation considered both free and confined jet configurations using circular and slot nozzles. Fifteen different disk or plate thicknesses ranging from 0 to 12 mm and eleven different nozzle heights from 0.4 mm to 12.5 mm were used. A number of heat source patterns were considered to explore the effects of magnitude and location of heat generation. Both steady state heat transfer and the transient start-up of power were investigated. It was found that the magnitude of local heat transfer coefficient or Nusselt number decreased with time at all locations on the disk. A higher heat transfer coefficient at the impingement location was seen at a smaller thickness, whereas a thicker plate provided a more uniform distribution of heat transfer coefficient. Materials with a higher thermal conductivity provided more uniform distribution of interface temperature as well as the heat transfer coefficient. Both local and average heat transfer coefficient increased with Reynolds number. For a given flow rate, a higher heat transfer coefficient was obtained with smaller nozzle diameter. Compared to MIL-7808 and FC-77, ammonia provided smaller solid-fluid interface temperature and higher heat transfer coefficient.</p>						
15. SUBJECT TERMS Jet Impingement, Conjugate Heat Transfer						
16. SECURITY CLASSIFICATION OF:			17. LIMITATION OF ABSTRACT: SAR	18. NUMBER OF PAGES 260	19a. NAME OF RESPONSIBLE PERSON (Monitor) Kirk Yerkes 19b. TELEPHONE NUMBER (Include Area Code) (937) 255-5721	
a. REPORT Unclassified	b. ABSTRACT Unclassified	c. THIS PAGE Unclassified				

## TABLE OF CONTENTS

Executive Summary	1
Axial Free Jet Impinging on a Uniformly Heated Disk: Steady State	3
Axial Free Jet Impinging on a Flat Disk with Discrete Heat Sources: Steady State	31
Axial Free Jet Impinging on a Uniformly Heated Disk: Transient Start-Up of Heating	57
Free Jet from a Slot Nozzle Impinging on a Plate with Discrete Heat Sources: Steady State	81
Free Jet from a Slot Nozzle Impinging on a Plate with Discrete Heat Sources: Transient Start-Up of Heating	101
Submerged Axial Free Jet Impinging on a Uniformly Heated Disk: Steady State	124
Radial Free Jet Impinging on a Uniformly Heated Disk: Steady State	153
Confined Jet of Ammonia from a Slot Nozzle Impinging on a Uniformly Heated Plate: Steady State	161
Confined Jet of Ammonia from a Slot Nozzle Impinging on a Plate with Discrete Heat Sources: Steady State	188
Confined Axial Jet of Ammonia Impinging on a Uniformly Heated Disk: Steady State	212
References	245

## EXECUTIVE SUMMARY

The objective of this project is to use computational fluid dynamics (CFD) to develop a comprehensive numerical simulation model for the prediction of heat transfer during jet impingement cooling. Calculations were done primarily for two working fluids: MIL-7808 and Ammonia. These fluids have strong potential for application in thermal management systems for aircraft and spacecraft respectively. In addition, water and FC-77 were simulated to explore the effects of fluid properties and to compare with experimental measurements. A number of substrate materials including Copper, Constantan, Silicon, Diamond, Aluminum, Silver, and Haynes 230 were considered during this study to explore different applications and to study the effects of solid properties on conjugate heat transfer.

The study considered both free jet and confined jet configurations. The free jet is formed when the liquid is issued from a nozzle or orifice to a gas environment. The shape of the free surface is governed by a balance of gravity, surface tension, and pressure forces. In the confined configuration, the jet is discharged into a body of surrounding fluid that is same as the jet itself. The fluid medium is bounded by impingement plate and confinement plate. In this investigation, a special case for free jet where the nozzle is placed very close to the impingement plate at a height lower than the surrounding liquid film has also been studied. This is named as submerged free jet. Computations were done for both axial and radial discharge from a circular jet using axisymmetric cylindrical coordinate system and for discharge from a two-dimensional slot jet using Cartesian coordinate system. The study considered 15 different disk or plate thicknesses ranging from 0 to 12 mm and 11 different nozzle heights from 0.4 mm to 12.5 mm.

A number of heat source patterns were considered to explore the effects of magnitude and location of heat generation on the conjugate heat transfer. In addition to the detailed study of steady state heat transfer, the transient heat transfer process during start up of power was investigated for most of the systems. Computations were done for velocity and temperature fields and height of the free surface (for the free jet). Results were obtained for different combinations of jet Reynolds number, nozzle height, nozzle diameter (of slot width), plate thickness, plate material, and heat source pattern. The variations of local and average heat transfer coefficient,

local and average Nusselt number, maximum temperature in the solid, maximum temperature at the solid-fluid interface, temperature range at the solid-fluid interface, and temperature contours within the solid are being presented.

It was found that, during the transient start-up of heating, the local interface temperature increased with time and eventually settled to the steady state condition. In the earlier part of the transient, the temperature distribution along the solid-fluid interface was almost uniform. As the thermal boundary layer developed with time, a lower temperature was seen in the stagnation region and it gradually increased as the fluid moved downstream. The magnitude of local heat transfer coefficient or Nusselt number decreased with time at all locations on the disk. At the stagnation point, local values of heat transfer coefficient was highest because of the pronounced convective effects. Heat transfer coefficient then reduced gradually towards the outflow boundary.

During both transient and steady state heat transfer, the distribution of local heat transfer coefficient was found to be sensitive to the thickness of the disk. A higher heat transfer coefficient at the impingement location was seen at a smaller thickness, whereas a thicker plate provided a more uniform distribution of heat transfer coefficient. The values of the local heat transfer coefficient at the solid-fluid interface also depended on disk material properties. Materials with a higher thermal conductivity provided more uniform distribution of interface temperature as well as the heat transfer coefficient. Both local and average heat transfer coefficient increased with Reynolds number. In addition, the nozzle diameter (or slot width) seemed to have an independent effect on the local distribution of heat transfer coefficient. For a given flow rate, a higher heat transfer coefficient was obtained with smaller nozzle diameter. In addition, the distance of the disk from the nozzle (impingement height) had a very strong influence on the magnitude of local Nusselt number. Compared to Mil-7808 and FC-77, ammonia provided smaller solid-fluid interface temperature and higher heat transfer coefficient.

# AXIAL JET IMPINGING ON A UNIFORMLY HEATED DISK: STEADY STATE

## INTRODUCTION

Jet impingement heat transfer is known for its ease of implementation and high heat transfer coefficients. It has been employed for the drying of paper and textiles, tempering glass, bearing cooling, turbine blade cooling, and electronics cooling. Although a poor heat transfer fluid, lubricating oil is an attractive coolant for aircraft applications because it is generally in close proximity to the electrical generating equipment. It is also pre-existing in the aircraft and therefore does not require flight qualification, new maintenance procedures, additional inventory space and logistics procedures, or additional environmental protection guidelines. These advantages translate into greatly reduced operational costs, which may far outweigh the loss in cooling efficiency. Lubricating oils are generally known for their large Prandtl number and strong dependence of viscosity on temperature. Alternately, air-cooling is generally inadequate or undesirable because of the additional drag imposed by ram air heat exchangers. Therefore, the investigation of jet impingement heat transfer for high Prandtl number fluids taking into account the effects of property variation with temperature is of great importance to the military and commercial aircraft industry.

Free-surface jets are formed when a liquid issues from a nozzle or orifice into a gas environment. The free surface forms immediately at the nozzle exit and prevails through the impingement region and into the wall jet region. The shape of the free surface depends on gravitational, surface tension, and pressure forces. The jet speed, size, and orientation determine the magnitude of these forces. In the past, several studies have been carried out on heat transfer during free jet impingement. Glauert [1] considered the flow due to a jet spreading out over a plane surface, either radially or in two dimensions. Solutions to the boundary layer equations were sought, according to which the form of the velocity distribution across the jet did not vary along its length. A solution for the laminar flow was obtained explicitly using a similarity transformation and, for turbulent flow, eddy diffusivity was introduced but the final result showed that the complete similarity solution was not attainable. Olsson and Turkdogan [2] studied the hydrodynamics of a jet impinging over a flat plate, in the region before the hydraulic jump. The experiment was carried out to determine the thickness of the film, the boundary layer, and the diameter of the potential core.

Metzger et al. [3] presented results for heat transfer characteristics of circular liquid jets impinging normally on plane surfaces. The experimental procedure was developed to cover single axisymmetric liquid jets formed by water or synthetic-base lubricating oil, and included a significant Prandtl number range so that extension to other liquids would be indicated. Nakoryakov et al. [4] presented a study, theoretically and experimentally, of hydrodynamics and mass transfer from an axisymmetric liquid jet impinging onto a horizontal plate. Simple formulae were obtained for the calculation of friction factor, liquid layer thickness, liquid surface velocity, and mass transfer coefficient as a function of discharge parameters. Hrycak [5] carried out an investigation of heat transfer from round jets impinging normally over a flat plate. This study was done for various nozzle-to-target distances, with Reynolds number varying from 14000 to 67000 (turbulent impinging flow), and different nozzle diameters. Liu and Lienhard [6] investigated a circular subcooled liquid jet impinging on a surface maintained at a uniform heat

flux. They used an integral method to obtain analytical predictions of temperature distribution in the liquid film and the local Nusselt number. They also carried out experiments to test the predictions of the theory.

Wang et al. [7, 8] presented an analytical study of heat transfer between an axisymmetrical free impinging jet and a solid flat surface with a non-uniform wall temperature or wall heat flux. The results obtained showed that the non-uniformity of wall temperature or wall heat flux has a considerable effect on the stagnation point Nusselt number. For the boundary layer region, a superposition solution was obtained beginning with the solution of a problem with a step change in the wall temperature or wall heat flux. The results indicated that the Nusselt number for increasing wall temperature or wall heat flux can be considerably higher than that for constant wall temperature or wall heat flux outside the stagnation region. Wang et al. [9] investigated the conjugate heat transfer between a laminar free impinging liquid jet and a laterally insulated disk with arbitrary temperature or heat flux distribution prescribed at the non-impingement surface. Their analytical solution showed that the heat transfer coefficient is influenced by the Prandtl number of the fluid, the ratio of the fluid to solid thermal conductivity, the ratio of the thickness to the radius of the disk, and the prescribed temperature or heat flux profile. Wang et al. [10] applied the previously developed analytical solution to the conjugate heat transfer problem of a laminar jet impingement cooling of a microelectronic chip. They presented results for two different nozzle diameters. Wolf et al. [11] performed experiments on a planar, free surface jet of water to investigate the effects of a nonuniform velocity profile on the local convective heat transfer coefficient for a uniform heat flux surface. The heat transfer coefficient was measured for different heat fluxes and Reynolds numbers. Vader et al. [12] measured temperature and heat flux distribution on a flat, upward facing, constant heat flux surface cooled by a planar, impinging water jet. The velocity at the exit of the nozzle, the temperature of the fluid, and heat flux were varied. They found that the stagnation convection coefficient exceeded those predicted by laminar flow analysis and this was caused by the existence of free stream turbulence.

Stevens and Webb [13] carried out an experimental investigation to characterize local heat transfer coefficient for round, free liquid jet impinging normally over a flat uniform heat flux surface. The parameters varied were Reynolds number, nozzle to plate distance, and jet diameter. Liu et al. [14] presented an analytical and experimental investigation for jet impingement cooling of uniformly heated surfaces to determine local Nusselt numbers from the stagnation point to radii up to 40 diameters. Turbulent transition in the film flow was observed experimentally at certain radius; beyond this point, a separate turbulent analysis was constructed. Pan et al. [15] presented a study on the flow structure and heat transfer characteristics of turbulent, free surface liquid jets. Ellison and Webb [16] studied transport from a small diameter, fully developed liquid jets impinging normally over a constant heat flux surface. The study focussed on varying Reynolds number spanning the laminar, transitional, and turbulent flow regimes at the nozzle exit. Both free-surface and submerged jets were studied and correlations for Nusselt number as a function of the Reynolds number were developed.

Ma et al. [17] performed an experimental study to investigate the local convective heat transfer from a vertical heated surface to an obliquely impinging circular free surface jet of transformer oil. The effect of the jet inclination was examined in a range of Reynolds number



between 235 and 1745, and the inclination angle between 45 and 90 degrees. Ma et al. [18] performed an experimental study to characterize recovery factor and heat transfer coefficient on vertical heaters impinged by submerged circular transformer oil jets issued from both pipe and orifice nozzles. Local Nusselt number at the stagnation point was found to be proportional nearly to square root of jet Reynolds number in the range 220-1500 and essentially non affected by the plate-to-nozzle distance for Reynolds number less than 600. Ma et al. [19] carried out measurements to determine recovery factor and heat transfer coefficients resulting from the impingement of transformer oil jets. This study focussed on initially laminar jets in the range of jet Reynolds number between 55-415, and Prandtl number between 200-270. This study was performed for confined slot jets. Lee et al. [20] conducted a numerical study to characterize the thermal behavior of laminar circular liquid jets. The effects of different parameters investigated included Reynolds number, Prandtl number, nozzle-to-plate distance, jet velocity, nozzle diameter, and velocity profile at nozzle exit.

Ma et al. [21] performed experimental measurements to investigate the local behavior of the recovery factor and heat transfer coefficient when a free surface oil jet impinges on a vertical uniformly heated surface. The results showed that the recovery factor was nearly independent of both Reynolds number and nozzle-to-plate distance. The heat transfer coefficient at the stagnation point was found independent of the nozzle-to-plate distance but proportional to the square root of Reynolds number. The recovery factor dependence on Prandtl number was expressed in different correlations.

Leland and Pais [22] performed an experimental investigation to determine the heat transfer rates for an impinging free surface axisymmetric jet of lubricating oil for a wide range of Prandtl numbers, and for conditions varying inside the fluid film. They concluded that the heat transfer surface configuration has an important effect on the Nusselt number. The effect of recovery temperature could be correlated by  $Pr^{0.47}$ . For constant flow rate or Reynolds number, larger nozzle diameters were shown to give higher heat transfer rates.

Even though there has been an impressive amount of research work on free jet impingement, there has been no attempt to numerically model the conjugate heat transfer process where heat is transmitted through a solid body from the heat source located on one side and fluid is impinging on the opposite side. In addition, the variation of fluid properties with temperature has not been taken into account in any previous numerical work, and has been assumed to be negligible in most analytical work. When the lubricating oil is used as a coolant and temperature difference between the jet and the disk is large, the property variation within the flow field greatly affects the heat transfer process. Therefore the development of a numerical model for conjugate heat transfer during free jet impingement taking into account the variation of fluid properties with temperature is expected to be a very valuable contribution to the state-of-the-art of jet impingement cooling system design.

## MATHEMATICAL MODEL

We consider an axisymmetric jet discharging from a nozzle and impinging on the center of a solid uniformly heated circular disk as shown in Figure 1. The working fluid is MIL-7808, a lubricating oil certified for military aircraft. The fluid is considered to be incompressible with density dependent on local temperature. The equations describing the conservation of mass, momentum, and energy in cylindrical coordinates can be written as [23]:

$$\frac{1}{r} \frac{\partial}{\partial r} (\rho_f r v_r) + \frac{\partial}{\partial z} (\rho_f v_z) = 0 \quad (1)$$

$$\rho_f \left( v_r \frac{\partial v_r}{\partial r} + v_z \frac{\partial v_r}{\partial z} \right) = -\frac{\partial p}{\partial r} + \frac{1}{r} \frac{\partial}{\partial r} \left[ \frac{2}{3} r \mu \left( 2 \frac{\partial v_r}{\partial r} - \frac{v_r}{r} - \frac{\partial v_z}{\partial z} \right) \right] + \frac{\partial}{\partial z} \left[ \mu \left( \frac{\partial v_r}{\partial z} + \frac{\partial v_z}{\partial r} \right) \right] \quad (2)$$

$$\rho_f \left( v_r \frac{\partial v_z}{\partial r} + v_z \frac{\partial v_z}{\partial z} \right) = -\rho_f g - \frac{\partial p}{\partial z} + \frac{1}{r} \frac{\partial}{\partial r} \left[ r \mu \left( \frac{\partial v_r}{\partial z} + \frac{\partial v_z}{\partial r} \right) \right] + \frac{\partial}{\partial z} \left[ \frac{2}{3} \mu \left( 2 \frac{\partial v_z}{\partial z} - \frac{v_r}{r} - \frac{\partial v_r}{\partial r} \right) \right] \quad (3)$$

$$\begin{aligned} \rho_f \left( v_r \frac{\partial (c_{p_f} T_f)}{\partial r} + v_z \frac{\partial (c_{p_f} T_f)}{\partial z} \right) &= \left[ \frac{1}{r} \frac{\partial}{\partial r} \left( r k_f \frac{\partial T_f}{\partial r} \right) + \frac{\partial}{\partial z} \left( k_f \frac{\partial T_f}{\partial z} \right) \right] + \left( v_z \frac{\partial p}{\partial z} + v_r \frac{\partial p}{\partial r} \right) \\ &+ \mu_f \left\{ 2 \left[ \left( \frac{\partial v_r}{\partial r} \right)^2 + \left( \frac{v_r}{r} \right)^2 + \left( \frac{\partial v_z}{\partial z} \right)^2 \right] + \left( \frac{\partial v_r}{\partial z} + \frac{\partial v_z}{\partial r} \right)^2 - \frac{2}{3} \left[ \frac{\partial v_r}{\partial r} + \frac{v_r}{r} + \frac{\partial v_z}{\partial z} \right]^2 \right\} \end{aligned} \quad (4)$$

Inside the solid, the variation of thermal conductivity with temperature was found to be negligible for all materials considered in the present investigation. Therefore considering constant properties, the equation describing the conservation of energy can be written as follows:

$$\frac{\partial^2 T_s}{\partial r^2} + \frac{1}{r} \frac{\partial T_s}{\partial r} + \frac{\partial^2 T_s}{\partial z^2} = 0 \quad (5)$$

To complete the set to be solved, equations (1-5) are subjected to the following boundary conditions:

$$\text{At } r = 0, 0 \leq z \leq b: \frac{\partial T_s}{\partial r} = 0 \quad (6)$$

$$\text{At } r = 0, b \leq z \leq H_n: v_r = 0, \frac{\partial v_z}{\partial r} = 0, \frac{\partial T_f}{\partial r} = 0 \quad (7)$$

$$\text{At } r = r_o, 0 \leq z \leq b: \frac{\partial T_s}{\partial r} = 0 \quad (8)$$

$$\text{At } r = r_o, b \leq z \leq \delta: p = 0, \frac{\partial T_f}{\partial r} = 0 \quad (9)$$

$$\text{At } z = 0: -k_s \frac{\partial T_s}{\partial z} = q \quad (10)$$

$$\text{At } z = b: T_s = T_f, v_r = 0, v_z = 0, k_s \frac{\partial T_s}{\partial z} = k_f \frac{\partial T_f}{\partial z} \quad (11)$$

$$\text{At } z = b + H_n, 0 \leq r \leq r_n: v_r = 0, v_z = -v_j, T_f = T_j \quad (12)$$

$$\text{At } z = \delta, r_n < r < r_o:$$

$$\frac{d\delta}{dr} = \frac{v_z}{v_r}, p = p_{atm} - \frac{\sigma \frac{d^2\delta}{dr^2}}{\left[1 + \left(\frac{d\delta}{dr}\right)^2\right]^{3/2}}, \frac{\partial v_t}{\partial n} = 0, \frac{\partial T_f}{\partial n} = 0 \quad (13)$$

## NUMERICAL COMPUTATION

The governing equations along with the boundary conditions described in the previous section were solved using the finite element method. The purpose of this method is to break down the continuum problem of essentially an infinite number of degrees of freedom to a finite number of degrees by discretizing the continuum into a number of simple shaped elements. The dependent variables, i.e., velocity, pressure, and temperature were interpolated to a set of nodal points that defined the finite element. In each element, the velocity, pressure, and temperature fields were approximated which led to a set of equations that defined the continuum. The approach used to solve the free surface problem described here was to introduce a new degree of freedom at the nodes on the free surface. This degree of freedom represented the position of the free surface. It was introduced as a new unknown into the global system of equations. The discretization of governing transport equations and boundary conditions was carried out using the Galerkin formulation. The solution of the resulting algebraic equations was carried out using the Newton-Raphson method. This method allowed a simultaneous solution of the discretized equations and a faster convergence when the guess used for the free surface was close enough to the final form. Since the solution of the momentum equation required only two out of the three boundary conditions at the free surface, the third condition was used to upgrade the position of the free surface at the end of each iteration step. The Newton-Raphson solver used spines to track the free surface and modify grid distribution with the movement of the free surface. These spines were straight lines passing through the free surface nodes and connecting the nodes underneath the free surface. The free surface movement affected only nodes along the spine.

Due to large number of iterations required to determine the location of the free surface, the solution was carried out in two steps. First, the computation in the fluid region was carried out solving equations for the conservation of mass and momentum. This resulted in the determination of the velocity field and the free surface height distribution. The drawback of this solution is that because of no heat transfer, the fluid remained isothermal, and therefore properties remained constant. This approximate solution was the starting point for the second level of computation where both solid and fluid regions were included and equations for the conservation of mass, momentum, and energy were solved simultaneously as a conjugate problem taking into account the variation of fluid properties with temperature. This split level computation procedure greatly reduced the run time for numerical computation. The solution

was considered converged when the field values did not change from one iteration to the next, and the sum of residuals for each degree of freedom was less than 1E-08.

## RESULTS AND DISCUSSION

The fluid considered in the present investigation was MIL 7808. The properties of this fluid can be written according to the following equations, which are valid for  $303\text{ K} < T < 390\text{ K}$ :  
 $c_p = 903.8 + 3.332T$  ,  $k = 0.18 - 1 \times 10^{-4}T$  ,  $\rho = 1181 - 0.708T$  , and  $\mu = 0.941 - 5.07 \times 10^{-3}T + 6.87 \times 10^{-6}T^2$  . For the temperature range encountered in this investigation, Pr varied between 48-71.

In order to determine the number of elements for accurate numerical solution, computation was performed for several combinations of grid distribution in the radial and axial directions covering the solid and fluid regions. The solid-fluid interface temperature for these simulations are plotted in Figure 2. It was observed that the solution becomes grid independent when the number of divisions in the radial direction was increased over 28 and at least 36 divisions were used in the axial direction. In order to have smooth variation of transport quantities,  $42 \times 36$  divisions in the radial and axial directions were chosen. The size of the elements was different in different regions of the computation domain.

The distribution of velocity vectors is presented in Figure 3. It can be seen that the velocity remains almost uniform at the potential core region of the jet. As the fluid gets closer to the stagnation region, the velocity decreases and the jet diameter increases. The direction of motion of the fluid particles shift by as much as  $90^\circ$ . At the stagnation zone, the velocity reaches its minimum value. After this point the fluid accelerates creating a region of minimum sheet thickness. This is the start of the boundary layer zone. It can be noticed that as the boundary layer thickness increases, the frictional resistance from the wall is eventually transmitted to the entire film thickness. This is called the fully viscous zone. The vectors show a parabolic behavior of the fluid velocity in this region, going from zero at the wall to the maximum at the free surface. Due to high viscosity of the working fluid, the boundary layer develops rapidly and the velocity of the fluid decreases as it spreads radially along the disk. The three different regions observed in the present investigation are in-line with the experiments of Liu and Lienhard [6].

Figure 4 presents the free surface height distribution for different Reynolds number when the jet strikes the center of the disk. It can be seen that the fluid spreads radially as a thin film. For the conditions considered in the present investigation, the flow was supercritical and a hydraulic jump did not occur within the computation domain. It can be observed that the minimum film height occurs at a radius larger than the radius of the nozzle and the film height gradually increases with radius after that location. A smaller thickness is seen at larger Reynolds number because of larger impingement velocity that translates to a larger fluid velocity in the film.

The temperature distribution at the solid-fluid interface is presented in Figure 5. As expected, the temperature is minimum at the center of the disk and gradually increases with radius. It can be noticed that the maximum-to-minimum temperature difference remained almost constant, with a value around  $4.1 \times 10^{-5}$ . The interface temperature decreases with increase in

Reynolds number because of larger local fluid velocity, which results in larger rate of heat transfer.

Figure 6 shows the variation of local Nusselt number for different Reynolds number. Nusselt number is maximum at the stagnation point and decreases along the radial coordinate. A rapid decrease occurs at the impingement region as the fluid particles turn by an angle of  $90^\circ$  from the axial to the radial direction. In the vicinity of  $\xi = 0.5$  ( $r = r_n$ ), Nusselt number attains an almost constant value. This local Nusselt number value was compared with stagnation Nusselt number correlations developed by Hrycak [5] and Ma et al. [21]. It was found that for Reynolds number considered in the present investigation, the difference between the present numerical solution and past experimental correlations ranged between 0.3-22.5%. The results compared better with Ma et al.[21] at lower Reynolds number and with Hrycak [5] at higher Reynolds number because of corresponding range of test data used to develop these correlations. This transition region near  $\xi = 0.5$  is also consistent with the previous observation of Wang et al. [8].

After the transition from stagnation region to boundary layer region has occurred, the Nusselt number decreases further showing a trend similar to the development of a thermal boundary layer during laminar forced convection. As the thickness of the thermal boundary layer increases, Nusselt number decreases in magnitude because of the increment in the thermal resistance between the wall and the low temperature free stream fluid. Due to large Prandtl number of the working fluid considered in the present investigation, the thickness of the thermal boundary layer does not reach the film height. Nusselt number continues to decrease with the radial distance until instabilities in the flow bring about a transition to turbulence. At this point, low temperature liquid from the free stream mixes with the boundary layer, increasing the heat transfer coefficient [11, 12]. The radius of the disk was not enough to bring the fluid to total turbulence, but the start of transition to turbulence is apparent in the increment of Nusselt number near the edge of the disk. The increase of Nusselt number with Reynolds number is due to higher impingement velocity that translates to higher velocity in the fluid film along the radial direction.

Figure 6 also reports the average Nusselt number for three different Reynolds numbers. As expected, the average Nusselt number increases with Reynolds number. These results were compared with the average Nusselt number correlation presented by Incropera and DeWitt [24] and found to be within 6-10%. The average heat transfer coefficient obtained from the present numerical simulation for different combinations of Reynolds number and input heat flux are listed in Table 1, where they are compared with the experimental data of Leland and Pais [22]. It may be noted that numerical predictions are within 11.7% of experimental measurements and a better correlation of results are obtained at larger heat fluxes. The measurement errors are expected to be larger at smaller heat fluxes because of smaller magnitude of temperature and more peripheral losses. Computationally, errors can be introduced because of round-off and discretization. Considering these factors, the overall comparison with test data is quite satisfactory.

Figure 7 presents the variation of Nusselt number when the heat flux at the bottom of the disk is changed. As the heat flux increases, the Nusselt number increases. It is important to notice that when the heat flux is increased from 63 to 252 kW / m<sup>2</sup> (by 300 %), the Nusselt

number increases by about 12 %. The effect of disk thickness on the variation of Nusselt number can be observed in Figure 8. It shows that the maximum local Nusselt number as well as the average value of Nusselt number over the disk decreases as the thickness increases. It may be noticed that Nusselt number becomes more uniform as the disk thickness increases because of larger radial conduction within the disk.

The numerical simulation was carried out for four different disk materials, namely copper, constantan, silver, and aluminum. Figure 9 shows that there is hardly any difference in the distribution of local Nusselt number for copper, aluminum, and silver. This is because of very similar thermal conductivity ( $k = 386, 204, 419 \text{ W /m K}$ ) of these materials. When the thermal conductivity is reduced to  $k = 22.7 \text{ W /m K}$  (constantan), the Nusselt number increases over the entire disk. The effect of disk thickness on the average Nusselt number for two different materials can be observed in Figure 10. It shows how the average Nusselt number decreases as the disk thickness increases. This effect is more significant at smaller thicknesses. It may be noticed that constantan have higher values of average Nusselt number than copper at all disk thicknesses. This is consistent with the local variation seen in Figure 9. A summary of average heat transfer coefficient and average Nusselt number for different combinations of disk material and disk thickness is presented in Table 2.

Figure 11 presents the maximum temperature in the solid, the maximum temperature at the interface, and the difference between the maximum and minimum temperature at the interface for two different disk materials. The maximum temperature inside the solid always occurred at the outer edge of the disk ( $r = r_o$ ) just next to the heater ( $z = 0$ ). The control of this temperature is crucial in the design of electronic packages. It may be noticed that the maximum temperature decreases with thickness, reaches a minimum around  $b = 2.5$  and increases with further increase of disk thickness. At smaller thicknesses, the radial heat conduction increases as the thickness increases and its magnitude is greater than the thermal resistance created by the increment in material. After reaching an equilibrium condition between the radial heat conduction and the thermal resistance, any increment in the material thickness only increases the thermal resistance and the radial heat conduction remains approximately constant. This indicates that increasing the wafer thickness beyond certain point may not be useful. However, the choice of the wafer material is crucial in determining the magnitude of this temperature. As expected, a material with larger thermal conductivity will facilitate a faster rate of heat transfer, and therefore will result in a lower maximum temperature within the solid. The maximum temperature at the interface can be observed in the same figure. It is noticed that this temperature decreases with thickness at smaller thicknesses and remains almost invariable at larger thicknesses. The temperature difference at the interface is an indication of the level of temperature non-uniformity at the impingement surface. When the disk thickness is negligible, the interface temperature is controlled by the uniform heat flux condition at the heater. However, when an adequate thickness is provided, the interface temperature becomes more uniform because of radial spreading of heat within the solid. It may also be noticed that the magnitude of maximum to minimum temperature difference is very strongly affected by the thermal conductivity of the disk material.

The dimensionless temperature contours within the impingement plate for different Reynolds number are presented in Figure 12. The minimum temperature occurs at the stagnation

point and the maximum temperature occurs across the disk at the largest radial location. The maximum-to-minimum temperature difference inside the disk remains almost constant with a value of around  $5e-5$ . It is important to notice that at higher Reynolds number, the isotherms become more parallel to each other. The magnitude of temperature within the solid is very strongly affected by Reynolds number.

The effect of disk thickness on temperature distribution within the solid is seen in Figure 13. It can be observed that the temperature becomes more uniform as the disk thickness is increased. It is interesting to notice that when the disk thickness is large, the temperature remains stratified over a significant part of the disk. The isothermal lines run parallel to the bottom of the disk indicating an almost one-dimensional heat conduction. However, in regions near the solid-fluid interface, the isothermal lines tend to be concentric around the stagnation point. The effect of non-uniform convection is felt only over a part of the disk. When the disk thickness is small, the temperature contours have entirely different orientation because of strong radial conduction over the entire disk thickness.

Figure 14 shows the temperature distribution inside the disk for two different materials. For copper it is seen that the temperature is more uniform and the maximum-to-minimum temperature difference is smaller ( $5e-5$ ). For constantan the maximum-to-minimum temperature difference is fairly large ( $7.2e-4$ ) because of much lower thermal conductivity. The shapes of the isotherms are not significantly affected by thermal conductivity.

Figure 15 presents the variation of average Nusselt number for different nozzle height. It can be seen that Nusselt number increases as the distance between the nozzle and the disk is increased. This is caused by acceleration of the fluid due to gravity as it exits the nozzle and approaches the plate. It may be noticed that smaller changes are seen at smaller height, whereas larger increases are observed when the nozzle height is increased over  $H = 5$ . Figure 16 shows how the maximum temperature in the solid varies with the nozzle height. It is important to notice that this temperature increases as the nozzle height increases up to a certain point, and then it starts to decrease as the nozzle height continues to increase. This indicates that certain nozzle height is least desirable for the cooling of electronics where controlling the source temperature to a minimum is crucial for high reliability. The maximum temperature at the interface presents a similar behavior to the one observed inside the solid. The same figure shows that the maximum-to-minimum temperature difference increases as the nozzle height increases. Despite these interesting behaviors, it is important to note that the magnitude of temperature variation with change in nozzle height is quite small.

## NOMENCLATURE

$b$	Dimensionless thickness of the disk, $th/d_n$
$c_p$	Specific heat at constant pressure [kJ / kg K]
$d_n$	Diameter of the nozzle [m]
$g$	Acceleration due to gravity [m / s <sup>2</sup> ]
$h$	Local heat transfer coefficient, $q_{int}/(T_{int} - T_b)$ [W / m <sup>2</sup> K]

$h_{av}$  Average heat transfer coefficient,  $Q/(\pi r_o^2)(\bar{T}_{int} - T_b)$  [W / m<sup>2</sup> K]

H Dimensionless nozzle height,  $H_n / d_n$

$H_n$  Height of the nozzle from the disk [m]

$k$  Thermal conductivity [W / m K]

$n$  Coordinate normal to the free surface [m]

$Nu$  Local Nusselt number,  $hr_o/k_f$

$Nu_{av}$  Average Nusselt number,  $h_{av}r_o/k_f$

$p$  Pressure [Pa]

$q$  Heat flux [W / m<sup>2</sup>]

$Q$  Total heat input rate [W]

$r$  Radial coordinate [m]

$r_n$  Radius of the nozzle [m]

$r_o$  Radius of the disk [m]

Re Reynolds number,  $\nu_j d_n / \nu_f$

th Thickness of the disk [m]

$T$  Temperature [K]

$T_b$  Average bulk temperature,  $(T_j + T_o)/2$  [K]

$\bar{T}_{int}$  Average temperature at the solid-fluid interface [K]

$T_j$  Jet temperature [K]

$T_o$  Average fluid temperature at the outer edge of the disk [K]

$\nu_j$  Jet velocity [m / s]

$\nu_r$  Radial velocity [m / s]

$\nu_t$  Velocity along the free surface [m / s]

$\nu_z$  Axial velocity [m / s]

$z$  Axial coordinate [m]

### Greek Symbols

$\delta$  Height of the free surface from the disk [m]

$\eta$  Dimensionless axial location,  $z/d_n$

$\theta$  Dimensionless temperature,  $k_f(T - T_j)d_n/Q$

$\mu$  Dynamic viscosity [kg / m s]

$\xi$  Dimensionless radial location,  $r/d_n$

$\rho$  Density [kg / m<sup>3</sup>]

$\sigma$  Surface tension coefficient [N / m]

### SUBSCRIPTS

atm Atmospheric condition

av Average

f Fluid

int Solid -fluid interface

s Solid



## CONCLUSIONS

A numerical model of conjugate heat transfer process where heat is transmitted through a solid body from a heater located on one side to a fluid jet impinging on the opposite side has been solved. The variation of fluid properties with temperature has been taken into account. It was found that the film thickness decreases as the impingement velocity increases. The Nusselt number showed a strong dependence on the impingement velocity; increasing their values as the velocity increased. The temperature at the solid-fluid interface decreased as the velocity increased. The average Nusselt number increased with Reynolds number. It also increased with the increase of input heat flux or the nozzle height. As the thickness of the disk was increased, the Nusselt number decreased. However, beyond a certain thickness, the disk showed a one dimensional heat conduction in regions away from the impingement surface and did not exert any significant influence on the convective heat transfer process. The maximum temperature inside the solid and the interface, and the maximum-to-minimum temperature difference at the interface were strongly affected by the variation of disk thickness. At smaller thicknesses, these three values decreased with thickness. After reaching an equilibrium point, the maximum temperature inside the solid increased while the maximum temperature and the interface and the maximum-to-minimum temperature at the interface remained almost invariable with thickness increments. The thermal conductivity of the disk material strongly affected the magnitude of maximum temperature in the solid, temperature difference at the interface, heat transfer coefficient, as well as the Nusselt number. Even though a lower thermal conductivity provided slightly better heat transfer coefficient, a higher thermal conductivity will maintain the disk at a lower temperature.

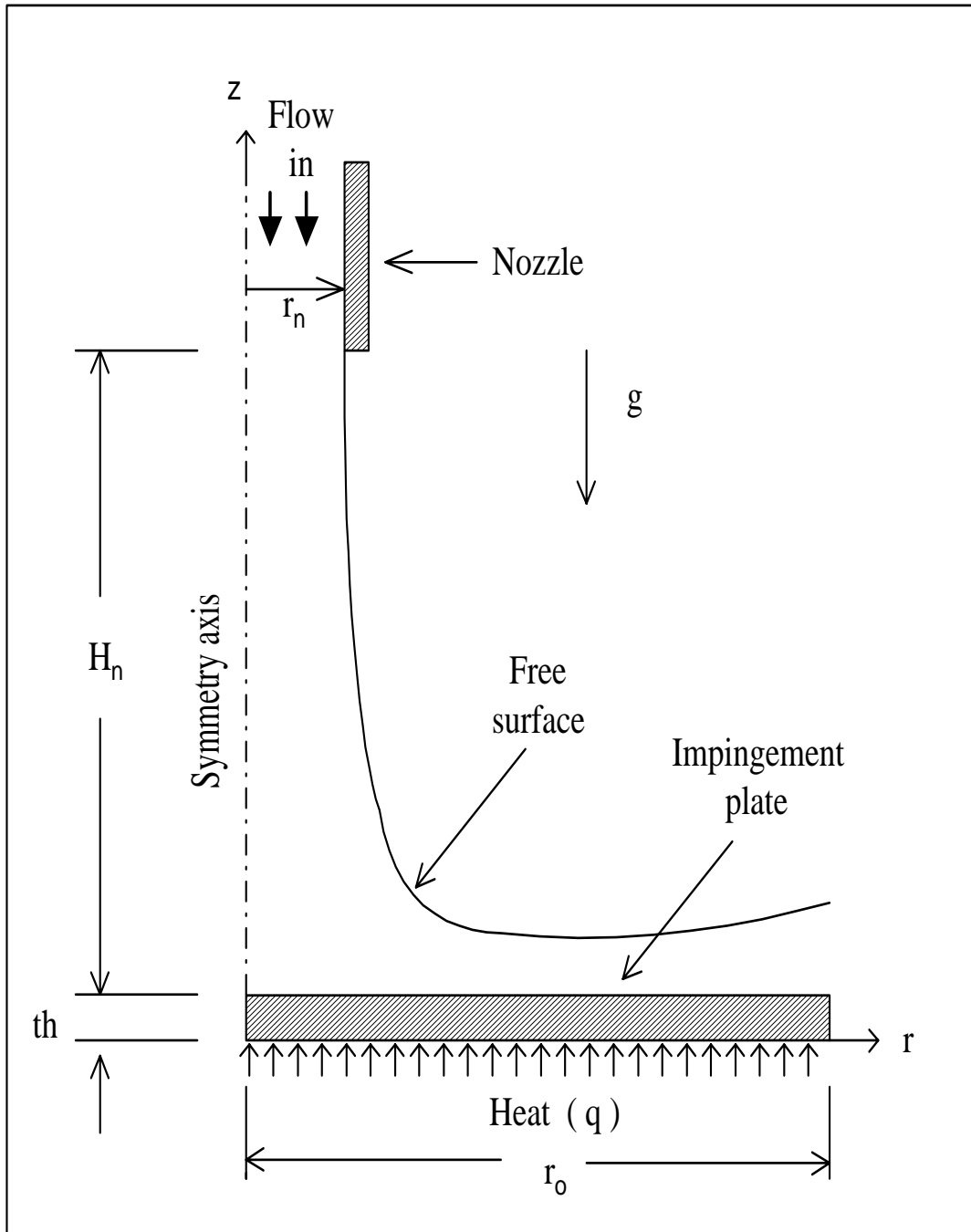


Figure 1. Schematic of an axial jet impingement

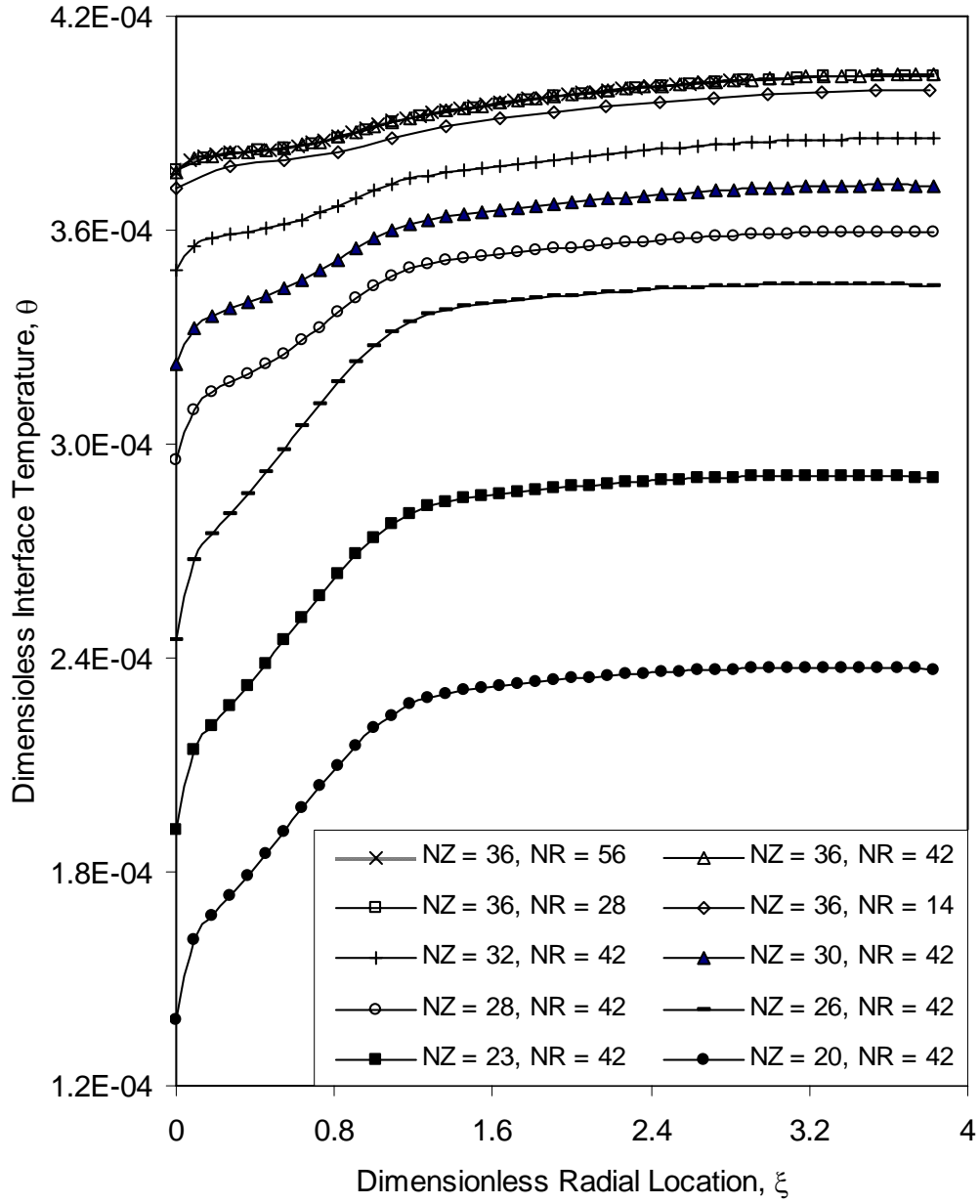


Figure 2. Dimensionless interface temperature for different number of elements in axial and radial directions  
(Re = 1100, b = 2.94, H = 5, Copper plate, q = 63 kW/m<sup>2</sup>, T<sub>j</sub> = 348 K, r<sub>n</sub> = 0.00085 m)

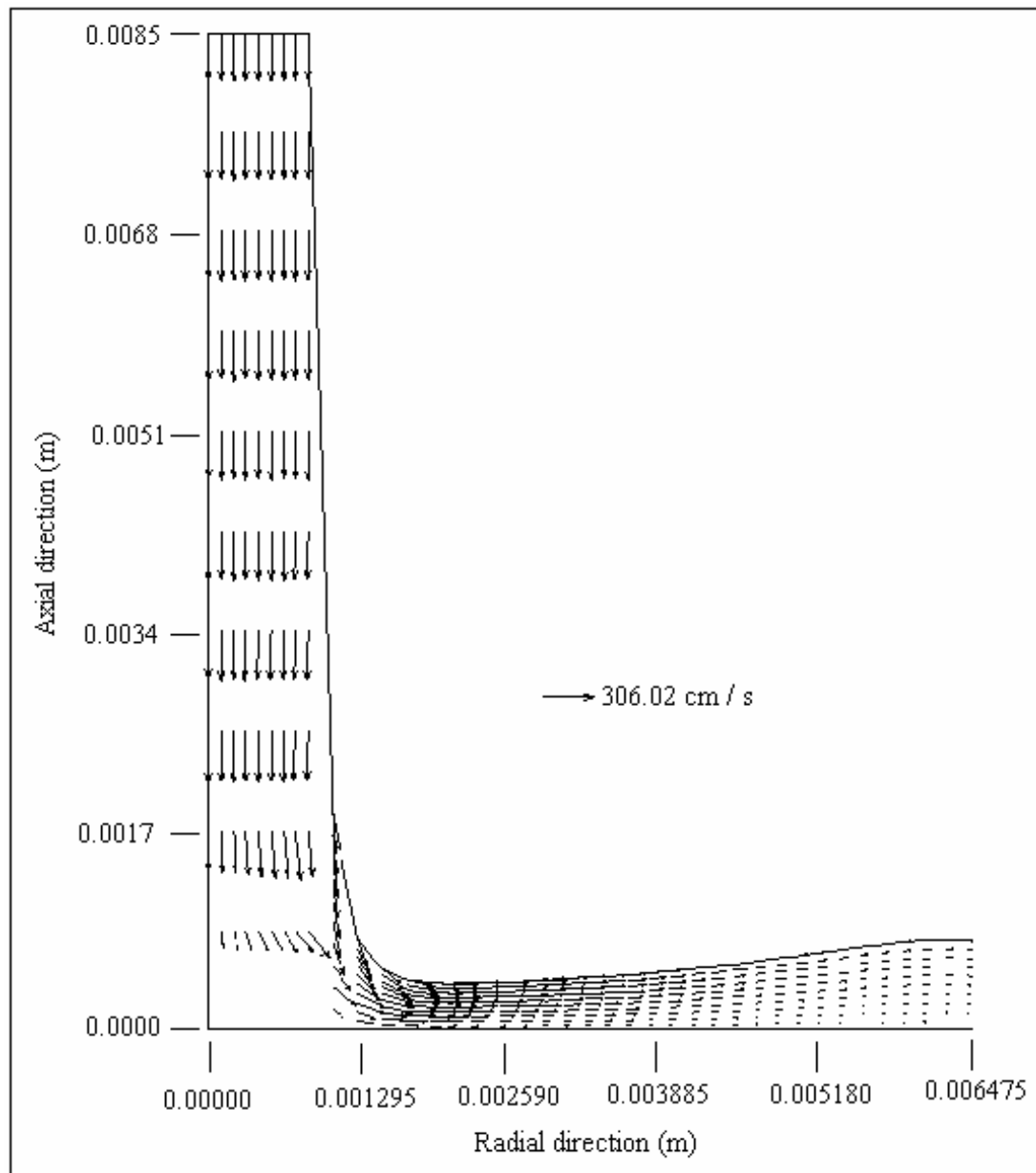


Figure 3. Velocity vectors ( $Re = 550$ ,  $H = 5$ )

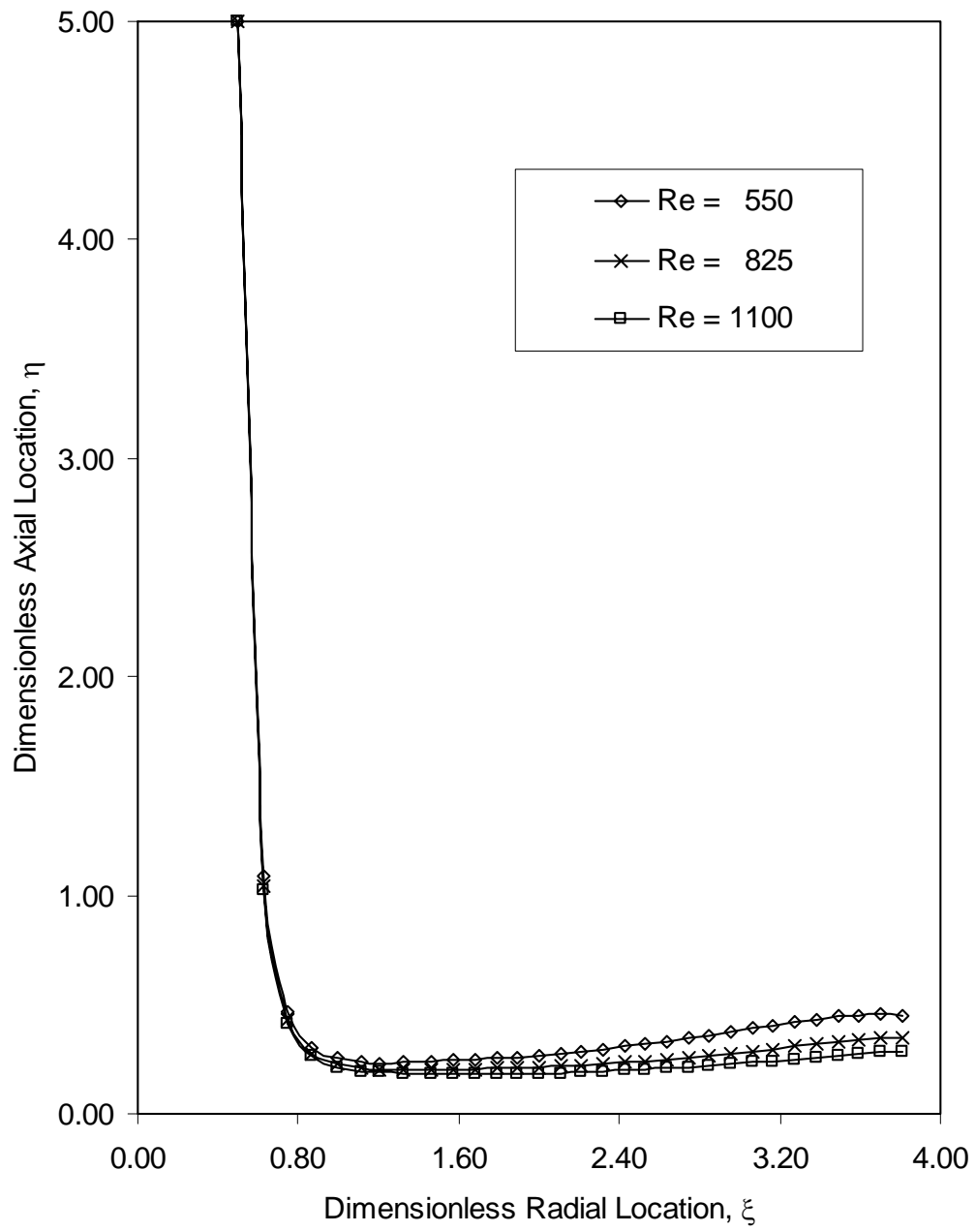


Figure 4. Free surface height distribution for different Reynolds number

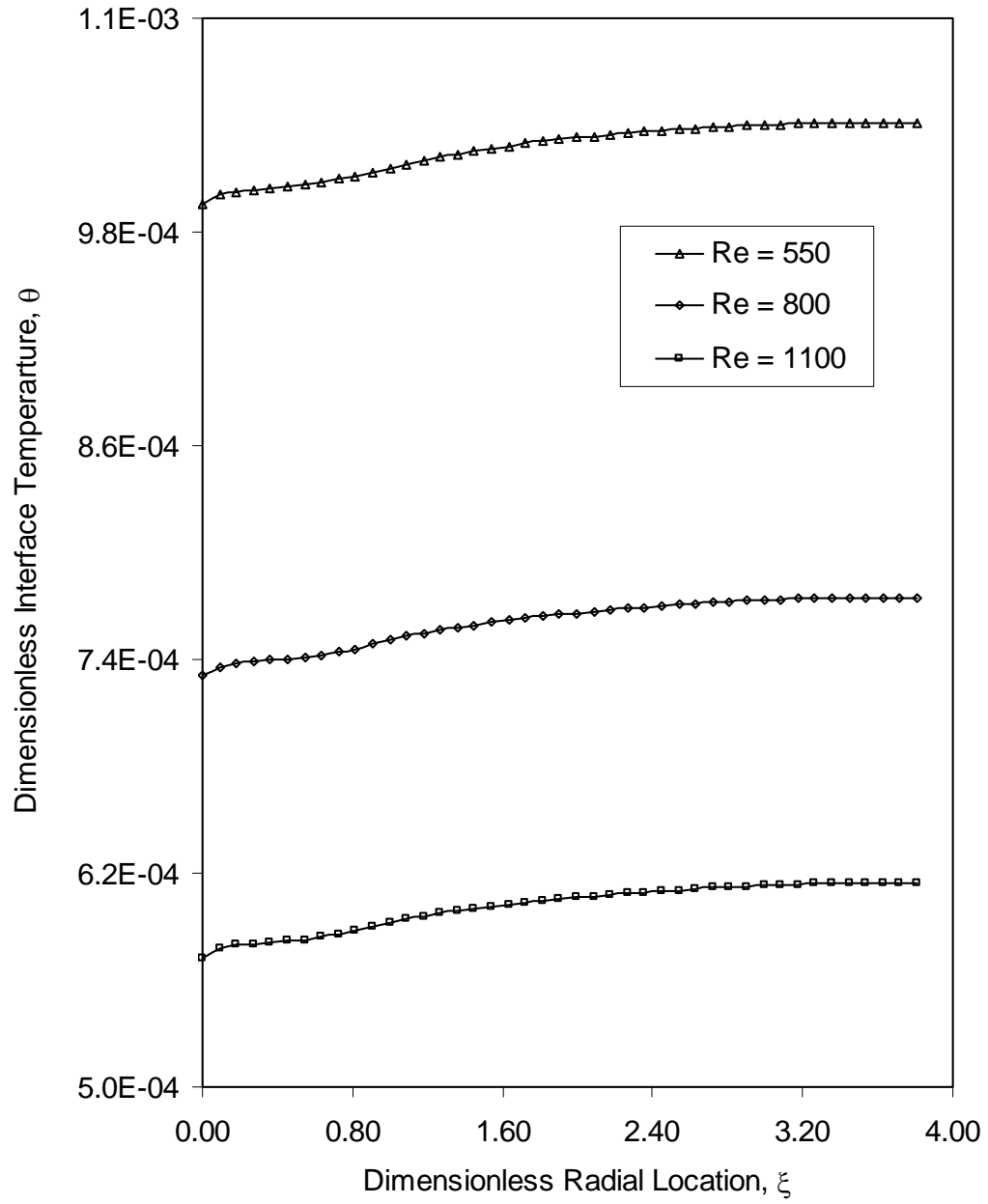


Figure 5. Temperature at solid-fluid interface for different Reynolds number  
 ( $b = 2.94$ ,  $H = 5$ , Copper plate,  $q = 63 \text{ kW/m}^2$ ,  $T_j = 348 \text{ K}$ ,  $r_n = 0.00085 \text{ m}$ )

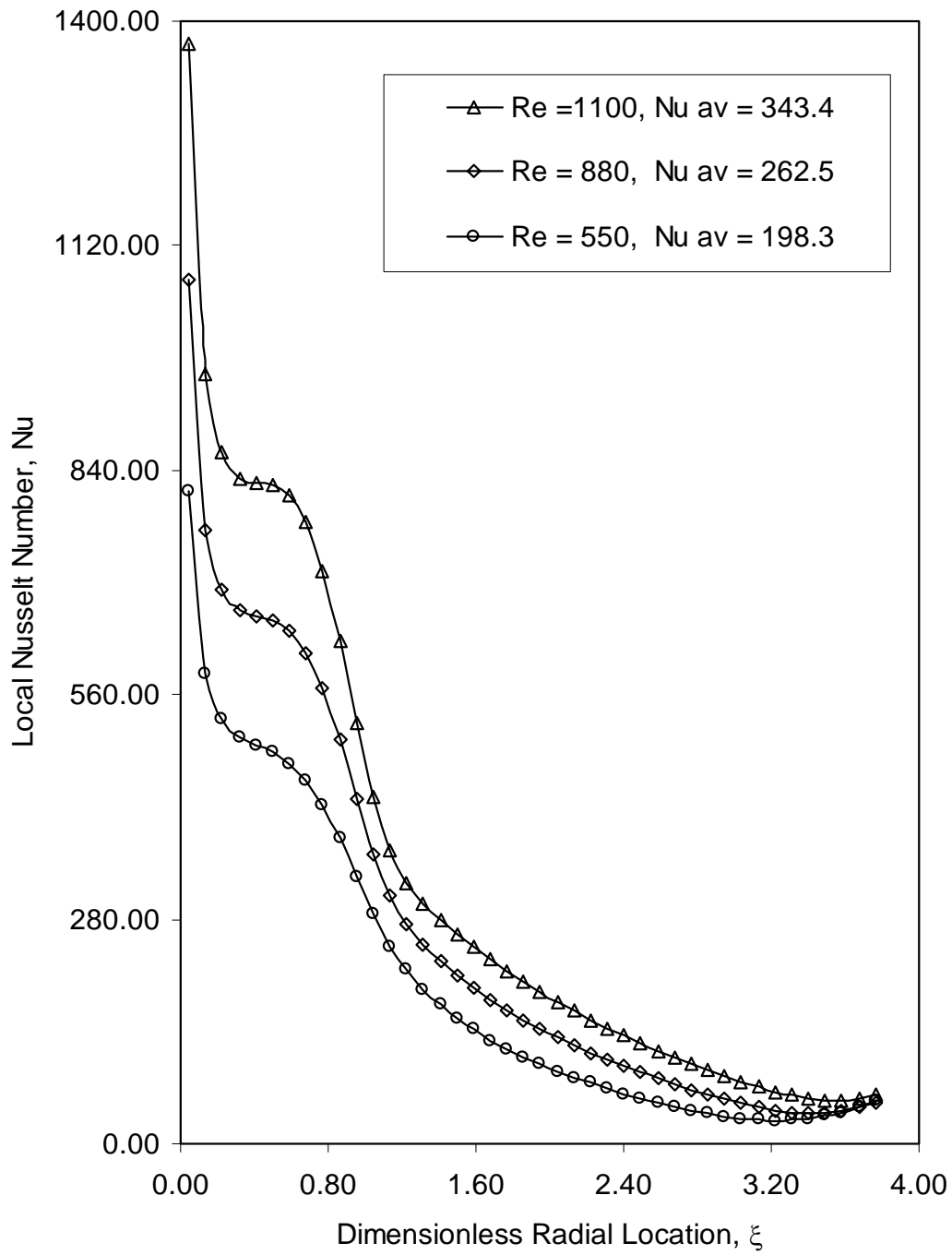


Figure 6. Local Nusselt number variation for different Reynolds number  
 ( $b = 2.94$ ,  $H = 5$ , Copper plate,  $q = 63 \text{ kW/m}^2$ ,  $T_j = 348 \text{ K}$ ,  $r_n = 0.00085 \text{ m}$ )

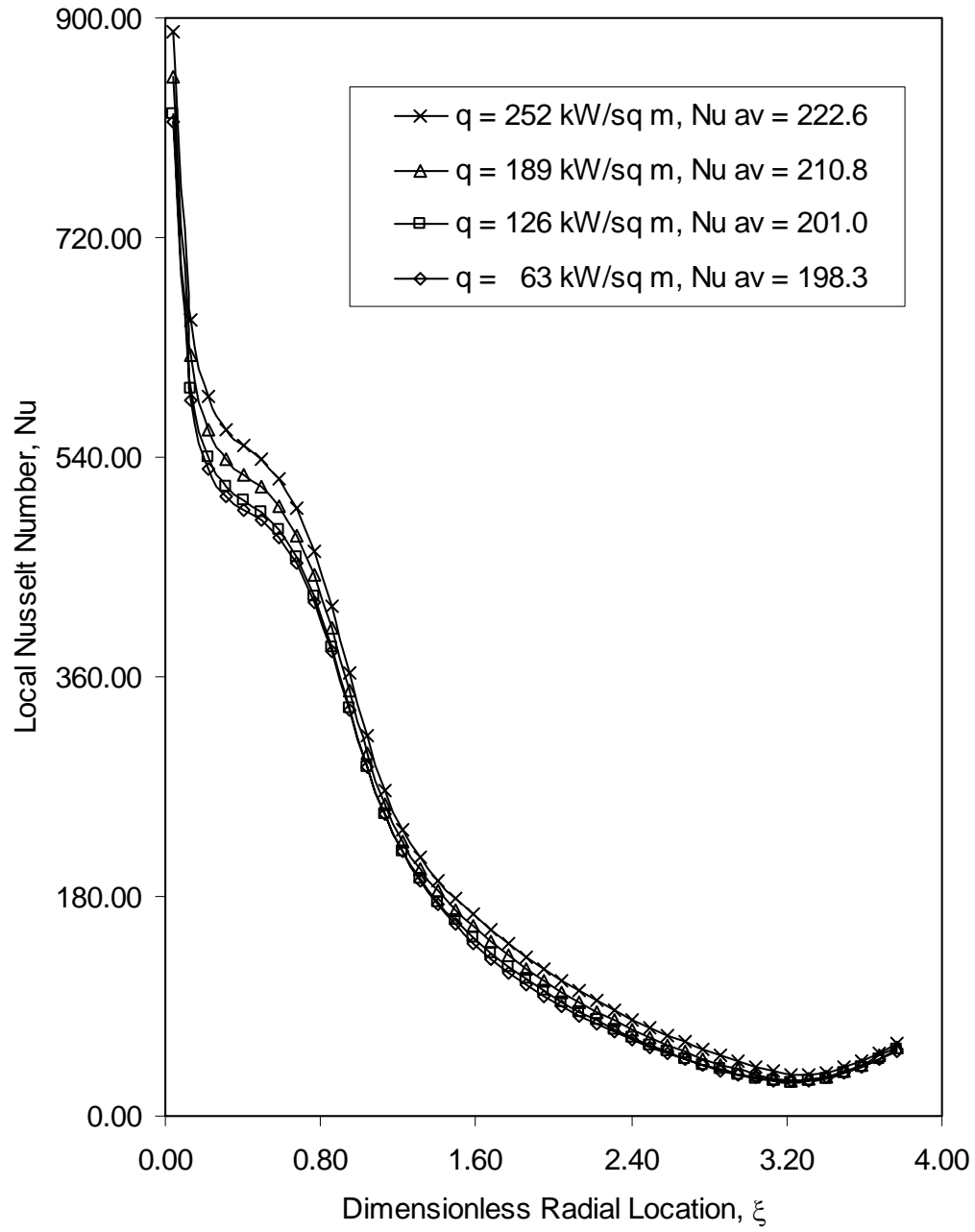


Figure 7. Local Nusselt number for different heat flux at the bottom of the disk  
 ( $Re = 550$ ,  $b = 2.94$ ,  $H = 5$ , Copper plate,  $q = 63 \text{ kW/m}^2$ ,  $T_j = 348 \text{ K}$ ,  
 $r_n = 0.00085 \text{ m}$ )



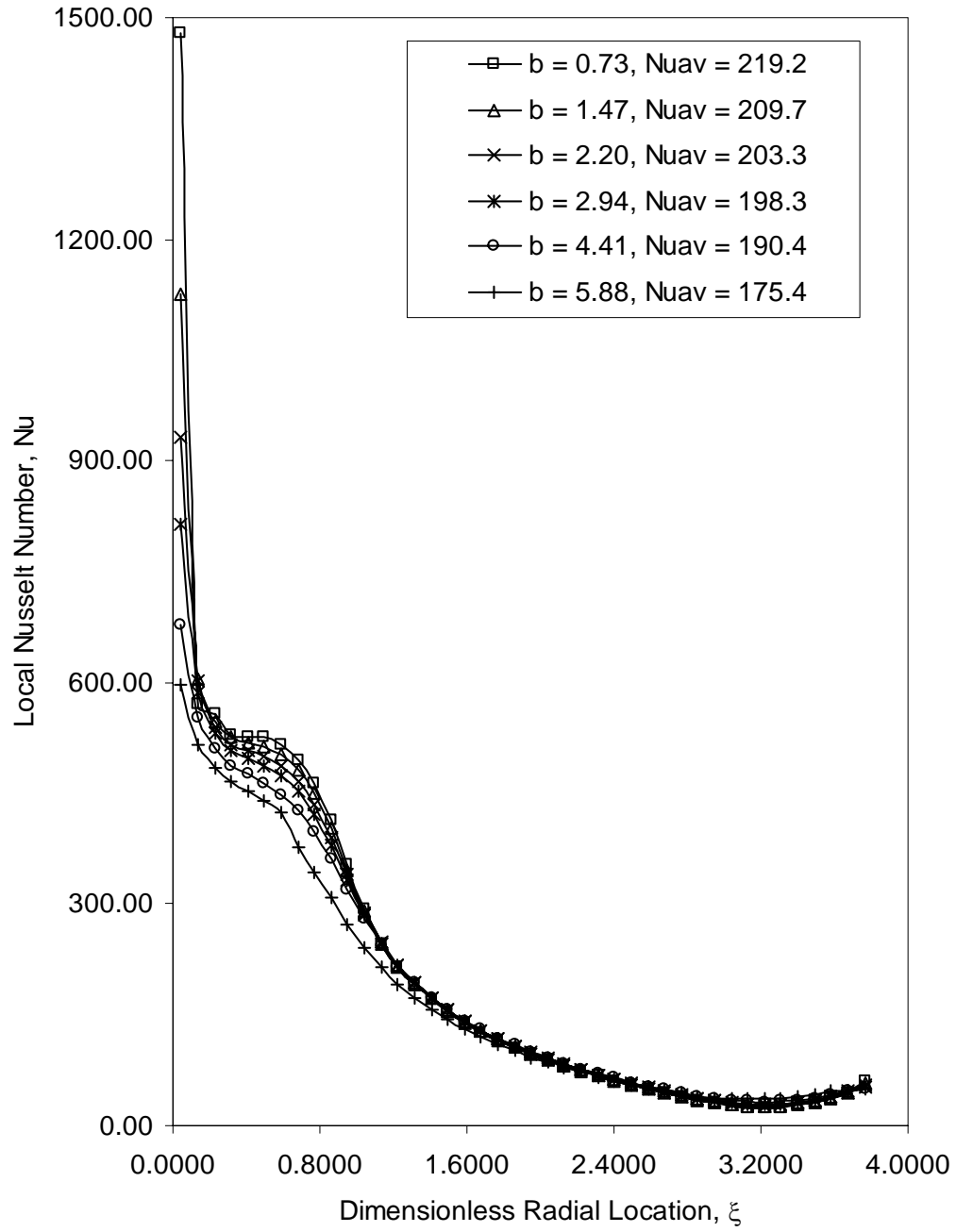


Figure 8. Local Nusselt number variation for different disk thickness  
 ( $Re = 550$ ,  $H = 5$ , Copper plate,  $q = 63 \text{ kW/m}^2$ ,  $T_j = 348 \text{ K}$ ,  $r_n = 0.00085 \text{ m}$ )

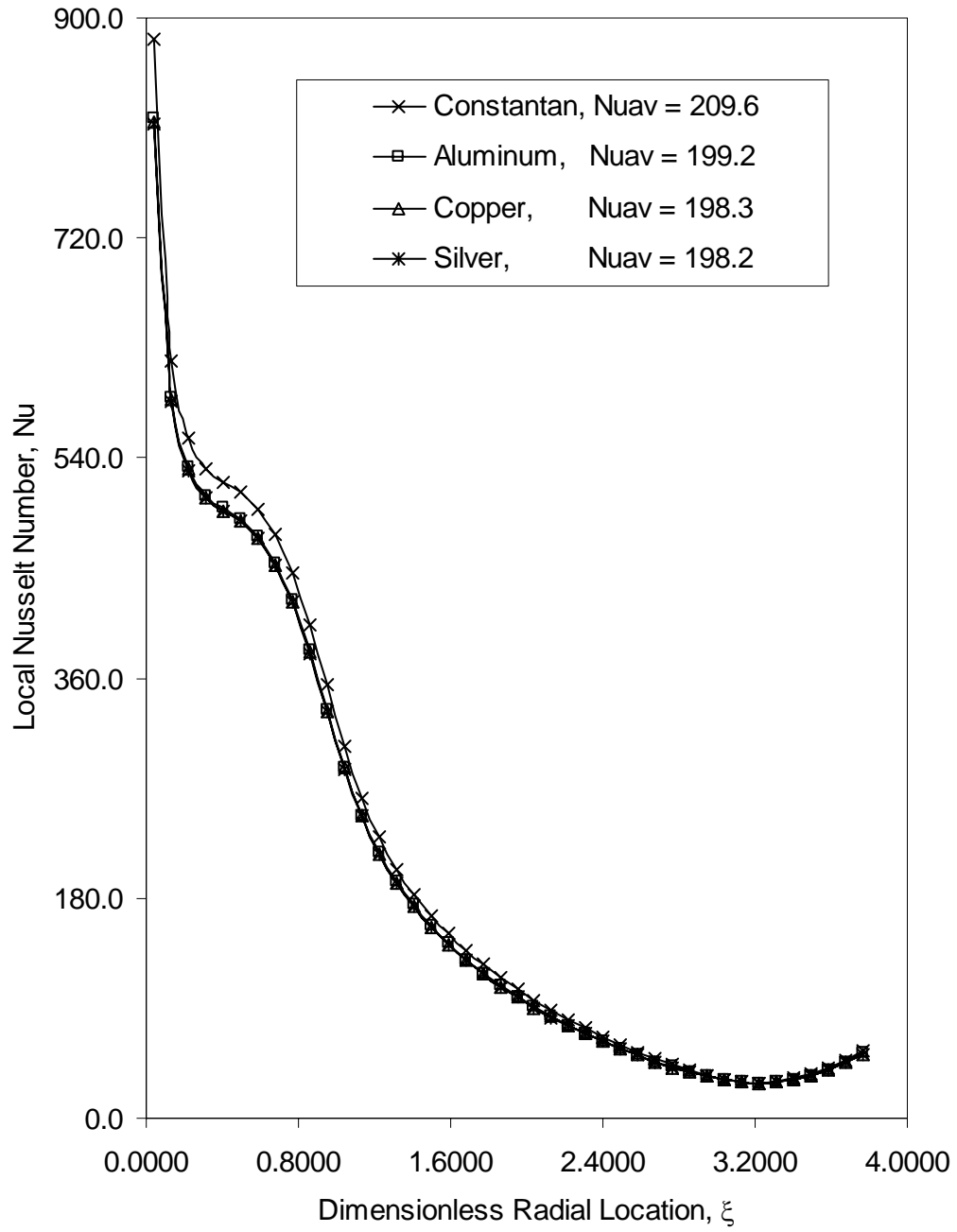


Figure 9. Local Nusselt number variation for different disk materials  
 ( $Re = 550$ ,  $b = 2.94$ ,  $H = 5$ ,  $q = 63 \text{ kW/m}^2$ ,  $T_j = 348 \text{ K}$ ,  $r_n = 0.00085 \text{ m}$ )

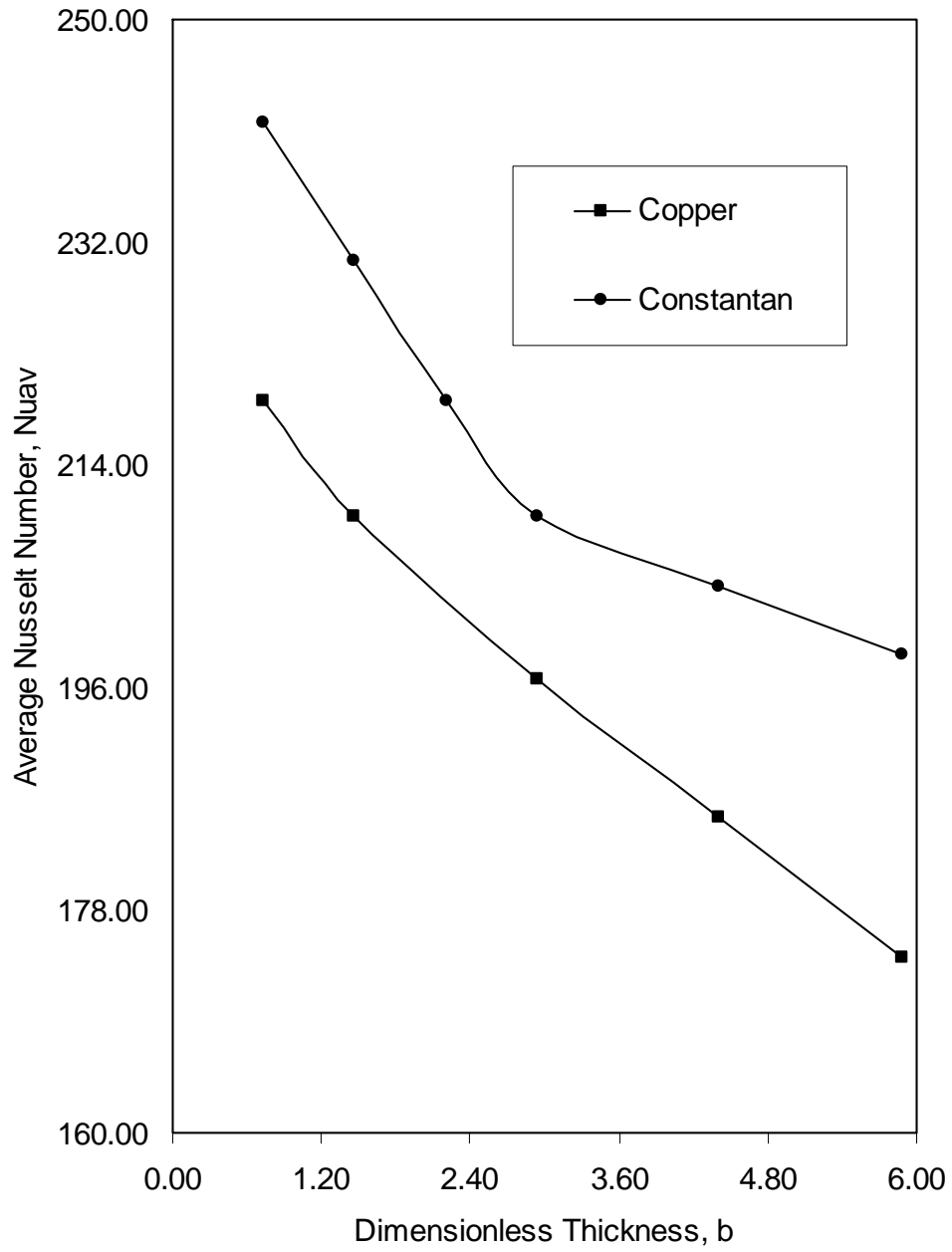


Figure 10. Average Nusselt number variation with disk thickness for two different materials ( $Re = 550$ ,  $b = 2.94$ ,  $H = 5$ ,  $q = 63 \text{ kW/m}^2$ ,  $T_j = 348 \text{ K}$ ,  $r_n = 0.00085 \text{ m}$ )

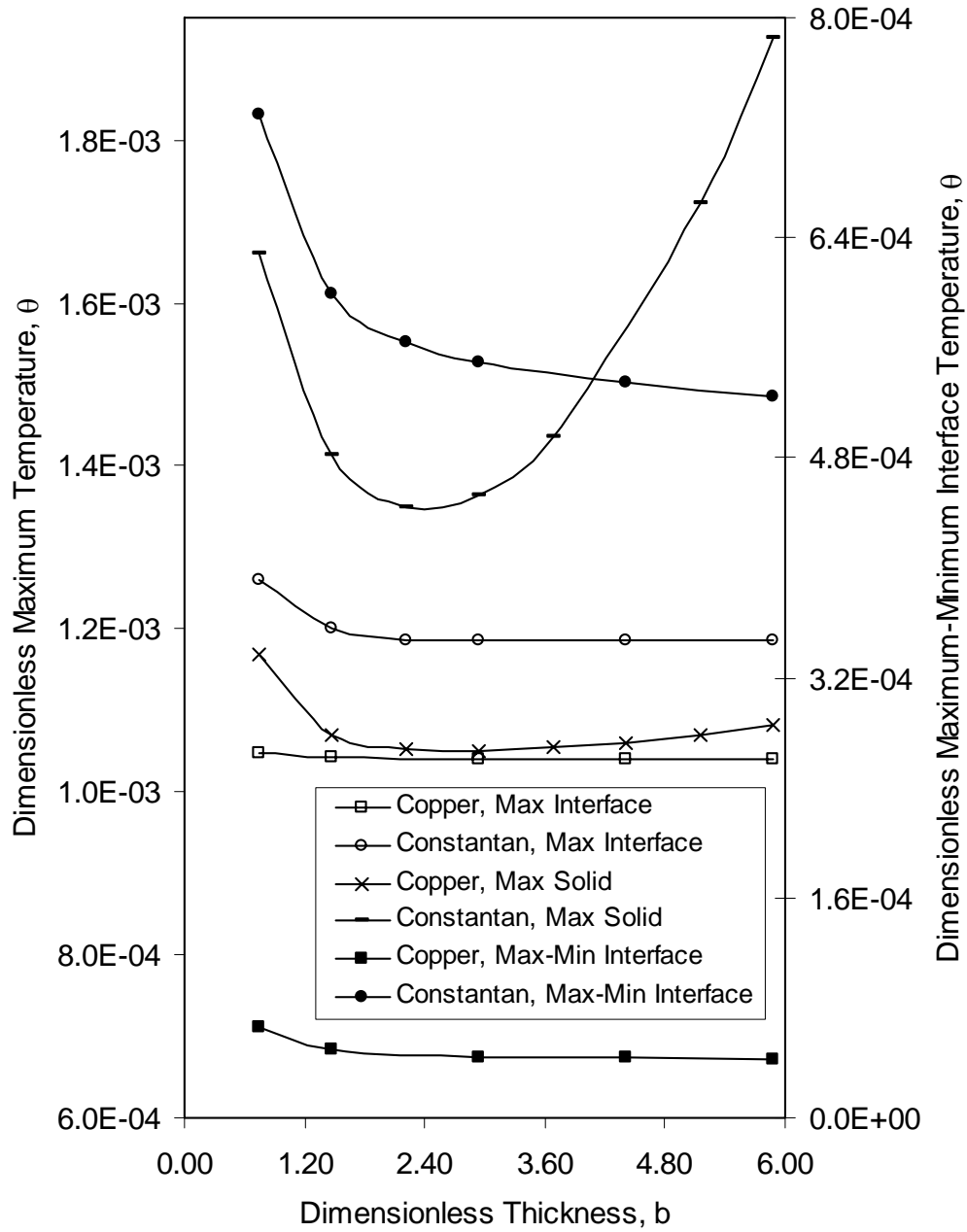


Figure 11. Maximum temperature at the interface, maximum temperature inside the solid, and temperature difference at the interface for different disk thickness and materials  
 $(Re = 550, H = 5, q = 63 \text{ kW/m}^2, T_j = 348 \text{ K}, r_n = 0.00085 \text{ m})$

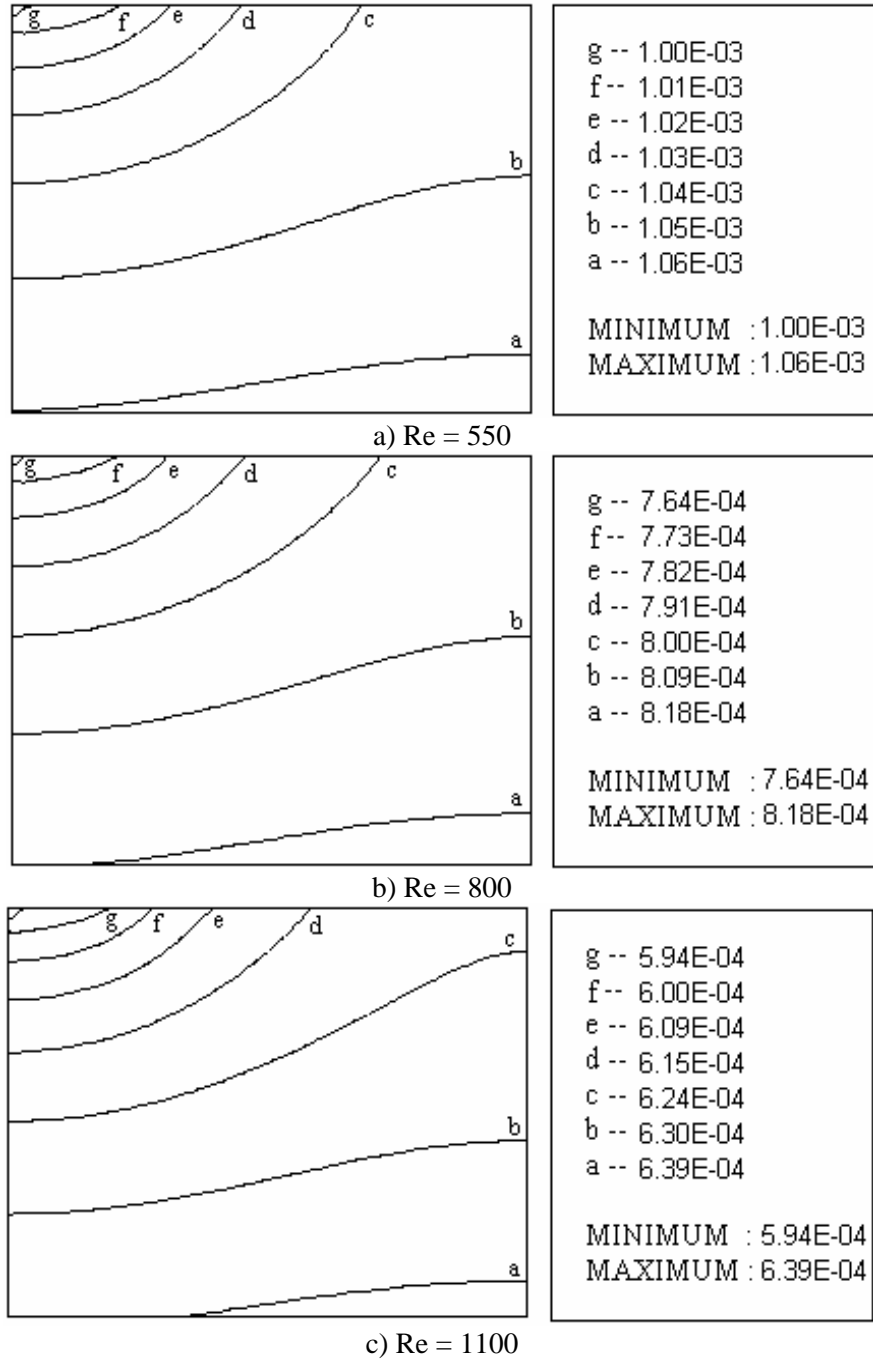
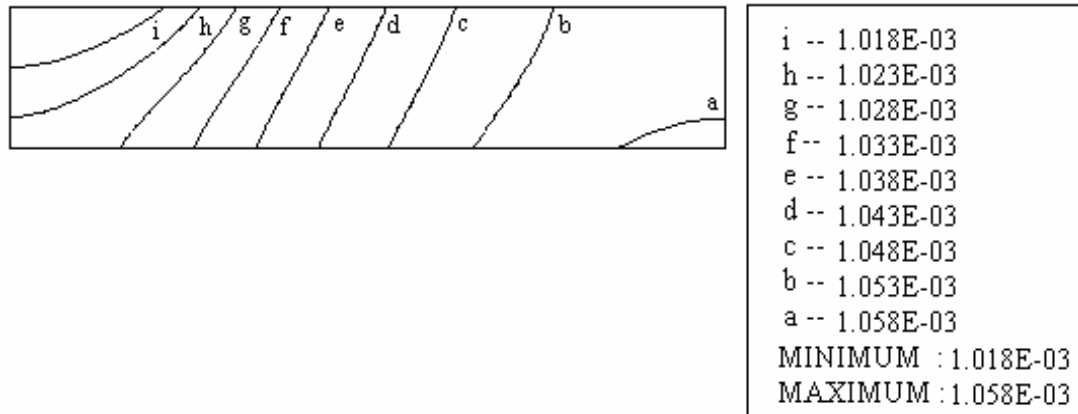
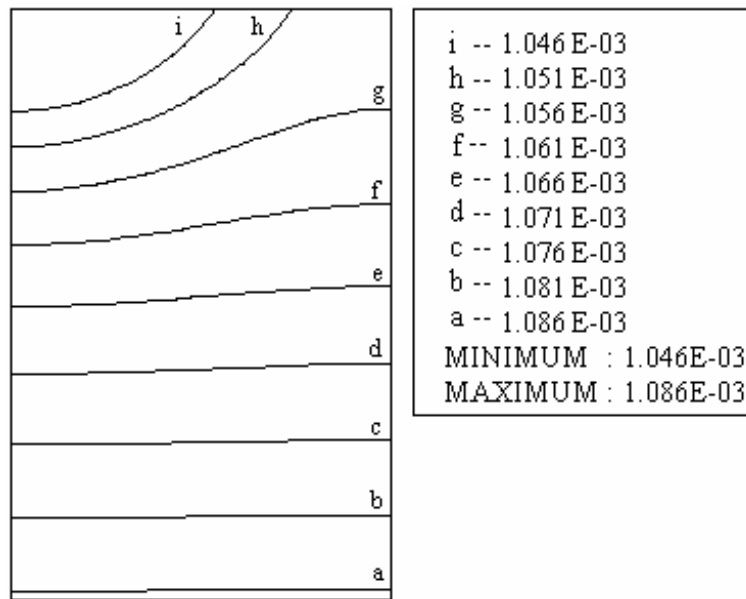


Figure 12. Isothermal lines within the disk for different Reynolds number  
(b = 2.94, H = 5, Copper plate, q = 63 kW/m<sup>2</sup>, T<sub>j</sub> = 348 K, r<sub>n</sub> = 0.00085 m)

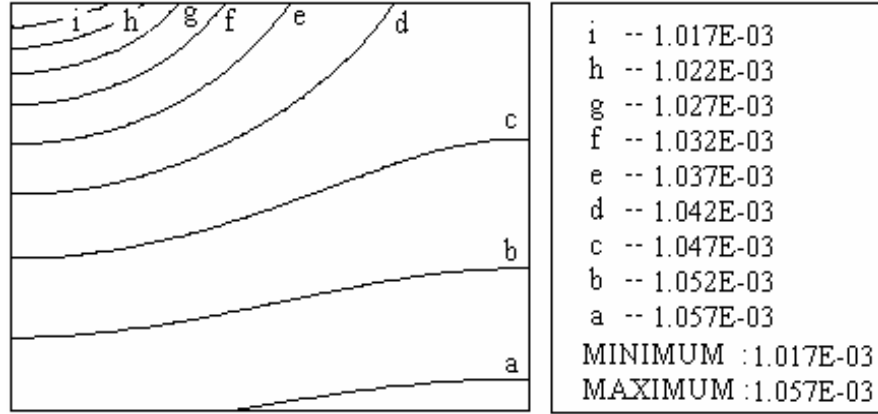


a)  $b = 0.73$

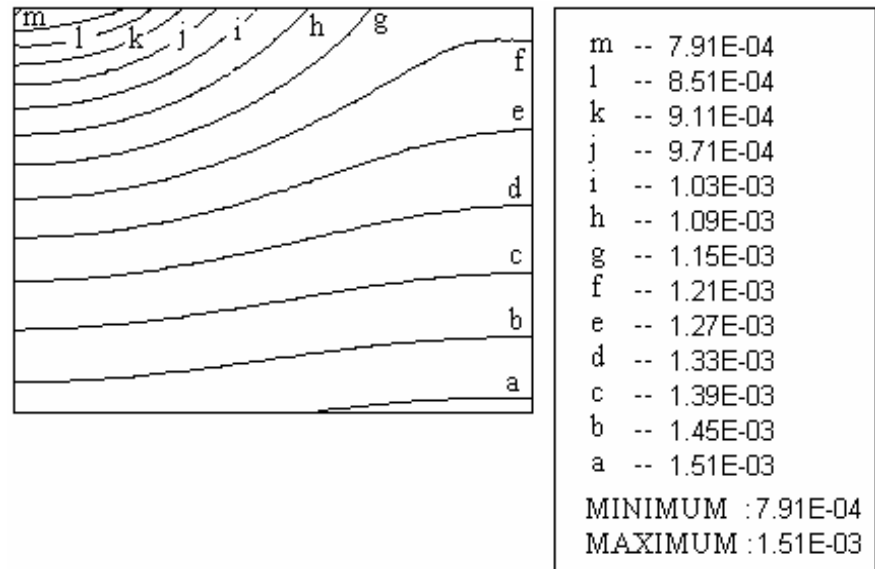


b)  $b = 5.88$

Figure 13. Isothermal lines within the disk for different thickness  
 ( $Re = 550$ ,  $H = 5$ , Copper plate,  $q = 63 \text{ kW/m}^2$ ,  $T_j = 348 \text{ K}$ ,  $r_n = 0.00085 \text{ m}$ )



a) Copper



b) Constantan

Figure 14. Isothermal lines within the disk for different materials  
 ( $Re = 550$ ,  $b = 2.94$ ,  $H = 5$ ,  $q = 63 \text{ kW/m}^2$ ,  $T_j = 348 \text{ K}$ ,  $r_n = 0.00085 \text{ m}$ )

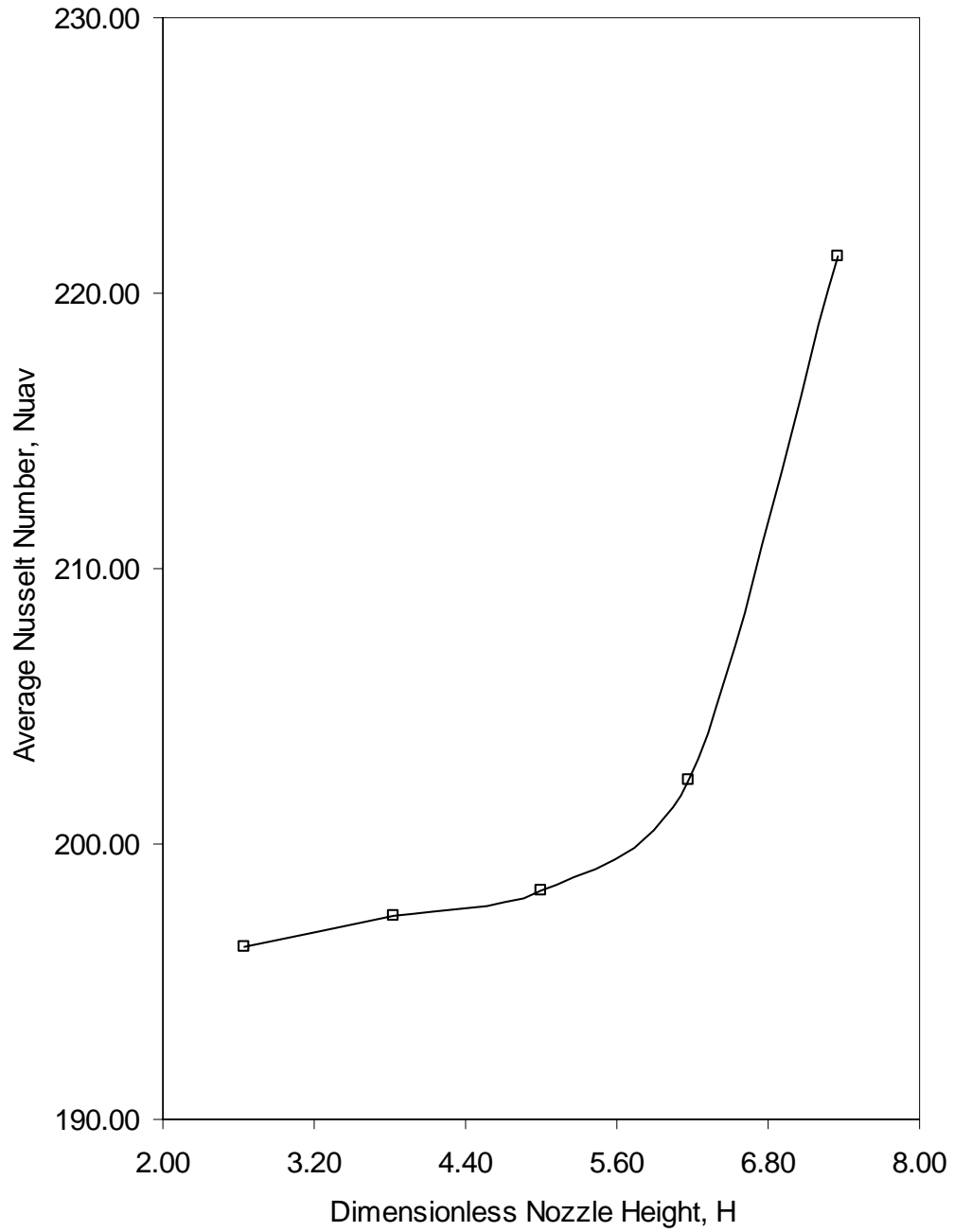


Figure 15. Average Nusselt number for different nozzle height  
( $Re = 550$ ,  $b = 2.94$ , Copper plate,  $q = 63 \text{ kW/m}^2$ ,  $T_j = 348 \text{ K}$ ,  $r_n = 0.00085 \text{ m}$ )



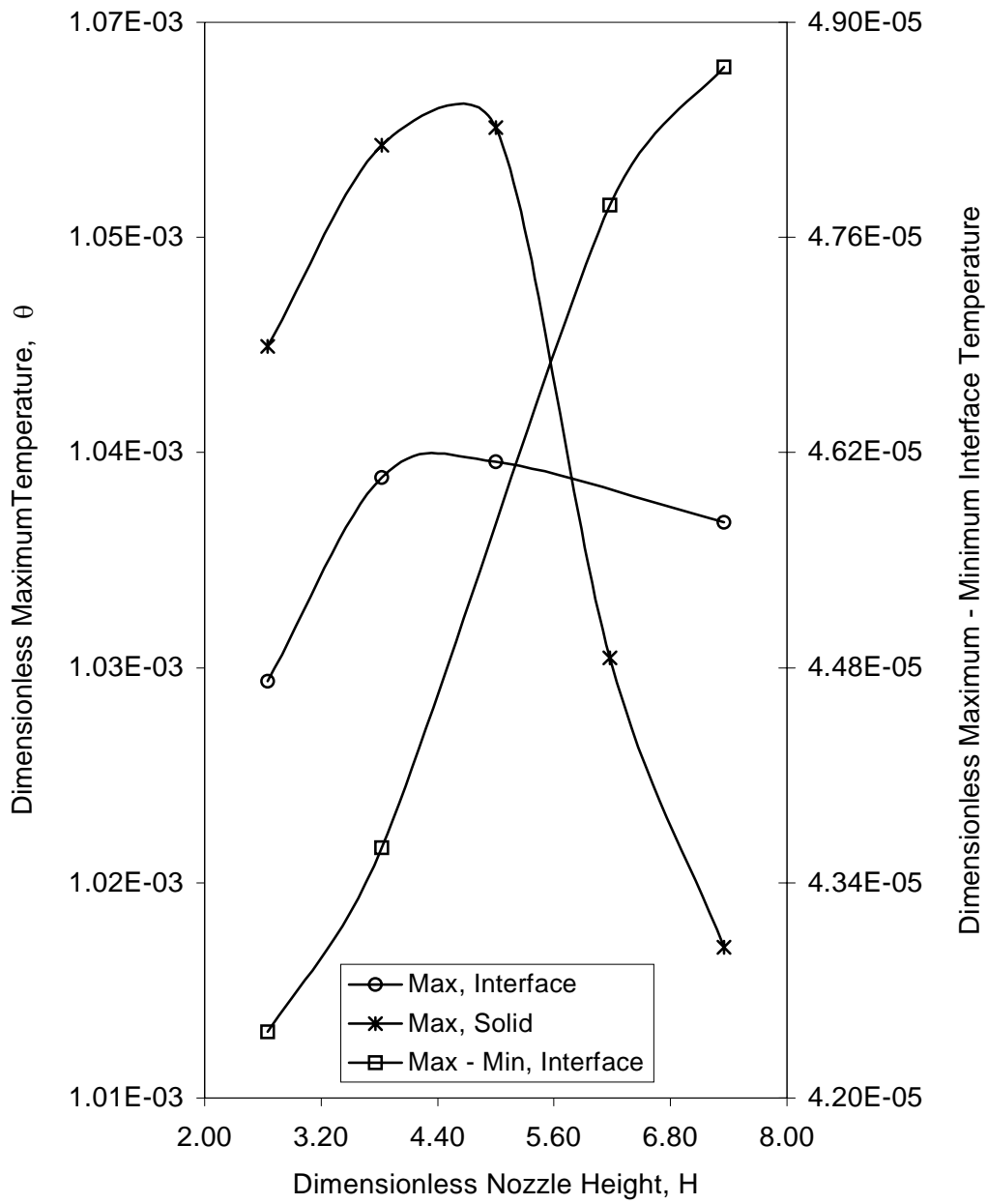


Figure 16. Maximum temperature in the solid, maximum temperature at the interface, and temperature difference at the interface for different nozzle height  
 ( $Re = 550$ ,  $b = 2.94$ , Copper plate,  $q = 63 \text{ kW/m}^2$ ,  $T_j = 348 \text{ K}$ ,  $r_n = 0.00085 \text{ m}$ )

TABLE 1. COMPARISON OF AVERAGE HEAT TRANSFER COEFFICIENT WITH EXPERIMENTAL RESULTS

Re	Heat Flux kW / m <sup>2</sup>	Average Heat Transfer Coefficient ( Numerical ) kW / m <sup>2</sup> K	Average Heat Transfer Coefficient ( Experimental ) kW / m <sup>2</sup> K	Percent Difference %
550	63.0	4.430	3.93	11.70
	126.0	4.480	4.43	1.00
	189.0	4.700	4.73	1.00
	252.0	4.970	4.89	1.00
800	63.0	5.910	5.35	10.10
	126.0	6.020	5.73	5.06
	189.0	6.150	6.02	2.10
	252.0	6.320	6.15	2.70
1100	63.0	7.490	6.74	11.20
	126.0	7.570	6.99	8.40
	189.0	7.700	7.32	5.10
	252.0	7.950	7.41	7.30
Material : Copper, b = 2.94, H = 5				

TABLE 2. AVERAGE HEAT TRANSFER COEFFICIENT AND AVERAGE NUSSELT NUMBER FOR DIFFERENT CONDITIONS

Disk Material	Dimensionless Height H	Dimensionless Thickness b	Average Heat Transfer Coefficient kW / m <sup>2</sup> K	Average Nusselt Number
Copper	2.64706	2.94118	4.386	196.264
	3.82353	2.94118	4.410	197.338
	5.00000	0.73529	4.897	219.130
		1.47059	4.687	209.733
		2.20588	4.543	203.289
		2.94118	4.523	198.227
		4.41176	4.431	190.400
		5.88235	3.919	175.366
	6.17647	2.94118	4.521	202.305
7.35294	2.94118	4.946	221.322	
Constantan	5.00000	0.73529	5.401	241.683
		1.47059	5.150	230.451
		2.20588	4.898	219.174
		2.94118	4.689	209.604
		4.41176	4.563	204.184
		5.88235	4.438	198.591
Silver	5.00000	2.94118	4.429	198.188
Aluminum	5.00000	2.94118	4.451	199.172
q = 63 kW / m <sup>2</sup> , Re = 550				

# **AXIAL FREE JET IMPINGING ON A FLAT DISK WITH DISCRETE HEAT SOURCES: STEADY STATE**

## **INTRODUCTION**

Liquid jets can be classified as submerged or free surface. A submerged jet is formed when a liquid jet is discharged into the same liquid medium. A free surface jet is formed when a liquid jet is discharged into a gaseous (or different liquid) medium. A vast amount of literature exists on free surface as well as submerged (including confined) jets. Examples of books and review articles include Rajaratnam [25], Martin [26], Rodi [27], and Polat et al. [28].

An interesting application of liquid jets impinging over a surface is for the cooling of microelectronics. Wadsworth and Mudawar [29] performed an experiment to investigate single-phase heat transfer from a simulated chip to a two dimensional free surface jet of dielectric fluid FC-72. They concluded that the rectangular jets are well suited for the cooling of high power density discrete heat sources. Schaffer et al. [30] presented the results of an experimental study measuring the average heat transfer coefficient for discrete sources located under a liquid jet issuing from a rectangular slot. The experiment was conducted for heat sources mounted on a channel (submerged jet). Besserman et al. [31] presented a numerical simulation of an axisymmetric, laminar jet impingement cooling of a circular heat source. The simulation includes the effect of the discharge fluid when redirected 180° to an annular exit. Their results demonstrated that the flow is strongly influenced by two recirculation zones near the exit and at the corner of the outside annulus. For nozzle parabolic velocity profile, the local Nusselt number presented a maximum at the stagnation point. Womac et al. [32] obtained experimental data for liquid jet impingement cooling of small square heat sources resembling integrated circuit chips. Both free surface and submerged jet configuration were studied for a range of velocities, nozzle diameters, and nozzle-to-heater distance. Two different liquids, water and FC-77, were used as coolants. Womac et al. [33] carried out an experiment to investigate single-phase heat transfer from a heat source to an array of free surface and submerged jets. They found that for a constant volumetric flow rate, the heat transfer for submerged jets exceeded or were approximately equal to those for the free surface jets. The average heat transfer coefficient increased with reduction in nozzle diameter. Rice and Garimella [34] reported an experimental study to determine the local heat transfer coefficient distribution for a submerged liquid jet impinging perpendicularly on a small, square heat source simulating an electronic cooling situation. They concluded that the local heat transfer coefficient at the stagnation point was independent of the nozzle-to-plate distance for small nozzle diameters, and for distances over 5 nozzle diameters the stagnation heat transfer coefficient decreased. Secondary peaks were observed as the fluid moved away from the stagnation point. Maddox and Bar-Cohen [35] carried out a study to help design a jet impingement cooling system in attaining the targeted thermal performance while considering the available liquid pressure, liquid flow rate, and pumping power, as well as jet plate manufacturing and maintenance constraints. Garimella and Rice [36] experimentally investigated the local heat transfer from a small heat source to a normally impinging axisymmetric and submerged liquid jet, in confined and unconfined configurations. Secondary peaks were more pronounced at smaller (confined) spacings and large nozzle diameters for a given Reynolds number. Correlations were presented for the average heat transfer coefficient and the Nusselt number.

From the above literature review, it appears that most jet impingement cooling studies involving discrete heat sources used either water or a fluorinert liquid as the cooling medium. In addition, the variation of fluid properties with temperature has not been taken into account in any previous numerical work, and has been assumed to be negligible in most analytical work. Although a poor heat transfer fluid, lubricating oil is an attractive coolant for aircraft applications because it is generally in close proximity to the electrical generating equipment. It is also pre-existing in the aircraft and therefore does not require flight qualification, new maintenance procedures, additional inventory space and logistics procedures, or additional environmental protection guidelines. These advantages translate into greatly reduced operational costs, which may far outweigh the loss in cooling efficiency. Lubricating oils are generally known for their high Prandtl number and strong dependence of viscosity on temperature. Alternately, air-cooling is generally inadequate or undesirable because of the additional drag imposed by ram air heat exchangers. Therefore, the investigation of jet impingement heat transfer for high Prandtl number fluids taking into account the effects of property variation with temperature is of great importance to the military and commercial aircraft industry, and is expected to be a valuable contribution to the state-of-the-art of jet impingement cooling system design.

## MATHEMATICAL MODEL

Consider an axisymmetric jet discharging from a nozzle and impinging perpendicularly at the center of a solid circular disk heated by discrete sources as shown in Figure 17. If the fluid is considered to be incompressible and its properties (density, viscosity, thermal conductivity, and specific heat) are dependent on temperature, the equations describing the conservation of mass, momentum, and energy in cylindrical coordinates can be written as [23]:

$$\frac{1}{r} \frac{\partial}{\partial r} (\rho_f r v_r) + \frac{\partial}{\partial z} (\rho_f v_z) = 0 \quad (14)$$

$$\rho_f \left( v_r \frac{\partial v_r}{\partial r} + v_z \frac{\partial v_r}{\partial z} \right) = -\frac{\partial p}{\partial r} + \frac{1}{r} \frac{\partial}{\partial r} \left[ \frac{2}{3} \mu r \left( 2 \frac{\partial v_r}{\partial r} - \frac{v_r}{r} - \frac{\partial v_z}{\partial z} \right) \right] + \frac{\partial}{\partial z} \left[ \mu \left( \frac{\partial v_r}{\partial z} + \frac{\partial v_z}{\partial r} \right) \right] \quad (15)$$

$$\begin{aligned} \rho_f \left( v_r \frac{\partial v_z}{\partial r} + v_z \frac{\partial v_z}{\partial z} \right) = & -\rho_f g - \frac{\partial p}{\partial z} + \frac{1}{r} \frac{\partial}{\partial r} \left[ \mu r \left( \frac{\partial v_r}{\partial z} + \frac{\partial v_z}{\partial r} \right) \right] \\ & + \frac{\partial}{\partial z} \left[ \frac{2}{3} \mu \left( 2 \frac{\partial v_z}{\partial z} - \frac{v_r}{r} - \frac{\partial v_r}{\partial r} \right) \right] \end{aligned} \quad (16)$$

$$\begin{aligned} \rho_f \left( v_r \frac{\partial (c_{p_f} T_f)}{\partial r} + v_z \frac{\partial (c_{p_f} T_f)}{\partial z} \right) = & \left[ \frac{1}{r} \frac{\partial}{\partial r} \left( k_f r \frac{\partial T_f}{\partial r} \right) + \frac{\partial}{\partial z} \left( k_f \frac{\partial T_f}{\partial z} \right) \right] + \left( v_z \frac{\partial p}{\partial z} + v_r \frac{\partial p}{\partial r} \right) \\ & + \mu_f \left\{ 2 \left[ \left( \frac{\partial v_r}{\partial r} \right)^2 + \left( \frac{v_r}{r} \right)^2 + \left( \frac{\partial v_z}{\partial z} \right)^2 \right] + \left( \frac{\partial v_r}{\partial z} + \frac{\partial v_z}{\partial r} \right)^2 - \frac{2}{3} \left[ \frac{\partial v_r}{\partial r} + \frac{v_r}{r} + \frac{\partial v_z}{\partial z} \right]^2 \right\} \end{aligned} \quad (17)$$

Considering variable thermal conductivity, the equation describing the conservation of energy inside the solid can be written as:

$$\frac{1}{r} \frac{\partial}{\partial r} \left( k_s r \frac{\partial T_s}{\partial r} \right) + \frac{\partial}{\partial z} \left( k_s \frac{\partial T}{\partial z} \right) = 0 \quad (18)$$

Equations (14-18) are subjected to the following boundary conditions:

$$\text{At } r = 0, 0 \leq z \leq b: \frac{\partial T_s}{\partial r} = 0 \quad (19)$$

$$\text{At } r = 0, b \leq z \leq H_n: v_r = 0, \frac{\partial v_z}{\partial r} = 0, \frac{\partial T_f}{\partial r} = 0 \quad (20)$$

$$\text{At } r = r_o, 0 \leq z \leq b: \frac{\partial T_s}{\partial r} = 0 \quad (21)$$

$$\text{At } r = r_o, b \leq z \leq \delta: p = 0, \frac{\partial T_f}{\partial r} = 0 \quad (22)$$

$$\text{At } z = b: T_s = T_f, v_r = 0, v_z = 0, k_s \frac{\partial T_s}{\partial z} = k_f \frac{\partial T_f}{\partial z} \quad (23)$$

$$\text{At } z = b + H_n, 0 \leq r \leq r_n: v_r = 0, v_z = -v_j, T_f = T_j \quad (24)$$

$$\text{At } z = \delta, r_n < r < r_o:$$

$$\frac{d\delta}{dr} = \frac{v_z}{v_r}, p = p_{atm} - \frac{\sigma \frac{d^2 \delta}{dr^2}}{\left[ 1 + \left( \frac{d\delta}{dr} \right)^2 \right]^{3/2}}, \frac{\partial v_t}{\partial n} = 0, \frac{\partial T_f}{\partial n} = 0 \quad (25)$$

Equations (25) essentially indicate the kinematic condition, balance of normal forces, balance of shear forces, and adiabatic condition at the free surface. These equations were derived from more general equations presented by White [37]. It can be noted that “n” indicates direction normal to the free surface. The frictional resistance and heat transfer to the surrounding gaseous medium have been assumed to be negligible. In order to simulate different positions of the discrete heat sources, the total heat introduced was taken as constant and the heat flux for the discrete sources was changed according to the total heated area. Figure 18 demonstrates the boundary condition at the bottom of the disk. For the base case, it can be written as:

$$\text{At } z = 0, 0 < r < (r_o/9): -k_s \frac{\partial T_s}{\partial z} = q_w \quad (26)$$

$$\text{At } z = 0, (r_o/9) < r < (r_o/3): \frac{\partial T_s}{\partial z} = 0 \quad (27)$$

$$\text{At } z = 0, (r_o/3) < r < (5r_o/9): -k_s \frac{\partial T_s}{\partial z} = q_w \quad (28)$$

$$\text{At } z = 0, (5r_o/9) < r < (7r_o/9): \frac{\partial T_s}{\partial z} = 0 \quad (29)$$

$$\text{At } z = 0, (7r_o/9) < r < r_o: -k_s \frac{\partial T_s}{\partial z} = q_w \quad (30)$$

The local heat transfer coefficient can be defined as:

$$h = \frac{q_{\text{int}}}{(T_{\text{int}} - T_j)} \quad (31)$$

The average heat transfer coefficient is obtained according to the following equation:

$$h_{av} = \frac{2}{r_o^2 \left( \overline{T_{\text{int}}} - T_j \right)} \int_0^{r_o} hr(T_{\text{int}} - T_j) dr \quad (32)$$

It can be noted that local heat transfer coefficient  $h$  and interfacial temperature  $T_{\text{int}}$  are both functions of radial location  $r$ .  $\overline{T_{\text{int}}}$  is the average temperature at the solid-fluid interface. It was calculated by taking the linear average of temperature from  $r = 0$  to  $r = r_o$ . The local Nusselt number and the average Nusselt number are calculated according to the following expressions:

$$\text{Nu} = \frac{hr_o}{k_f} \quad (33)$$

$$\text{Nu}_{av} = \frac{h_{av}r_o}{k_f} \quad (34)$$

## COMPUTATION AND DISCUSSION OF RESULTS

The governing equations along with the boundary conditions described in the previous section were solved by using the Galerkin finite element method [38]. The dependent variables, i.e., velocity, pressure, and temperature were interpolated to a set of nodal points that defined the finite element. In each element, the velocity, pressure, and temperature fields were approximated which led to a set of equations that defined the continuum. The approach used to model the free surface was to introduce a new degree of freedom at the nodes on the free surface. This degree of freedom represented the position of the free surface. The discretization of governing transport equations and boundary conditions was carried out using the Galerkin formulation. The solution of the resulting algebraic equations was carried out using the Newton-Raphson method. Since the solution of the momentum equation required only two out of the three boundary conditions at the free surface, the third condition was used to update the position of the free surface at the end of each iteration step.

Due to large number of iterations required to determine the location of the free surface, the solution was carried out in two steps. First, the computation in the fluid region was carried out solving equations for the conservation of mass and momentum; this resulted in the determination of the velocity field and the free surface height distribution. The drawback of this solution is that because of no heat transfer, the fluid remained isothermal, and therefore properties remained constant. This approximate solution was used as the starting point for the second level of computation where both solid and fluid regions were included and equations for the conservation of mass, momentum, and energy were solved simultaneously as a conjugate problem taking into account the variation of properties with temperature. This split level computation procedure greatly reduced the run time for numerical computation. The solution was considered converged when the field values did not change from one iteration to the next, and the sum of residuals for each degree of freedom was less than  $1\text{E-}08$ . Except for comparison with Womac et al. [32], the working fluid used for the present numerical simulation is MIL-7808, a lubrication oil certified for military aircraft. The relevant fluid properties were calculated from the following correlating equations which are valid for  $303\text{ K} < T < 390\text{ K}$ :  $c_p = 903.8 + 3.332T$ ,  $k = 0.18 - 1 \times 10^{-4}T$ ,  $\rho = 1181 - 0.708T$ , and  $\mu = 0.941 - 5.07 \times 10^{-3}T + 6.87 \times 10^{-6}T^2$ . The range of Prandtl number encountered in the present investigation was 48 - 71. The range of variation of different parameters were:  $\text{Re} = 550\text{-}2200$  and  $b = 0.000125\text{-}0.01\text{ m}$ . Three different disk materials and three different heating arrangements were studied. This choice of parameters was essentially driven by applications and past studies of laminar jet impingement heat transfer.

A comparison between the present numerical simulation and the experimental data obtained by Womac et al. [32] is presented in Table 3. In order to carry out this comparison, numerical simulations were performed using the appropriate test fluids and heat flux conditions used in the experiment. The table shows a good agreement between the simulation and the experimental data, with a maximum deviation of 4.4 %. This comparison validates the results obtained in the present investigation.

Figure 19 presents the free surface height distribution for different Reynolds number when the jet strikes the center of the disk. It can be seen that the fluid spreads radially as a thin film. For the conditions considered in the present investigation, the flow was supercritical and a hydraulic jump did not occur within the computation domain. It can be observed that the minimum film height occurs at a radius larger than the radius of the nozzle and the film height gradually increases with radius after that location. A smaller thickness is seen at larger Reynolds number because of larger impingement velocity that translates to a larger fluid velocity in the film. From the plot of velocity vectors, it was observed that, due to high viscosity of the working fluid, the boundary layer develops rapidly and the velocity of the fluid decreases as it spreads radially along the disk.

The effect of Reynolds number on the temperature at the interface is observed in Figure 20. It can be seen that as Reynolds number increases, the temperature at the interface decreases. This is because of larger local fluid velocity, which results in larger rate of heat transfer between the disk and the liquid. The temperature is minimum at the stagnation point. As the fluid moves downstream, the temperature increases. The location where the fluid goes from the stagnation to

boundary layer region (transition region) is about  $r = r_n$ . The temperature distribution shows steeper slope at locations where the heat sources are located, especially in the boundary layer region,  $r > r_n$ . It is important to notice that as the Reynolds number increases, the maximum-to-minimum temperature difference decreases, ranging from 9.4 K to 7.9 K between Re of 550 and 1100. This is because of decreasing thermal resistance at the solid-fluid interface.

Figure 21 presents the effect of Reynolds number on the local Nusselt number. It is observed that the maximum is located at the stagnation point. As the fluid goes through the stagnation zone ( $r \leq 0.002$  m), the local heat transfer coefficient decreases rapidly. As the fluid reaches the location where the boundary layer starts to develop, a second peak is attained. After that point, the heat transfer coefficient continues to decrease until reaching the edge of the disk, presenting the pattern of an external flow over a flat surface. As the fluid moves over the last heat source, the heat transfer coefficient slightly increases. This phenomenon was observed in previous studies by Wolf et al. [11] and Vader et al. [12]. The rise of heat transfer coefficient near the outer edge of the disk is possibly due to transition to turbulence. It should be noted, however, that for the conditions considered in the present investigation, a fully turbulent flow regime could not be attained. It is important to note that there is a heat source located exactly under the stagnation zone (base case). It can be noted that the maximum (located at the stagnation point), the average, and the second peak (attained at the beginning of the boundary layer region) of Nusselt number increase with Reynolds number. The second peak appears at the position where the fluid has its minimum thickness and maximum velocity over the plate and this is the reason for the enhancement of the heat transfer process at that location. It can also be associated with the transition of flow from stagnation to boundary layer zone.

Figure 22 presents the local and average Nusselt number for different disk thicknesses. It is important to notice that the main differences are present at the stagnation region, and as soon as the fluid gets into the boundary layer region, the distributions of Nusselt number for different thickness get close to each other. As the thickness of the disk increases, the temperature distribution at the solid-fluid interface becomes more uniform due to thermal spreading by radial conduction. Therefore, the heat transfer coefficient at the center of the disk decreases. It is noticed that the average Nusselt number increases as the disk thickness increases and reaches a maximum value around 0.00125 m. After this point, the average Nusselt number presents a decreasing trend.

The numerical simulation was carried out for three different disk materials, namely copper, constantan, and silicon. Both copper and constantan have been used in previous experimental studies on jet impingement cooling. Silicon was chosen because of its application in electronics fabrication. Figure 23 shows that the local Nusselt number increases with decrease of thermal conductivity of the disk material. A small difference is seen between copper and silicon because  $k_{copper} = 2.6 k_{silicon}$ , whereas a large difference is seen between copper and constantan because of  $k_{copper} = 17 k_{constantan}$ . It can be noticed that at large radial locations, the Nusselt number for the different materials practically match each other. The reason why a material with a lower thermal conductivity achieves a higher average Nusselt number lies specifically in its inability to conduct heat. It produces a lower temperature at the stagnation region that reflects as a higher heat transfer coefficient. At the boundary layer region, the difference in temperature for different materials is not significant and the values get closer all the



way to the edge of the disk. The local Nusselt number at the center of the disk for different materials were compared with the stagnation Nusselt number correlation developed by Hrycak [5]. It was found that the numerical predictions are within 5-8% of this experimental correlation.

Figure 24 presents the maximum temperature as well as the difference between the maximum and minimum temperature at the interface, and the maximum temperature inside the solid for the three different disk materials and different disk thicknesses. The control of these temperatures is crucial in the design of electronic packages. It may be noticed that the maximum temperature at the interface decreases with increasing thickness when  $b < 0.005$  m,  $b < 0.00375$  m, and  $b < 0.00125$  m, for constantan, silicon and copper respectively; whereas remains almost constant thereafter. The maximum temperature inside the solid has an interesting behavior. It decreases as the disk thickness increases when  $b < 0.00125$  m,  $b < 0.002$  m, and  $b < 0.0025$  m, for constantan, silicon, and copper respectively; after this point, the temperature increases as the disk thickness increases. This indicates that increasing the wafer thickness beyond a certain limit, depending on the solid material, may not be useful. The choice of the wafer material is however crucial in determining the magnitude of this temperature. As expected, a material with larger thermal conductivity will facilitate a faster rate of heat transfer, and therefore will result in a lower maximum temperature at the interface and inside the solid. The temperature difference at the interface is an indication of the level of temperature non-uniformity at the impingement surface, while the maximum temperature inside the solid indicates the thermal resistance generated by the wafer material. When the disk thickness is negligible, the interface temperature is controlled by the heat flux condition at the heater. However, when an adequate thickness is provided, the interface temperature becomes more uniform because of radial spreading of heat within the solid. The magnitude of maximum to minimum temperature difference is strongly affected by the thermal conductivity of the disk material, decreasing as the disk thermal conductivity increases. The material with lower thermal conductivity results in higher temperature at the interface and inside the solid.

The effect of disk thickness on average Nusselt number for three different materials can be observed in Figure 25. It shows how the average values of heat transfer coefficient and Nusselt number attain a peak around  $b = 0.00125$  m. For  $b < 0.00125$  m, the average value of Nusselt number increases as the disk thickness increases. On the other hand, for  $b > 0.00125$  m, the average value of Nusselt number slightly decreases as the disk thickness increases. It may be noticed that constantan has a higher value of average heat transfer coefficient than copper or silicon at all disk thicknesses. This is consistent with local variations seen in Figure 23. For  $b < 0.00125$  m, the radial spreading due to conduction increases as the disk thickness increases and there is a better heat distribution at the interface, this creates a better opportunity for the heat to be transferred to the fluid. For  $b > 0.00125$  m, the increment in the solid thickness creates more thermal resistance, which ends up crippling the heat transfer process.

In order to study how the position of the discrete heat sources affects the heat transfer phenomenon, it was necessary to input the same power dissipation in the system. For that reason, for different positions, the heat flux varies as shown in figure 18. The results for the temperature distribution at the interface and local Nusselt number are presented in Figures 26 and 27. It may be observed that the location of the heat sources strongly affects the local variation of interface temperature and heat transfer coefficient. The magnitudes of the maximum temperature,

maximum-to-minimum temperature difference at the interface, and average Nusselt number are also strongly affected by the location of heat sources. Case (a) is just the opposite of the base case in terms of heater location. For thin disks, as the heat sources are moved closer to the stagnation region, the average heat transfer coefficient increases, presenting maximum values for Case (a). Since no heat source is present at the exit edge of the disk, the maximum temperature for Case (a) is also lower. This case provides much more uniform temperature at the solid-fluid interface compared to the other two cases. Case (b) is somewhat similar to the base case except that the central heater is removed and heat flux at the other two heaters is increased to provide the same total power dissipation. It may be noticed that because of higher heat flux,  $T_{\max}$  increased. Case (b), presents the minimum temperature at the interface because of the lack of heat source under the impingement zone (stagnation point).

The temperature contours within the disk for different Reynolds number are presented in Figure 28. The minimum temperature occurs at the stagnation point, the maximum temperature occurs across the disk at the largest radial location. It is observed that the isothermal lines grow around the heat sources in the lower part of the disk and matches with isotherms concentric with the impingement location in the upper part of the disk. The maximum-to-minimum temperature difference inside the disk remains almost constant (1.3 - 1.4 K). It is important to notice that Reynolds number does not have a strong effect on the pattern of temperature distribution inside the solid. It seems that this is more controlled by the distribution of heat sources. On the other hand, the magnitude of temperature within the solid is very strongly affected by Reynolds number.

The effect of disk thickness on temperature distribution within the solid is seen in Figure 29. It can be observed that the temperature becomes more uniform as the disk thickness is increased. It is interesting to notice that when the disk thickness is large, the temperature remains stratified over a part of the disk. The isothermal lines start growing around the heat sources and become parallel to the bottom of the disk indicating an almost one-dimensional heat conduction. However, in regions near the solid-fluid interface, the isothermal lines tend to be concentric around the stagnation point. The effect of non-uniform heat transfer is felt only over a part of the disk. When the disk thickness is small, the temperature contours have entirely different orientation because of strong radial conduction over the entire disk thickness. The temperature difference inside the solid remains almost constant, with a value around 1.6 K.

Figure 30 shows the temperature distribution inside the disk for the three different materials. For copper and silicon, the temperature is more uniform and the maximum-to-minimum temperature difference is smaller, 1.3 K and 4.2 K respectively. For constantan the maximum-to-minimum temperature difference is fairly large (18.2 K) because of much lower thermal conductivity. The shapes of the isotherms are not significantly affected by thermal conductivity.

In order to compare a uniformly heated disk with a discretely heated one (base case), the total heat introduced was uniformly distributed. The temperature at the interface and local Nusselt number are shown in Figures 31 and 32 respectively. It is noticed that a uniformly heated disk presents a more uniform temperature and the maximum temperature reached is lower. Since uniform and discrete heating had the same rate of total heat transfer, the heat flux at discrete heat

sources was higher. This resulted in higher local temperature for the discrete source at the edge of the disk. The local Nusselt number plot shows that the discrete heat sources attain higher values due to the concentration of power; but as the fluid moves downstream, there is only slight difference between the two cases. The average Nusselt number for the discrete case is higher.

## NOMENCLATURE

$b$	Thickness of the disk [m]
$c_p$	Specific heat at constant pressure [kJ / kg K]
$g$	Acceleration due to gravity [ $\text{m} / \text{s}^2$ ]
$h$	Heat transfer coefficient [ $\text{W} / \text{m}^2 \text{ K}$ ]
$H_n$	Height of the nozzle from the disk [m]
$k$	Thermal conductivity [ $\text{W} / \text{m K}$ ]
$n$	Coordinate normal to the free surface [m]
$\text{Nu}$	Nusselt number [ $h r_o / k_f$ ]
$p$	Pressure [Pa]
$q$	Heat flux [ $\text{W} / \text{m}^2$ ]
$q_o$	Total heat transfer rate [W]
$r$	Radial coordinate [m]
$r_n$	Radius of the nozzle [m]
$r_o$	Radius of the disk [m]
$\text{Re}$	Reynolds number, $2r_n v_j / \nu_f$
$T$	Temperature [K]
$\bar{T}$	Average temperature [K]
$T_j$	Jet temperature [K]
$v_j$	Jet velocity [ $\text{m} / \text{s}$ ]
$v_r$	Radial velocity [ $\text{m} / \text{s}$ ]
$v_t$	Velocity along the free surface [ $\text{m} / \text{s}$ ]
$v_z$	Axial velocity [ $\text{m} / \text{s}$ ]
$z$	Axial coordinate [m]

### Greek Symbols

$\delta$	Liquid film thickness [m]
$\mu$	Dynamic viscosity of fluid [kg / m s]
$\rho$	Density [ $\text{kg} / \text{m}^3$ ]
$\sigma$	Surface tension coefficient [N / m]

### Subscripts

atm	Atmospheric condition
av	Average
f	Fluid
int	Solid-fluid interface
s	Solid

## CONCLUSIONS

A theoretical model of conjugate heat transfer process where heat is transmitted through a solid body from discrete heat sources located on one side to a fluid jet impinging on the opposite side has been solved. The variation of fluid properties with temperature has been taken into account. It was found that the film thickness decreases as the impingement velocity increases. The heat transfer coefficient as well as the Nusselt number showed a strong dependence on the impingement velocity; increasing their values as the velocity increased. The temperature at the solid-fluid interface decreased as the velocity increased. The average Nusselt number increased with Reynolds number. As the thickness of the disk was increased, the heat transfer coefficient and the Nusselt number presented a thickness where they attained peak values, showing that there is an ideal disk thickness for best performance. The isothermal lines inside the solid showed that beyond a certain thickness, the disk presented a one dimensional heat conduction in regions away from the impingement plane and the heated surface, and therefore discrete heat sources did not exert much influence on the convective heat transfer process. Similarly, the maximum temperature as well as the difference of maximum and minimum temperature at the interface was strongly affected by the variation of disk thickness at smaller thicknesses, but did not vary significantly at larger thicknesses. The thermal conductivity of the disk material strongly affected the magnitude of maximum temperature in the solid, temperature difference at the interface, heat transfer coefficient, as well as the Nusselt number. It was found that a lower thermal conductivity in the solid results in slightly higher heat transfer coefficient, whereas a higher thermal conductivity material will maintain the disk at a lower temperature. The location of the discrete heat sources affected the temperature distribution within the solid and consequently the average Nusselt number.

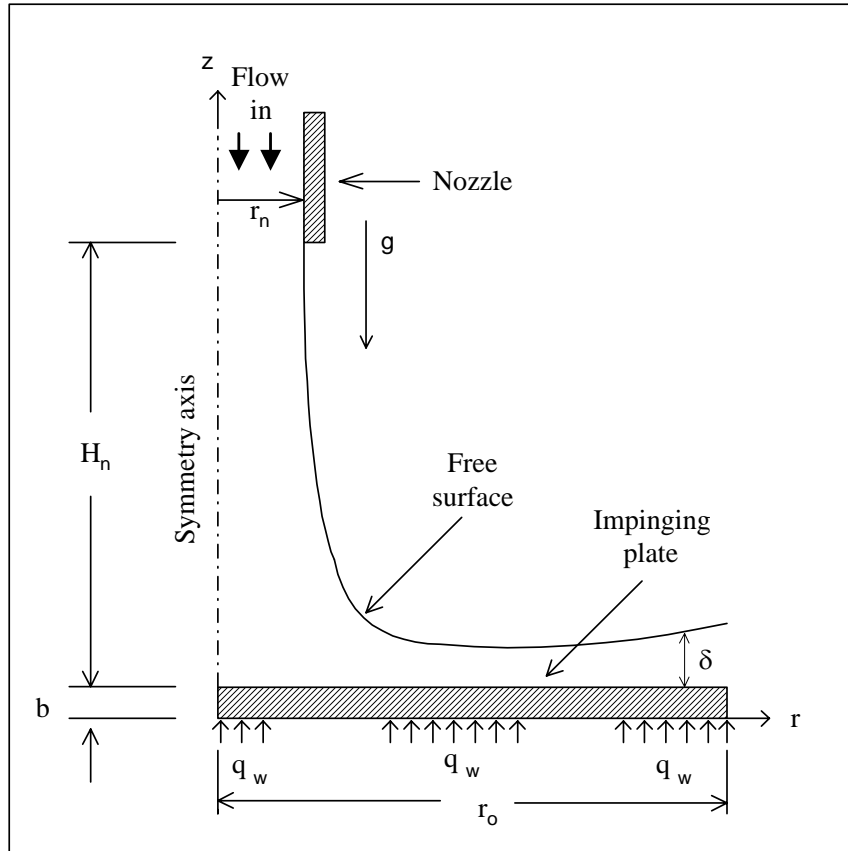


Figure 17. Schematic of a free axial jet impinging over a flat disk

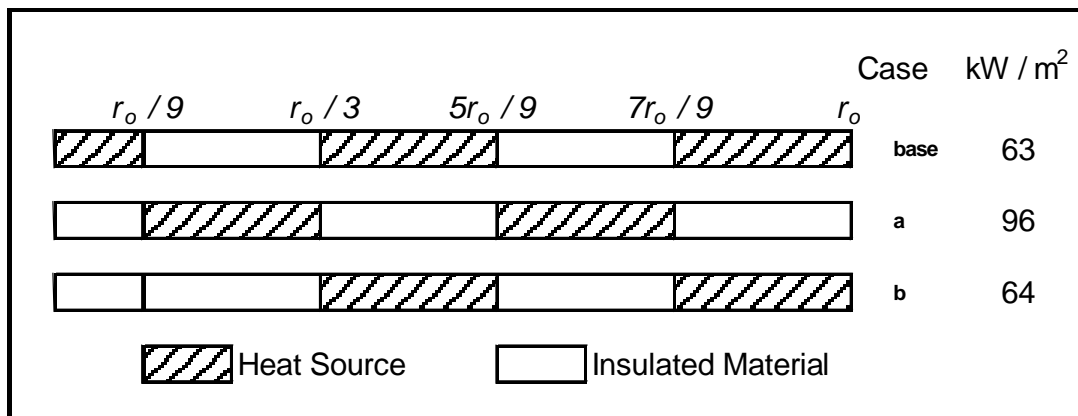


Figure 18. Different location of heat sources and their heat flux ( $q_o = 1.59 \text{ W}$ )

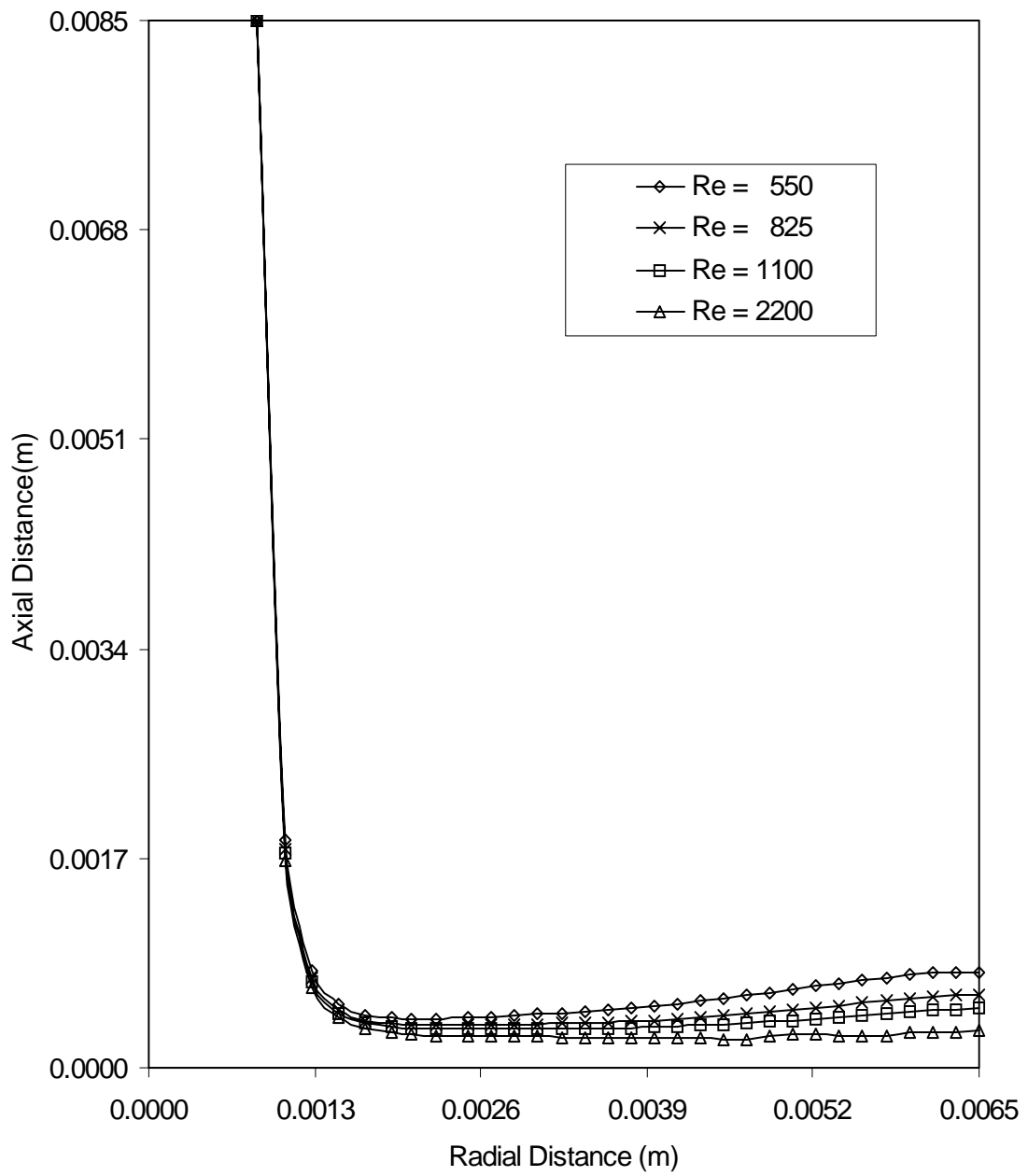


Figure 19. Free surface height distribution for different Reynolds number  
( $H_n = 0.0085$  m,  $r_n = 0.00085$  m)

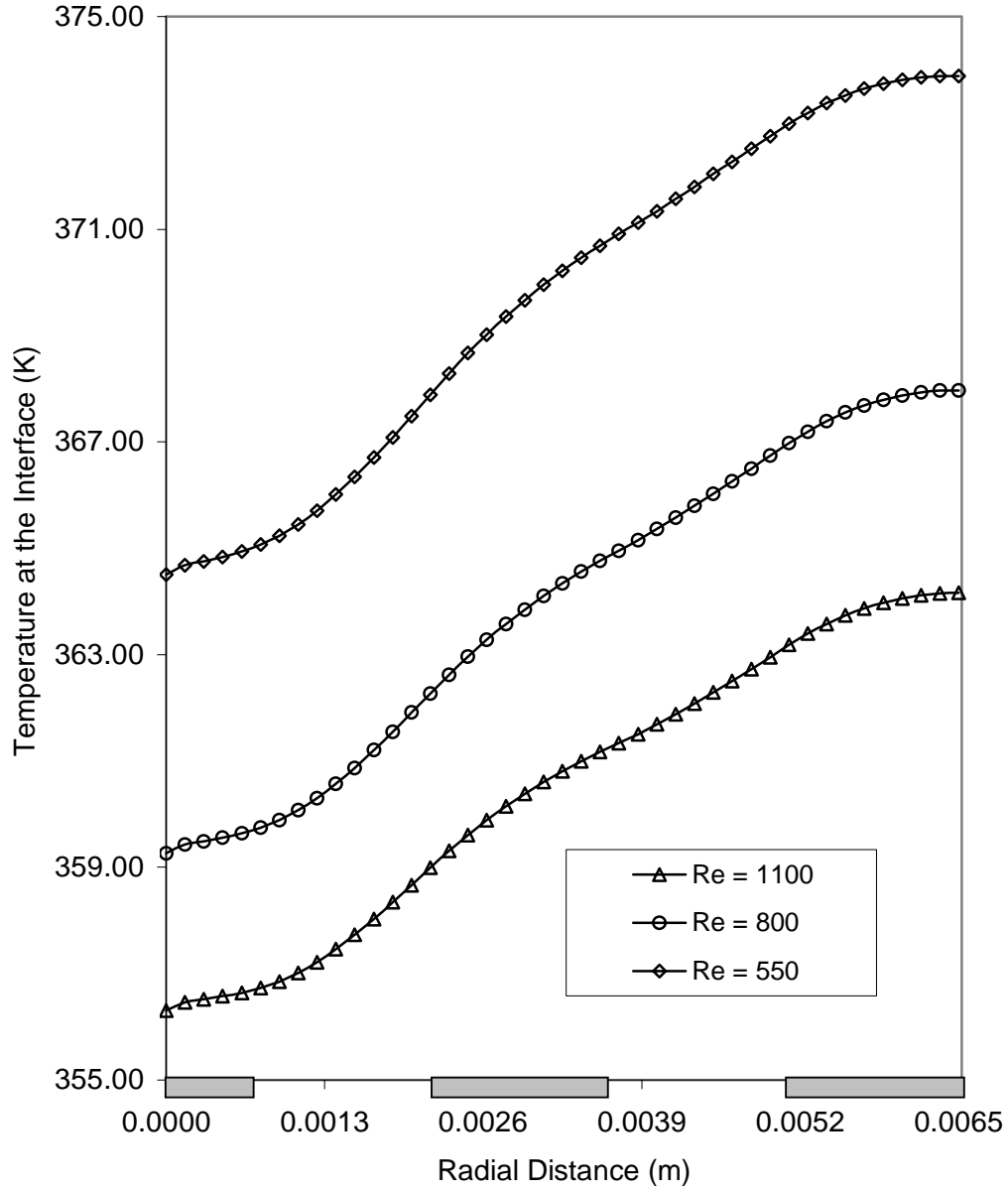


Figure 20. Temperature at the interface for different Reynolds number ( $T_j = 348$  K,  $b = 0.000125$  m,  $H_n = 0.0085$  m,  $r_n = 0.00085$  m, Copper plate,  $q_w = 63$  kW/m<sup>2</sup>)

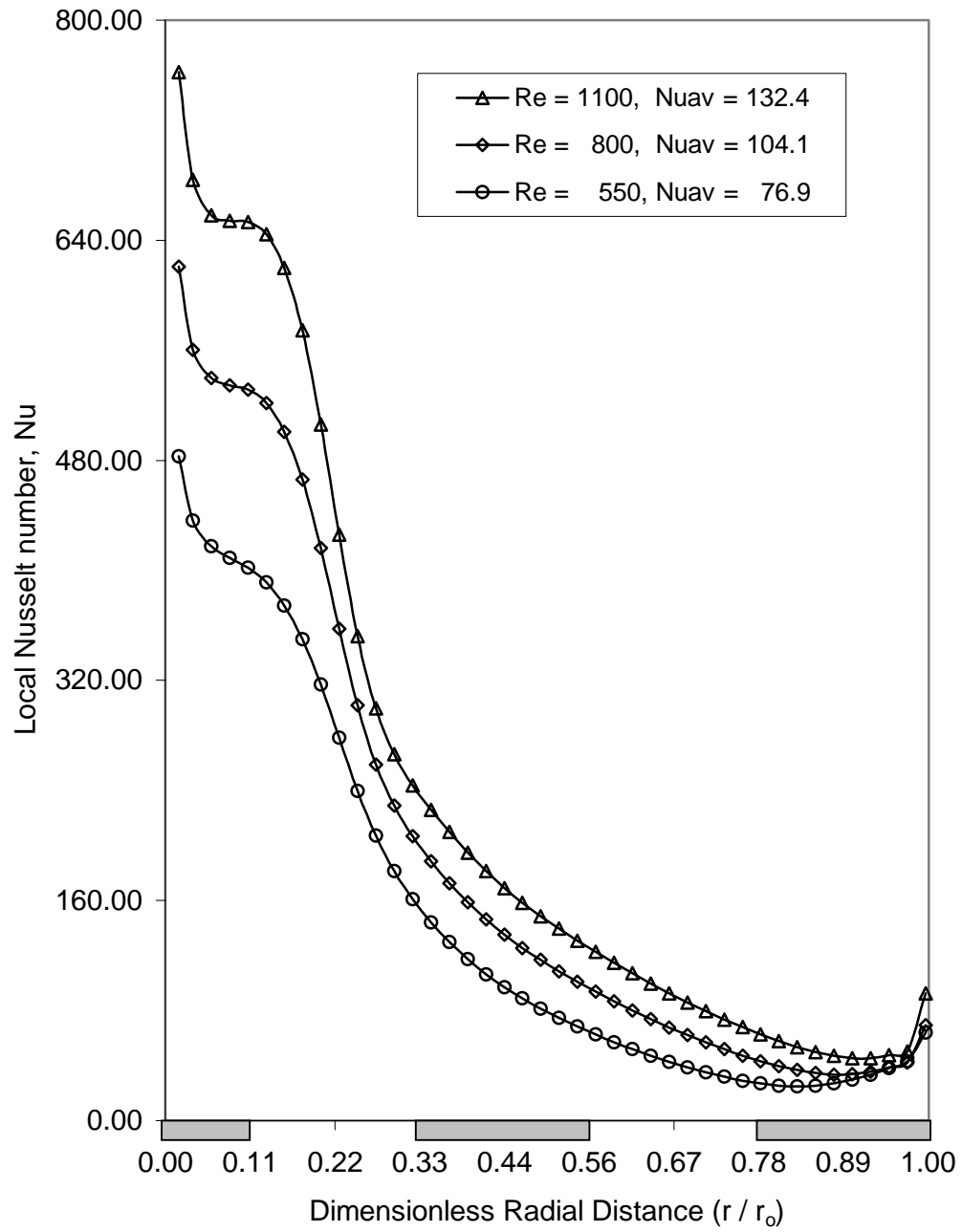


Figure 21. Local Nusselt number variation for different Reynolds number ( $T_j = 348$  K,  $b = 0.005$  m,  $H_n = 0.0085$  m,  $r_n = 0.00085$  m, Copper plate,  $q_w = 63$  kW/m<sup>2</sup>)



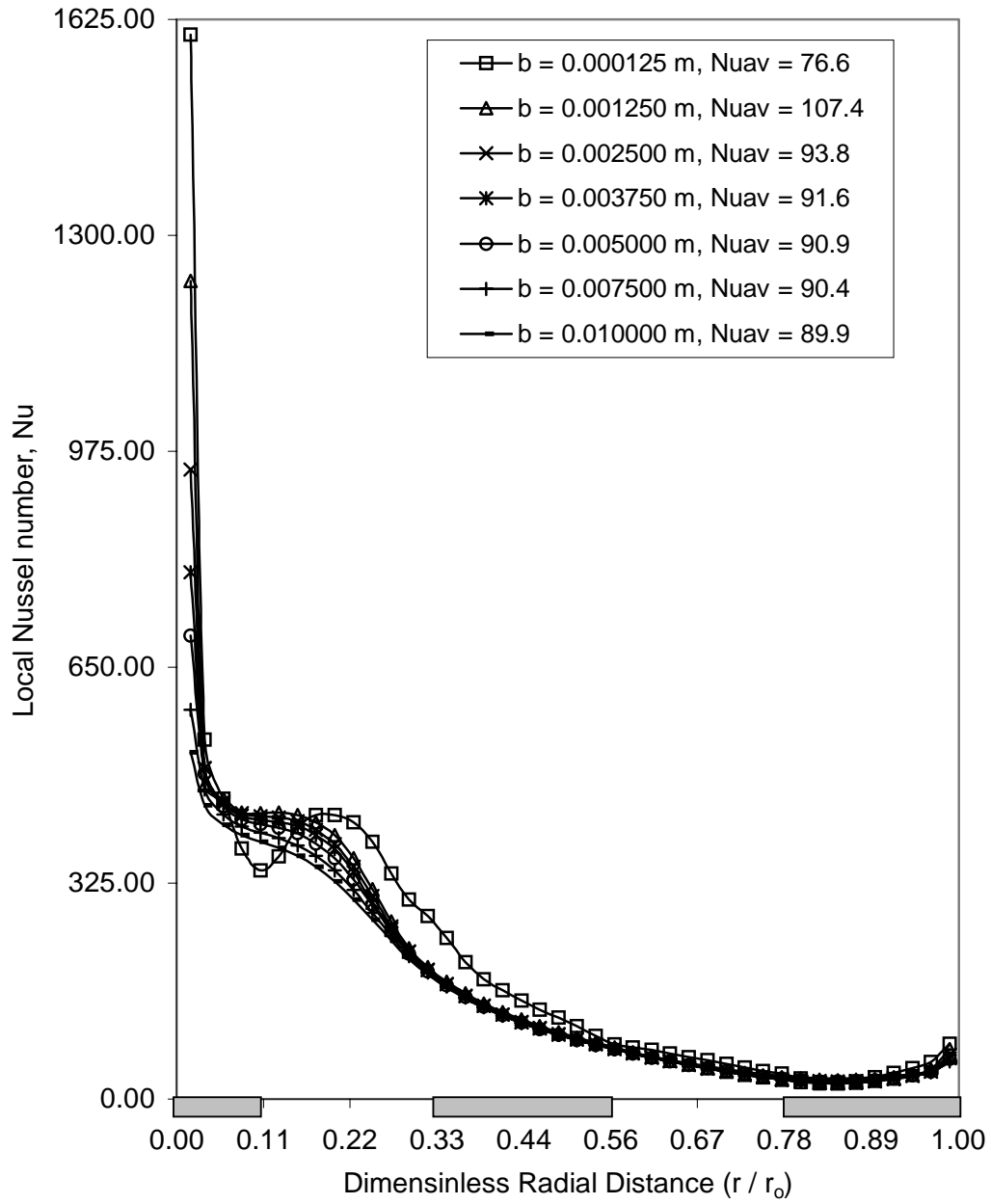


Figure 22. Local Nusselt number variation for different disk thickness ( $Re = 550$ ,  $T_j = 348$  K,  $H_n = 0.0085$  m,  $r_n = 0.00085$  m, Constantan plate,  $q_w = 63$  kW/m<sup>2</sup>)

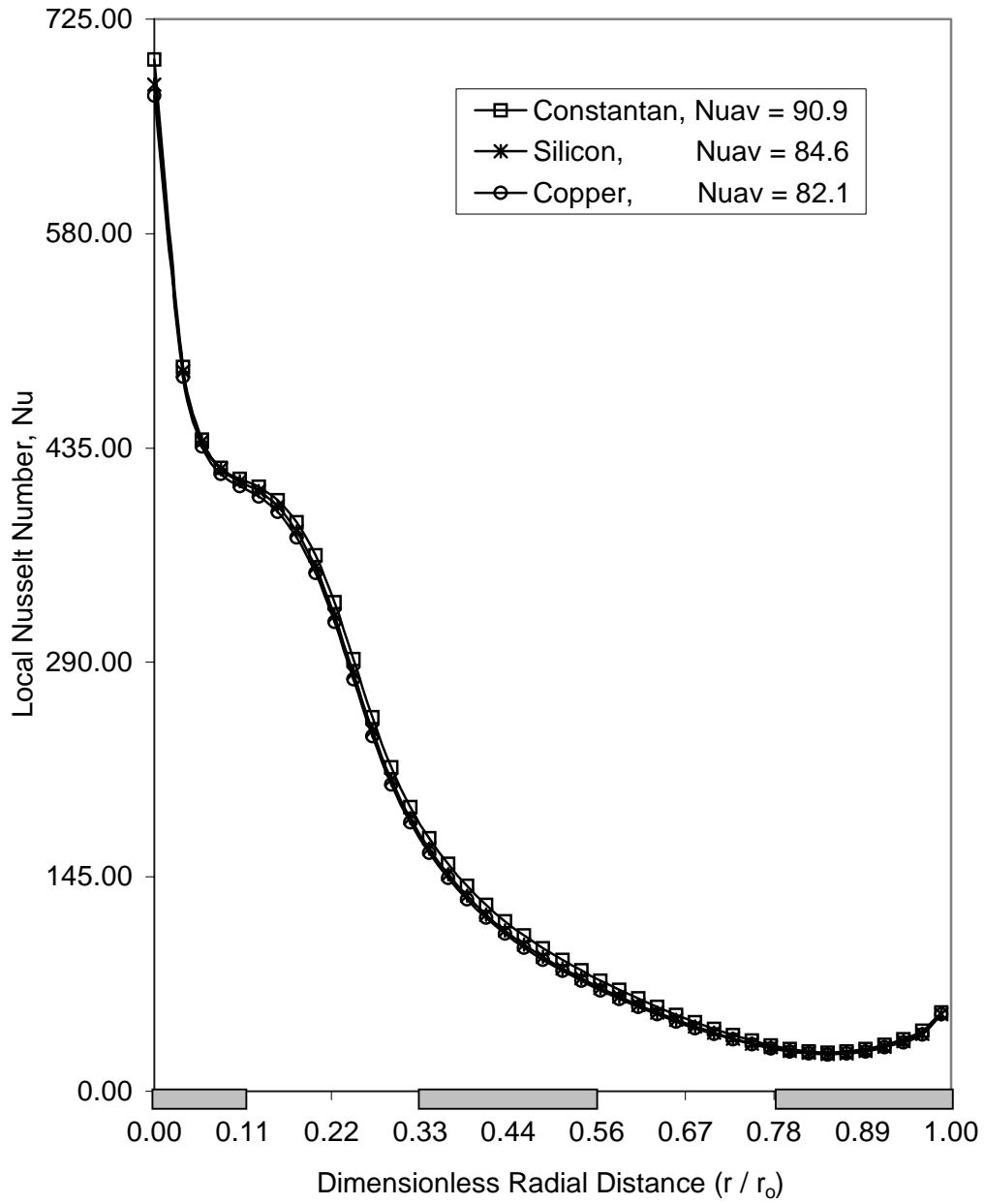


Figure 23. Local Nusselt number variation for different materials ( $Re = 550$ ,  $T_j = 348$  K,  $b = 0.005$  m,  $H_n = 0.0085$  m,  $r_n = 0.00085$  m,  $q_w = 63$  kW/m<sup>2</sup>)

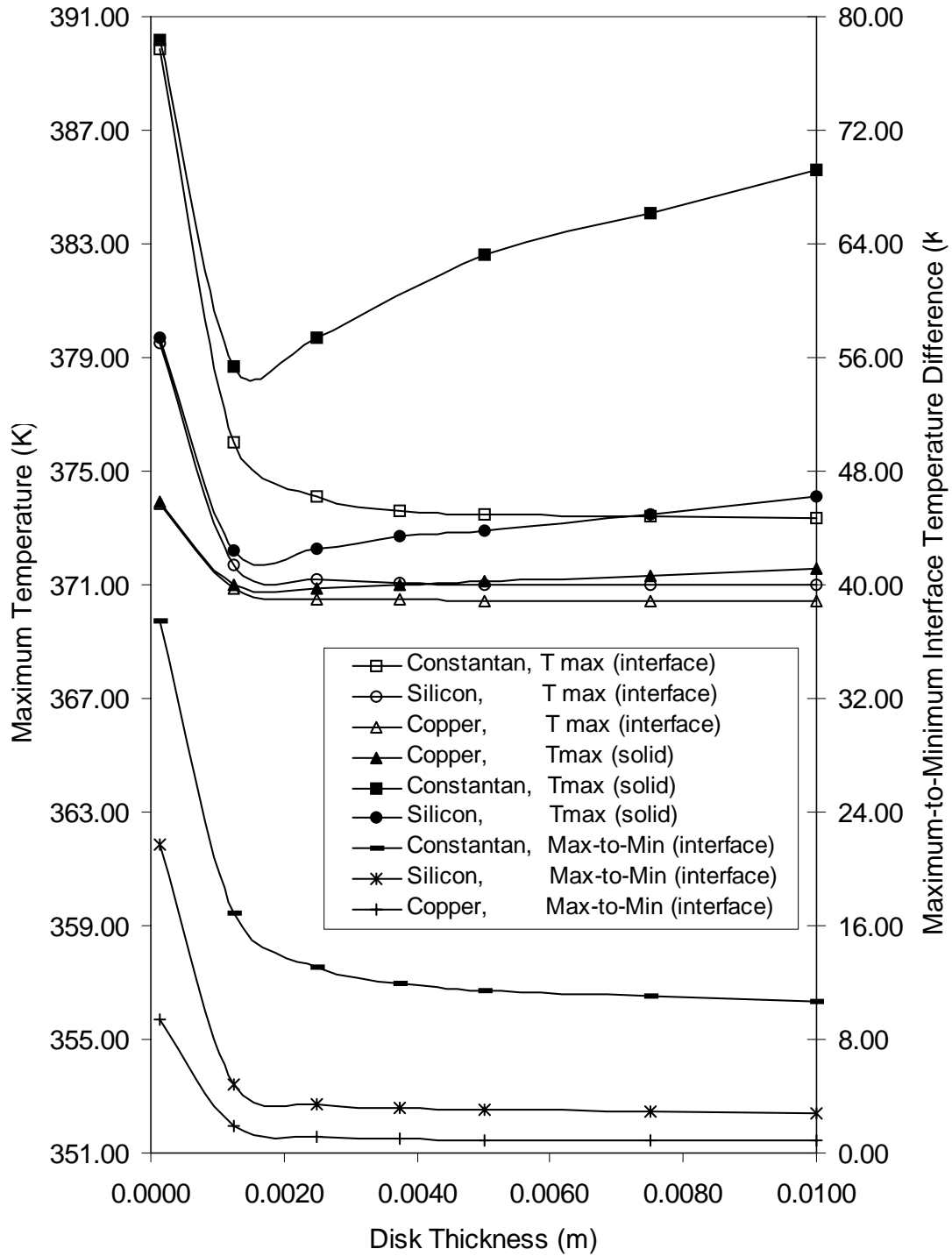


Figure 24. Interface temperature difference and maximum temperature variation with disk thickness (base case,  $Re = 550$ ,  $T_j = 348$  K,  $H_n = 0.0085$  m,  $r_n = 0.00085$  m,  $q_w = 63$  kW/m<sup>2</sup>)

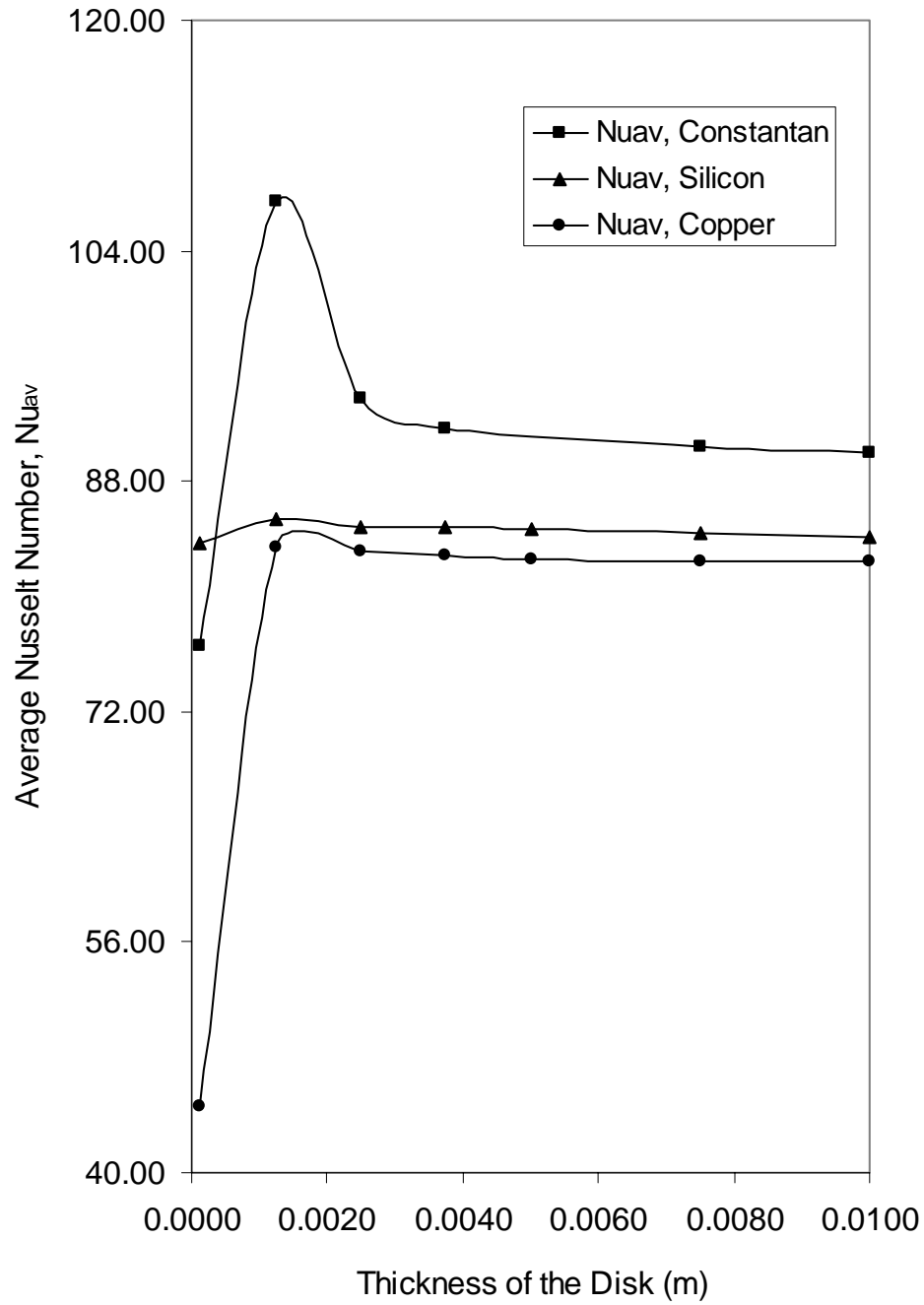


Figure 25. Average Nusselt number variation with disk thickness for different materials (base case,  $Re = 550$ ,  $T_j = 348$  K,  $H_n = 0.0085$  m,  $r_n = 0.00085$  m,  $q_w = 63$  kW/m<sup>2</sup>)

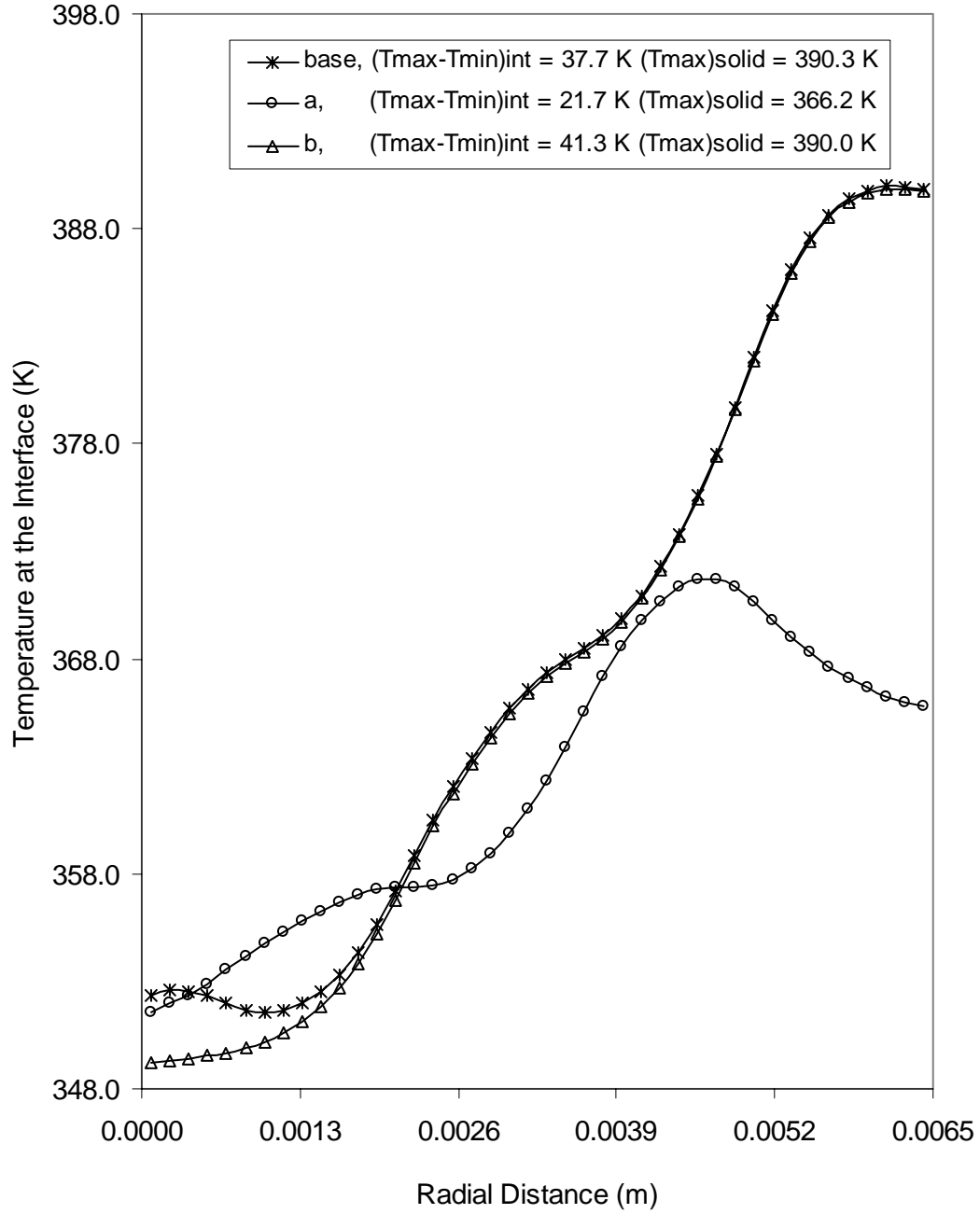


Figure 26. Temperature distribution at the interface for different positions of heat sources  
 $(\text{Re} = 1100, T_j = 348 \text{ K}, b = 0.000125 \text{ m}, H_n = 0.0085 \text{ m}, r_n = 0.00085 \text{ m},$   
 Constantan plate,  $q_o = 1.59 \text{ W}$ )

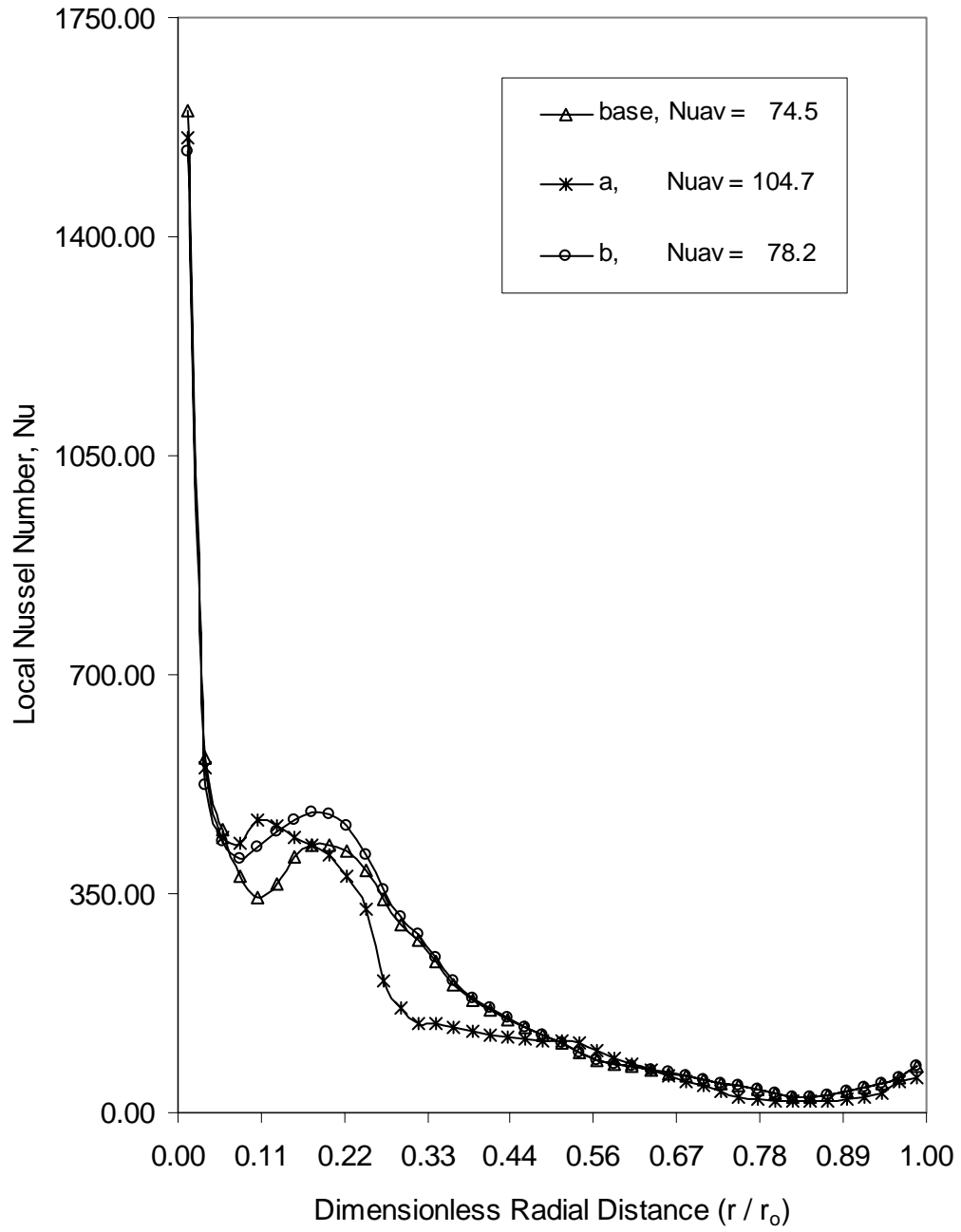


Figure 27. Local Nusselt number for different heat sources position and heat flux ( $Re = 1100$ ,  $T_j = 348$  K,  $b = 0.000125$  m,  $H_n = 0.0085$  m,  $r_n = 0.00085$  m, Constantan plate,  $q_o = 1.59$  W)

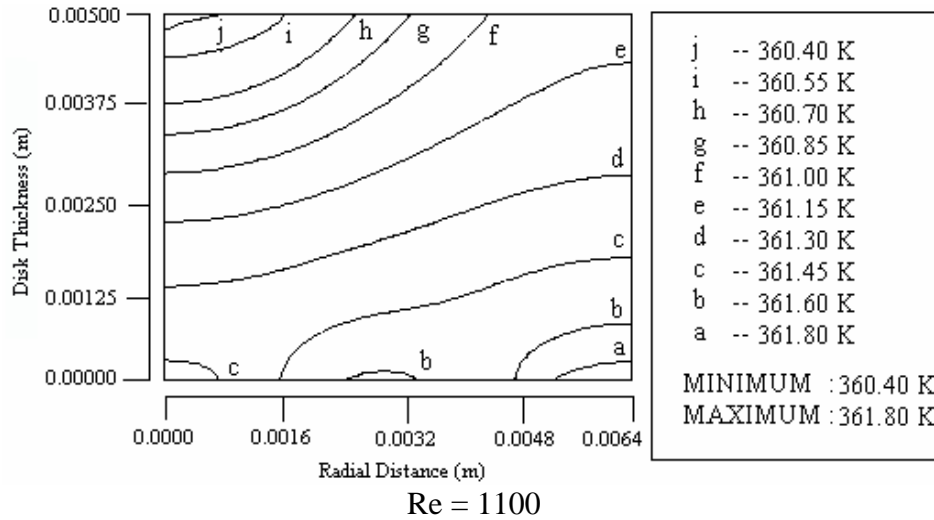
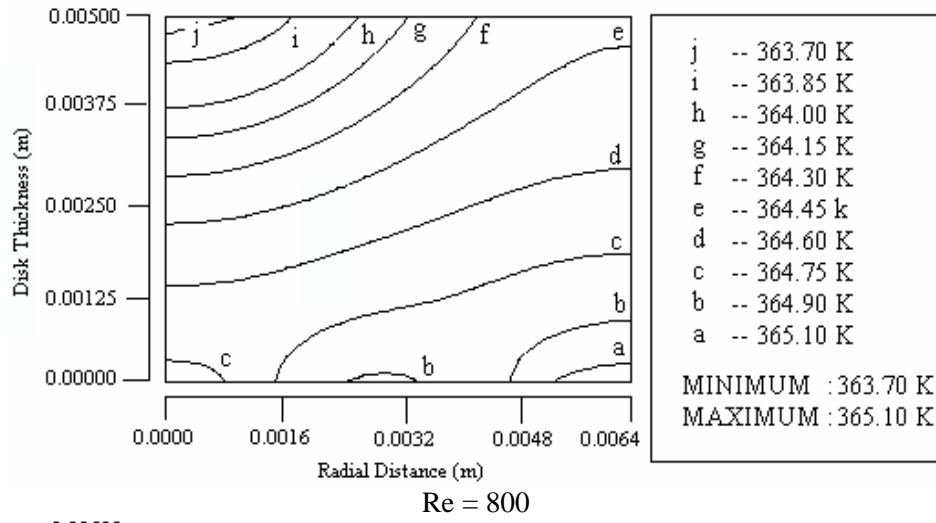
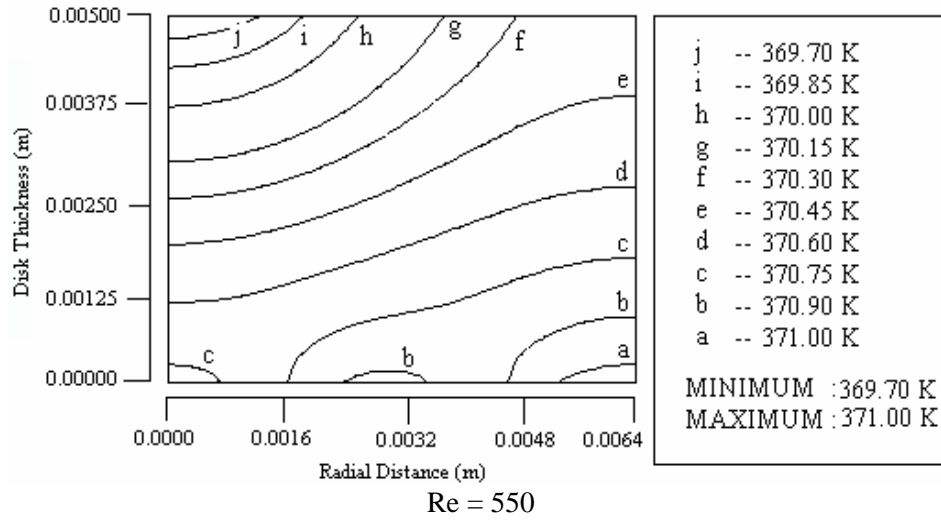
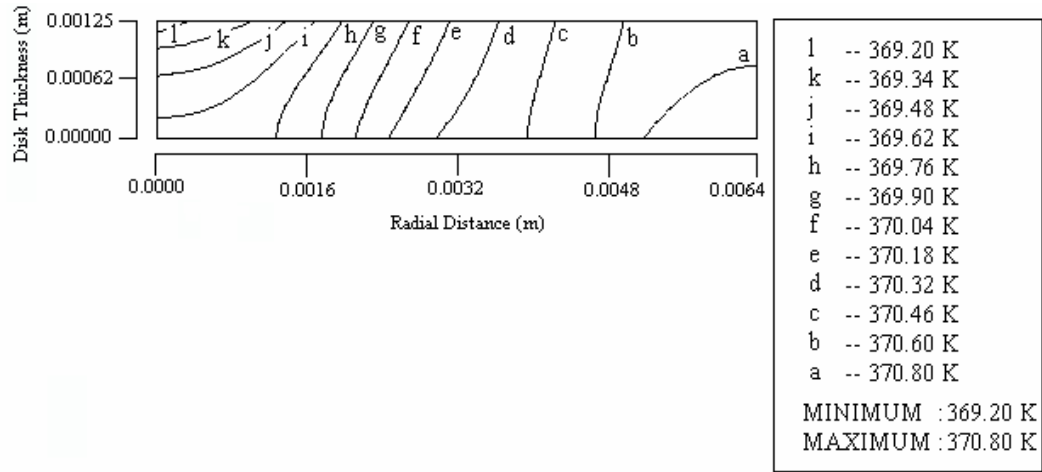
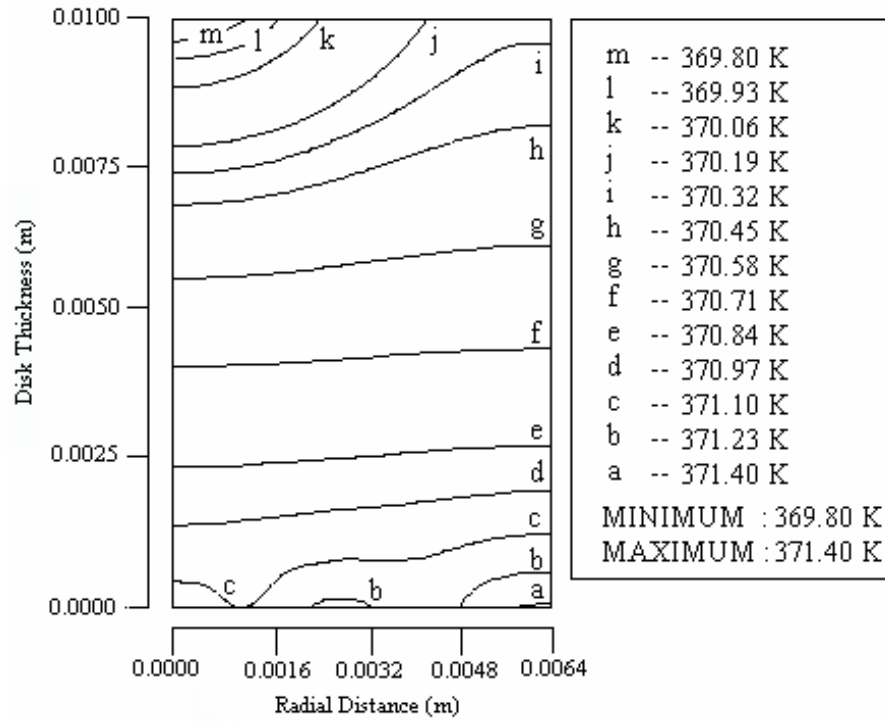


Figure 28. Isothermal lines within the disk for different Reynolds number (base case,  $T_j = 348$  K,  $b = 0.005$  m,  $H_n = 0.0085$  m,  $r_n = 0.00085$  m, Copper plate,  $q_w = 63$  kW/m<sup>2</sup>)



$b = 0.00125 \text{ m}$



$b = 0.01 \text{ m}$

Figure 29. Isothermal lines within the disk for different disk thickness (base case,  $Re = 550$ ,  $T_j = 348 \text{ K}$ ,  $H_n = 0.0085 \text{ m}$ ,  $r_n = 0.00085 \text{ m}$ , Copper plate,  $q_w = 63 \text{ kW/m}^2$ )



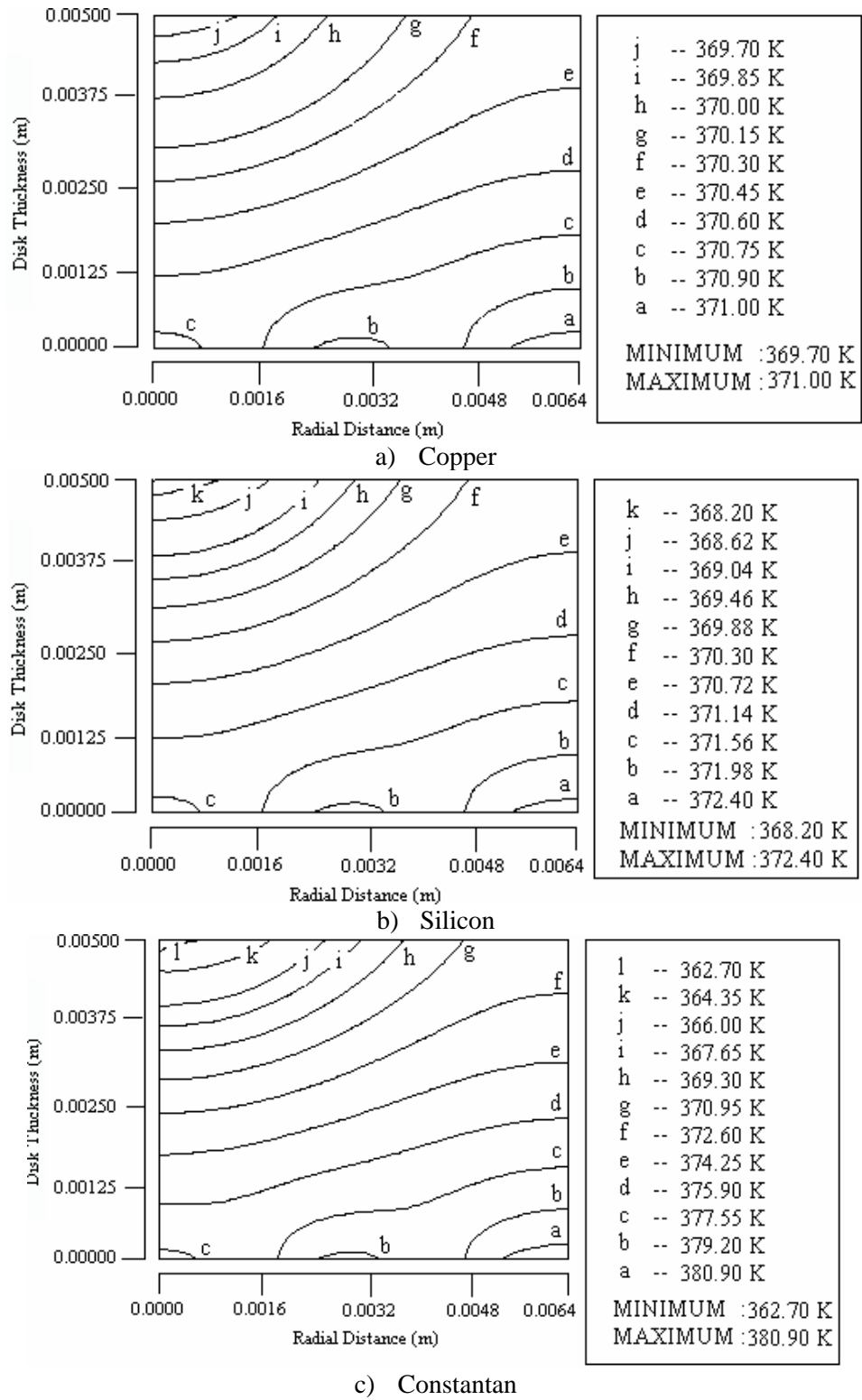


Figure 30. Isothermal lines within the disk for different materials (base case,  $Re = 550$ ,  $T_j = 348$  K,  $b = 0.005$  m,  $H_n = 0.0085$  m,  $r_n = 0.00085$  m,  $q_w = 63$  kW/m<sup>2</sup>)

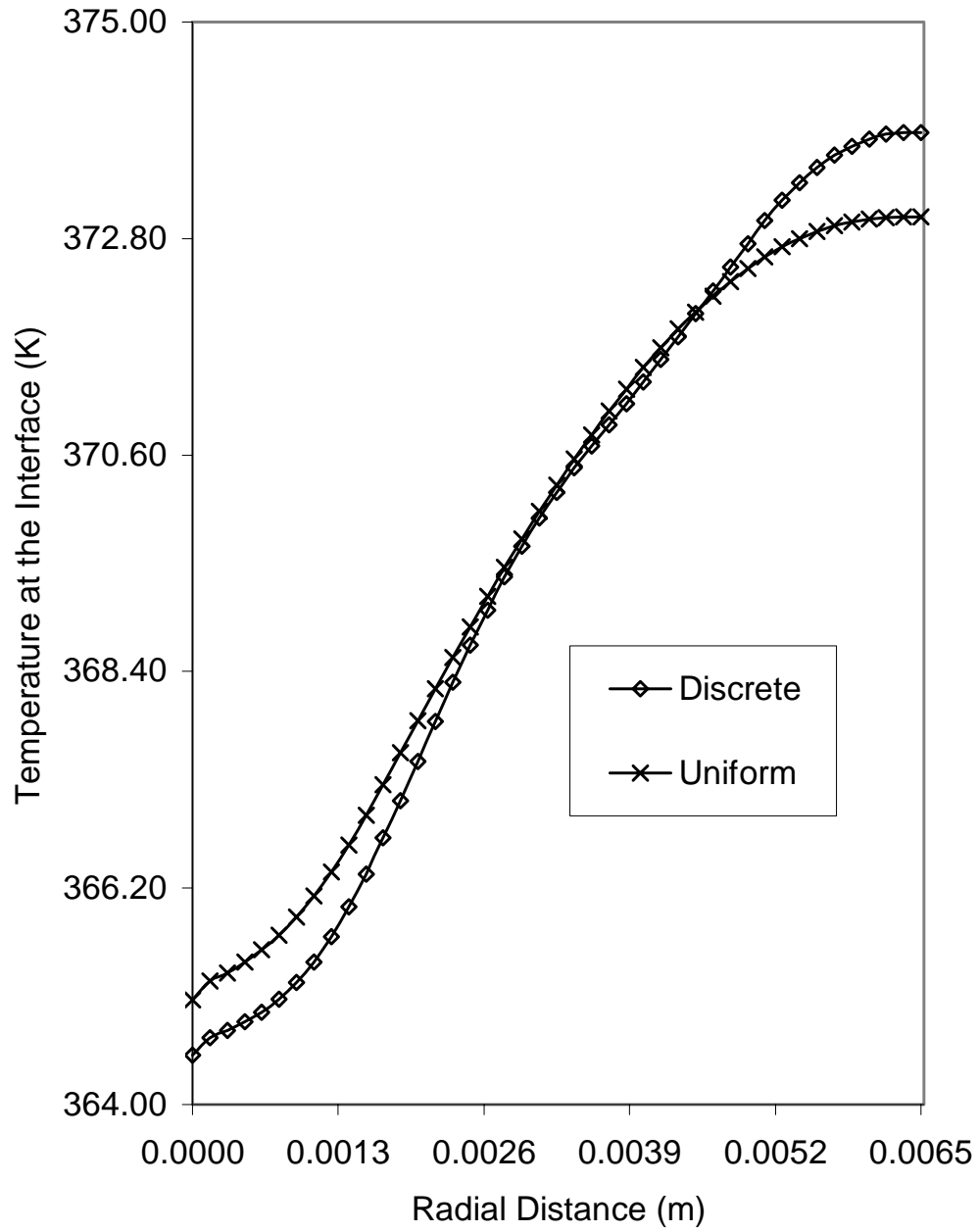


Figure 31. Temperature distribution at the Interface for discrete (base case) and uniform heat flux distribution ( $Re = 550$ ,  $T_j = 348$  K,  $b = 0.000125$  m,  $H_n = 0.0085$  m,  $r_n = 0.00085$  m, Constantan plate,  $q_o = 1.59$  W)

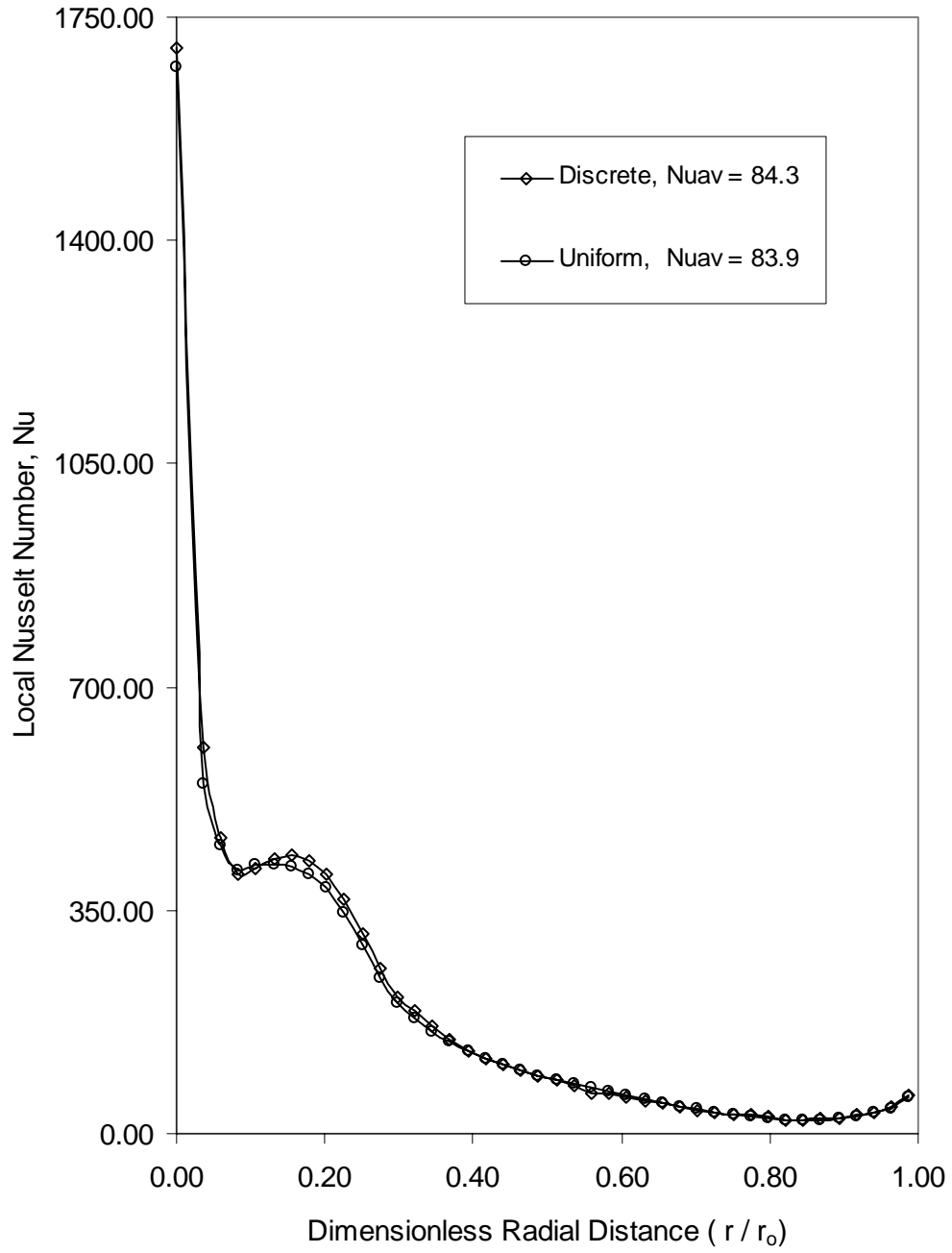


Figure 32. Local Nusselt number for discrete (base case) and uniform heat flux distribution ( $Re = 550$ ,  $T_j = 348$  K,  $b = 0.000125$  m,  $H_n = 0.0085$  m,  $r_n = 0.00085$  m, Constantan plate,  $q_o = 1.59$  W)

Table 3. Comparison between present simulation and Womac et al. [32]  
 $(T_j = 310 \text{ K}, b = 0.003 \text{ m}, H_n = 0.0165 \text{ m})$

Fluid	Re	$T_{\max} - T_{\min}$ Interface	$T_{\max}$ Interface	$Nu_{av}$ Womac et al. (1993)	$Nu_{av}$ Present study	Difference %
FC77	1200	0.084	322.6	181.0	189.0	4.4
Water	1465	0.186	312.9	199.0	197.0	1.0

# AXIAL FREE JET IMPINGING ON A UNIFORMLY HEATED DISK: TRANSIENT START-UP OF HEATING

## INTRODUCTION

Alkam and Butler [39] applied an explicit finite difference technique to solve the case of transient, forced convective conjugate heat transfer between an axisymmetric incompressible laminar impinging jet and a solid disk at the stagnation zone. Constant properties were considered and no viscous dissipation was taken into account. When the lubricating oil is used as the coolant and temperature difference between the jet and the disk is large, the property variation within the flow field can greatly affect the heat transfer process. Therefore the development of a numerical model for transient conjugate heat transfer during free jet impingement taking into account the variation of fluid properties with location and time is expected to be a very valuable contribution to the state-of-the-art of jet impingement cooling system design for aircraft applications.

## MATHEMATICAL MODEL

Consider an axial jet discharging from a circular nozzle and impinging on a uniformly heated solid disk as shown in Figure 1. The power is turned on and the heat source start supplying the heat after an isothermal steady state flow fluid has been established on the disk. When the fluid is considered to be incompressible with properties dependent on temperature only, the equations describing the conservation of mass, momentum, and energy in cylindrical coordinates can be written as [23]:

$$\frac{1}{r} \frac{\partial}{\partial r} (\rho_f r v_r) + \frac{\partial}{\partial z} (\rho_f v_z) = 0 \quad (35)$$

$$\begin{aligned} \rho_f \left( \frac{\partial v_r}{\partial t} + v_r \frac{\partial v_r}{\partial r} + v_z \frac{\partial v_r}{\partial z} \right) = & -\frac{\partial p}{\partial r} + \frac{1}{r} \frac{\partial}{\partial r} \left[ \frac{2}{3} r \mu \left( 2 \frac{\partial v_r}{\partial r} - \frac{v_r}{r} - \frac{\partial v_z}{\partial z} \right) \right] \\ & + \frac{\partial}{\partial z} \left[ \mu \left( \frac{\partial v_r}{\partial z} + \frac{\partial v_z}{\partial r} \right) \right] \end{aligned} \quad (36)$$

$$\begin{aligned} \rho_f \left( \frac{\partial v_z}{\partial t} + v_r \frac{\partial v_z}{\partial r} + v_z \frac{\partial v_z}{\partial z} \right) = & -\rho_f g - \frac{\partial p}{\partial z} + \frac{1}{r} \frac{\partial}{\partial r} \left[ r \mu \left( \frac{\partial v_r}{\partial z} + \frac{\partial v_z}{\partial r} \right) \right] \\ & + \frac{\partial}{\partial z} \left[ \frac{2}{3} \mu \left( 2 \frac{\partial v_z}{\partial z} - \frac{v_r}{r} - \frac{\partial v_r}{\partial r} \right) \right] \end{aligned} \quad (37)$$

$$\begin{aligned}
\rho_f \left( \frac{\partial(c_{p_f} T_f)}{\partial t} + v_r \frac{\partial(c_{p_f} T_f)}{\partial r} + v_z \frac{\partial(c_{p_f} T_f)}{\partial z} \right) &= \left[ \frac{1}{r} \frac{\partial}{\partial r} \left( r k_f \frac{\partial T_f}{\partial r} \right) + \frac{\partial}{\partial z} \left( k_f \frac{\partial T_f}{\partial z} \right) \right] \\
&+ \left( v_z \frac{\partial p}{\partial z} + v_r \frac{\partial p}{\partial r} \right) + \mu_f \left\{ 2 \left[ \left( \frac{\partial v_r}{\partial r} \right)^2 + \left( \frac{v_r}{r} \right)^2 + \left( \frac{\partial v_z}{\partial z} \right)^2 \right] + \left( \frac{\partial v_r}{\partial z} + \frac{\partial v_z}{\partial r} \right)^2 \right. \\
&\quad \left. - \frac{2}{3} \left[ \frac{\partial v_r}{\partial r} + \frac{v_r}{r} + \frac{\partial v_z}{\partial z} \right]^2 \right\} \quad (38)
\end{aligned}$$

The variation of thermal conductivity within the solid was found to be significant for some materials such as diamond. Therefore, considering variable properties, the equation describing the conservation of energy can be written as follows:

$$\frac{1}{r} \frac{\partial}{\partial r} \left( r k_s \frac{\partial T_s}{\partial r} \right) + \frac{\partial}{\partial z} \left( k_s \frac{\partial T_s}{\partial z} \right) = \rho_s c_{p_s} \frac{\partial T_s}{\partial t} \quad (39)$$

Equations (35-39) are subjected to the boundary conditions described by equations (6-13). The disk and the fluid were assumed to be in equilibrium isothermal condition at the start of the transient heating process. This is expressed as:

$$\text{At } t = 0: T_s = T_f = T_j, \quad v = v_i(r, z) \quad (40)$$

It may be noted that the above mathematical model is based on the assumption of two-dimensional axisymmetric flow and heat transfer. In practice, such free surface liquid flows are often three-dimensional, despite the two-dimensionality of the jet generation apparatus. The secondary flows are results of vortices which develop upon stagnation in the flow, and whose axes extend radially outward from the stagnation point.

## NUMERICAL COMPUTATION

The governing equations along with the boundary conditions described in the previous section were solved using the finite-element method. The computation domain was divided into a number of quadrilateral elements. The dependent variables, i.e., velocity, pressure, and temperature were interpolated to a set of nodal points that defined the elements. In each element, the velocity, pressure, and temperature fields were approximated which led to a set of equations that defined the continuum. To solve the position of the free surface, a new degree of freedom at the nodes on the free surface was introduced into the global system of equations. The discretization of governing transport equations and boundary conditions were carried out using the Galerkin formulation. The solution of the resulting algebraic equations was carried out using the Newton-Raphson method. Since the solution of the momentum equation required only two out of the three boundary conditions at the free surface, the third condition was used to upgrade the position of the free surface at the end of each iteration step.

In order to determine the initial velocity field,  $v_i(r, z)$ , equations for the conservation of mass and momentum were solved. Once the initial free surface height distribution and the flow field for an isothermal equilibrium condition has been established, the power at the heat source was turned on. The computation domain covered both solid and fluid regions and equations for the conservation of mass, momentum, and energy were solved simultaneously as a conjugate problem taking into account the variation of fluid and solid properties with temperature. At each time step, the solution was considered converged when the field values did not change from one iteration to the next, and the sum of residuals for each degree of freedom was less than 1E-08. Computation was continued marching forward with time until a steady state condition was reached. Due to large changes at the outset of the transient and very small changes when the solution approached the steady state condition, a variable time step was used for the computation.

## RESULTS AND DISCUSSION

The simulation was carried out for three different materials, namely: copper, diamond, and constantan. The working fluid used for the simulation was Mil-7808, which is a lubricating oil used in aircrafts. The relevant fluid properties were calculated from the following correlating equations which are valid for  $303 \text{ K} < T_f < 390 \text{ K}$ :  $c_{pf} = 903.8 + 3.332T_f$ ,  $k_f = 0.18 - 1 \times 10^{-4} T_f$ ,  $\rho_f = 1181 - 0.708T_f$ , and  $\mu = 0.941 - 5.07 \times 10^{-3} T_f + 6.87 \times 10^{-6} T_f^2$ . The range of Prandtl number encountered in the present investigation was 169-384. The distance of the nozzle from the disk ( $H_n = 0.0085 \text{ m}$ ), diameter of the nozzle ( $d_n = 0.0017 \text{ m}$ ), and radius of the disk ( $r_o = 0.0065 \text{ m}$ ) were kept constant during the simulation.

Computations were performed to calculate a suitable time step in order to determine its sensitivity on the transient solution. Figure 33 plots the variation of maximum temperature at the interface with time for different values of time increments. It is observed that the simulation is not very sensitive to the size of time step. A time increment of 1 second was selected to ensure a smooth variation.

In order to validate the present fluid flow model with previous experimental and theoretical research, computation was carried out for a jet of water impinging perpendicularly at the center of a circular disk. The free surface height distribution is shown in Figure 34. The present results compared quite well with experimental data of Stevens and Webb [40] and analytical results of Watson [41]. The maximum deviation of test data from theoretical results is seen in the transition region between the stagnation zone and the boundary layer flow. The computed maximum velocity at the free surface also compared within 4% of the value reported by Stevens and Webb [40].

A key parameter for understanding the transient heat transfer process is the local heat flux imparted to the jet at the solid-fluid interface and the total rate of heat transfer from the heat source to the coolant. These are important variables in assessing the thermal response of solid materials to the turning on of power of the heat source located on one surface and a coolant jet impinging on the opposite surface. The local heat flux distribution for different times is presented in Figure 35. Because of initial isothermal condition, the interfacial heat flux is zero at

$t=0$ . It may be noted that heat flux at the interface increases with time. A large heat flux is seen at the stagnation region because the cold fluid at the jet strikes that location and maintains the minimum temperature at the interface. The heat transfer at that location is highest because of constant renewal of cold fluid to carry away the heat. The heat dissipated at the heater is utilized to increase the temperature of the solid as well as the fluid. As the temperature rises with time, the thermal storage in the solid decreases and more heat proceeds to the interface and dissipated to the liquid. The interfacial heat flux increases rapidly with time in the earlier part of the transient, and more slowly as the steady state condition is approached. For  $t > 65$  s ( $Fo > 1.8$ ), the interfacial heat flux practically reaches the steady state distribution. The figure also shows the average dimensionless interfacial heat flux at different time instants.

Figure 36 presents the interfacial temperature distribution at different time. It is noticed that at early stages of the heat transfer process, the temperature at the interface rises uniformly at all locations resulting in a practically isothermal interface condition. This behavior is due to transient thermal storage in the fluid required to develop a thermal boundary layer starting with an isothermal initial condition. The thickness of this boundary layer increases with time and becomes significant only in the later part of the transient. The interface temperature responds accordingly. Since the leading edge of this boundary layer is located at the stagnation point and its thickness increases downstream; it can be noticed that in the later part of the transient, the temperature becomes minimum at the impinging point and maximum at the outer edge of the disk. The same figure presents the values for maximum-to-minimum temperature difference at the interface. As expected, the maximum-to-minimum temperature difference increases with time.

The variation of local Nusselt number with time is presented in Figure 37. The local heat transfer coefficient increased with time in the stagnation region but decreased with time in the thin film region further downstream. Because of linear rise of length scale 'r' used for the definition of Nusselt number, changes in heat transfer coefficient are magnified at larger distances downstream. The average heat transfer coefficient as well as the average Nusselt number decrease with time and reach their respective minimum values and thereafter increase with time all the way to the steady state condition. This undershoot in the average heat transfer coefficient is a result of different rate of increment for interfacial heat flux and interface temperature during the transient heating process. The local steady state heat transfer coefficient at the stagnation region was compared with the correlation developed by Liu et al.[42] for the stagnation region heat transfer of an impinging jet including the effects of surface tension. The difference between present computation and that predicted by the correlation was found to be around 3.9%.

The variation of maximum temperature in the solid, maximum temperature at the interface, and the maximum-to-minimum temperature difference at the interface during the transient process are presented in Figure 38 for two different Reynolds number. As expected, the temperature increases with time starting from the initial isothermal condition. A rapid increment is seen at the earlier part of the transient and it levels off as the thermal storage capacity of the solid diminishes and becomes zero at the steady state condition. It is noticed that the time required to reach the steady state condition is lower at higher Reynolds number because a higher velocity of fluid helps to enhance the convective heat transfer process. The average Nusselt



number variation with time for two different Reynolds numbers is presented in Figure 39. It is noticed that average Nusselt number decreases with time at early stages of the transient process, after that increases and reaches the steady state value. Figure 40 presents the time required to reach the steady state condition as a function of Reynolds number. The duration of the transient decreases as the Reynolds number increases. The time to reach steady state was defined as the time needed to approach 99% of steady state local Nusselt number over the entire solid-fluid interface.

Another important factor that controls the transient heat transfer process is the thickness of the disk. Its effect on the maximum temperature in the solid, maximum temperature at the interface, and maximum-to-minimum temperature difference at the interface can be observed in Figure 41. As the thickness increases, the time required to reach steady state increases. This is expected because the thermal storage capacity of the disk is directly proportional to its thickness. Figure 42 presents the average Nusselt number variation with time for two different disk thicknesses. Over the entire duration of the transient process, the average Nusselt number is larger for smaller thickness. The smaller thickness presents a lower thermal resistance to heat flux and allows it to reach the interface faster.

The maximum temperature at the interface for different materials is shown in Figure 43. It can be noticed that the material with larger thermal diffusivity reaches the steady state faster. The values of thermal diffusivity for the materials considered here at 293 K are:  $\alpha_{diamond} = 1.29e^{-3} \text{ m}^2/\text{s}$ ,  $\alpha_{copper} = 1.12e^{-4} \text{ m}^2/\text{s}$ , and  $\alpha_{constantan} = 6.12e^{-6} \text{ m}^2/\text{s}$ . As expected, the temperature changes are faster at the earlier part of the transient, and only gradual as the steady state is approached. The magnitude of temperature non-uniformity at the interface at steady state is controlled by the thermal conductivity of the material. It can be noticed that constantan with  $k_{constantan} = 22.7 \text{ W / m.K}$  has maximum-to-minimum temperature difference of 11.1 K, whereas diamond with  $k_{diamond} = 2330 \text{ W / m.K}$  has only 0.2 K temperature difference at the interface. Figure 44 presents the variation of average Nusselt number with time for different materials considered in this study. In the earlier part of the transient (before the undershoot), diamond shows a larger average heat transfer coefficient compared to copper. However, after the undershoot all the way to the steady state, the material with lower thermal conductivity attains the higher value in the average Nusselt number. A material with lower thermal conductivity provides a higher thermal resistance within the solid. This results in a lower temperature at the solid-fluid interface when the steady state condition is approached. This combined with the changes in local thermal conductivity of the fluid with temperature results in a higher Nusselt number. The time required to reach steady state for different materials and different disk thicknesses is presented in Figure 45. As expected, as the thickness increases, the time to reach steady state increases.

Figure 46 shows the growth of the isothermal lines inside the solid at different time instants for  $b = 0.005 \text{ m}$  ( $b/d_n = 2.94$ ). It can be observed that at the beginning of the transient process the isothermal lines grow parallel to the bottom heated surface of the disk. As the time progresses, the isothermal lines start moving upward like a one dimensional heat conduction phenomenon. When the transient isothermal lines reach the area close to the interface, they start forming concentric lines around the stagnation point. As the time progresses, the effects of the

heat sink is propagated down into the solid. An equilibrium is established as the steady state is approached. It can be noticed that temperature over the entire solid domain rises with time. Figure 47 plots the isothermal lines within the solid for  $b = 0.0025$  m ( $b/d_n = 1.47$ ). The behavior at the beginning of the transient process is similar to that observed in Figure 17, but as the transient process progresses, the concentric isothermal lines around the stagnation point continue to grow and reach the bottom surface of the disk.

## NOMENCLATURE

$b$	Thickness of the disk [m]
$c_p$	Specific heat at constant pressure [kJ / kg K]
$d_n$	Diameter of the nozzle [m]
Fo	Fourier number, $\alpha_f t / d_n^2$
$g$	Acceleration due to gravity [m / s <sup>2</sup> ]
$h$	Heat transfer coefficient [W / m <sup>2</sup> K], $q_{\text{int}} / (T_{\text{int}} - T_j)$
$h_{\text{av}}$	Heat transfer coefficient [W / m <sup>2</sup> K], $\frac{2}{r_o^2 \left( \bar{T}_{\text{int}} - T_j \right)} \int_0^{r_o} h r (T_{\text{int}} - T_j) dr$
$H_n$	Distance of the nozzle from the disk [m]
$k$	Thermal conductivity [W / m K]
$n$	Coordinate normal to the free surface [m]
Nu	Nusselt number, $h r / k_f$
$\text{Nu}_{\text{av}}$	Average Nusselt number, $h_{\text{av}} r_o / k_f$
$p$	Pressure [Pa]
$q$	Heat flux [W / m <sup>2</sup> ]
$\bar{q}$	Average heat flux [W / m <sup>2</sup> ]
$r$	Radial coordinate [m]
$r_n$	Radius of the nozzle [m]
$r_o$	Radius of the disk [m]
Re	Reynolds number, $\rho_f v_j d_n / \mu$
$t$	Time [s]
$T$	Temperature [K]
$\bar{T}_{\text{int}}$	Average interface temperature [K], $\frac{2}{r_o^2} \int_0^{r_o} T_{\text{int}} r dr$
$T_j$	Jet temperature [K]
$v_i$	Initial velocity field [m / s]
$v_j$	Jet velocity [m / s]
$v_t$	Velocity along the free surface [m / s]
$v_r$	Radial velocity [m / s]

$v_z$  Axial velocity [m / s]

$z$  Axial coordinate [m]

### **Greek Symbols**

$\alpha$  Thermal diffusivity [ $\text{m}^2/\text{s}$ ]

$\delta$  Height of the free surface from the disk [m]

$\mu$  Dynamic viscosity of the fluid [kg / m s]

$\theta$  Dimensionless temperature [K],  $(T-T_j)/(q_w d_n/k_f)$

$\rho$  Density [kg /  $\text{m}^3$ ]

$\sigma$  Surface tension coefficient [N / m]

### **Subscripts**

atm Atmospheric condition

av Average

f Fluid

int Solid-fluid interface

s Solid

w Bottom surface of the disk

## **CONCLUSIONS**

A number of important conclusions can be derived from the present numerical results. The local temperature in the fluid and solid regions as well as the heat flux at the solid fluid interface increase with time, but at different rates. The average heat transfer coefficient and average Nusselt number decrease with time at early stages of the transient process, after reaching a minimum; they increase to attain their steady state values. The jet Reynolds number was found to be an important parameter controlling the transient process. The time required to reach steady state condition decreases as the Reynolds number increases. The maximum temperature at the interface and the maximum temperature inside the solid decrease as Reynolds number increases, while the maximum-to-minimum temperature difference at the interface increases with Reynolds number. The time required to reach steady state condition increases as the thickness of the disk is increased. Over the entire duration of the transient process, the average heat transfer coefficient is larger for smaller thickness. The duration of the transient is shorter for a material with higher thermal diffusivity.

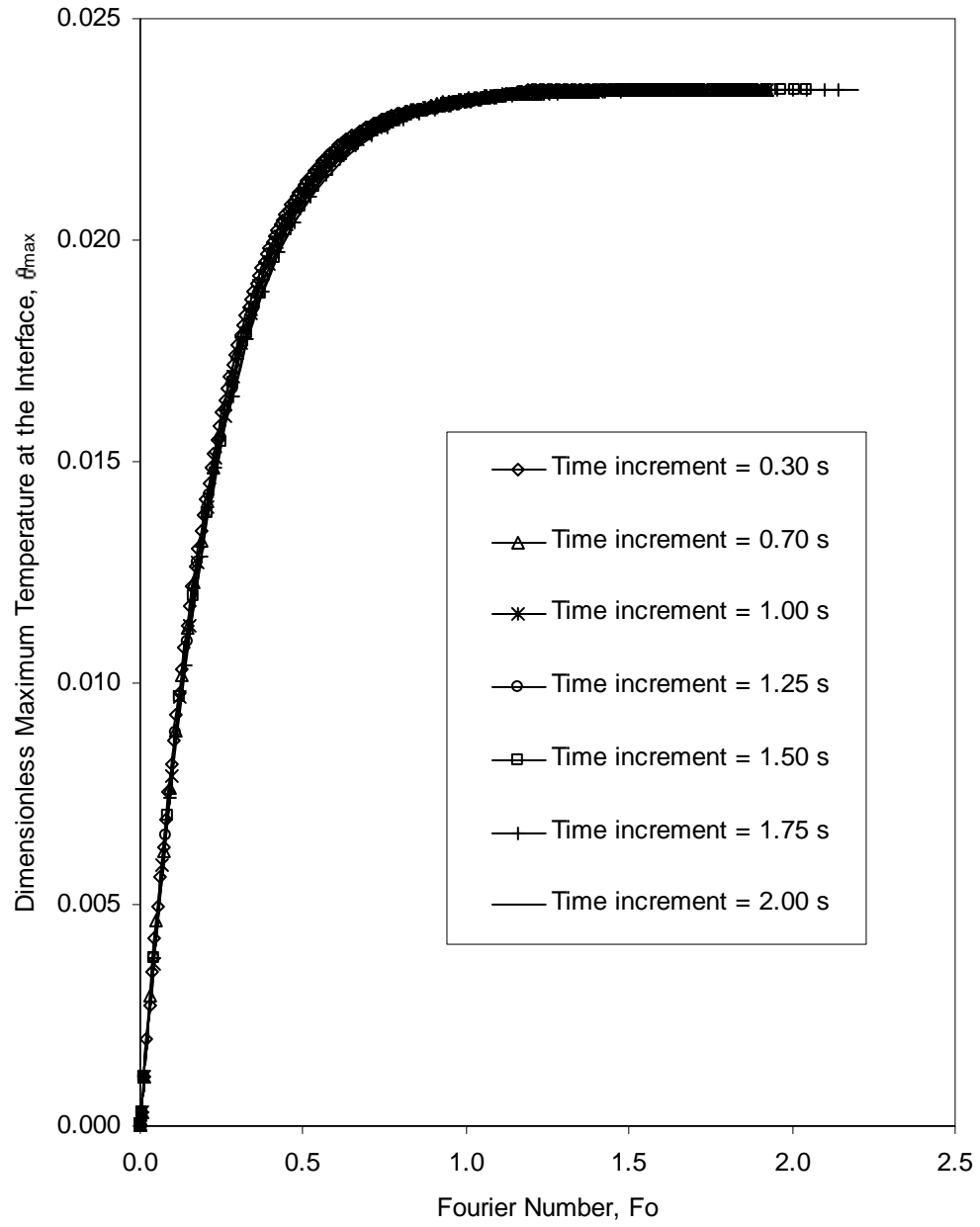


Figure 33. Dimensionless temperature variation for different time steps  
 ( $Re = 550$ ,  $T_j = 310$  K,  $b/d_n = 2.94$ ,  $H_n/d_n = 5$ , Copper plate,  $q_w = 63$  kW/m<sup>2</sup>)

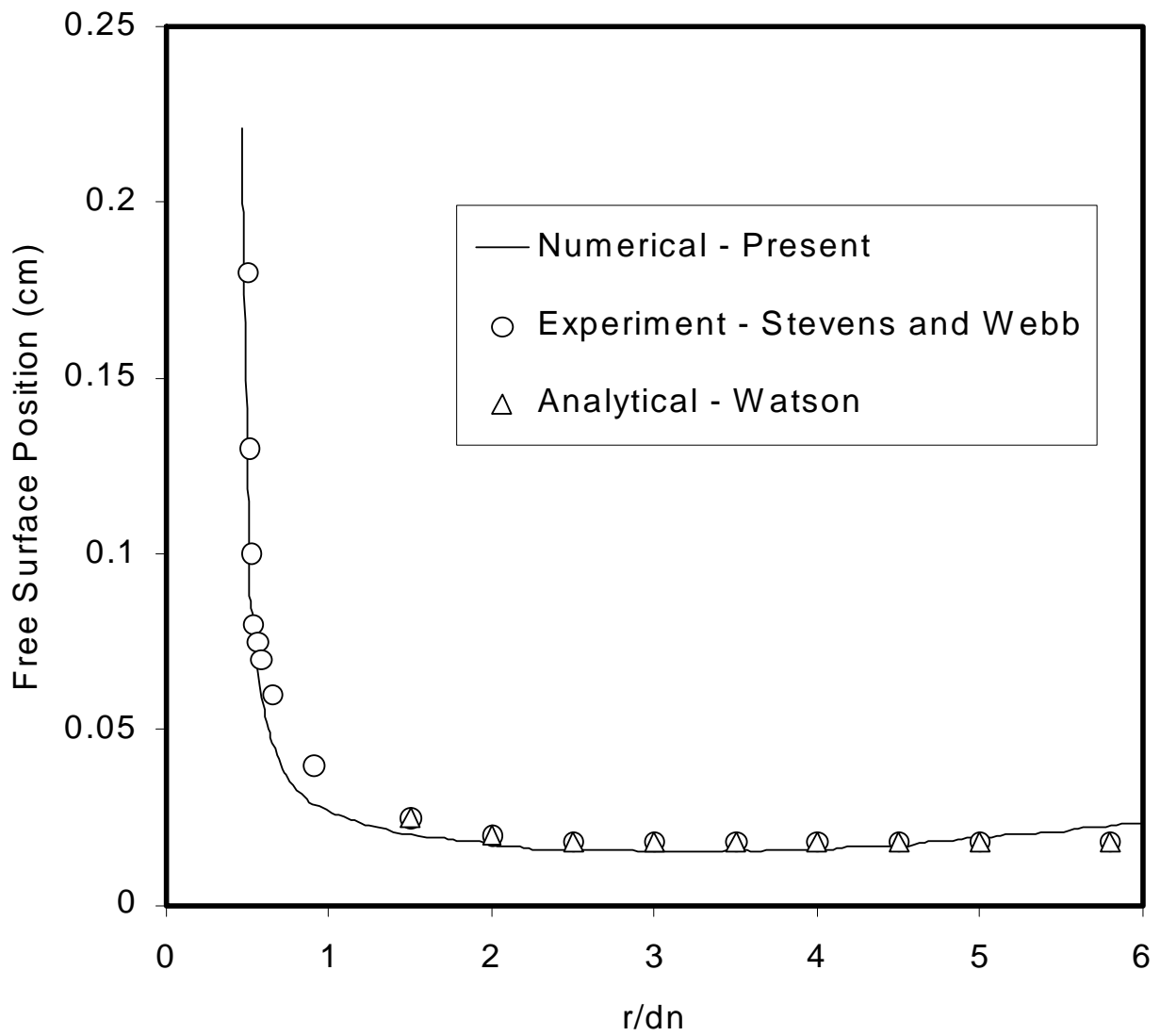


Figure 34. Comparison of free surface height with previous investigations by Stevens and Webb [40] and Watson [41] using water as the working fluid

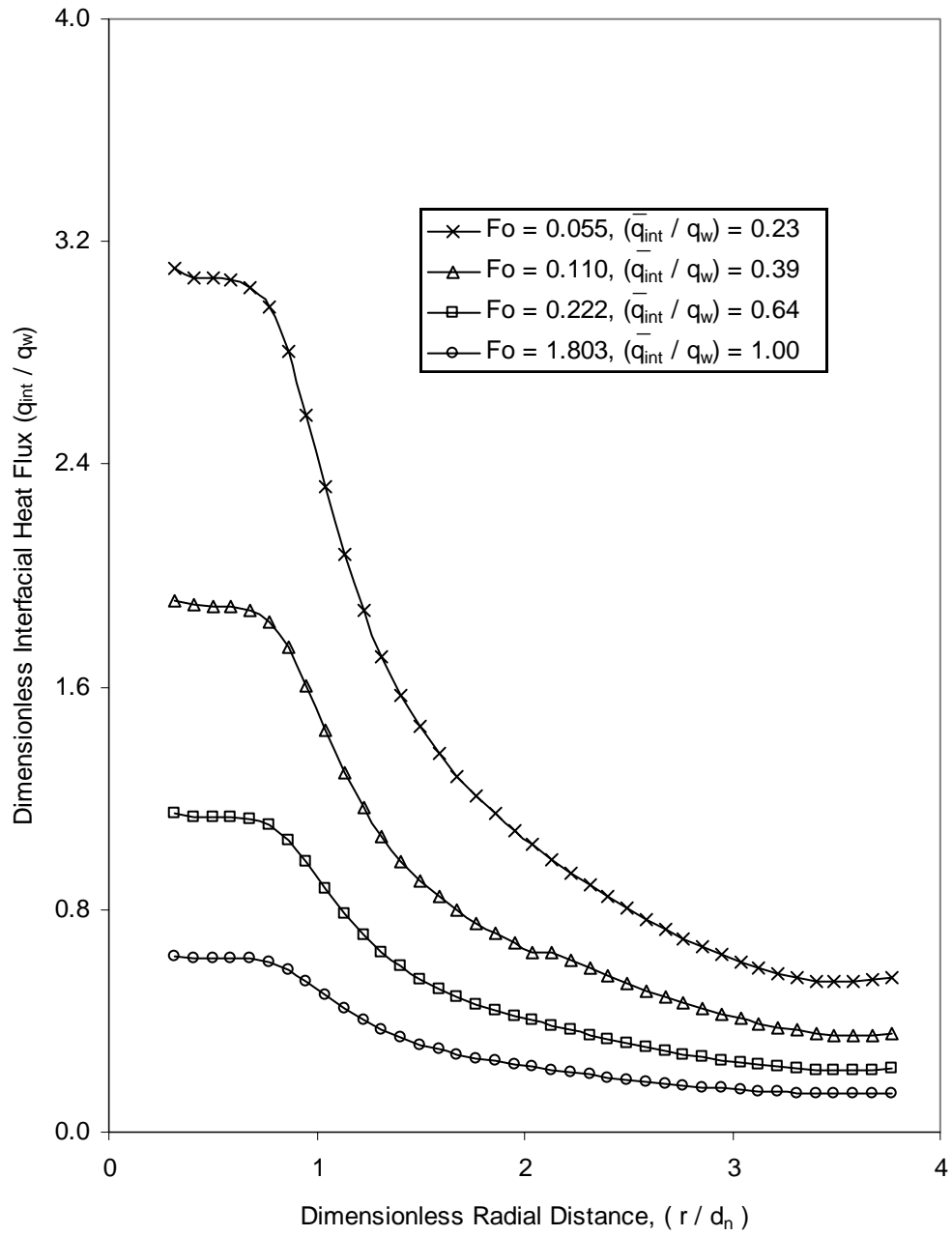


Figure 35. Dimensionless local heat flux distribution at the interface ( $Re = 550$ ,  $T_j = 310$  K,  $b/d_n = 2.94$ ,  $H_n/d_n = 5$ , Copper plate,  $q_w = 63$  kW/m<sup>2</sup>)

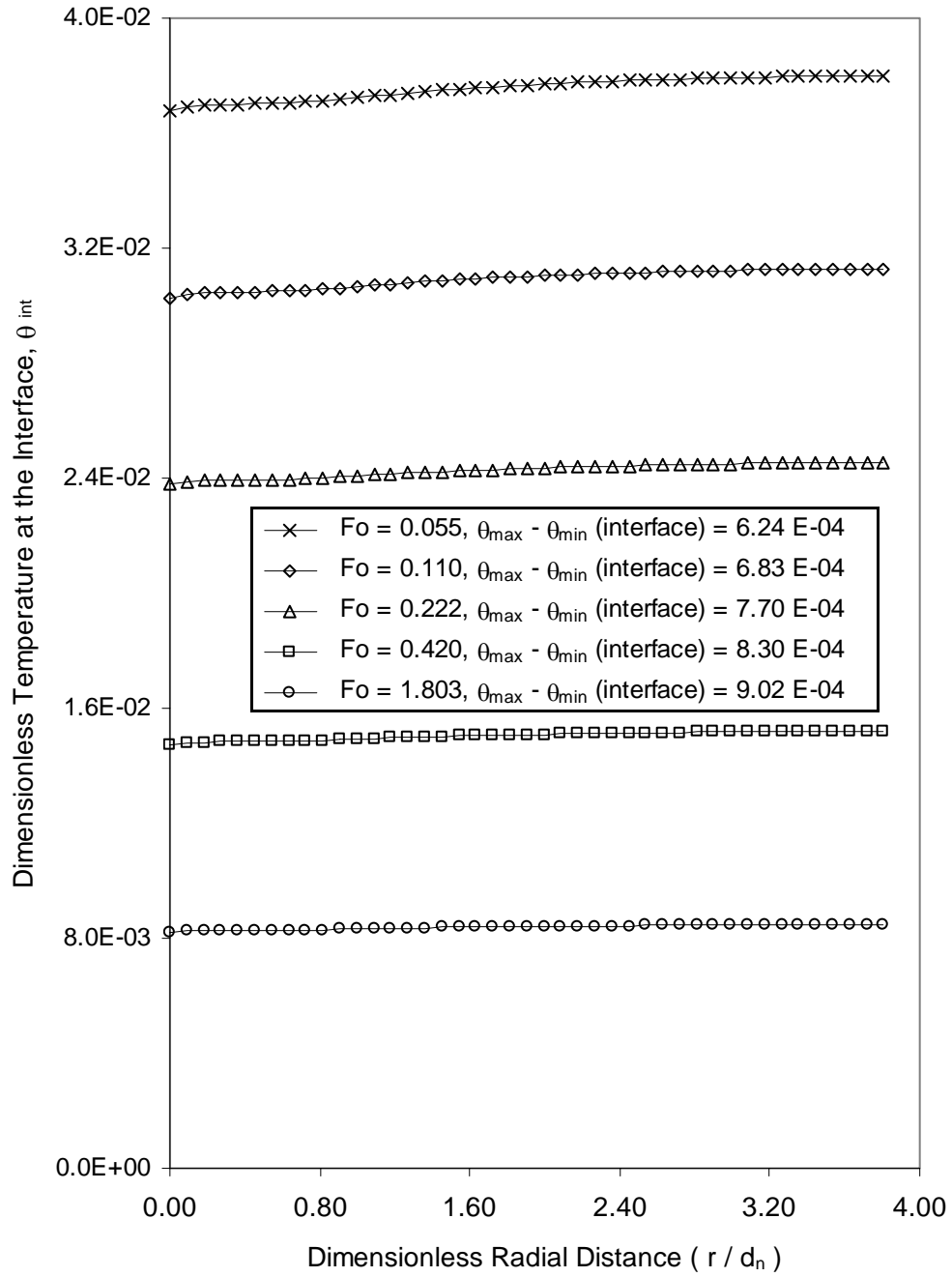


Figure 36. Dimensionless local temperature distribution at the interface ( $Re = 550$ ,  $T_j = 310$  K,  $b/d_n = 2.94$ ,  $H_n/d_n = 5$ , Copper plate,  $q_w = 63$  kW/m<sup>2</sup>)

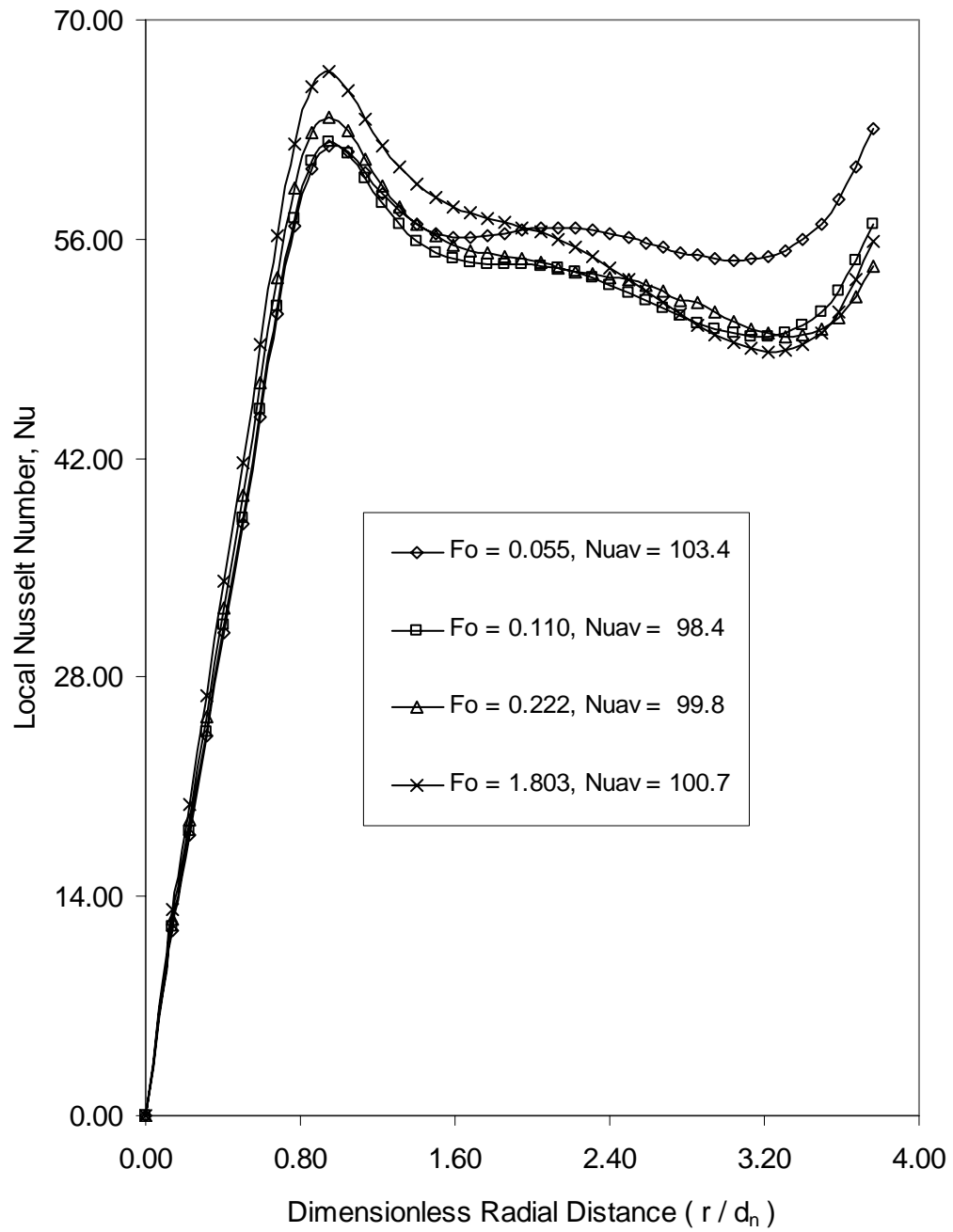


Figure 37. Distribution of local Nusselt number ( $Re = 550$ ,  $T_j = 310$  K,  $b/d_n = 2.94$ ,  $H_n/d_n = 5$ , Copper plate,  $q_w = 63$  kW/m<sup>2</sup>)



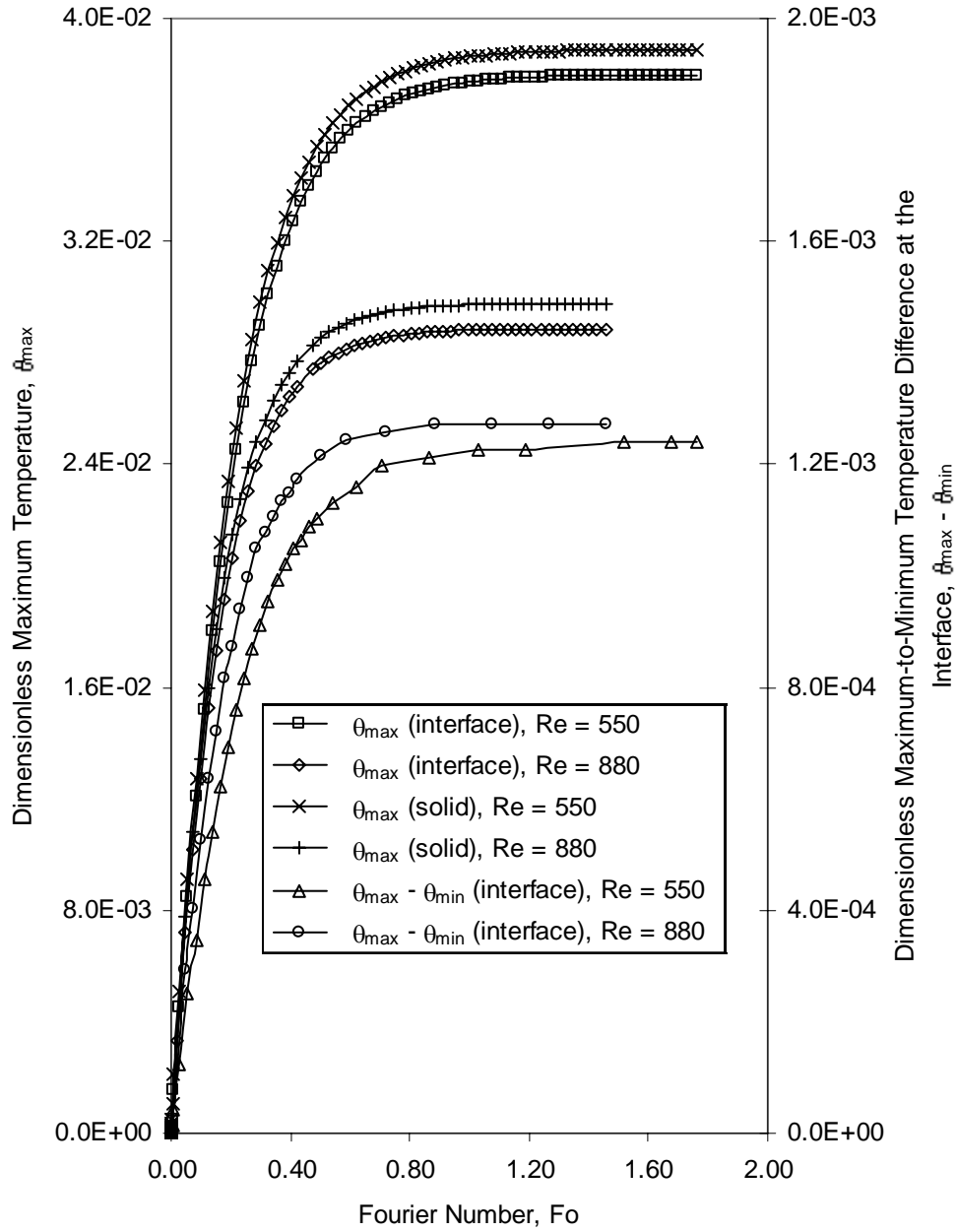


Figure 38. Variation of dimensionless maximum temperature at the interface, inside the solid, and maximum-to-minimum temperature difference at the interface with time for different Reynolds numbers ( $T_j = 310$  K,  $b/d_n = 2.94$ ,  $H_n/d_n = 5$ , Copper plate,  $q_w = 63$  kW/m<sup>2</sup>)

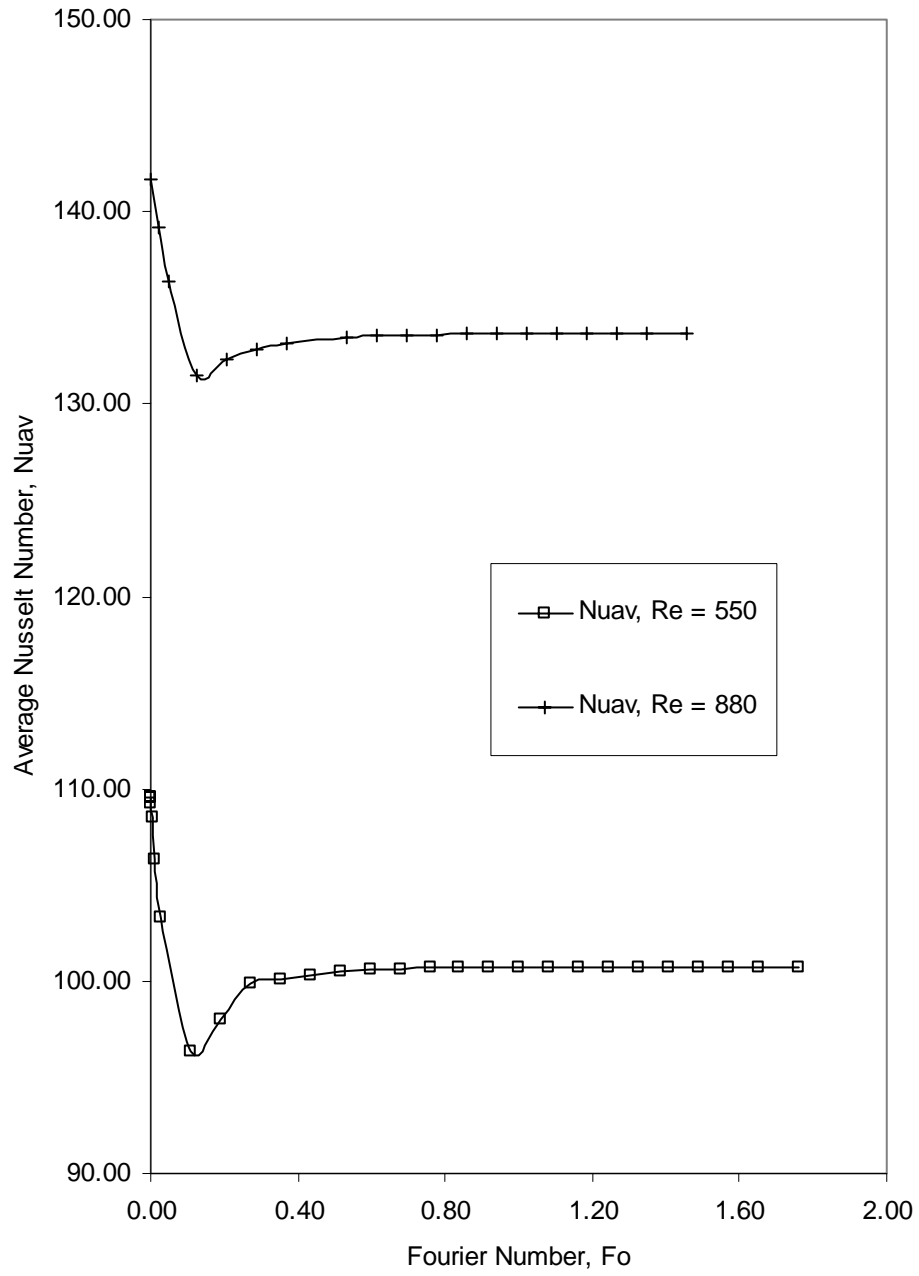


Figure 39. Variation of average Nusselt number with time ( $T_j = 310$  K,  $b/d_n = 2.94$ ,  $H_n/d_n = 5$ , Copper plate,  $q_w = 63$  kW/m<sup>2</sup>)

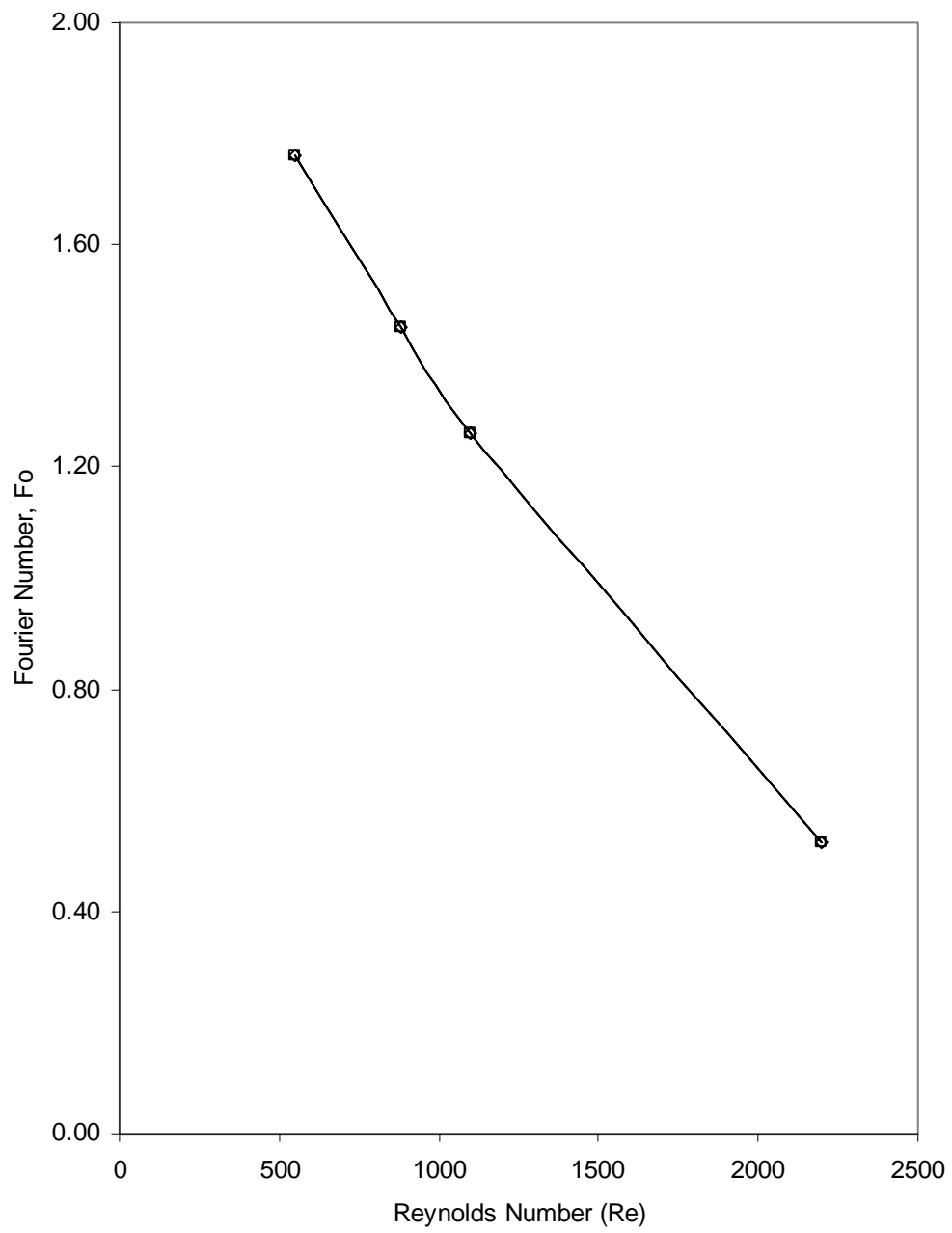


Figure 40. Variation of time required to reach steady state with Reynolds number  
 $(T_j = 310 \text{ K}, b/d_n = 2.94, H_n/d_n = 5, \text{Copper plate}, q_w = 63 \text{ kW/m}^2)$

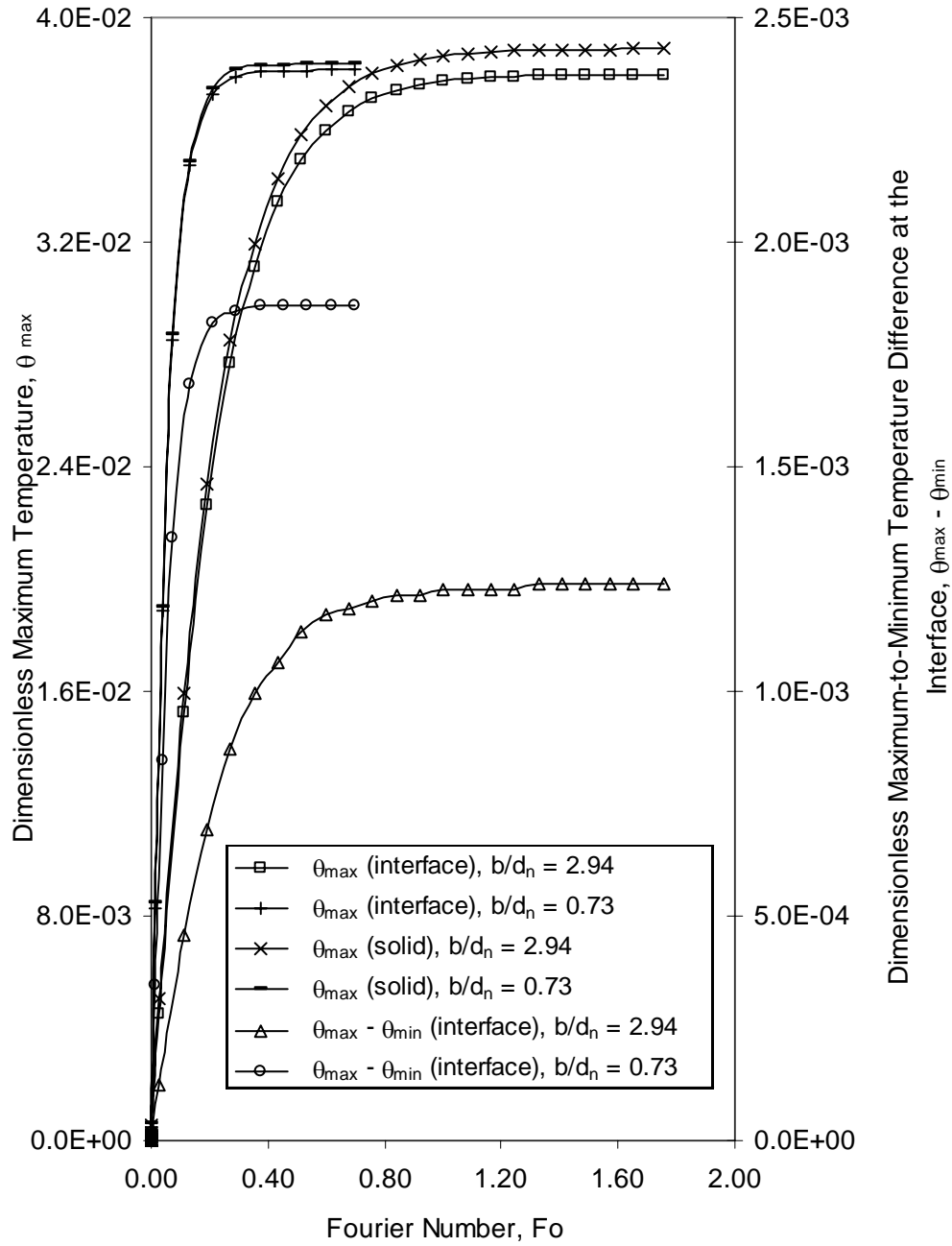


Figure 41. Variation of dimensionless maximum temperature at the interface, inside the solid, and maximum-to-minimum temperature difference at the interface, with time for different plate thicknesses ( $Re = 550$ ,  $T_j = 310$  K,  $H_n/d_n = 5$ , Copper plate,  $q_w = 63$  kW/m<sup>2</sup>)

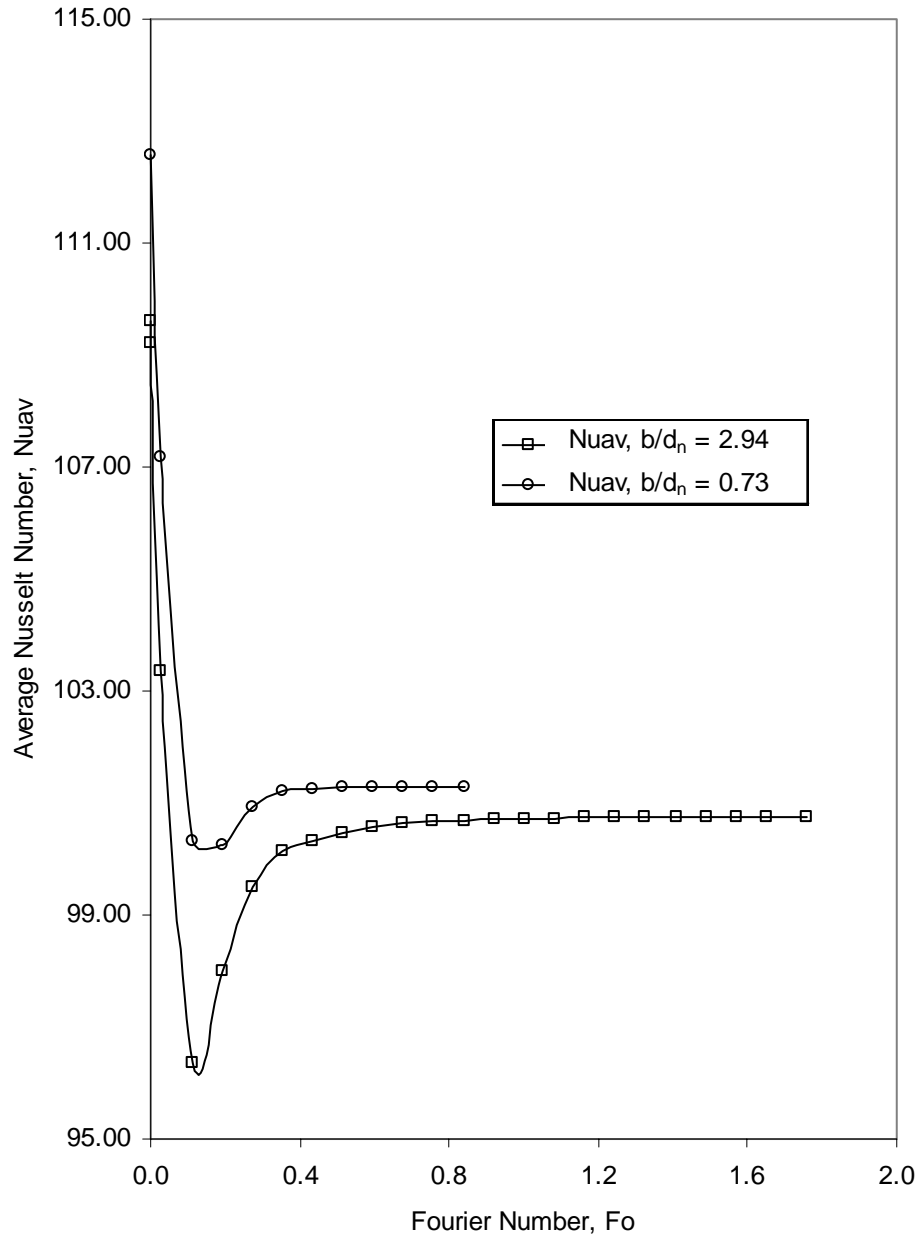


Figure 42. Average Nusselt number variation with time for two plate thicknesses  
 ( $Re = 550$ ,  $T_j = 310$  K,  $H_n/d_n = 5$ , Copper plate,  $q_w = 63$  kW/m<sup>2</sup>)

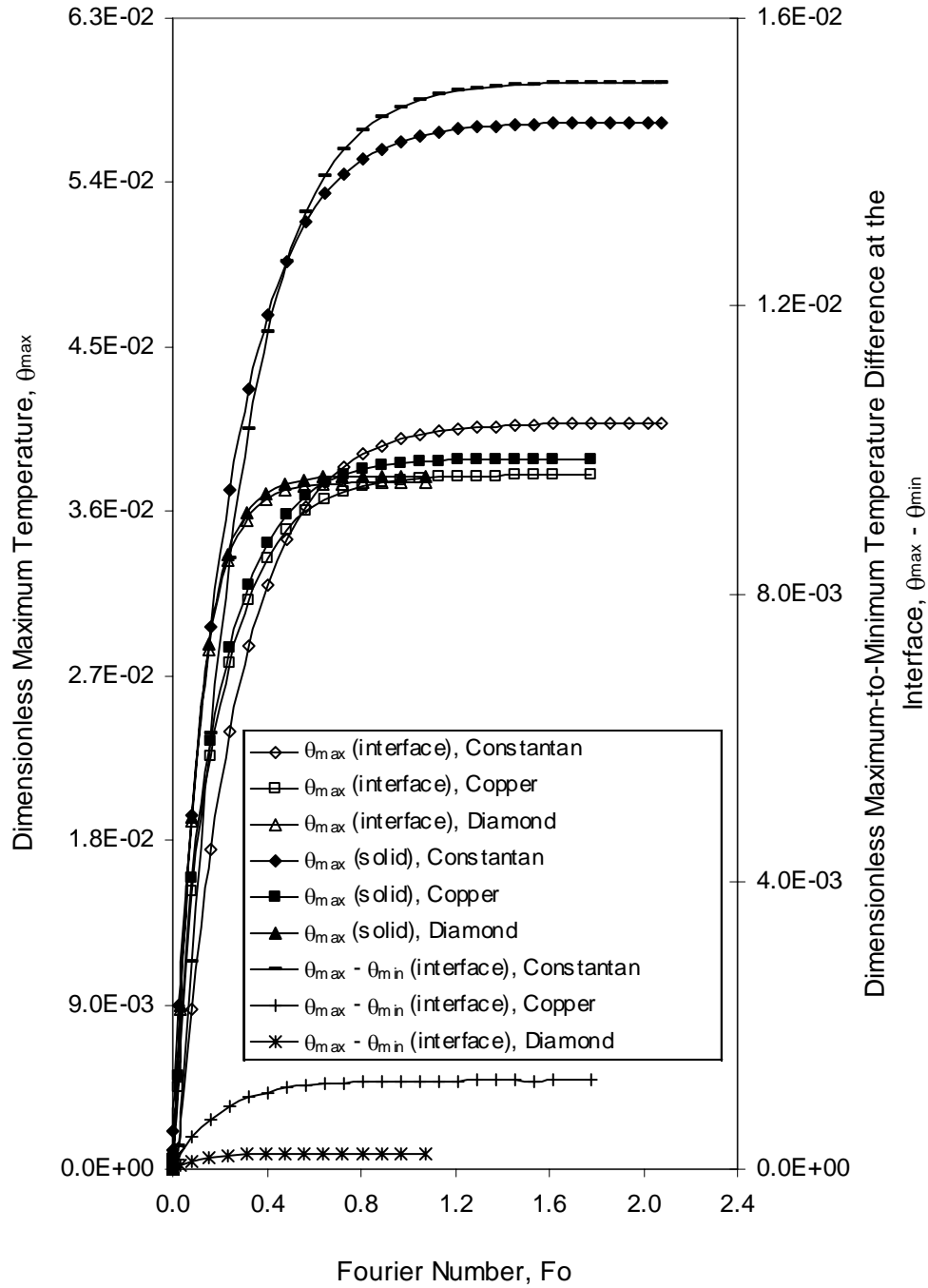


Figure 43. Variation of dimensionless maximum temperature at the interface, inside the solid, and maximum-to-minimum temperature difference at the interface with time for different materials ( $Re = 550$ ,  $T_j = 310$  K,  $b/d_n = 2.94$ ,  $H_n/d_n = 5$ ,  $q_w = 63$  kW/m<sup>2</sup>)

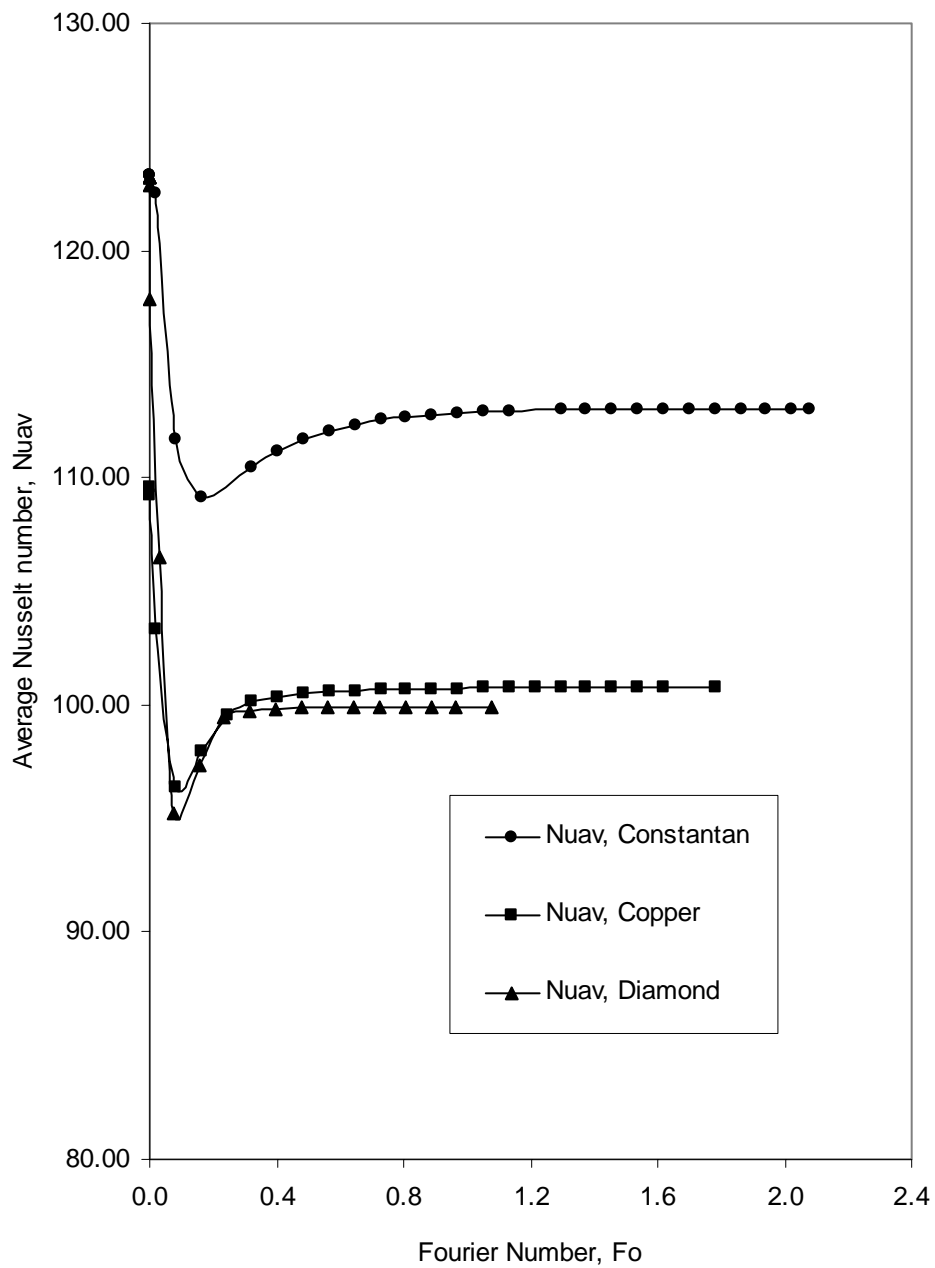


Figure 44. Variation of average Nusselt number with time for different materials ( $Re = 550$ ,  $T_j = 310\text{ K}$ ,  $b/d_n = 2.94$ ,  $H_n/d_n = 5$ ,  $q_w = 63\text{ kW/m}^2$ )

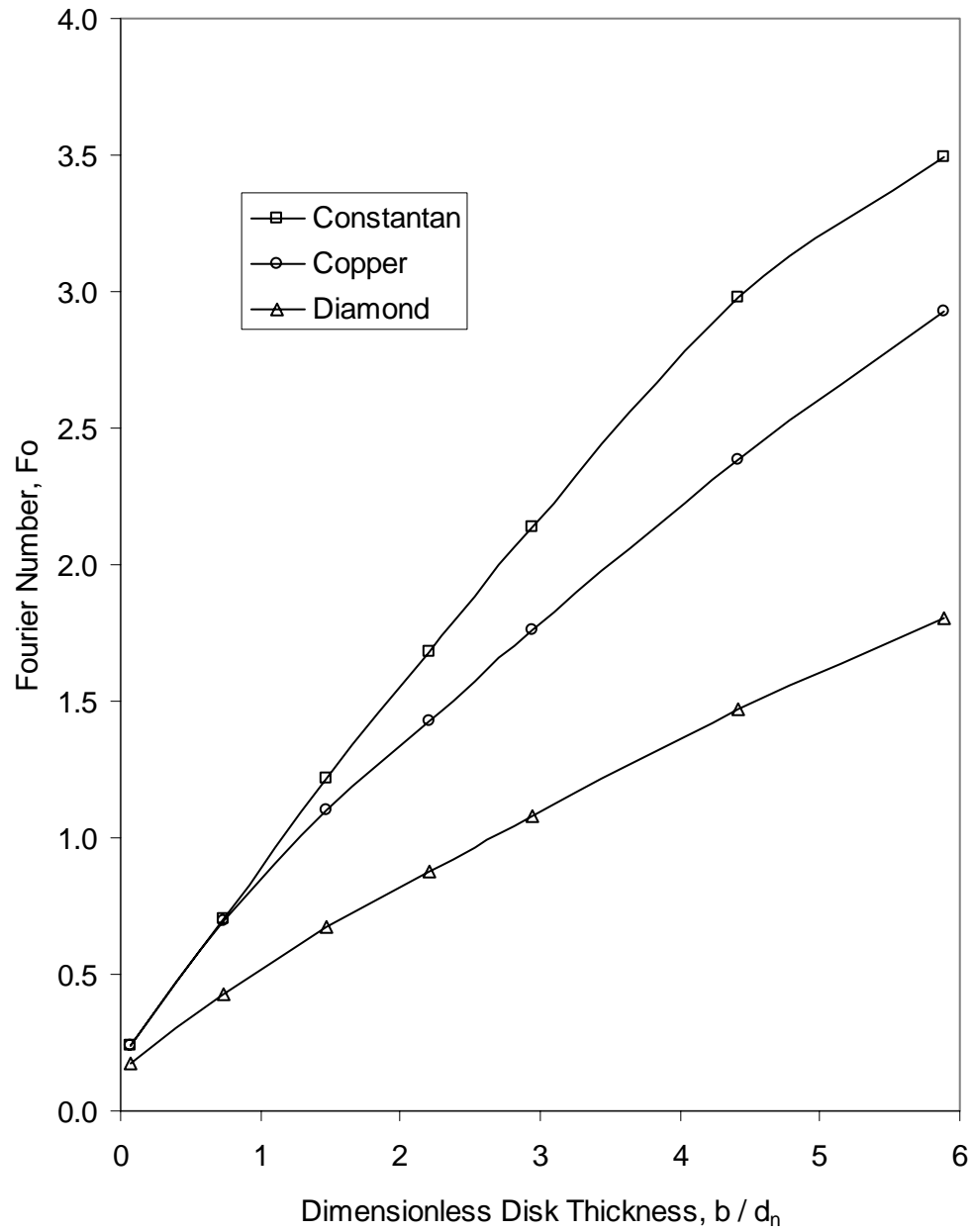


Figure 45. Time required to reach steady state for different materials and plate thicknesses  
 $(Re = 550, T_j = 310 \text{ K}, H_n/d_n = 5, q_w = 63 \text{ kW/m}^2)$



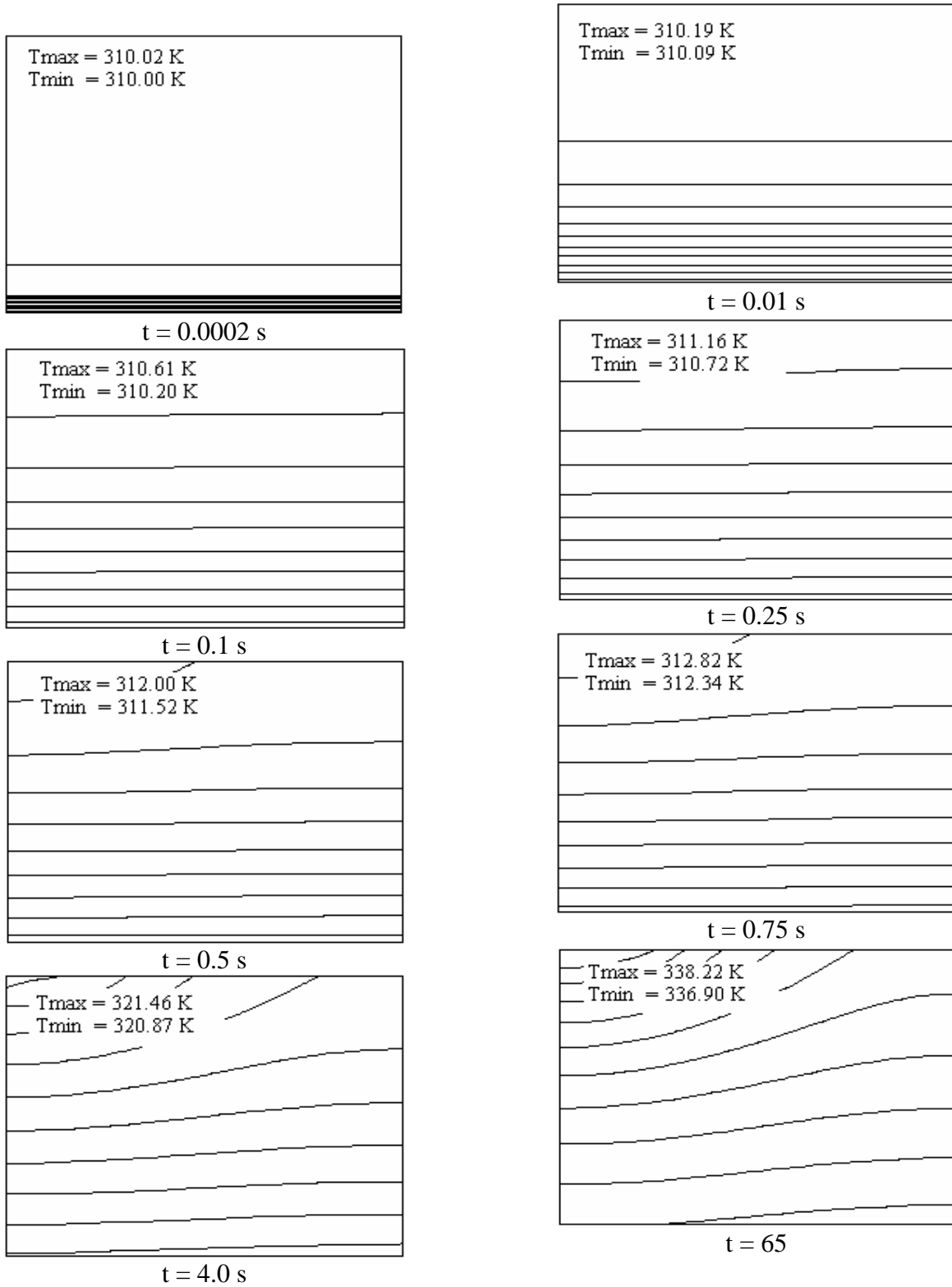


Figure 46. Isothermal lines at different time instants for a disk of  $b/d_n = 2.94$  ( $Re = 550$ ,  $T_j = 310$  K,  $H_n/d_n = 5$ , Copper plate,  $q_w = 63$  kW/m<sup>2</sup>)

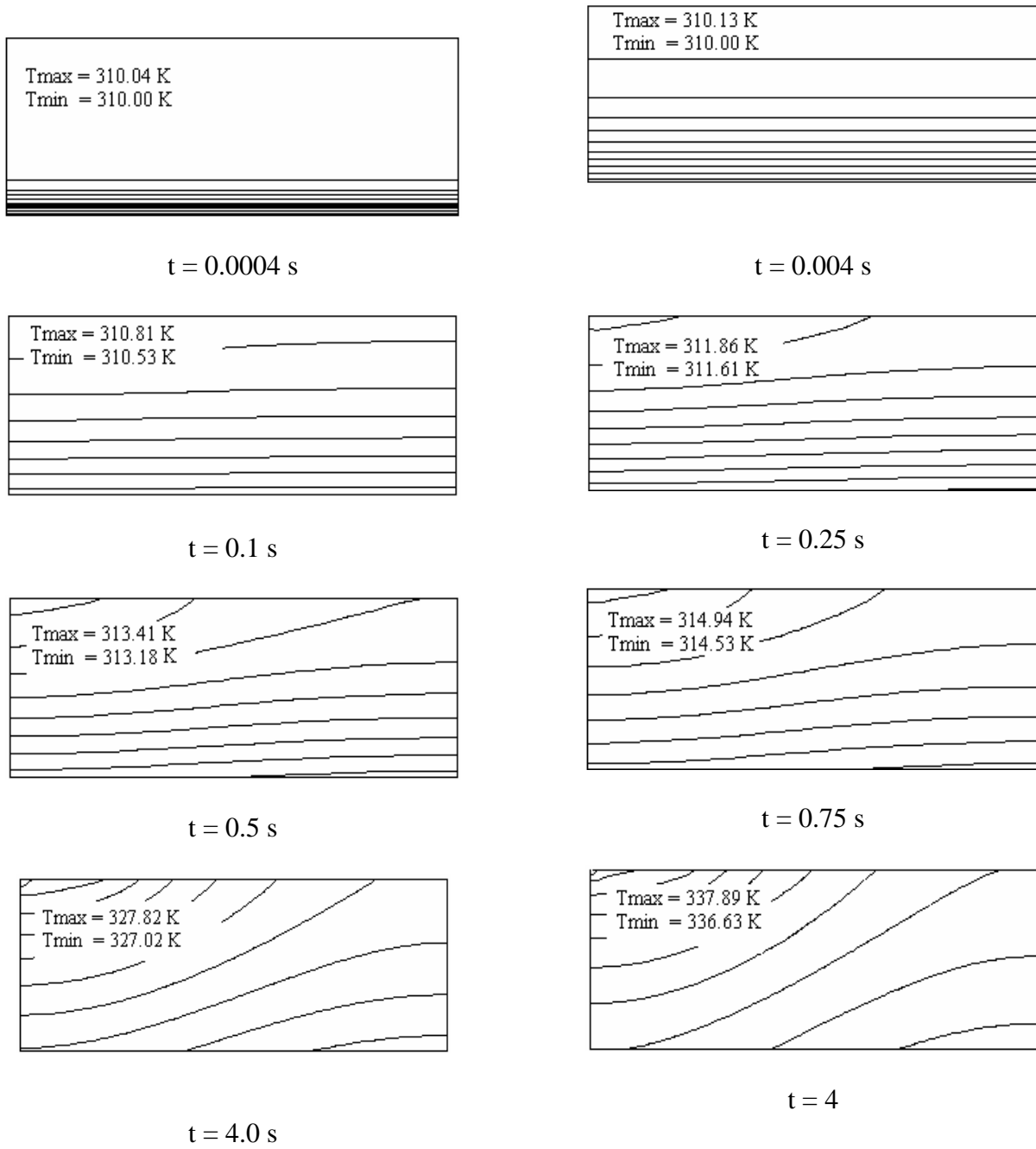


Figure 47. Isothermal lines at different time instants for a disk of  $b/d_n = 1.47$  ( $Re = 550$ ,  $T_j = 310$  K,  $H_n/d_n = 5$ , Copper plate,  $q_w = 63$  kW/m<sup>2</sup>)

# **FREE JET FROM A SLOT NOZZLE IMPINGING ON A PLATE WITH DISCRETE HEAT SOURCES: STEADY STATE**

## **INTRODUCTION**

Jet impingement from a slot nozzle is widely employed in industries for highly localized heating or cooling. Some examples include annealing of metal or glass, tempering, turbine blade cooling, and drying of paper and textiles. In recent years, the demand for compactness and higher operational processors has led to high power density in electronic packages. Improvements on the cooling method are required in order to avoid unacceptable temperature rise, and to maintain high efficiency and reliability during its operation. An enhanced heat transfer method such as jet impingement will be required to provide the desired thermal environment.

Inada et al. [43] obtained solution of the boundary layer momentum and energy equations for a wedge-type flow with constant heat flux from the flat surface. They deduced an approximate equation of the temperature gradient at the wall and the local heat transfer coefficient. They concluded that as the distance from the stagnation point increases, the local heat transfer coefficient decreases and approaches its asymptotic value for uniform parallel flow over a flat plate. Garg and Jayaraj [44] theoretically analyzed the laminar boundary layer flow when a two dimensional slot jet impinges over a flat plate at some angle. The analysis was performed using a finite-difference technique, and the results were presented for impinging angles of  $0^\circ$  and  $90^\circ$ . The presence of a stagnation point when the plate is not parallel to the flow was found to considerably affect the local Nusselt number and the skin friction coefficient.

Polat et al. [45] measured local and average heat transfer coefficient for a confined turbulent slot jet impinging on a permeable surface with thorough flow. Measurements were carried out for a wide range of jet Reynolds number and thorough flow velocity. Polat et al. [46] measured local and average heat transfer coefficient for a confined turbulent slot jet impinging on a moving surface considering through flow. Al-Sanea [47] developed a finite-difference numerical model to calculate the steady state fluid flow and heat transfer characteristics for a laminar slot jet impinging on an isothermal flat surface. The study was performed for free jet, semiconfined jet, and semiconfined jet in cross flow. The study showed that the cross flow could degrade the average Nusselt number by as much as 60%.

Chou and Hung [48] presented an analytical study for cooling of an isothermal heated surface with a confined slot jet. Chou and Hung [49] performed a numerical study for fluid flow and heat transfer of slot jet impingement with an extended nozzle. The parametric study included jet Reynolds number, nozzle-to-surface distance, and nozzle length. Seyedein et al. [50] presented results of a numerical simulation of two dimensional flow field and heat transfer due to a turbulent single heated slot jet discharging normally into a confined channel. Low and high Reynolds number versions of  $k - \varepsilon$  turbulence models were used to model the turbulent jet flow. Seyedein et al. [51] presented results of numerical simulation for turbulent flow field and heat transfer due to three and five turbulent heated slot jets discharging normally into a confined channel.

Laschefski et al. [52] numerically analyzed the velocity field and heat transfer in rows of rectangular impinging jets in transient state. Axial and radial jets coming out of rectangular nozzles were considered. Cziesla et al. [53] simulated turbulent flow issuing from a slot jet array using a subgrid stress model. The code showed good agreement with experimental data. Ashfort-Frost et al. [54] experimentally investigated the velocity and turbulence characteristics of a semiconfined slot jet impinging over a plate. Lin et al. [55] presented an experimental study on heat transfer behavior of a confined slot jet using Reynolds number and nozzle-to-plate distance as parameters.

Gordon and Akfirat [56] presented experimental measurements of local as well as average heat transfer coefficients between an isothermal flat plate and impinging two-dimensional air jets. Both single jet and array of jets were considered. Correlations for local Nusselt number at the stagnation point and average Nusselt number over the plate were developed based on the test data. Sezai and Mohamad [57] presented numerical simulation results for the flow and heat transfer characteristics of an impinging laminar jet issuing from a rectangular slot. Slots of different aspect ratios were studied. Chen and Modi [58] reported mass transfer characteristics of a turbulent confined slot jet impinging normally on a target wall. Yang et al. [59] performed an experimental study of jet impingement cooling of a semi-circular concave surface. Three different nozzle geometries: round, rectangular, and 2-D contoured were tested. Their results indicated that a higher heat transfer rate compared to flat plate can be achieved due to the effects of surface curvature.

From the above literature review, it is apparent that most studies on slot jet impingement has been for confined jets. Only Inada et al. [43], Wolf et al. [11], and Vader et al [12] have studied liquid jets containing a free surface. FC-72 and water have been used as working fluids in these research, where changes in density, viscosity, and thermal conductivity with temperature have been assumed to be negligible. Moreover, it has been assumed that thickness of the plate has no significant effect on the rate of heat transfer, which is not always true. The modeling of conjugate heat transfer during slot jet impingement of a high Prandtl number fluid, such as lubricating oil has not been attempted in any previous work. Although a poor heat transfer fluid, lubricating oil is an attractive coolant for aircraft applications because it is generally in close proximity to the electrical generating equipment. It is also pre-existing in the aircraft and therefore does not require flight qualification, new maintenance procedures, additional inventory space and logistics procedures, or additional environmental protection guidelines. These advantages translate into greatly reduced operational costs, which may far outweigh the loss in cooling efficiency. Lubricating oils are generally known for their high Prandtl number and large variation of viscosity with temperature. Therefore, the investigation of jet impingement heat transfer for high Prandtl number fluids taking into account the effects of property variation with temperature is of great importance to the military and commercial aircraft industry.

## **MATHEMATICAL MODEL**

A two-dimensional jet discharging from a slot nozzle and impinging perpendicularly on a solid plate heated by discrete sources as shown in Figure 48 is considered. If the fluid is considered to be incompressible with density dependent on temperature only, the equations

describing the conservation of mass, momentum, and energy in Cartesian coordinates can be written as [23]:

$$\frac{\partial}{\partial x}(\rho_f v_x) + \frac{\partial}{\partial z}(\rho_f v_z) = 0 \quad (41)$$

$$\rho_f \left( v_x \frac{\partial v_x}{\partial x} + v_z \frac{\partial v_z}{\partial z} \right) = -\frac{\partial p}{\partial x} + \frac{2}{3} \frac{\partial}{\partial x} \left[ \mu \left( 2 \frac{\partial v_x}{\partial x} - \frac{\partial v_z}{\partial z} \right) \right] + \frac{\partial}{\partial z} \left[ \mu \left( \frac{\partial v_z}{\partial x} + \frac{\partial v_x}{\partial z} \right) \right] \quad (42)$$

$$\begin{aligned} \rho_f \left( v_x \frac{\partial v_z}{\partial x} + v_z \frac{\partial v_z}{\partial z} \right) = & -\frac{\partial p}{\partial z} + \frac{2}{3} \frac{\partial}{\partial z} \left[ \mu \left( 2 \frac{\partial v_z}{\partial z} - \frac{\partial v_x}{\partial x} \right) \right] \\ & + \frac{\partial}{\partial x} \left[ \mu \left( \frac{\partial v_z}{\partial x} + \frac{\partial v_x}{\partial z} \right) \right] - \rho_f g \end{aligned} \quad (43)$$

$$\begin{aligned} \rho_f \left( v_x \frac{\partial c_{pf} T_f}{\partial x} + v_z \frac{\partial c_{pf} T_f}{\partial z} \right) = & \left[ \frac{\partial}{\partial x} \left( k_f \frac{\partial T_f}{\partial x} \right) + \frac{\partial}{\partial z} \left( k_f \frac{\partial T_f}{\partial z} \right) \right] \\ & + \mu \left[ \frac{4}{3} \left( \frac{\partial^2 v_x}{\partial x^2} + \frac{\partial^2 v_z}{\partial z^2} - \frac{\partial v_x}{\partial x} \frac{\partial v_z}{\partial z} \right) + \left( \frac{\partial v_x}{\partial z} + \frac{\partial v_z}{\partial x} \right)^2 \right] \end{aligned} \quad (44)$$

Inside the solid, the variation of the thermal conductivity was found to be significant for silicon and diamond substrates, but not for copper. Therefore, considering variable properties, the equation describing the conservation of energy can be written as follows:

$$\frac{\partial}{\partial x} \left( k_s \frac{\partial T_s}{\partial x} \right) + \frac{\partial}{\partial z} \left( k_s \frac{\partial T_s}{\partial z} \right) = 0 \quad (45)$$

To complete the set to be solved, equations (41-45) are subjected to the following boundary conditions:

$$\text{At } x = 0, 0 \leq z \leq b: \frac{\partial T_s}{\partial x} = 0 \quad (46)$$

$$\text{At } x = 0, b \leq z \leq H_n: v_x = 0, \frac{\partial v_z}{\partial x} = 0, \frac{\partial T_f}{\partial x} = 0 \quad (47)$$

$$\text{At } x = L, 0 \leq z \leq b: \frac{\partial T_s}{\partial x} = 0 \quad (48)$$

$$\text{At } x = L, b \leq z \leq \delta: p = 0, \frac{\partial T_f}{\partial x} = 0 \quad (49)$$

$$\text{At } z = b: T_s = T_f, v_x = 0, v_z = 0, k_s \frac{\partial T_s}{\partial z} = k_f \frac{\partial T_f}{\partial z} \quad (50)$$

$$\text{At } z = b + H_n, 0 \leq x \leq W/2: v_x = 0, v_z = -v_j, T_f = T_j \quad (51)$$

At the free surface, the boundary condition can be expressed as:

At  $z = \delta$ ,  $W/2 < x < L$ :

$$\frac{d\delta}{dx} = \frac{v_z}{v_x}, p = p_{atm} - \frac{\sigma \frac{d^2\delta}{dx^2}}{\left[1 + \left(\frac{d\delta}{dx}\right)^2\right]^{3/2}}, \frac{\partial v_t}{\partial n} = 0, \frac{\partial T_f}{\partial n} = 0 \quad (52)$$

For this simulation, the position of the discrete heat sources was varied as shown in Figure 49(a). The boundary condition at the bottom surface of the plate changes according to the location of the heat sources. In addition, the magnitude of heat flux was varied in order to study its effect. They are presented in Figure 49(b). For the base case (shown in Figure 1), this boundary condition can be written as:

$$\text{At } z=0, 0 < x < (L/9): -k_s \frac{\partial T_s}{\partial z} = q_w \quad (53)$$

$$\text{At } z=0, (L/9) < x < (L/3): \frac{\partial T_s}{\partial z} = 0 \quad (54)$$

$$\text{At } z=0, (L/3) < x < (5L/9): -k_s \frac{\partial T_s}{\partial z} = q_w \quad (55)$$

$$\text{At } z=0, (5L/9) < x < (7L/9): \frac{\partial T_s}{\partial z} = 0 \quad (56)$$

$$\text{At } z=0, (7L/9) < x < L: -k_s \frac{\partial T_s}{\partial z} = q_w \quad (57)$$

The local heat transfer coefficient and the average heat transfer coefficient can be defined as:

$$h = \frac{q_{\text{int}}}{(T_{\text{int}} - T_j)} \quad (58)$$

$$h_{av} = \frac{1}{L(\bar{T}_{\text{int}} - T_j)} \int_0^L h(T_{\text{int}} - T_j) dx \quad (59)$$

where  $\bar{T}_{\text{int}}$  is defined as the average temperature at the solid-liquid interface. The local Nusselt number and the average Nusselt number are calculated according to the following expressions:

$$Nu = \frac{hx}{k_f} \quad (60)$$

$$Nu_{av} = \frac{h_{av}L}{k_f} \quad (61)$$

## NUMERICAL COMPUTATION

The governing equations along with the boundary conditions described in the previous section were solved using the finite-element method. The discretization was carried out using the Galerkin formulation. The entire computation domain, covering the solid and fluid regions was discretized into a number of quadrilateral elements with four nodes. The dependent variables, i.e., velocity, pressure, and temperature were interpolated to a set of nodal points that defined the element. In each element, the velocity, pressure, and temperature fields were approximated which led to a set of equations that defined the continuum. The approach used to solve the free surface problem was to introduce a new degree of freedom at the nodes on the free surface. This degree of freedom represented the position of the free surface. It was introduced as a new unknown into the global system of equations. The solution was carried out using the Newton-Raphson method. It has the advantage of faster convergence if the guess used for the free surface is close enough to the final form. Since the solution of the momentum equation required only two out of the three boundary conditions at the free surface, the third condition was used to upgrade the position of the free surface at the end of each iteration step.

Due to large number of iterations required to determine the location of the free surface, the solution was carried out in two steps. First, the computation in the fluid region was carried out solving equations for the conservation of mass and momentum; this resulted in the determination of the velocity field and the free surface height distribution. The drawback of this solution is that because of no heat transfer, the fluid remained isothermal, and therefore properties remained constant. This approximate solution was the starting point for the second level of computation where both solid and fluid regions were included and equations for the conservation of mass, momentum, and energy were solved simultaneously as a conjugate problem taking into account the variation of fluid properties with temperature. This split level computation procedure greatly reduced the run time for numerical computation. The solution was considered converged when the field values did not change from one iteration to the next, and the sum of residuals for each variable was less than 1E-08.

## RESULTS AND DISCUSSION

The simulation was carried out for three different materials, namely copper, diamond, and silicon. The distance of the nozzle from the plate ( $H_n = 0.0085$  m), width of the nozzle ( $W = 0.0017$  m), and length of the plate ( $L = 0.0065$  m) were kept constant during the simulation. The jet temperature at the nozzle exit ( $T_j = 310$  K) was also kept constant. The fluid used for the simulation was Mil-7808, which is a lubricating oil used in the aircraft industry. All material properties ( $\rho$ ,  $\mu$ ,  $c_p$ ,  $k$ ) were allowed to vary as a function of local temperature. The range of fluid Prandtl number encountered was 159-372. In order to determine the number of elements for accurate numerical solution, computation was performed for several combinations of grid distribution in the horizontal and vertical directions covering the solid and fluid regions. The dimensionless solid-fluid interface temperature is plotted in Figure 50. It was observed that the solution becomes grid independent when the number of divisions in the horizontal direction was increased up to 42 and at least 16 divisions were used in the vertical direction.

Figure 51 presents the free surface height for different jet Reynolds numbers as the jet strikes the impinging surface. As soon as the fluid leaves the stagnation zone, it moves along the horizontal axis as a thin film. At the conditions considered in the present simulation, a hydraulic jump was not present in the computation domain. It is however observed that the free surface height increases along the horizontal axis due to loss of momentum by plate friction.

The heat transfer results for the "base" case is presented in Figures 52-56. Figure 52 presents the dimensionless solid-fluid interface temperature distribution for different heat fluxes. It can be observed that the minimum temperature is present at the stagnation point and the maximum at the edge of the plate. As expected, the interface temperature, as well as the minimum-to-maximum temperature difference at the interface increase with heat flux.

The distribution of local Nusselt number along the horizontal axis for different heat fluxes is presented in Figure 53(a). Nusselt number increases rapidly as the fluid moves along the horizontal axis in the stagnation region. As the fluid turns and gets into the boundary layer region, the Nusselt number reaches a peak. From that point, the Nusselt number starts decreasing until it reaches  $x/W = 2.2$ , at that position the Nusselt number increases as the flow proceeds downstream. There is only a slight increment of the average Nusselt number, from 166.6 to 179.9 (8%) as the heat flux increases by 300% (from 63 to 252 kW / m<sup>2</sup>). Since the length scale as well as the thermal conductivity used in the calculation of Nusselt number varied with location, it will be interesting to discuss the variation of heat transfer coefficient over the plate. The heat transfer coefficient was found to be maximum at the stagnation point ( $x=0$ ) and decreased along the horizontal axis. A large decrease was seen at the stagnation region ( $x < W/2$ ), where the flow suffered a change of direction of about 90°; after this point, the heat transfer coefficient continued to decrease as the thickness of the thermal boundary layer increased. This trend continued until around  $x/W = 2.2$ , where the fluid approached a transition to laminar flow with rippling. According to Bird et al. [60], rippling occurs when the Reynolds number defined using the film height as the length scale exceeds 25. This caused a slow increase in the heat transfer coefficient beyond  $x/W = 2.2$ . The value of the average heat transfer coefficient showed an increment of only 8% (from 3.83 to 4.14 kW / m<sup>2</sup> K) when the heat flux is increased from 63 to 252 kW / m<sup>2</sup> (300%).

Figure 53(b) shows the variation of local Nusselt number with Reynolds number. The heat transfer coefficient increases with Reynolds number because of higher velocity of the fluid impinging on the plate. It is observed that as Reynolds number increases, the peak between the stagnation zone and the wall jet also increases. Both average heat transfer coefficient and average Nusselt number increase with Reynolds number. The computed average heat transfer coefficient in the stagnation region ( $x < W/2$ ) was compared with the stagnation heat transfer correlation presented by Zumbrunnen et al. [61] that was developed from the experimental data of water jets. For the three Reynolds number presented in Figure 53(b), the difference ranged between 0.25% and 7.6%.

Figure 54(a) presents the local Nusselt number variation for different plate thicknesses. It can be noticed that larger differences in local Nusselt number are present at the peak and valley of the distribution. The average Nusselt number increases as the plate thickness increases up to a certain point, for silicon this value is  $b/W = 2.2$ . After this point, the average Nusselt number



decreases slightly with plate thickness. The numerical simulation was carried out for three different plate materials, namely copper, diamond, and silicon. The thermal conductivity of these materials evaluated at 310 K are:  $k_{copper} = 393$  W/m.K,  $k_{diamond} = 2300$  W/m.K,  $k_{silicon} = 147$  W/m.K. Figure 54(b) shows the variation of local Nusselt number. Because of higher thermal conductivity, diamond facilitates faster heat transfer within the substrate and consequently results in more uniform temperature at the solid-fluid interface. The local Nusselt number for this case is higher. However, silicon attains the highest value for the average Nusselt number. Because of larger thermal resistance within the solid, a lower temperature is encountered at the stagnation region. This combined with the changes of local thermal conductivity with temperature results in a higher average heat transfer coefficient for silicon.

Figure 55 presents the maximum temperature at the solid-fluid interface and inside the solid, as well as the maximum-to-minimum temperature difference at the solid-fluid interface for different plate thicknesses and materials. It is noticed that the maximum to minimum temperature difference decreases as the plate thickness increases and the plate thermal conductivity increases. It is important to mention that after certain plate thickness, the solid-fluid interface becomes practically isothermal. It happens at  $b/W$  of 2.9, 2.2, and 1.5 for silicon, copper, and diamond respectively, which shows that a material with higher thermal conductivity requires a thinner plate in order to attain a low temperature and more isothermal condition at the solid-fluid interface. The maximum temperature at the interface is practically controlled by the thermal conductivity, the material with the higher thermal conductivity attains the lower value of temperature at all thicknesses. It may be noticed that when the plate thickness is large, the maximum interface temperature attains a constant value. An important observation that can be made from this plot, is that for thin plates ( $b/W < 0.74$ ), the maximum temperature inside the solid decreases as the plate thickness increases. After this point, the maximum temperature inside the solid starts to increase as the plate thickness increases. It is necessary to keep in mind that the control of this temperature is very important in the design of any electronic package. The explanation for this behavior rests on the increment of horizontal heat conduction as the plate thickness increases, but after certain point, the thermal resistance generated by the solid takes control over the heat transfer process, and the temperature increases.

Figure 55 also presents the variation of average Nusselt number with plate thickness for different materials. It can be noticed that there is a peak in the average Nusselt number. This happens at  $b/W = 0.74$  for diamond,  $b/W = 1.5$  for copper, and  $b/W = 2.2$  for silicon. This shows that there is an ideal plate thickness depending on the physical properties of the solid. After reaching the peak point, the average Nusselt number decreases as the plate thickness increases until about the thickness of  $b/W = 1.5$  for diamond,  $b/W = 2.2$  for copper, and  $b/W = 4.4$  for silicon. At this point, the average Nusselt number attains an almost constant value and does not change with further increase of plate thickness. It may be noted that the local heat transfer distribution becomes more uniform as the disk thickness is increased because of conduction within the plate. Therefore, the overall heat transfer performance is improved at the expense of somewhat lower heat transfer coefficient at the impingement location. The average Nusselt number, which is an indicator of overall performance, improves with disk thickness, passes through a peak and eventually settles to a constant value when enough thickness is provided for the maximum re-distribution of heat by conduction within the plate. The peak may be related to more parallel isotherm pattern within the disk indicating smallest resistance to heat transfer.

The effect of the position of the discrete heat sources on the average heat transfer coefficient, average Nusselt number, maximum temperature in the solid, maximum temperature at the interface, and maximum-to-minimum temperature difference at the interface are presented in Figure 49(a). Two discrete heat sources were simulated, and the location was varied along the horizontal axis. It is observed that as the discrete heat sources move away from the stagnation zone, the maximum temperature, and maximum-to-minimum temperature difference increase and average heat transfer coefficient and average Nusselt number decrease. This shows that the impingement process has a significant impact on the heat transfer rate. A better cooling can be achieved by positioning heat sources closer to the jet. The effect of the combination of the heat flux can be observed in Figure 49(b). Case m1, m2, and m3 simulate two heat sources with the same heat flux input while the other maintains a higher heat flux. It is noticed that if the heat source with greater heat flux is moved towards the edge of the plate, the maximum temperature at the interface and inside the solid and maximum-to-minimum temperature difference at the interface increase. Case nx and xn represent the heat flux variation from minimum-to-maximum and maximum-to-minimum respectively. The maximum temperature at the interface and inside the solid, maximum-to-minimum temperature difference at the interface, average heat transfer coefficient, and average Nusselt number increases as the discrete heat source with the highest heat flux moves away from the impingement location. This phenomenon is the result of lower fluid temperature adjacent to the plate when sources with lower power dissipation rate are placed closer to the impingement zone.

The isothermal lines within the solid for different jet Reynolds number are presented at Figure 56. At the bottom of the plate, the isothermal lines are concentric around the discrete heat sources. As the heat propagates through the solid, the isothermal lines start turning parallel and as they get close to the interface, they become concentric around the stagnation point. As the Reynolds number becomes higher, the temperature difference becomes smaller and isotherms are more influenced by heat transfer at the impingement location. Figure 56 also shows the isothermal lines for different plate thickness. As the thickness of the plate becomes larger, the temperature remains stratified in the middle section of the plate, indicating an almost one-dimensional heat conduction. When the plate thickness is small, the temperature contours change direction because of strong horizontal conduction over the entire plate.

The effect of location and power combination of discrete heat sources is observed in Figure 57. It is observed that the heat source with the highest power moves the location with highest temperature with it. An interesting behavior is noticed in Case m3, where the cold and hot spot are located at the left-top corner and right-bottom corner, respectively; the isothermal lines show an almost one-dimensional heat conduction process. Figure 57 also shows the effect of arranging the heat sources from minimum-to-maximum (Case nx) and maximum-to-minimum (Case xn) power dissipation. It is noticed that as the input heat flux increases in the horizontal direction, the heat transfer process turns almost one-dimensional with the axis running across the solid from the hot to the cold spot; the trend that is very similar to the one presented for Case m3. When the input power decreases along the horizontal axis, the trend presented by the isothermal lines is similar to the one showed for case m1.

## NOMENCLATURE

$b$	Thickness of the plate [m]
$c_p$	Specific heat at constant pressure [kJ / kg K]
$g$	Acceleration due to gravity [m / s <sup>2</sup> ]
$h$	Heat transfer coefficient [W / m <sup>2</sup> K]
$H_n$	Height of the nozzle from the plate [m]
$k$	Thermal conductivity [W / m K]
$L$	Length of the plate [m]
$n$	Coordinate normal to the free surface [m]
$Nu$	Nusselt number, $h x / k_f$
$p$	Pressure [Pa]
$q$	Heat flux [W / m <sup>2</sup> ]
$\bar{q}$	Average heat flux [W / m <sup>2</sup> ]
$q_w$	Discrete heat flux [W / m <sup>2</sup> ]
$Re$	Reynolds number, $\rho W v_j / \mu_f$
$T$	Temperature [K]
$\bar{T}$	Average temperature [K]
$T_j$	Jet temperature [K]
$v_j$	Jet velocity [m / s]
$v_t$	Velocity along the free surface [m / s]
$v_x$	Horizontal velocity [m / s]
$v_z$	Vertical velocity [m / s]
$W$	Width of the slot nozzle [m]
$x$	Horizontal coordinate [m]
$z$	Vertical coordinate [m]

### Greek Symbols

$\alpha$	Thermal diffusivity [m <sup>2</sup> / s]
$\delta$	Height of the free surface from the plate [m]
$\mu$	Dynamic viscosity of the fluid [kg / m s]
$\rho$	Density [kg / m <sup>3</sup> ]
$\theta$	Dimensionless temperature, $(T - T_j) / (\bar{q}_{int} W / k_f)$
$\sigma$	Surface tension coefficient [N / m]

### Subscripts

atm	Atmospheric condition
av	Average
f	Fluid
int	Solid-fluid interface
s	Solid

## CONCLUSIONS

The effect of the heat flux, jet Reynolds number, physical properties of the substrate material, position, and power of the discrete heat sources on the maximum substrate temperature, temperature variation at the solid-fluid interface, local and average heat transfer coefficient, and local and average Nusselt number was studied. It is observed that the heat flux has a minor effect on the magnitude of local and average heat transfer coefficient, and local and average Nusselt number; while the temperature increases dramatically with heat flux. The heat transfer coefficient increases with Reynolds number. The physical properties of the material used as the substrate greatly affect the heat transfer process. The results show that there is an ideal design plate thickness depending on the material properties. Another interesting result is that an almost constant temperature at the interface can be attained after certain plate thickness. The position of discrete heat sources plays a very important role in determining the temperature and the heat transfer rate.

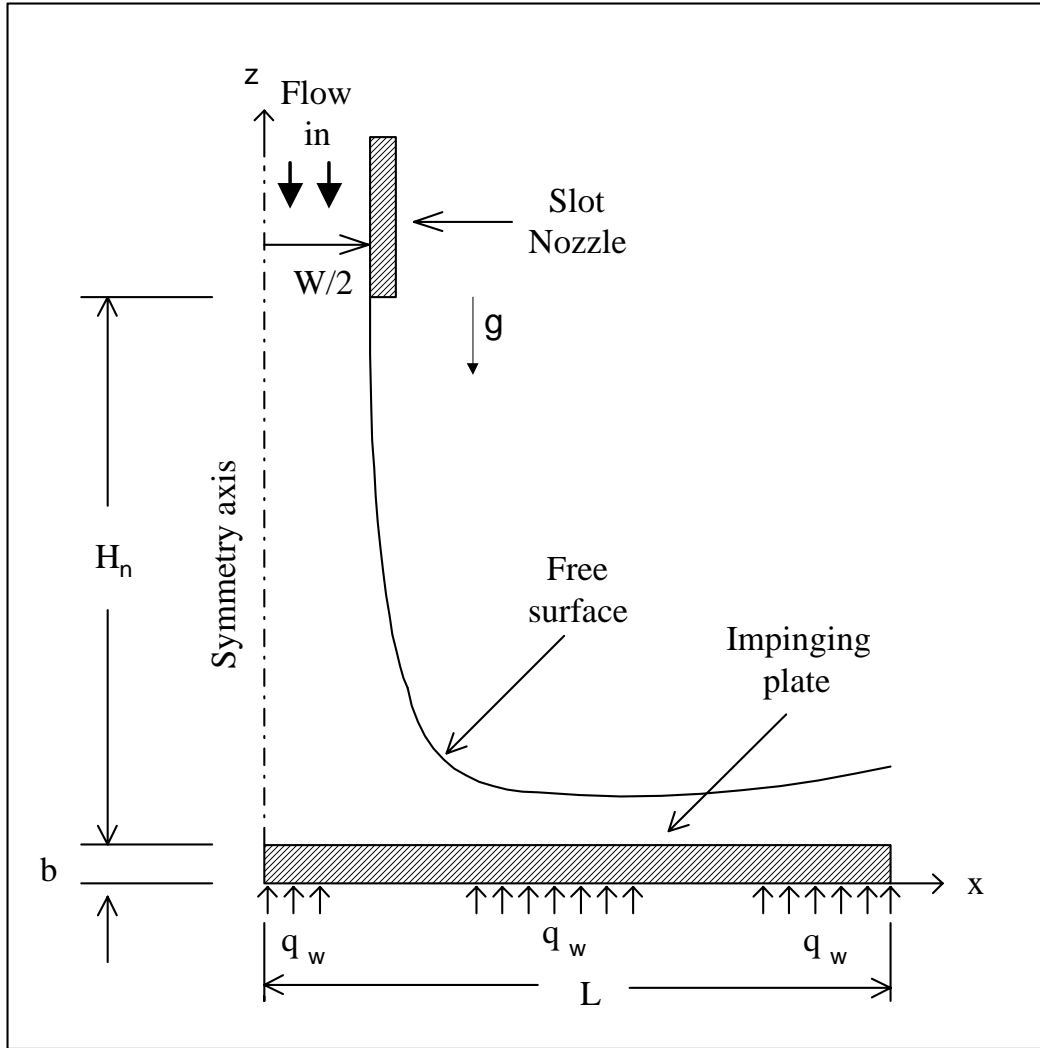


Figure 48. Schematic of a free slot jet impinging over a solid plate with discrete heat sources

(x / W) Positions						$\Delta \theta$ (int)	$\theta$ max (int)	$\theta$ max (solid)	h av	Nu av	
0	0.4	1.3	2.1	3.0	3.8						
						<b>a</b>	7.4E-03	2.1E-02	2.1E-02	3.68	159.76
						<b>b</b>	1.5E-02	2.4E-02	2.4E-02	3.53	153.37
						<b>c</b>	1.9E-02	2.6E-02	2.9E-02	3.17	137.58
						<b>d</b>	1.0E-02	2.2E-02	2.2E-02	3.52	153.11
						<b>e</b>	1.5E-02	2.3E-02	2.7E-02	3.28	142.68
						<b>f</b>	1.0E-02	2.1E-02	2.4E-02	3.28	142.45
						<b>l</b>	1.3E-03	1.7E-02	1.9E-02	3.68	159.75
						<b>m</b>	5.5E-03	2.0E-02	2.0E-02	3.50	152.19
						<b>n</b>	8.1E-03	2.1E-02	2.2E-02	3.25	141.16
						<b>o</b>	1.1E-02	2.2E-02	2.4E-02	3.58	155.49
						<b>p</b>	1.3E-02	2.3E-02	2.4E-02	3.31	143.78
						<b>q</b>	1.7E-02	2.6E-02	2.6E-02	3.16	137.23

(a) Discrete heat source positions

(x / W) Positions										
0	0.4	1.3	2.1	3.0	3.8					
Heat Flux kW / m <sup>2</sup>	Heat Flux kW / m <sup>2</sup>	Heat Flux kW / m <sup>2</sup>		$\Delta \theta$ (int)	$\theta$ max (int)	$\theta$ max (solid)	h av	Nu av		
1 2 6	6 3	6 3	<b>m1</b>	1.6E-03	2.4E-02	2.5E-02	4.02	174.8		
6 3	1 2 6	6 3	<b>m2</b>	1.7E-03	2.4E-02	2.5E-02	4.09	177.5		
6 3	6 3	12 6	<b>m3</b>	1.8E-03	2.4E-02	2.5E-02	4.07	177.1		
63	1 2 6	1 8 9	<b>nx</b>	1.8E-03	2.3E-02	2.4E-02	4.28	185.9		
1 8 9	1 2 6	6 3	<b>xn</b>	1.6E-03	2.3E-02	2.4E-02	4.18	181.7		

(b) Discrete heat source power dissipation

Figure 49. Variation of dimensionless maximum-to-minimum temperature difference at the interface, maximum temperature at the interface, maximum temperature inside the solid, average heat transfer coefficient, and average Nusselt number with discrete heat source position and power dissipation ( $Re = 550$ ,  $b/W = 2.94$ ,  $q = 63 \text{ kW/m}^2$ , Copper plate)

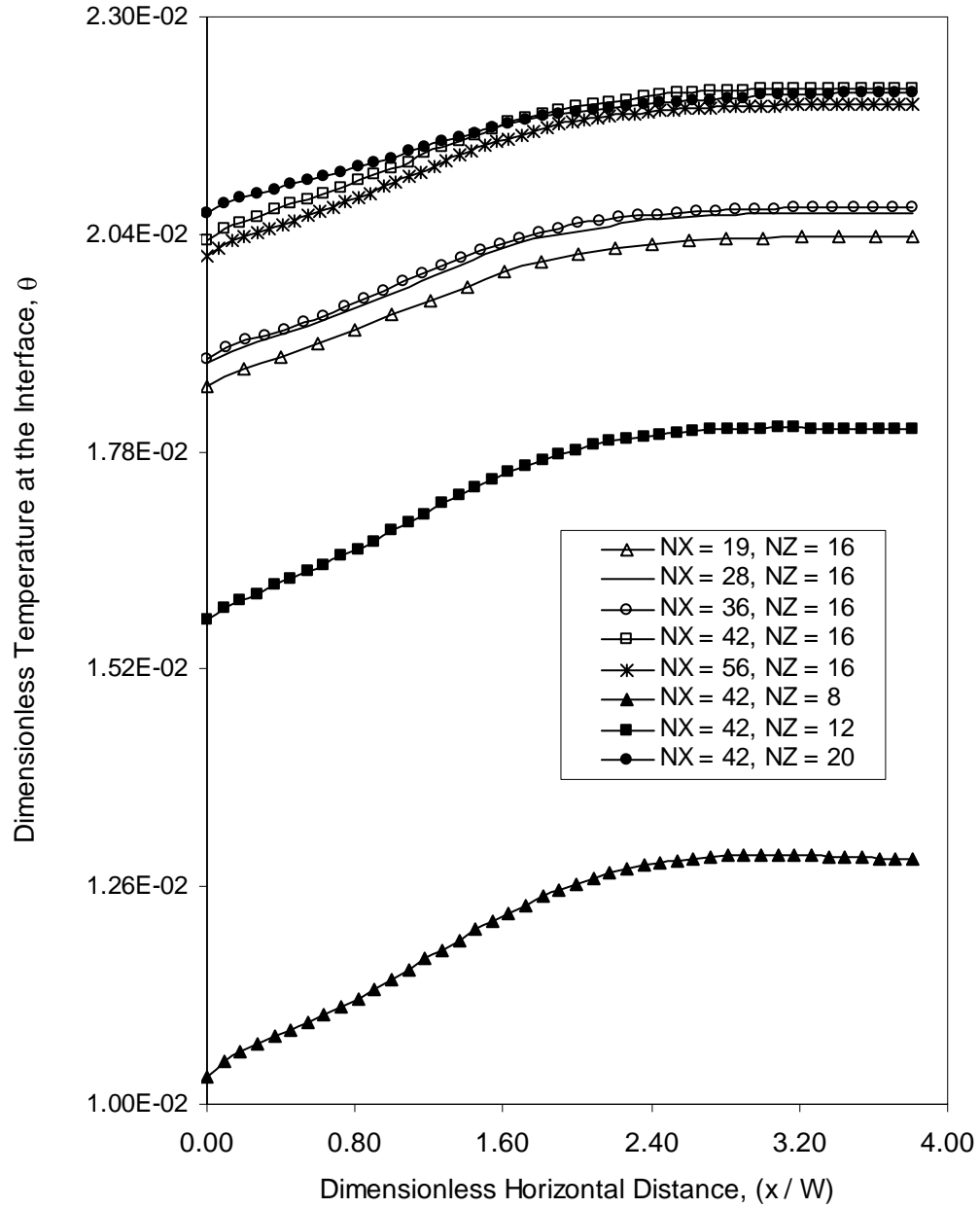


Figure 50. Dimensionless interface temperature for different number of elements in horizontal and vertical directions ( $Re = 550$ ,  $b/W = 2.94$ , Copper plate,  $q = 63 \text{ kW/m}^2$ )

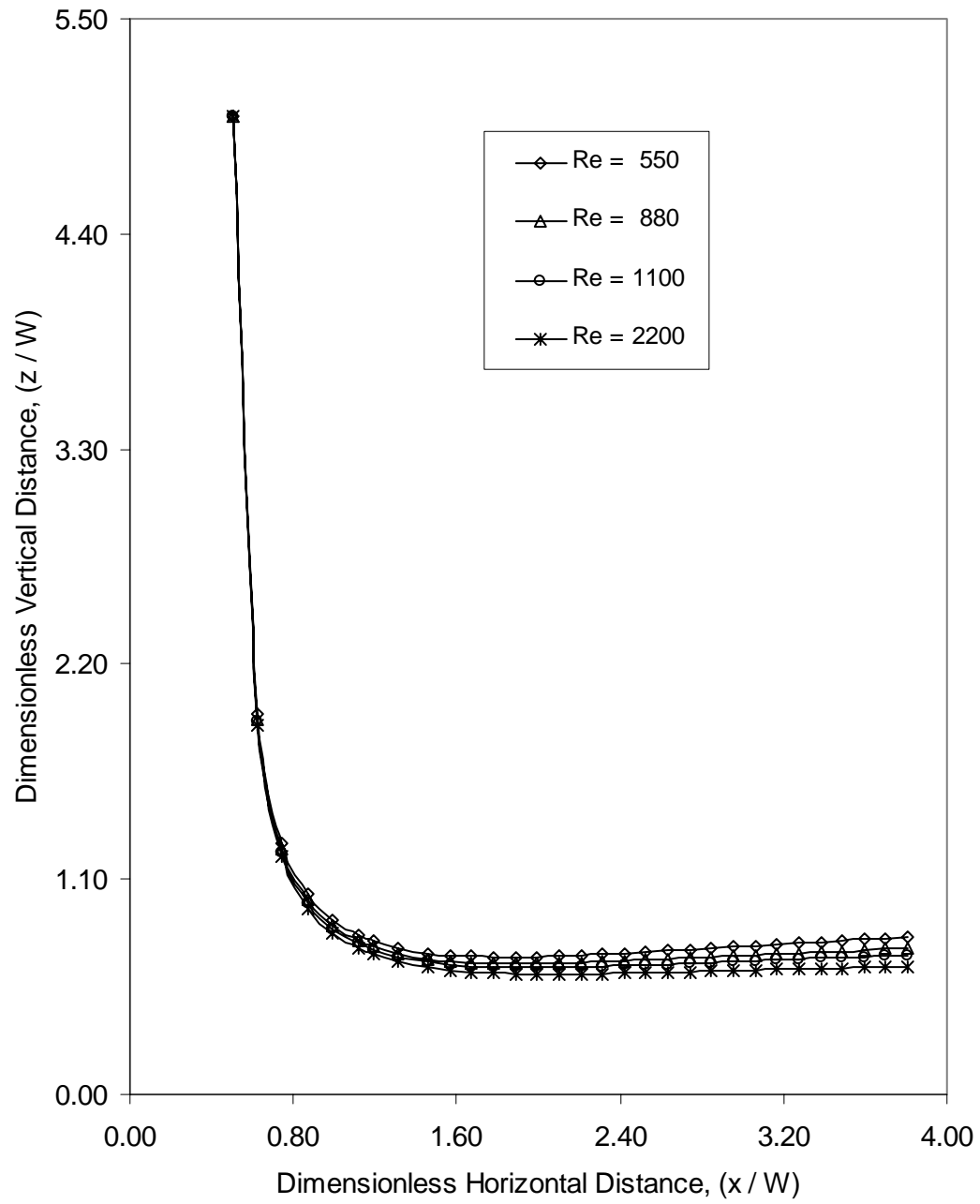


Figure 51. Free surface height distribution for different Reynolds number ( $H_n / W = 5$ )



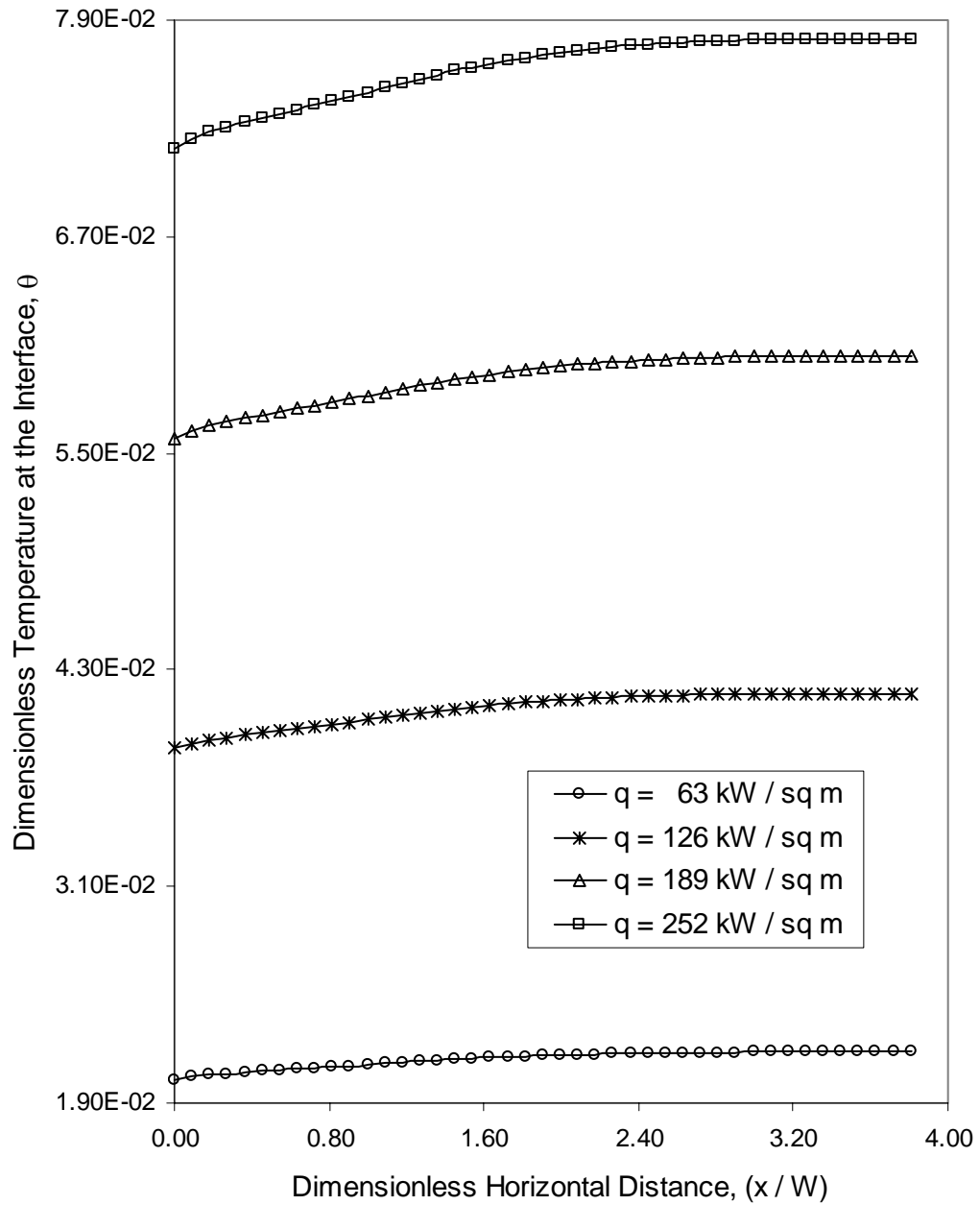
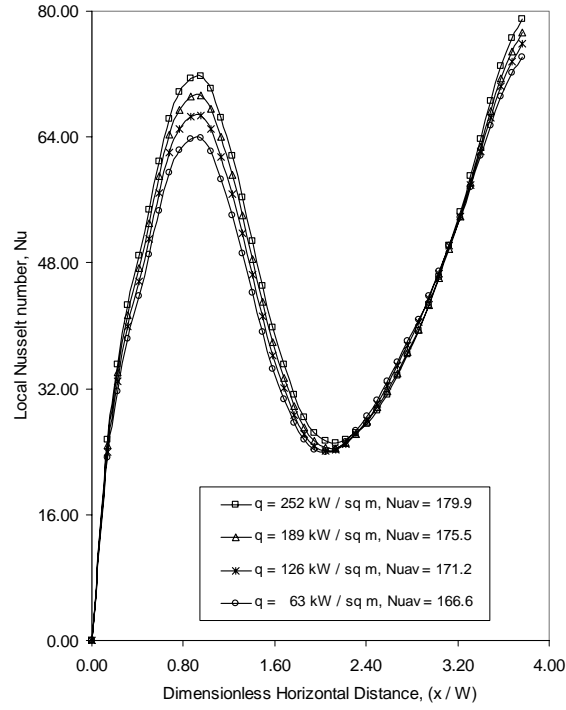
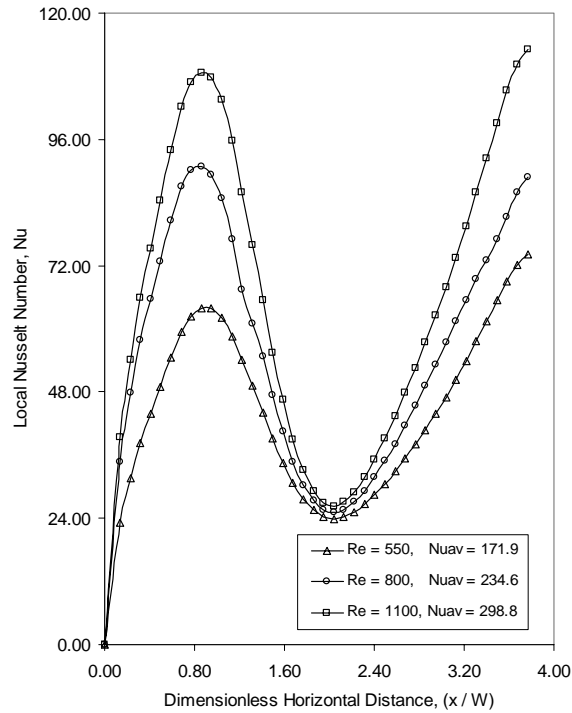


Figure 52. Dimensionless temperature at the interface for different heat flux (Re = 550, b/W = 2.94, Copper plate)

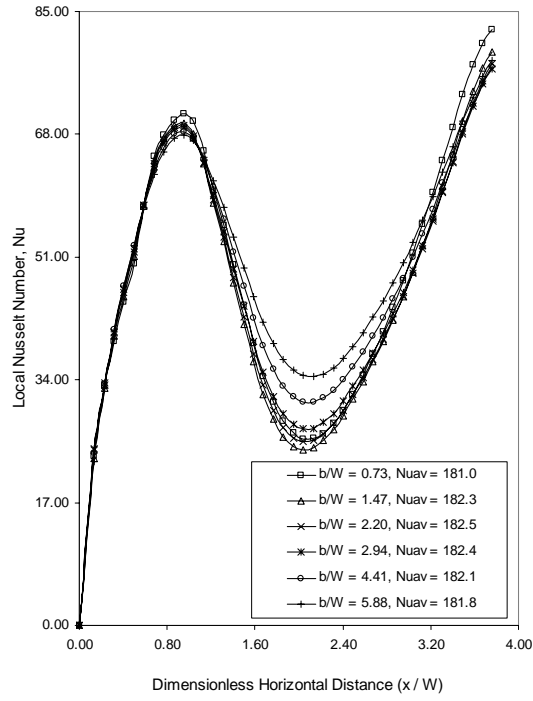


(a) Effect of heat flux

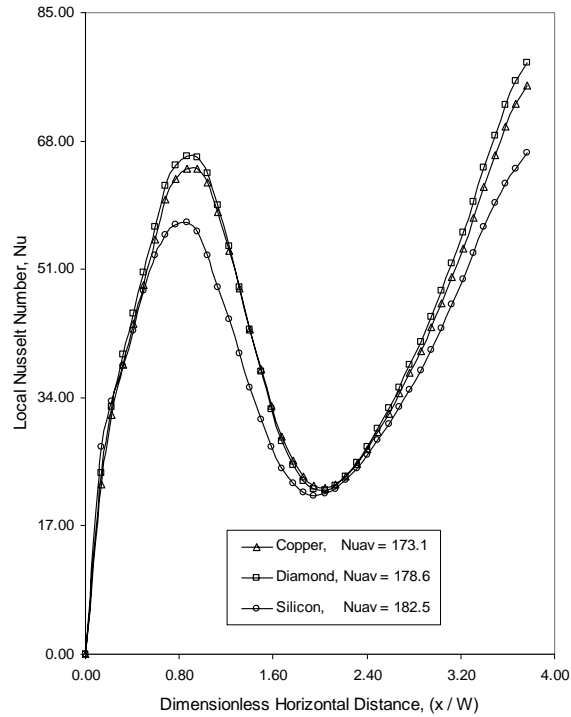


(b) Effect of Reynolds number

Figure 53. Local Nusselt number for different heat flux ( $Re = 550$ ) and for different Reynolds number ( $q = 63 \text{ kW/m}^2$ ) ( $b/W = 2.94$ , Copper plate)



(a) Effect of plate thickness



(b) Effect of plate material

Figure 54. Local Nusselt number variation for different plate thickness (Silicon) and for different plate materials ( $b/W = 2.2$ ) ( $Re = 550$ ,  $q = 63 \text{ kW/m}^2$ )

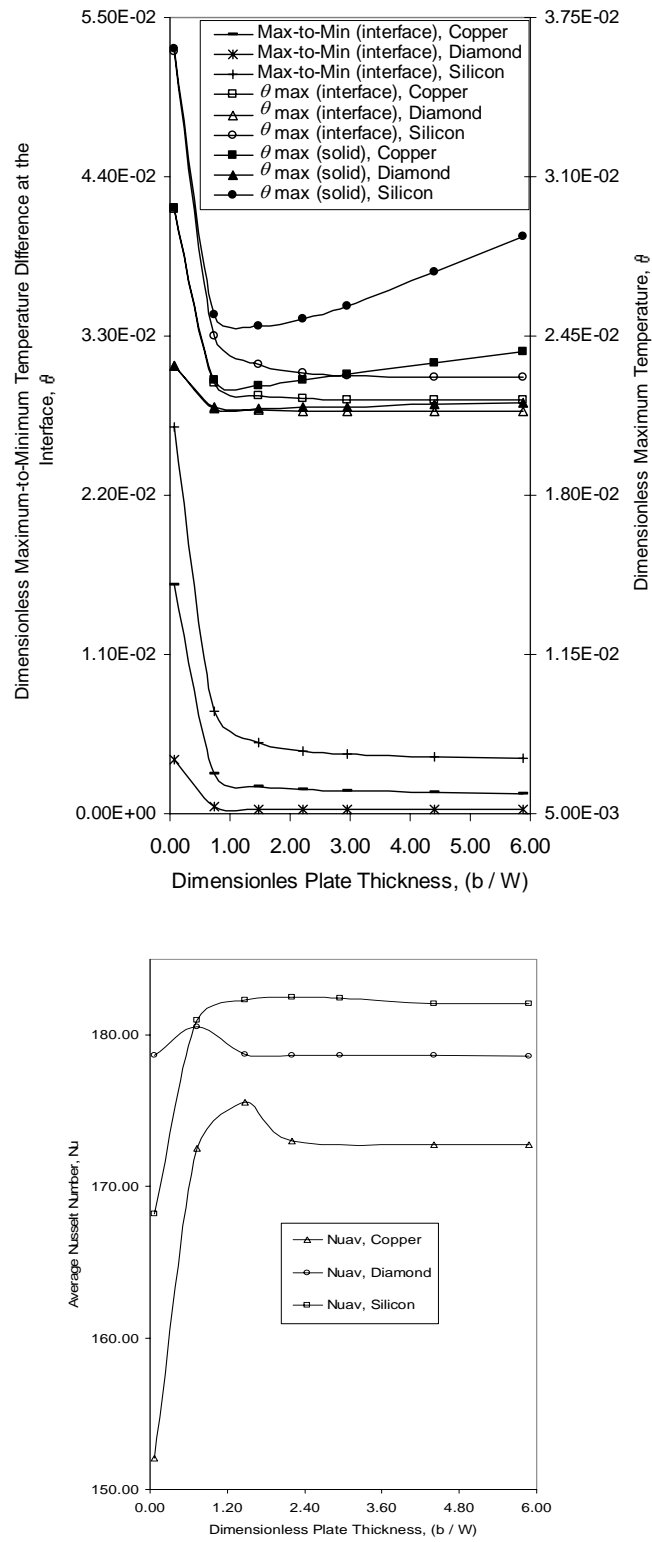
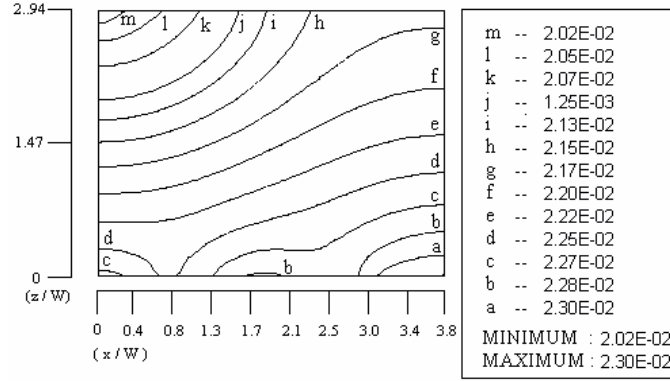
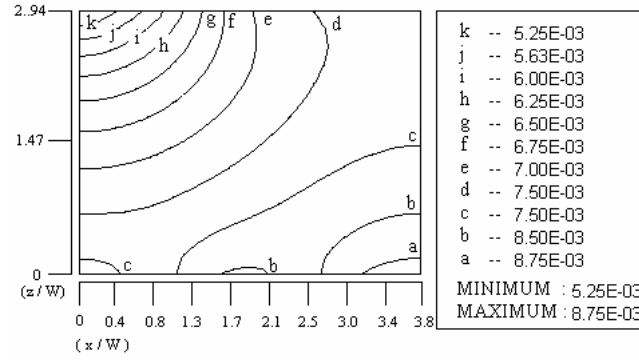


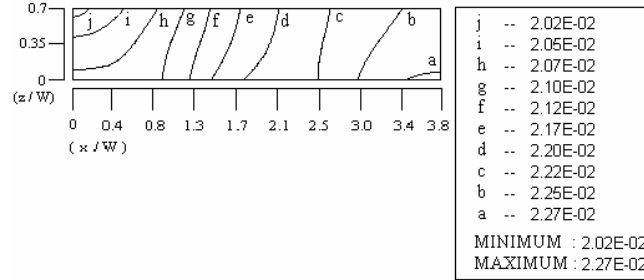
Figure 55. Maximum temperature, interface temperature non-uniformity, and average Nusselt number for different thickness and materials ( $Re = 550$ ,  $q = 63 \text{ kW/m}^2$ )



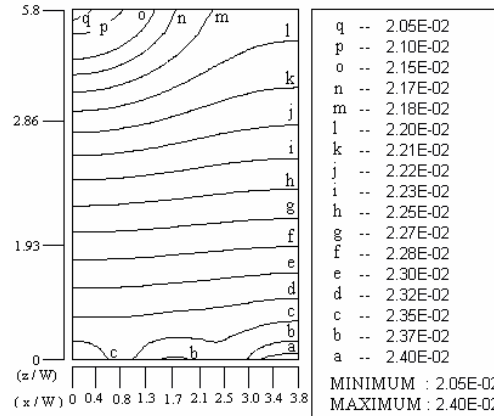
Re = 550



Re = 1100

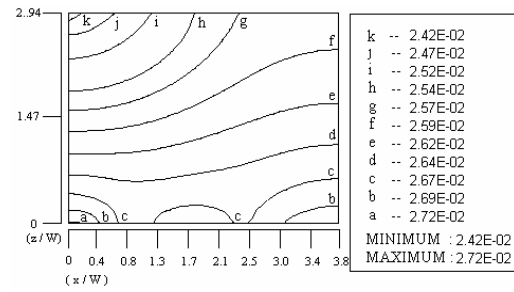


(b/W) = 0.7

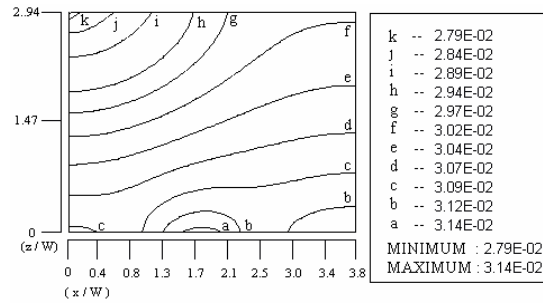


(b/W) = 5.8

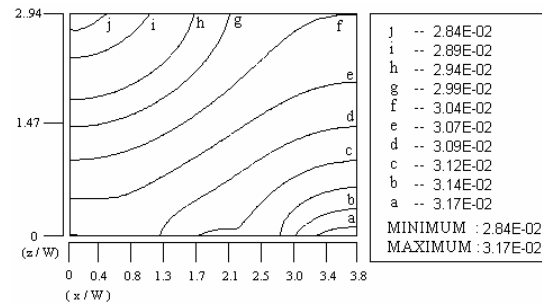
Figure 56. Isothermal lines within the plate for different Reynolds number and for different plate thickness (Re = 550) (Copper plate,  $q = 63 \text{ kW/m}^2$ )



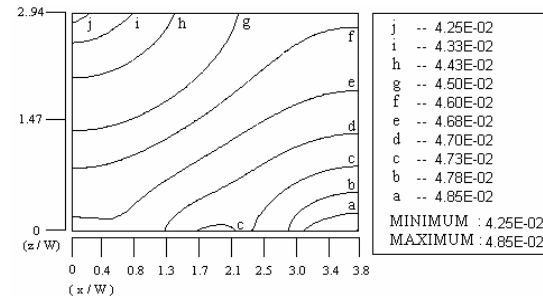
Case m1



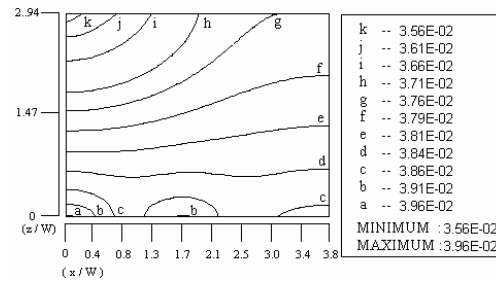
Case m2



Case m3



Case nx



Case xn

Figure 57. Isothermal lines within the plate for different heat source position and power dissipation ( $Re = 550$ , Copper plate)

# FREE JET FROM A SLOT NOZZLE IMPINGING ON A PLATE WITH DISCRETE HEAT SOURCES: TRANSIENT START-UP OF HEATING

## INTRODUCTION

The development of an effective cooling technology is one of the limiting factors in the advancement of circuit integration and near-term utilization of advanced chips. To avoid unacceptable temperature rise in high power density electronic packages and to maintain their operational safety, efficiency, and reliability, a highly effective thermal management technique such as liquid jet impingement will be required. Two-dimensional jets issuing from a slot nozzle has been used in the industry for annealing of metal or glass, tempering, turbine blade cooling, and drying of paper and textiles. Kumagai et al. [62] presented experimental data for transient boiling heat transfer rate to a two dimensional water jet impinging over a thick rectangular plate. The cooling process was from 400 °C to 100 °C. The study showed that the cooling line moves from the impinging zone towards the edge of the plate in accordance with the boiling peak heat flux line. Temperature profiles inside the solid were calculated from the measured transient heat flux distribution at the solid surface. The cooling rate was very sensitive to jet velocity and degree of subcooling.

## MATHEMATICAL MODEL

Consider a two-dimensional jet discharging from a slot nozzle and impinging on a solid plate heated by discrete sources as shown in Figure 48. The power is turned on and the discrete heat sources start supplying the heat when an isothermal steady state flow field has been established on the plate. If the fluid is considered to be incompressible with properties dependent on temperature only, the equations describing the conservation of mass, momentum, and energy in Cartesian coordinates can be written as [23]:

$$\frac{\partial}{\partial x}(\rho_f v_x) + \frac{\partial}{\partial z}(\rho_f v_z) = 0 \quad (62)$$

$$\rho_f \left( \frac{\partial v_x}{\partial t} + v_x \frac{\partial v_x}{\partial x} + v_z \frac{\partial v_x}{\partial z} \right) = -\frac{\partial p}{\partial x} + \frac{2}{3} \frac{\partial}{\partial x} \left[ \mu \left( 2 \frac{\partial v_x}{\partial x} - \frac{\partial v_z}{\partial z} \right) \right] + \frac{\partial}{\partial z} \left[ \mu \left( \frac{\partial v_z}{\partial x} + \frac{\partial v_x}{\partial z} \right) \right] \quad (63)$$

$$\begin{aligned} \rho_f \left( \frac{\partial v_z}{\partial t} + v_x \frac{\partial v_z}{\partial x} + v_z \frac{\partial v_z}{\partial z} \right) = & -\frac{\partial p}{\partial z} + \frac{2}{3} \frac{\partial}{\partial z} \left[ \mu \left( 2 \frac{\partial v_z}{\partial z} - \frac{\partial v_x}{\partial x} \right) \right] \\ & + \frac{\partial}{\partial x} \left[ \mu \left( \frac{\partial v_z}{\partial x} + \frac{\partial v_x}{\partial z} \right) \right] - \rho_f g \end{aligned} \quad (64)$$

$$\rho_f \left( \frac{\partial c_{pf} T_f}{\partial t} + v_x \frac{\partial c_{pf} T_f}{\partial x} + v_z \frac{\partial c_{pf} T_f}{\partial z} \right) = \left[ \frac{\partial}{\partial x} \left( k_f \frac{\partial T_f}{\partial x} \right) + \frac{\partial}{\partial z} \left( k_f \frac{\partial T_f}{\partial z} \right) \right] + \mu \left[ \frac{4}{3} \left( \frac{\partial^2 v_x}{\partial x^2} + \frac{\partial^2 v_z}{\partial z^2} - \frac{\partial v_x}{\partial x} \frac{\partial v_z}{\partial z} \right) + \left( \frac{\partial v_x}{\partial z} + \frac{\partial v_z}{\partial x} \right)^2 \right] \quad (65)$$

The variation of thermal conductivity within the solid was found to be significant for some materials such as silicon and diamond. Therefore, considering variable properties, the equation describing the conservation of energy can be written as follows:

$$\frac{\partial}{\partial x} \left( k_s \frac{\partial T_s}{\partial x} \right) + \frac{\partial}{\partial z} \left( k_s \frac{\partial T_s}{\partial z} \right) = \rho_s c_{ps} \frac{\partial T_s}{\partial t} \quad (66)$$

Equations (62-66) are subjected to the following boundary conditions described by equations (46-57). The plate and the fluid were assumed to be in equilibrium isothermal condition at the start of the transient heating process. This can be expressed as:

$$\text{At } t = 0: T_s = T_f = T_j, v = v_i(x, z) \quad (67)$$

In order to determine the initial velocity field,  $v_i(x, z)$ , equations for the conservation of mass and momentum were solved. Once the initial free surface height distribution and the flow field for an isothermal equilibrium condition was established, the power at the heat sources was turned on at  $t = 0$ . The computation domain covered both solid and fluid regions and equations for the conservation of mass, momentum, and energy were solved simultaneously as a conjugate problem taking into account the variation of fluid and solid properties with temperature. At each time step, the solution was considered converged when the field values did not change from one iteration to the next, and the sum of residuals for each degree of freedom was less than 1E-08. Computation was continued marching forward with time until a steady state condition was reached. Due to large changes at the outset of the transient and very small changes when the solution approached the steady state condition, a variable time step was assumed for the computation. In addition, a maximum limit on the time step size was set to assure smooth variations with time.

## RESULTS AND DISCUSSION

The simulation was carried out for three different materials, namely: copper, diamond, and silicon. The working fluid used for the simulation was Mil-7808, which is a lubricating oil used in the aircraft industry. In order to determine the number of elements for accurate numerical solution, computation was performed for several combinations of grid distribution in the horizontal and vertical directions covering the solid and fluid regions. The solution became grid independent when the number of divisions in the horizontal direction was increased up to 42 and at least 16 divisions were used in the vertical direction. Computations were also performed to calculate the suitable time increment in order to determine its sensitivity on the transient solution. Figure 58 plots the variation of maximum temperature in the fluid with time for



different values of time increments. It can be observed that the solution does not change any further if the time step size is reduced below 0.75s. A time increment of 0.5 s second was selected to ensure a smooth variation.

A key parameter for understanding the transient heat transfer process is the local heat flux imparted to the jet at the solid-fluid interface and the total rate of heat transfer from the discrete heat sources to the coolant. These are important variables in assessing the thermal response of solid materials to the turning on of power in discrete heat sources located on one surface and a coolant jet impinging on the opposite surface. The local heat flux distribution for different times is presented in Figure 59. Because of initial isothermal condition, the interfacial heat flux is zero at  $t = 0$ . It may be noted that heat flux at the interface increases with time. A large heat flux is seen at the stagnation region because the cold fluid at the jet strikes that location and maintains the minimum value of the interface temperature. The heat transfer at that location is highest because of constant renewal of cold fluid to carry away the heat. The heat dissipated at discrete heat sources is utilized to increase the temperature of the solid as well as the fluid. As the temperature rises with time, the thermal storage in the solid decreases and more and more heat proceed to the interface and dissipated to the liquid. The interfacial heat flux increases rapidly with time in the earlier part of the transient, and more slowly as the steady state condition is approached. For  $t > 40$  s, the interfacial heat flux practically reaches the steady state distribution. The figure also shows the average interfacial heat flux at different time instants.

Figure 60 presents the interfacial temperature distribution at different time instants. It is noticed that at the early stages of the heat transfer process, the temperature at the interface rises uniformly at all locations resulting in a practically isothermal interface condition. This behavior is due to transient thermal storage in the fluid required to develop a thermal boundary layer starting with an isothermal initial condition. The thickness of this boundary layer increases with time and becomes significant only in the later part of the transient. The interface temperature responds accordingly. Since the leading edge of this boundary layer is located at the stagnation point and its thickness increases downstream; it can be noticed that in the later part of the transient, the temperature turns minimum at the impinging point and maximum at the edge of the plate. The same figure presents the values for maximum-to-minimum temperature difference at the interface. As expected, the minimum to maximum temperature range at the interface increases with time.

The development of the local heat transfer coefficient with respect to time is presented in Figure 61. It can be noticed that, in general, the local heat transfer coefficient decreases with time. The maximum change is seen in the thin film region where the horizontal flow has been established. At the stagnation region, the values do not change much with time. The magnitude of heat transfer coefficient is determined by the magnitude of interface heat flux and the interface temperature. The denominator of equation (58),  $(T_{\text{int}} - T_j)$  increases around 14 times from  $t = 0.5$  s to steady state, while the heat flux increases around 8 times in the same period. This faster increment in the temperature difference compared to the heat flux is the reason for the decrease of the heat transfer coefficient with time.

The variation of local Nusselt number distribution and the value of the average Nusselt number with time can be observed in Figure 62. Larger changes are seen at larger distances

downstream because of larger changes in heat transfer coefficient as well as the linear rise of length scale 'x' used for the definition of Nusselt number. At all locations, the local Nusselt number decreases with Fourier number and reaches the final steady state condition.

The variation of maximum temperature in the solid, maximum temperature at the interface, and the maximum-to-minimum temperature difference at the interface during the transient process are presented in Figure 63 for two different Reynolds number. As expected, the temperature increases with time starting from the initial isothermal condition. A rapid increment is seen at the earlier part of the transient and it levels off as the thermal storage capacity of the solid diminishes and becomes zero at the steady state condition. It is noticed that the time required to reach the steady state is lower at higher Reynolds number. It changes from 40 s at  $Re = 550$  to 33 s at  $Re = 880$ , because the higher velocity of the fluid helps to enhance the convective heat transfer process.

The average heat transfer coefficient and average Nusselt number variation with time for two different Reynolds numbers is presented in Figure 64. It is noticed that both average heat transfer coefficient and average Nusselt number decreases with time and reach their steady state values as an exponential decay function. Figure 65 presents the time required to reach steady state as a function of Reynolds number. The duration of the transient decreases as the Reynolds number increases.

Another important factor that controls the transient heat transfer process is the thickness of the impinging plate. Its effect on the maximum temperature in the solid, maximum temperature at the interface, and maximum-to-minimum temperature difference at the interface can be observed in Figure 66. As the thickness increases, the time required to reach steady state increases. This is expected because the thermal storage capacity of the plate is directly proportional to its thickness. Figure 67 presents the average heat transfer coefficient and average Nusselt number variation with time for two different plate thicknesses. At early part of the transient process, the average heat transfer coefficient is larger for smaller thickness; as the transient phenomenon progresses, the average heat transfer coefficient becomes almost equal for both cases. A smaller thickness presents a lower thermal resistance to heat flux, and allows it to reach the interface faster, while in a thicker plate the heat flux reaches the interface in a more distributed form. The variation of the average Nusselt number with time is similar to the one described for the average heat transfer coefficient.

The maximum temperature in the solid, the maximum temperature at the interface, and maximum-to-minimum temperature difference at the interface for different materials is shown in Figure 68. It can be noticed that the material with the highest thermal diffusivity reaches the steady state faster. Out of three materials considered in our study, diamond has much higher thermal diffusivity compared to silicon or copper. At 293 K, the values are  $\alpha_{diamond} = 1.29e^{-3} \text{ m}^2/\text{s}$ ,  $\alpha_{copper} = 1.12e^{-4} \text{ m}^2/\text{s}$ , and  $\alpha_{silicon} = 0.984e^{-4} \text{ m}^2/\text{s}$ . It can be also noticed that even though copper has a slightly higher thermal diffusivity than silicon, it reaches the steady state somewhat slower. Comparing the thermal storage capacity of these materials, it can be noticed that  $(\rho c_p)_{copper} = 3.43 \times 10^6 \text{ J / K m}^3$  is quite larger than  $(\rho c_p)_{silicon} = 1.66 \times 10^6 \text{ J / K m}^3$ . Therefore, at similar values of thermal diffusivity, the thermal storage

capacity determines the amount of energy that can be stored in the solid, this capacity to store energy creates transient thermal resistance and slows down the heat conduction through the plate.

Figure 69 presents the variation of the average heat transfer coefficient and average Nusselt number with time for different materials considered in this study. It is noticed that materials with the ability to transport the heat faster through them (diamond, silicon) have higher values at early stages of the transient process. The time required to reach steady state for different materials and different plate thicknesses is presented in Figure 70. As expected, as the thickness increases, the time to reach steady state increases.

Figure 71 shows the growth of the isothermal lines inside the solid at different time instants for  $b = 0.005$  m. It can be observed that at the beginning of the process the isothermal lines grow around the discrete heat sources. As the time progresses, the isothermal lines start moving upward like a one dimensional heat conduction phenomenon. When the transient isothermal lines reach the area close to the interface, they start forming concentric lines around the stagnation point, and when the process reaches steady state, it resembles a one-dimensional heat conduction process at the central part of the solid. Figure 72 plots the isothermal lines within the solid for  $b = 0.0025$  m. The behavior at the beginning of the transient process is similar to the one observed in Figure 71, but as the transient process progresses, the concentric isothermal lines around the stagnation point continue to grow and reach the bottom edge of the plate.

Due to the lack of experimental information on the transient phenomenon, the results obtained with the present numerical model were validated by comparing with steady state test data acquired by Vader et al. [12]. For this comparison, water was used as the working fluid and the run used all experimental conditions except for the length of the plate to keep within the laminar flow regime. The results are presented in Figure 73 that shows the variation of temperature at the interface and the local heat transfer coefficient. It can be seen that numerical results compare reasonably well with experimental data. The trend is similar and the curves cross each other. The maximum deviation is seen at the stagnation point. It is 20% for temperature, and 18% for the local heat transfer coefficient. The deviation of average heat transfer coefficient is only 4%.

## NOMENCLATURE

$b$	Thickness of the plate [m]
$c_p$	Specific heat at constant pressure [kJ / kg K]
$Fo$	Fourier number, $\alpha_f t / W^2$
$g$	Acceleration due to gravity [m / s <sup>2</sup> ]
$h$	Heat transfer coefficient [W / m <sup>2</sup> K]
$H_n$	Height of the nozzle from the plate [m]
$k$	Thermal conductivity [W / m K]
$L$	Width of the plate [m]
$n$	Coordinate normal to the free surface [m]
$Nu$	Nusselt number [ $h r / k_f$ ]

p	Pressure [Pa]
q	Heat flux [ $\text{W} / \text{m}^2$ ]
$\bar{q}$	Average heat flux [ $\text{W} / \text{m}^2$ ]
$q_w$	Discrete heat flux [ $\text{W} / \text{m}^2$ ]
Re	Reynolds number, $\rho_f \nu_j W / \mu$
t	time [s]
T	Temperature [K]
$\bar{T}$	Average temperature [K]
$T_j$	Jet temperature [K]
$\nu_i$	Initial velocity field [m / s]
$\nu_j$	Jet velocity [m / s]
$\nu_t$	Velocity along the free surface [m / s]
$\nu_x$	Horizontal velocity [m / s]
$\nu_z$	Vertical velocity [m / s]
W	Width of the slot nozzle [m]
x	Horizontal coordinate [m]
z	Vertical coordinate [m]

#### **Greek Symbols**

$\alpha$	Thermal diffusivity [ $\text{m}^2/\text{s}$ ]
$\delta$	Height of the free surface from the plate [m]
$\mu$	Dynamic viscosity [ $\text{kg} / \text{m s}$ ]
$\rho$	Density [ $\text{kg} / \text{m}^3$ ]
$\sigma$	Surface tension coefficient [N / m]

#### **Subscripts**

atm	Atmospheric condition
av	Average
f	Fluid
int	Interface
s	Solid

## **CONCLUSIONS**

The conclusions derived from the results of the present study can be summarized as follows:

1. The local temperature as well as the local heat flux at the solid-fluid interface increase with time. The local heat transfer coefficient and local Nusselt number decrease with time and gradually reach their steady state distribution.
2. The variation of average heat transfer coefficient and average Nusselt number with time present an exponential decay behavior over the duration of the transient.

4. The velocity of the jet impinging on the plate is an important parameter that affects the transient process. As the jet Reynolds number increases, the time required to reach steady state decreases.
5. The maximum temperature at the interface and the maximum temperature inside the solid decrease when Reynolds number increases, while the maximum-to-minimum temperature difference at the interface increases with Reynolds number.
6. The thickness of the plate plays an important role in the transient phenomenon; the transient time increases with thickness because the thermal storage capacity of the plate is directly proportional to its thickness. At the earlier part of the transient, the average heat transfer coefficient and average Nusselt number, are larger for smaller thickness.
7. For the materials considered (copper, diamond, silicon), it was found that the thermal storage capacity ( $\rho c_p$ ) controls the duration of the transient process, increasing the time required to reach steady state as the thermal storage increases.
8. The limiting steady state results using the present numerical model compared well with experimental measurements.

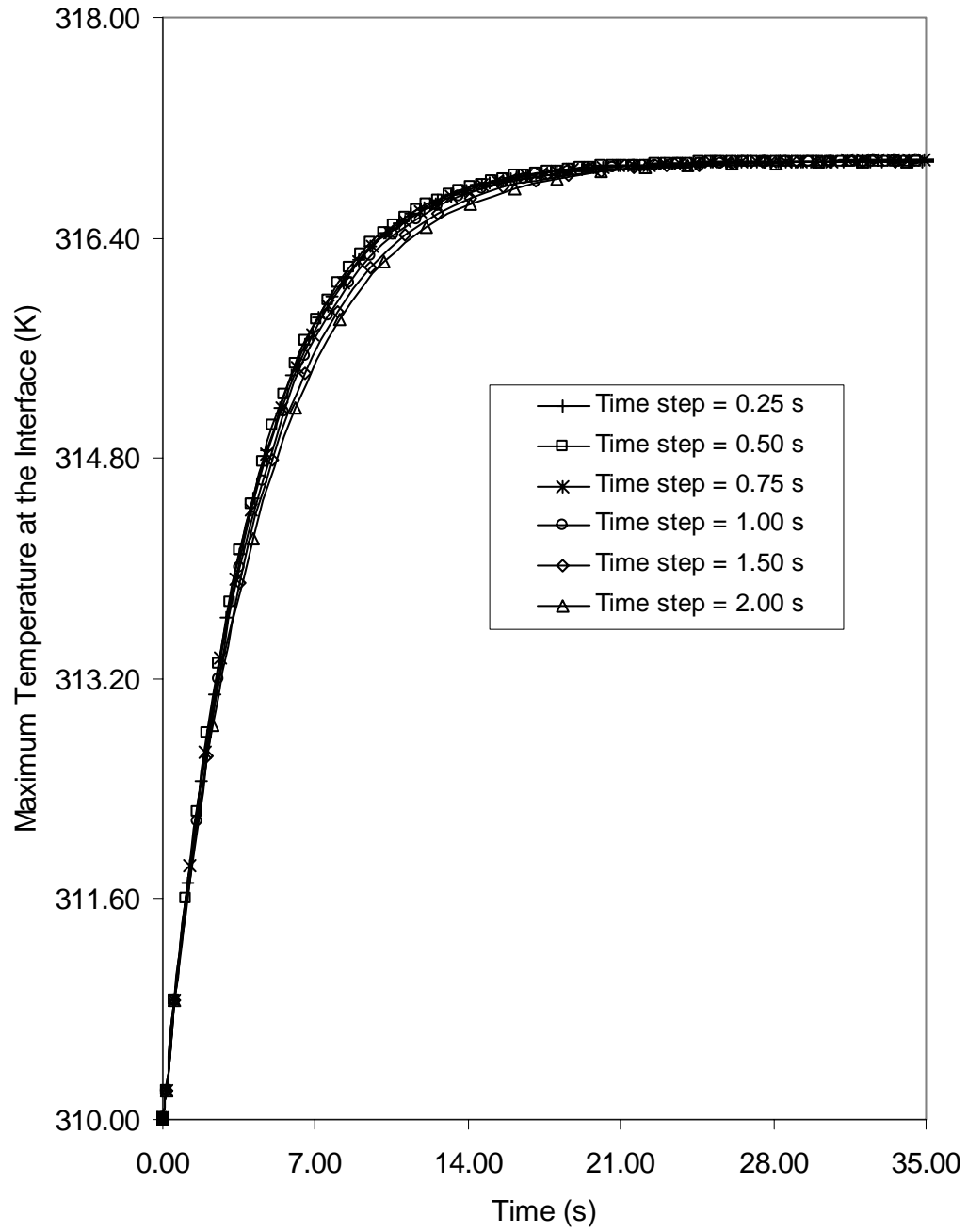


Figure 58. Temperature variation for different time steps  
 ( $Re = 550$ ,  $T_j = 310$  K,  $b = 0.005$  m,  $H_n = 0.0085$  m, Copper plate,  $q_w = 63$  kW/m<sup>2</sup>)

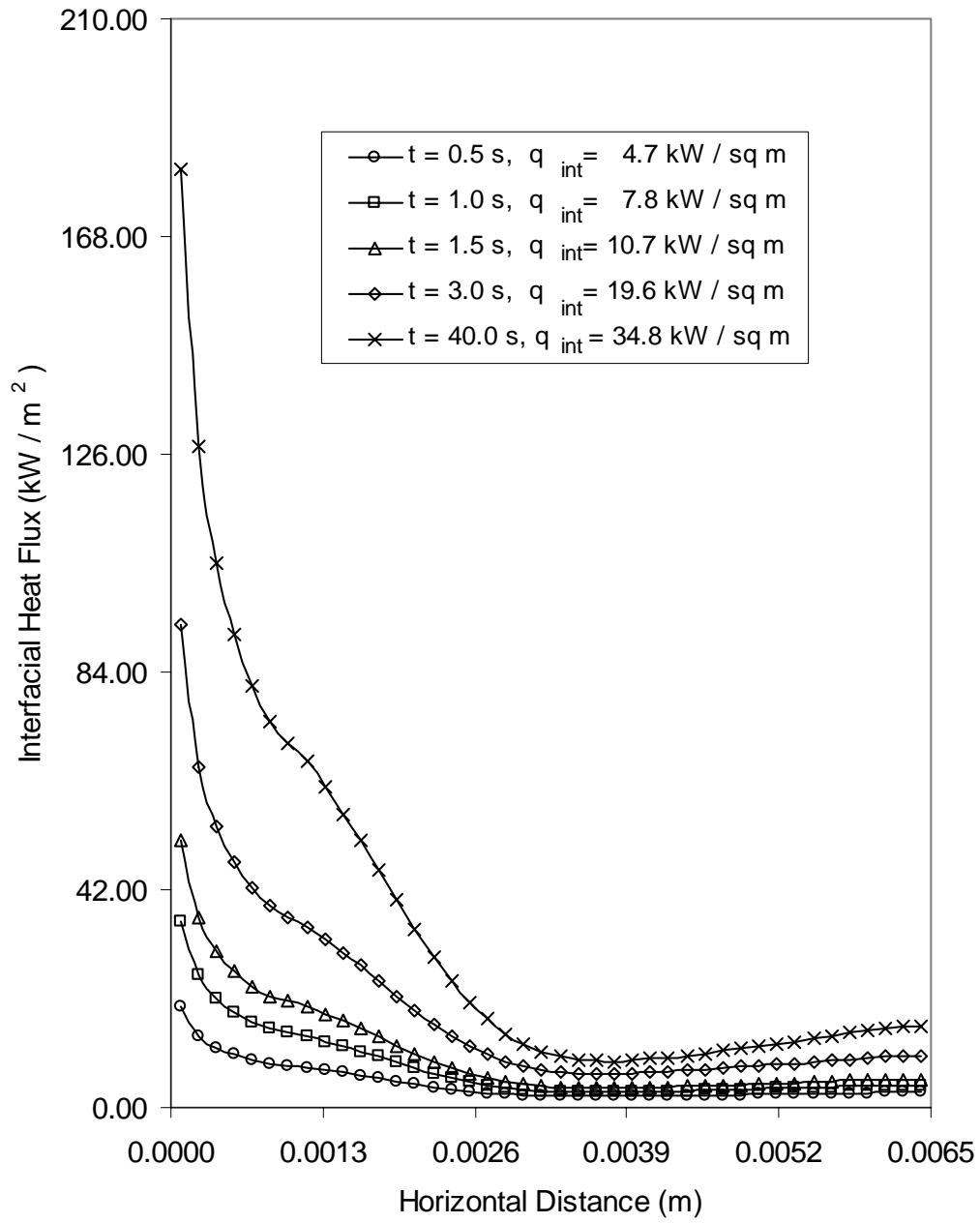


Figure 59. Local heat flux distribution at the interface  
(Re = 550,  $T_j = 310$  K,  $b = 0.005$  m,  $H_n = 0.0085$  m, Copper plate,  $q_w = 63$  kW/m<sup>2</sup>)

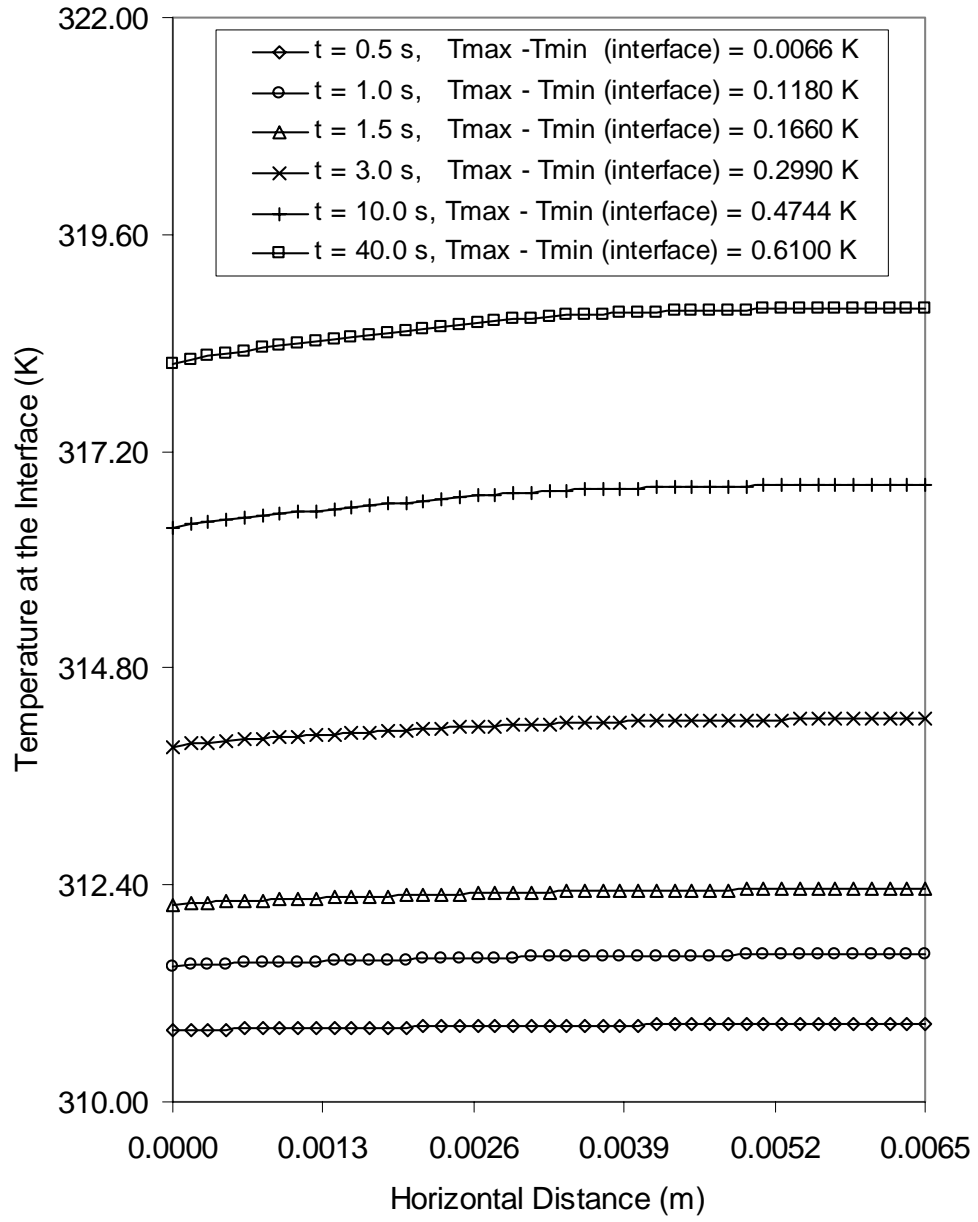


Figure 60. Local temperature distribution at the interface  
 ( $Re = 550$ ,  $T_j = 310$  K,  $b = 0.005$  m,  $H_n = 0.0085$  m, Copper plate,  $q_w = 63$  kW/m<sup>2</sup>)



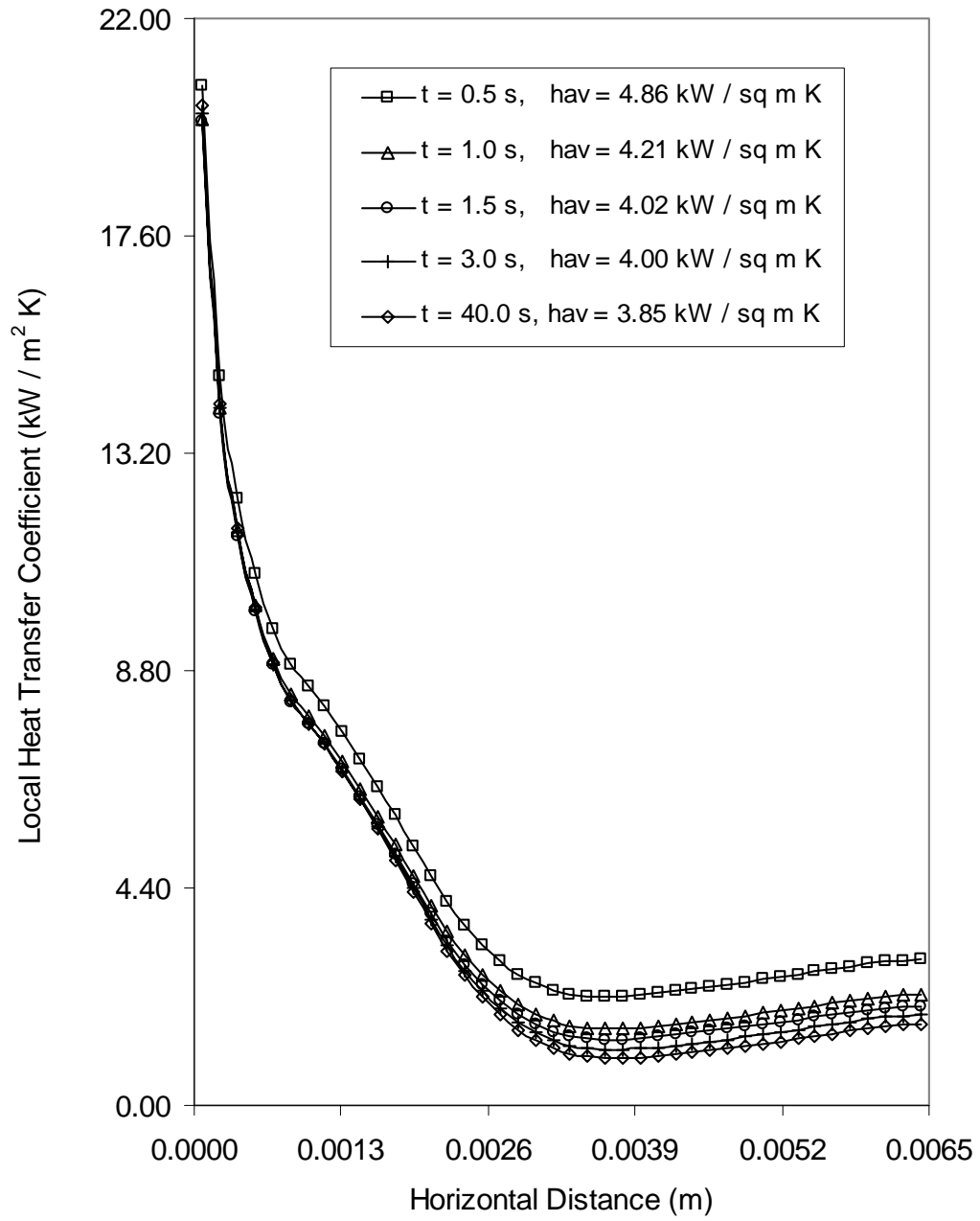


Figure 61. Distribution of local heat transfer coefficient  
 $(\text{Re} = 550, T_j = 310 \text{ K}, b = 0.005 \text{ m}, H_n = 0.0085 \text{ m}, \text{Copper plate}, q_w = 63 \text{ kW/m}^2)$

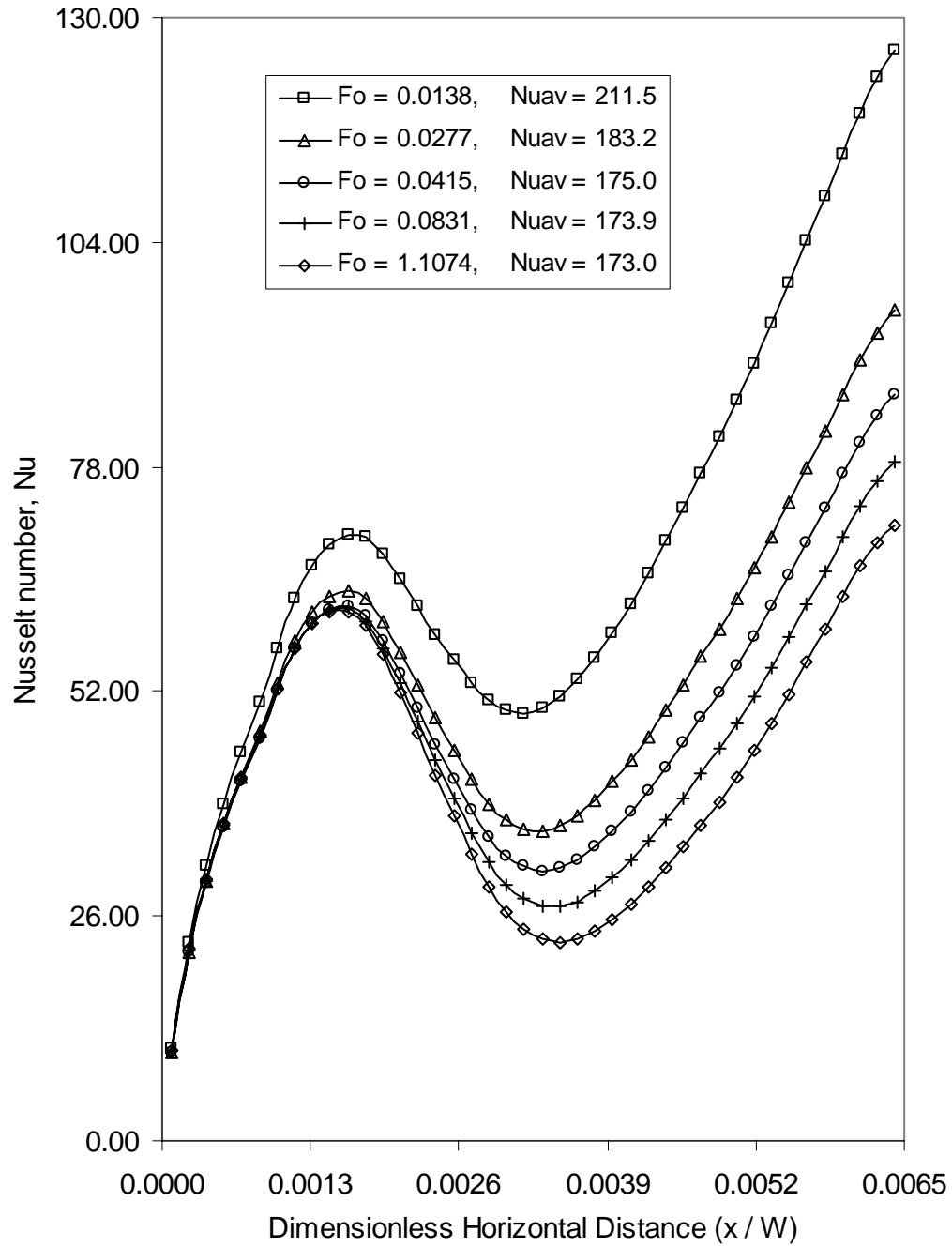


Figure 62. Distribution of local Nusselt number  
 ( $Re = 550$ ,  $T_j = 310$  K,  $b = 0.005$  m,  $H_n = 0.0085$  m, Copper plate,  $q_w = 63$  kW/m<sup>2</sup>)

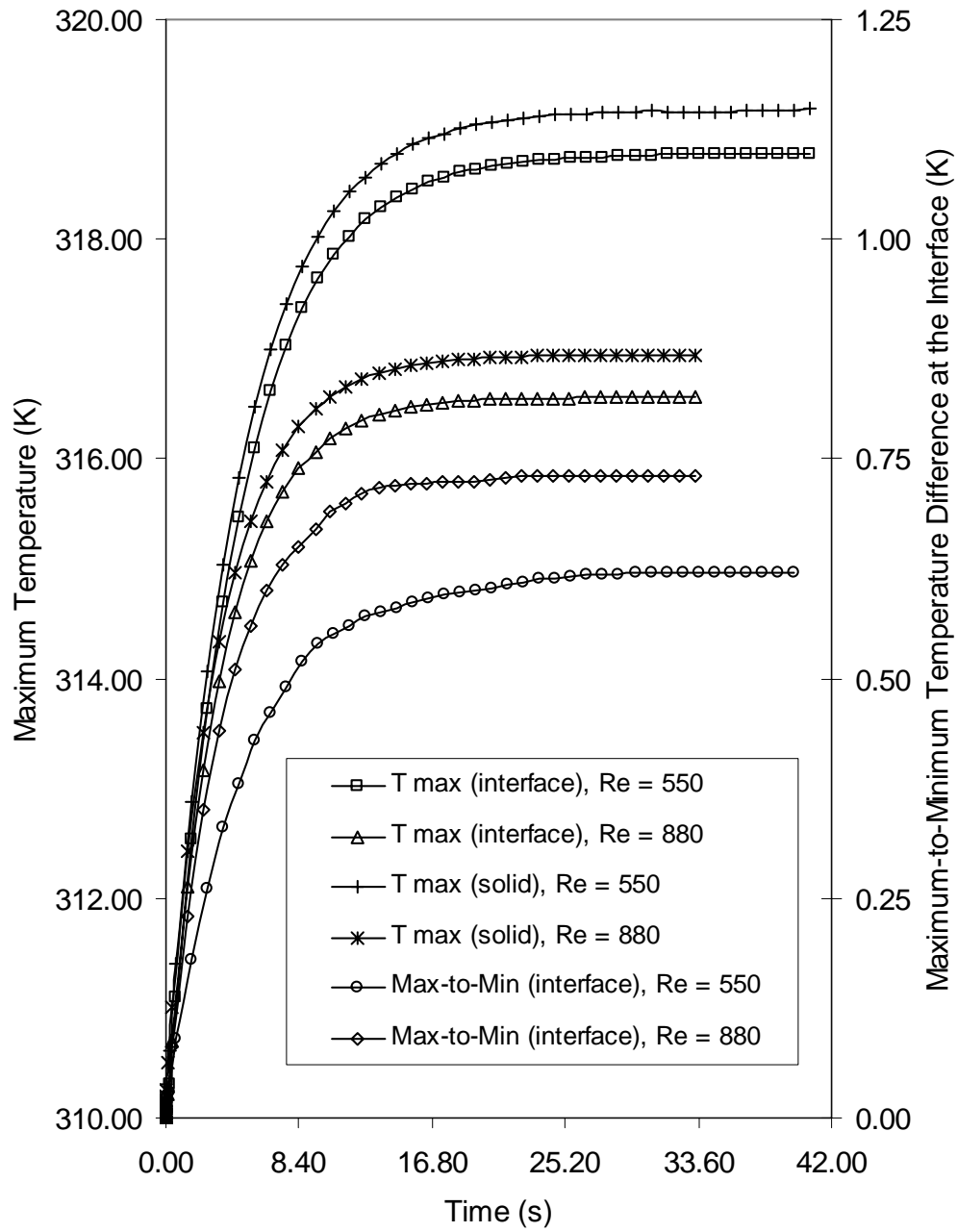


Figure 63. Variation of maximum temperature at the interface, maximum temperature inside the solid, and maximum-to-minimum temperature difference at the interface with time for different Reynolds numbers ( $T_j = 310$  K,  $b = 0.005$  m,  $H_n = 0.0085$  m, Copper plate,  $q_w = 63$  kW/m<sup>2</sup>)

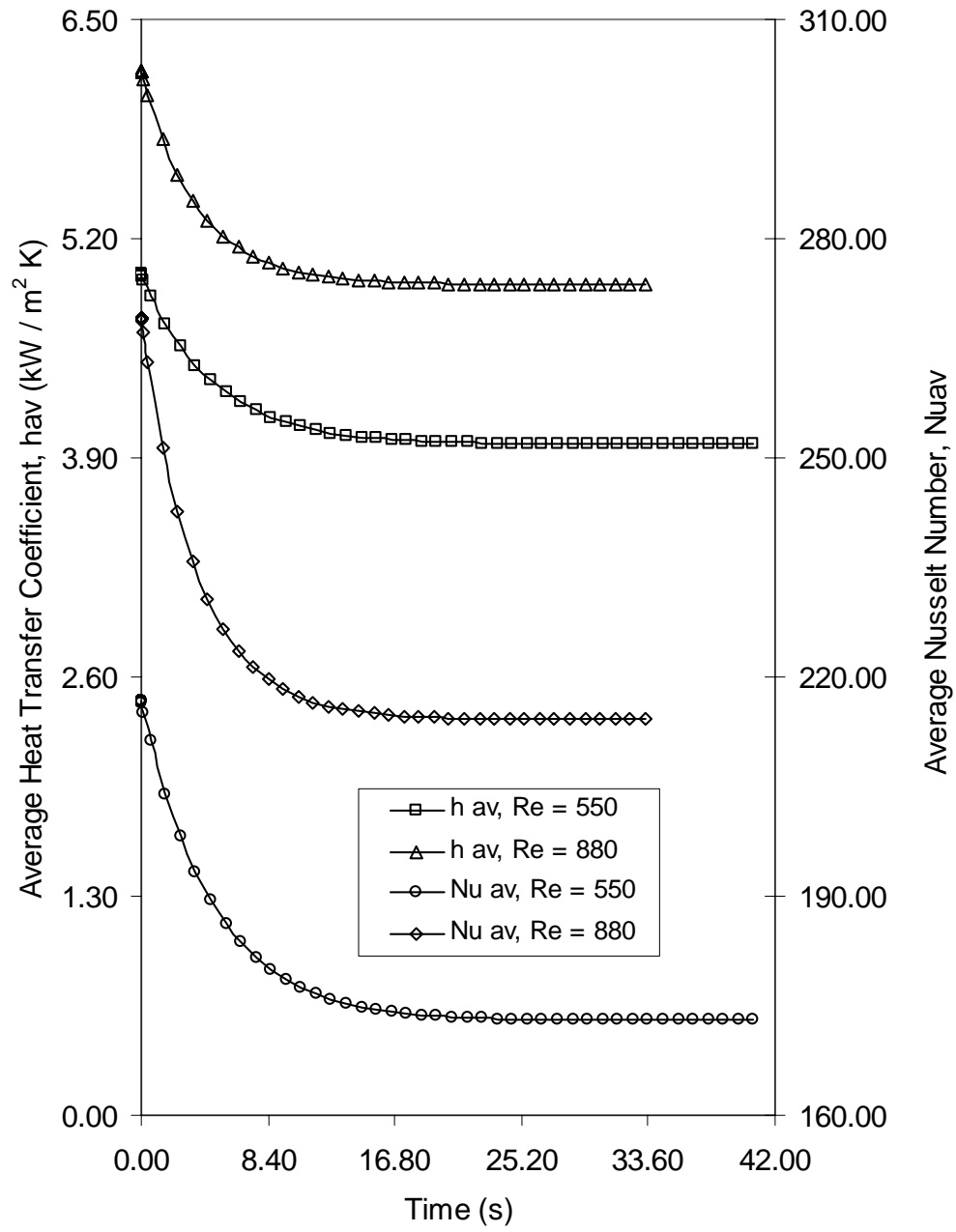


Figure 64. Variation of average heat transfer coefficient and average Nusselt Number with time  
 $(T_j = 310 \text{ K}, b = 0.005 \text{ m}, H_n = 0.0085 \text{ m}, \text{Copper plate}, q_w = 63 \text{ kW/m}^2)$

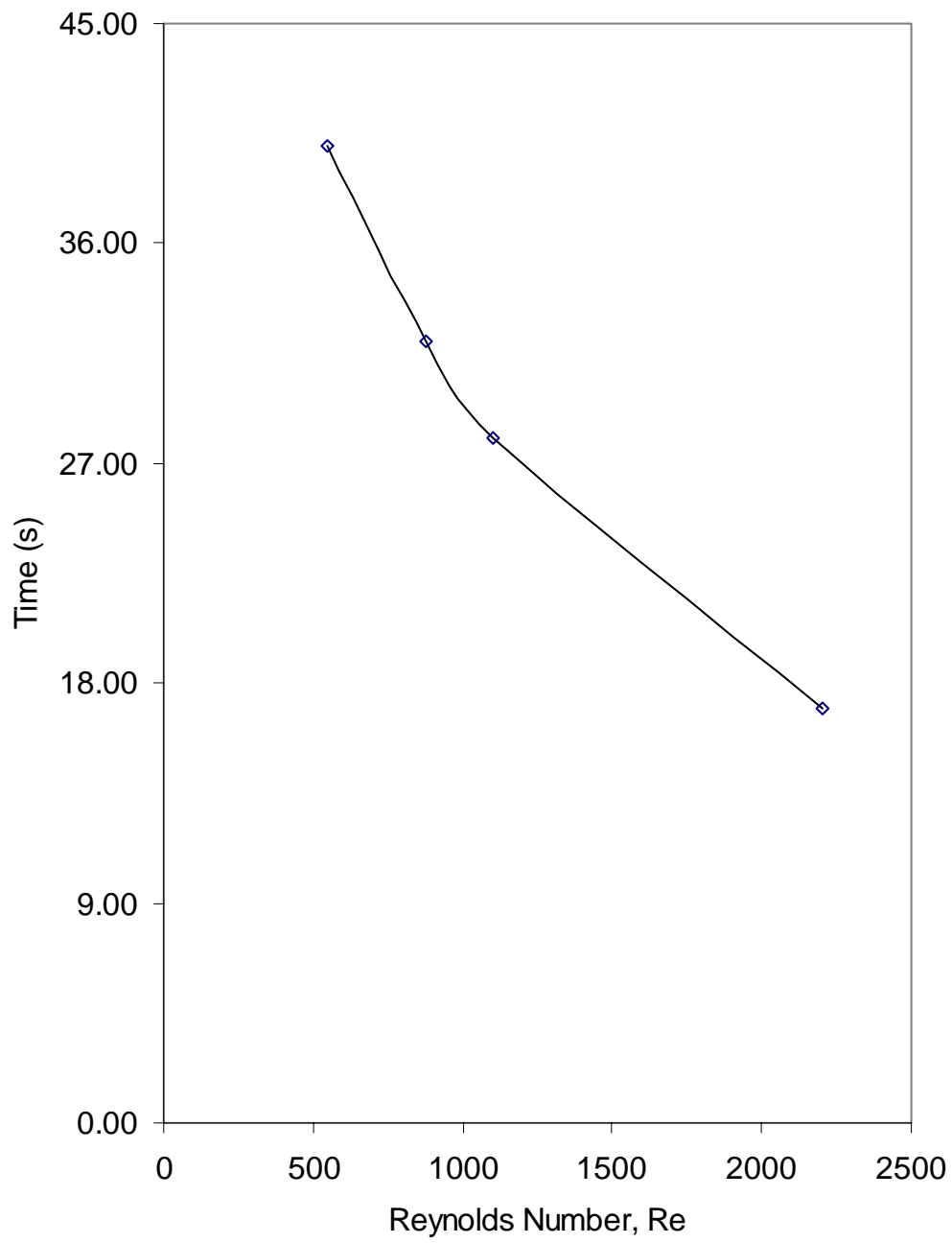


Figure 65. Variation of time required to reach steady state  
with Reynolds number  
( $T_j = 310 \text{ K}$ ,  $b = 0.005 \text{ m}$ ,  $H_n = 0.0085 \text{ m}$ , Copper plate,  $q_w = 63 \text{ kW/m}^2$ )

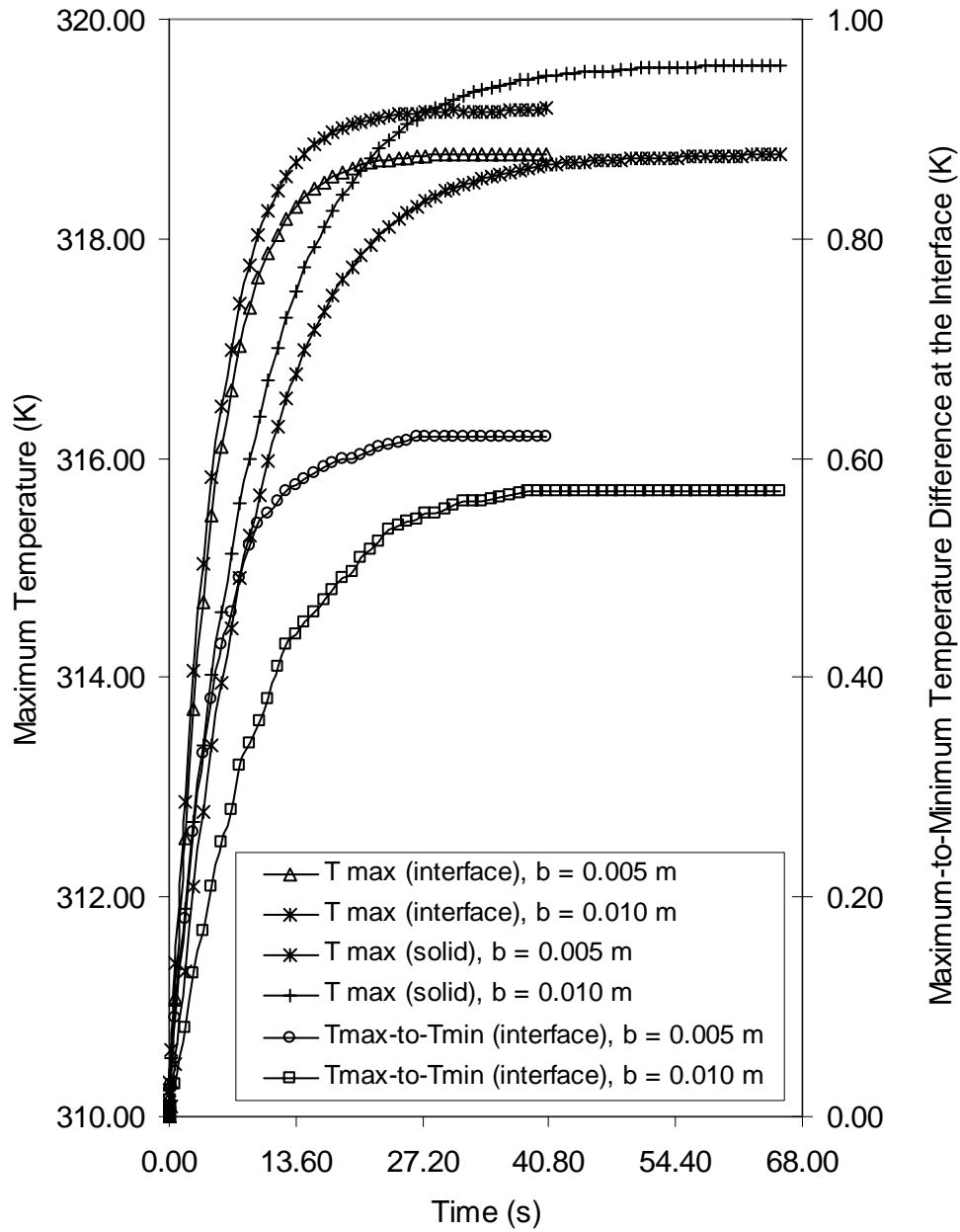


Figure 66. Variation of maximum temperature at the interface, maximum-to-minimum temperature difference at the interface, and maximum temperature inside the solid with time for different plate thicknesses  
 (Re = 550,  $T_j = 310$  K,  $H_n = 0.0085$  m, Copper plate,  $q_w = 63$  kW/m<sup>2</sup>)

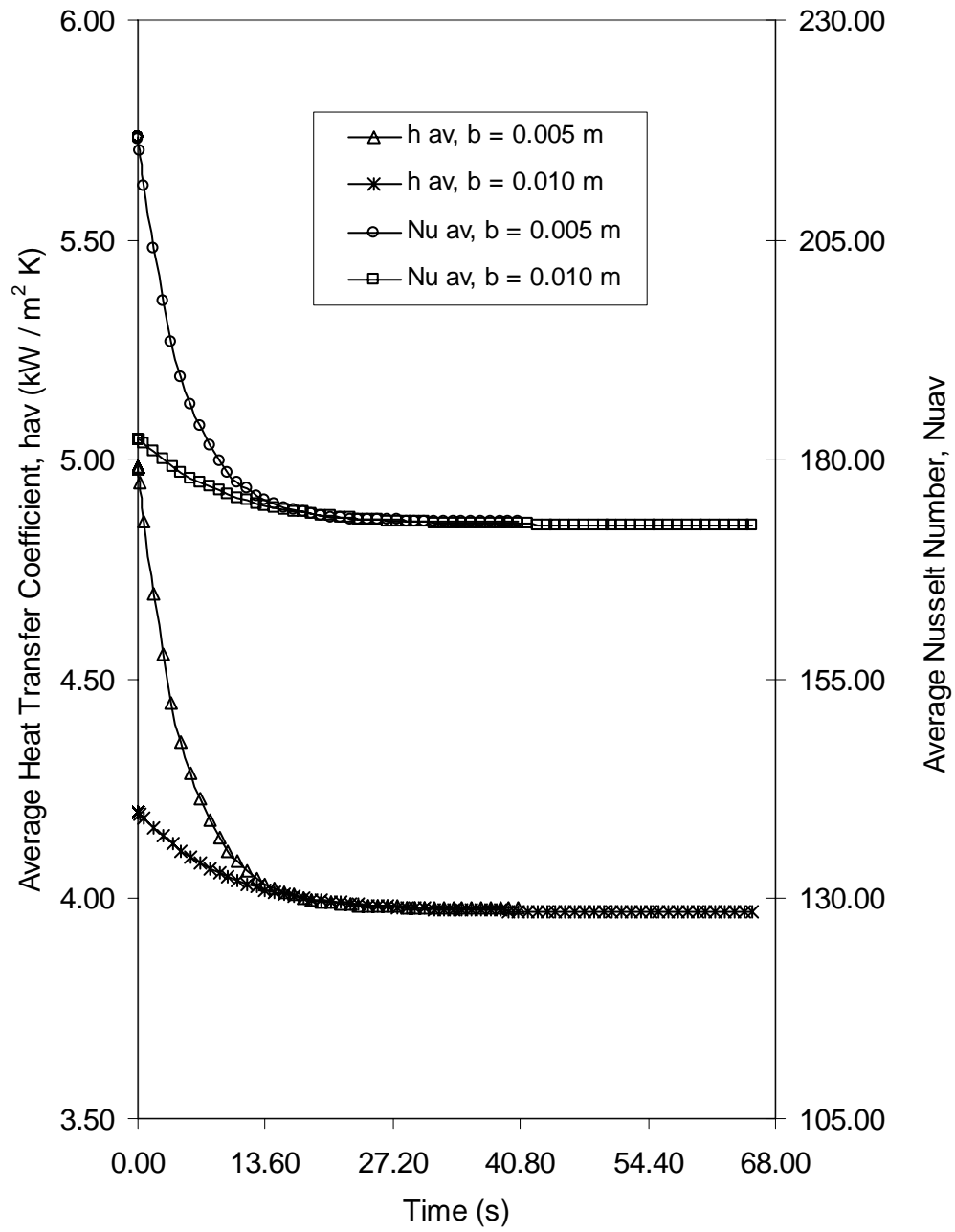


Figure 67. Average heat transfer coefficient and average Nusselt number variation with time for two plate thicknesses ( $Re = 550$ ,  $T_j = 310$  K,  $H_n = 0.0085$  m, Copper plate,  $q_w = 63$  kW/m<sup>2</sup>)

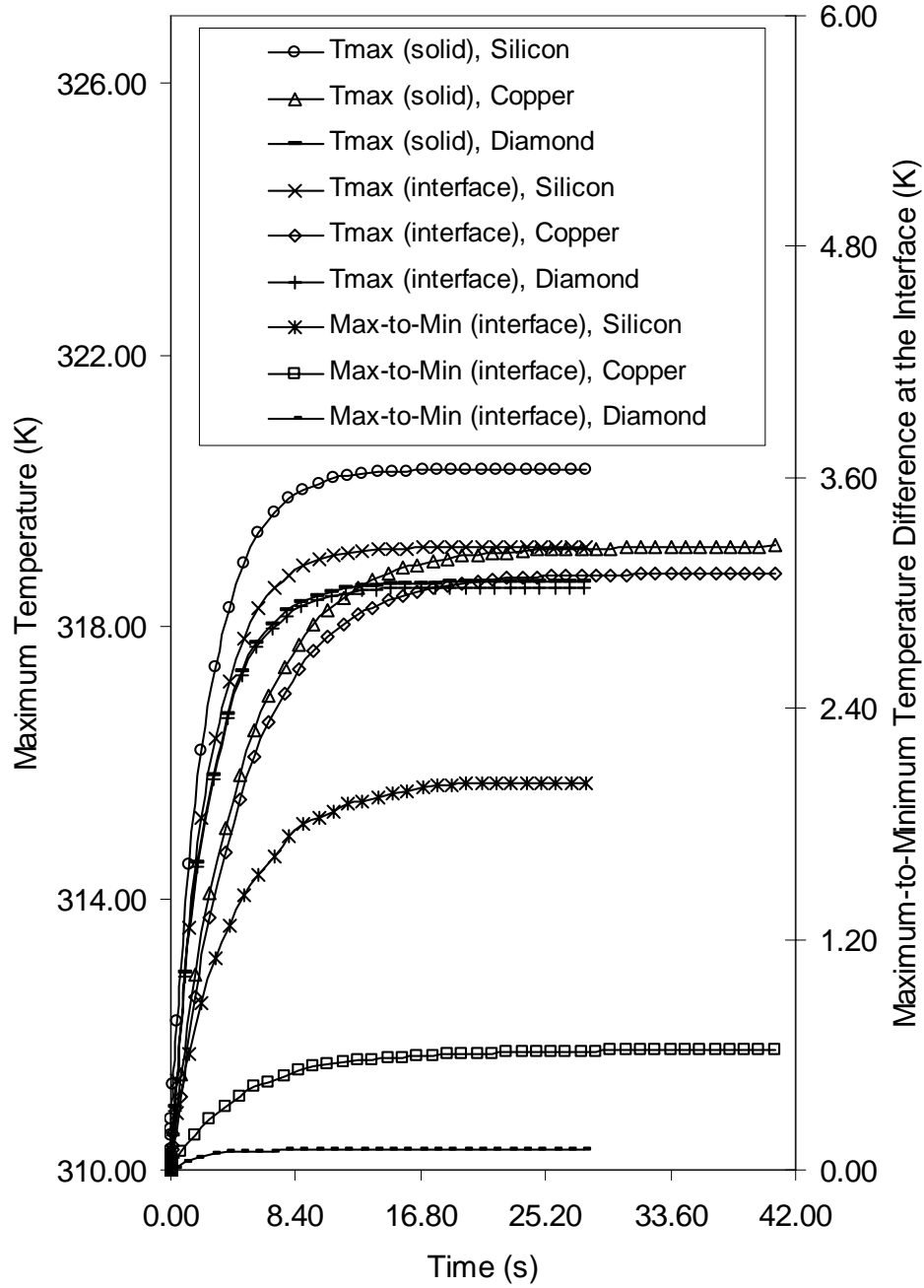


Figure 68. Variation of maximum temperature at the interface, maximum temperature inside the solid, and maximum-to-minimum temperature difference at the interface with time for different materials  
 $(Re = 550, T_j = 310 \text{ K}, b = 0.005 \text{ m}, H_n = 0.0085 \text{ m}, q_w = 63 \text{ kW/m}^2)$



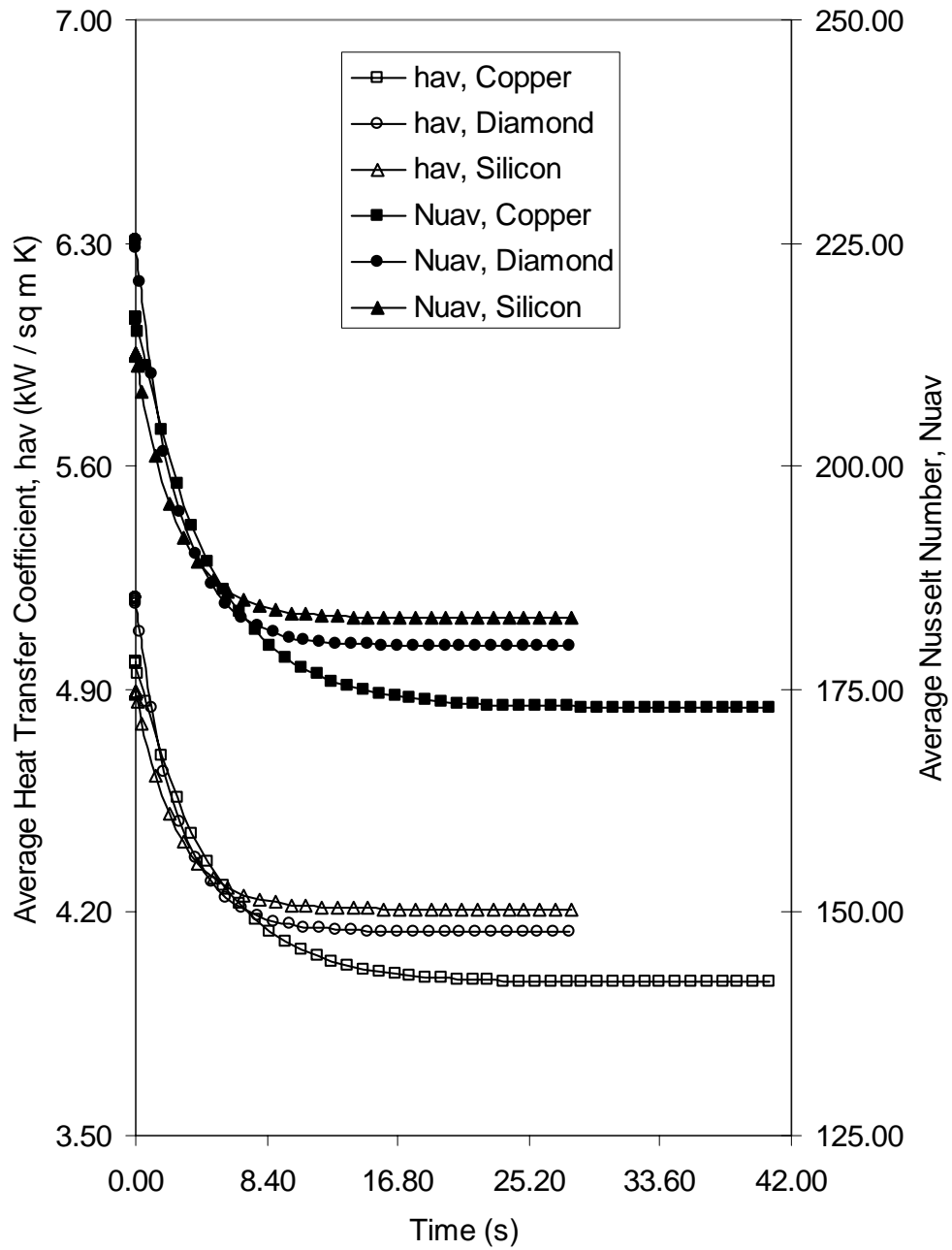


Figure 69. Variation of average heat transfer coefficient and average Nusselt number with time for different materials

( $Re = 550$ ,  $T_j = 310$  K,  $b = 0.005$  m,  $H_n = 0.0085$  m,  $q_w = 63$  kW/m<sup>2</sup>)

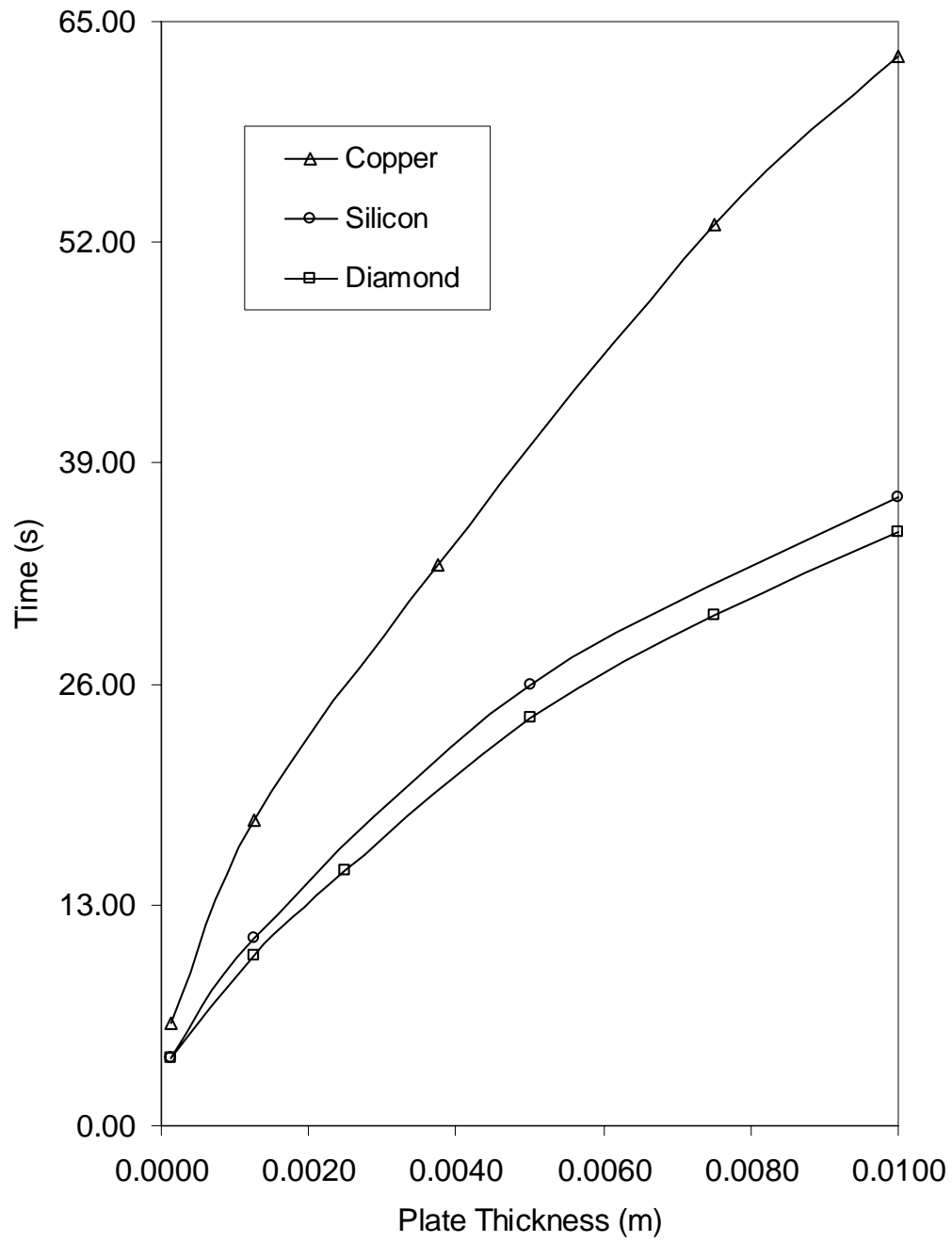


Figure 70. Time required to reach steady state for different materials and plate thicknesses  
 ( $Re = 550$ ,  $T_j = 310$  K,  $H_n = 0.0085$  m,  $q_w = 63$  kW/m<sup>2</sup>)

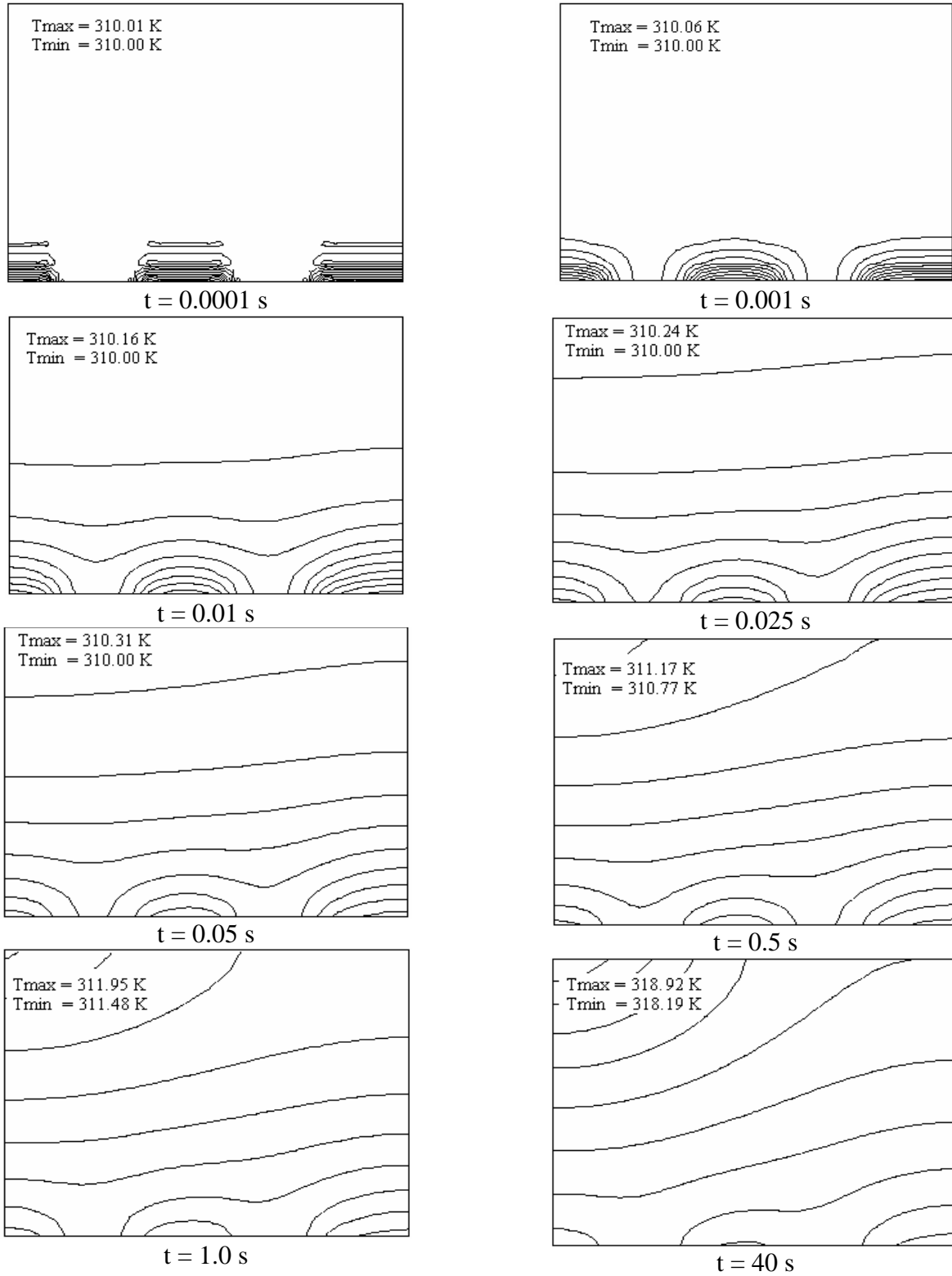
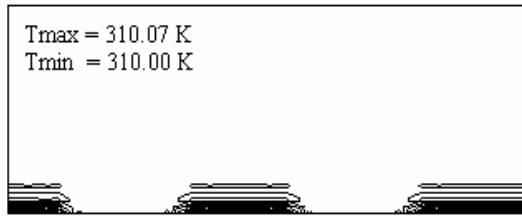
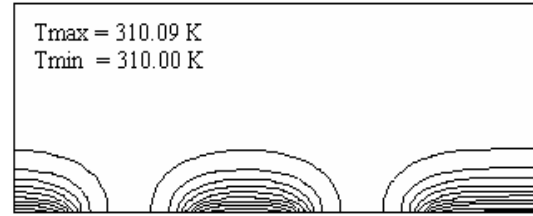


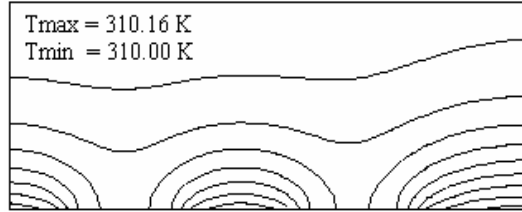
Figure 71. Isothermal lines for different time steps  
 ( $Re = 550$ ,  $T_j = 310$  K,  $b = 0.005$  m,  $H_n = 0.0085$  m, Copper plate,  $q_w = 63$  kW/m<sup>2</sup>)



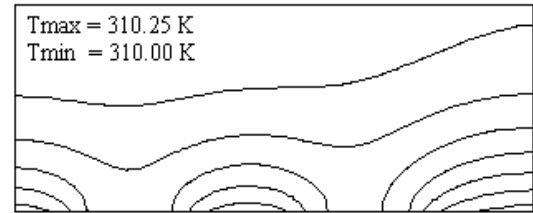
$t = 0.0001 \text{ s}$



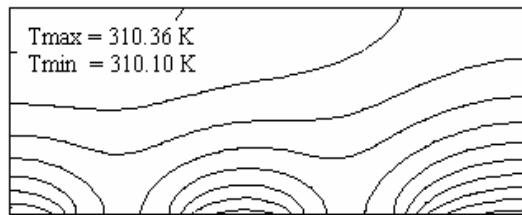
$t = 0.001 \text{ s}$



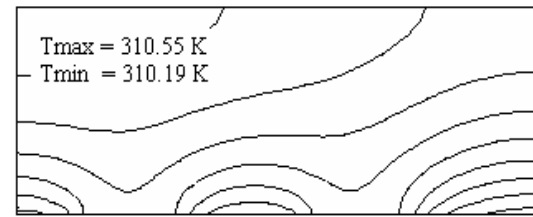
$t = 0.01 \text{ s}$



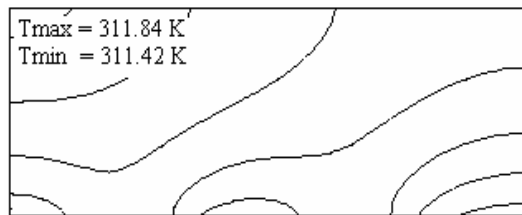
$t = 0.025 \text{ s}$



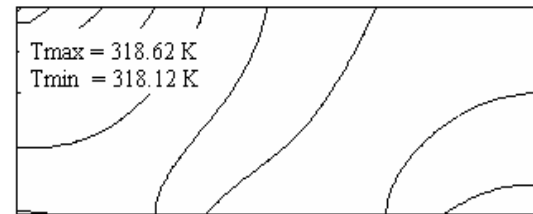
$t = 0.05 \text{ s}$



$t = 0.5 \text{ s}$



$t = 1.0 \text{ s}$



$t = 21 \text{ s}$

Figure 72. Isothermal lines for different time steps  
 $(\text{Re} = 550, T_j = 310 \text{ K}, b = 0.0025 \text{ m}, H_n = 0.0085 \text{ m}, \text{Copper plate}, q_w = 63 \text{ kW/m}^2)$

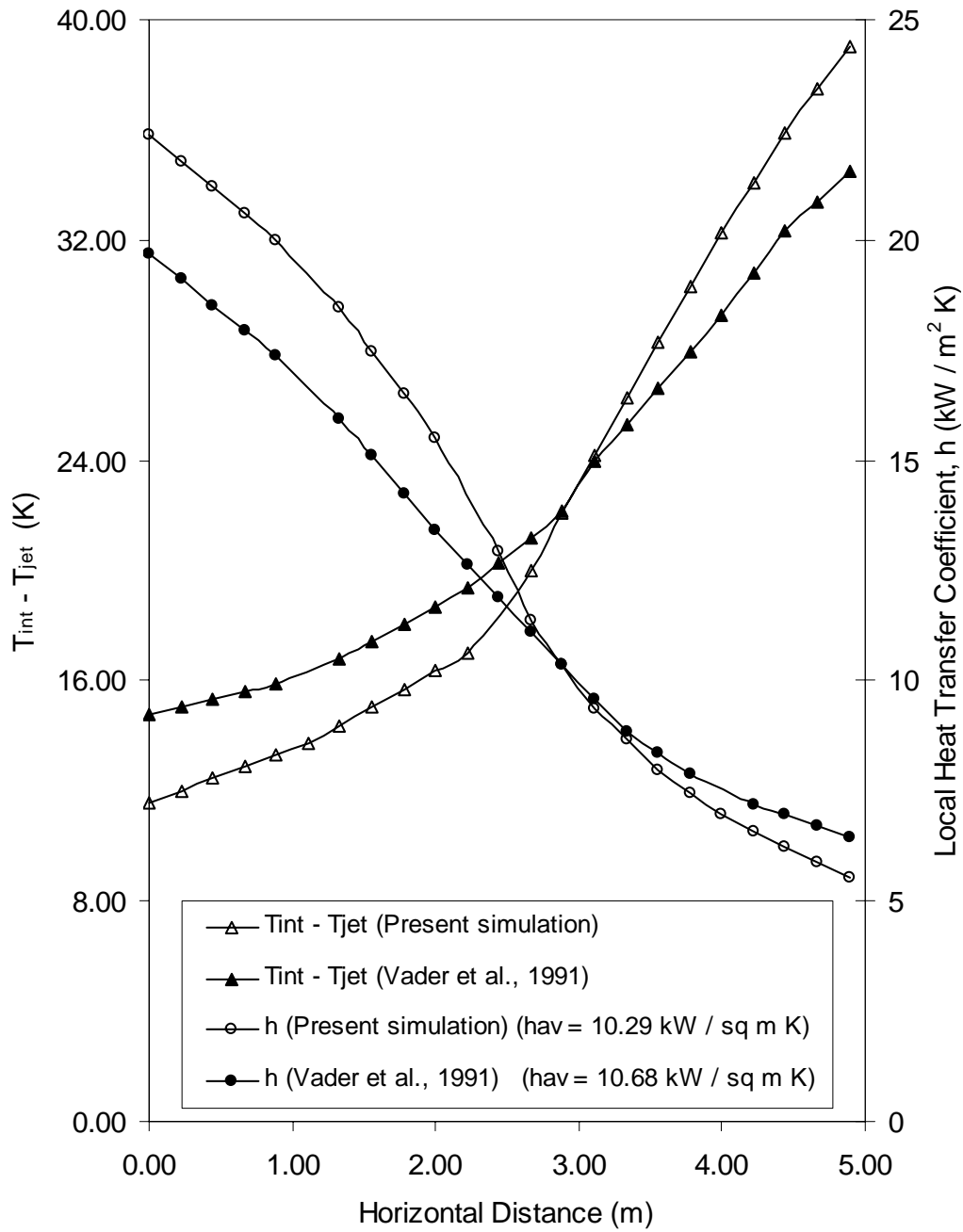


Figure 73. Temperature difference between the wall and the jet and local heat transfer coefficient comparison between present simulation and Vader et al. [12]

( $Re = 38000$ ,  $T_j = 303$  K,  $b = 0.000635$  m,  $H_n = 0.089$  m,

Haynes 230 plate,  $q = 250$  kW/m<sup>2</sup>)

# **SUBMERGED AXIAL FREE JET IMPINGING ON A UNIFORMLY HEATED DISK: STEADY STATE**

## **INTRODUCTION**

This two-part study presents numerical simulations of heat transfer with a free surface jet of high Prandtl number fluid impinging axially on a solid plate. All models simulated are treated as a conjugate problem in which the heat conduction in the solid disk was included in the numerical simulation model. Equations for the conservation of mass, momentum, and energy were solved taking into account the transport processes at the solid-liquid and liquid-gas interfaces. The shape and location of the free surface (liquid-gas interface) was determined iteratively as a part of the solution process by satisfying the kinematic conditions as well as the balance of normal and shear forces at this interface.

The first part seeks to validate the model by comparing the numerical results with experimental results obtained by Leland [63]. The second part, seeks to investigate the effect of submerging the inlet nozzle below the fluid surface making the model a submerged, free surface impinging jet. Five different fluid models were developed with three of them being unsubmerged and the last two being submerged. Comparisons were then made between heat transfer coefficient characteristics at the solid / fluid interface for both types of jets. Further parametric variations included the variation of inlet Reynolds number with values of 1400, 1000, and 750, solid properties (copper, constantan, and silicon) and solid thickness (2mm, 3mm, and 4mm). The heat flux at the solid base was maintained constant at 62 kW/ m<sup>2</sup> in all cases. Figure 1 shows a sample of the model geometry.

We consider an axisymmetric jet discharging from a nozzle and impinging perpendicularly at the center of a solid circular disk heated by a constant heat flux as shown in Figure 1. The mathematical model for this problem is described by equations (1-13). The local and average heat transfer coefficient were calculated using equations (31-32). The local Nusselt number and the average Nusselt number were calculated according to the following expressions:

$$Nu = \frac{hr_n}{k_f} \quad (68)$$

$$Nu_{av} = \frac{h_{av}r_n}{k_f} \quad (69)$$

## **DISCUSSION OF RESULTS**

A comparison between the present numerical simulation and the experimental data obtained by Leland [63] is presented in Table 4. In order to carry out this comparison, numerical simulations were performed using the appropriate test conditions. The table shows a good agreement between the simulation and the experimental data, with a maximum deviation of 8.4 %. This comparison validates the results obtained in the present investigation.

Figures 74 to 78 show the converged free surface for models at five different impingement heights, namely 6.47mm, 4.6mm, 1.75mm, 0.6mm, and 0.4mm. The last two,

(figures 77 and 78) represent the submerged free surface jets. From the distribution of the velocity vectors, it can be seen that the velocity remains almost uniform at the potential core region of the jet. As the fluid gets closer to the stagnation region, the velocity decreases while jet diameter increases and the direction of the fluid particles shift by as much as  $90^\circ$ . At the stagnation zone, the velocity reaches its minimum value and the fluid profile reaches a minimum sheet thickness. This is the start of the hydrodynamic boundary layer zone. As the hydrodynamic boundary layer thickness grows, the frictional resistance from the wall is eventually transmitted to the entire film thickness.

Figure 79 presents the free surface height distribution for different Reynolds numbers when the jet strikes the center of the disk, i.e. the relative heights of the five previously mentioned converged free surfaces. It can be observed that the minimum film height occurs at a radius larger than the radius of the nozzle and the film height gradually increases with radius after that location. It may be noted that due to radial spread of the fluid, the film height is expected to decrease, whereas the frictional resistance at the surface slows down the fluid and increases its height. The resulting free surface height is determined by these competing effects while preserving the continuity of the flow. Figure 80 shows a temperature contour plot over the whole conjugate domain for an impingement height of 0.4mm using silicon as the solid. Expectedly, the lowest temperatures within the solid domain can be found around the disk center (the stagnation point) increasing gradually outwards. The same observation can be made within the fluid domain and the formation of a thermal boundary layer is apparent near the solid-fluid interface within the fluid domain. Figure 81 shows a pressure contour plot using an impingement height of 1.75mm. Again, the highest pressure values can be seen at the stagnation point where the fluid impinges directly on the solid disk surface. Figure 82 shows streamline contours for the same flow configuration. The streamlines are well defined and stratified with the thermal and hydrodynamic boundary layers evident near the fluid-solid interface.

The temperature distribution at the solid-fluid interface for different Reynolds numbers is presented in figure 83. The submerged free surface jet model with an impingement height of 0.4mm has been used and as expected, the temperature is minimum in all cases at the disk center (the stagnation point). It increases sharply along the radius up to a length approximately equal to the nozzle radius and then increases gradually to the outer disk edge. The difference in temperature for the three Reynolds numbers simulated is each about 10K and as usual the interface temperature decreases with increase in Reynolds number. Figure 84 plots the interface heat transfer coefficient against radial distance for the same configuration. Local heat transfer coefficient generally increases with Reynolds number for the three cases considered. All three curves have the same profile, with a relatively sharp decline in heat transfer coefficient around the stagnation zone but with a more gradual reduction away towards the disk edge. The actual values vary between  $17 \text{ kW/m}^2\text{K}$  ( $\text{Re} = 750$ ) and  $22 \text{ kW/m}^2\text{K}$  ( $\text{Re} = 1400$ ).

Figure 85 shows the plots of solid-fluid interface temperature against radial distance for three different disk thicknesses (2mm, 3mm, and 4mm) with Reynolds number of 1400 and for copper as the solid material. Again, the submerged nozzle model at an

impingement height of 0.4mm has been used. The values of temperature along the solid fluid interface are not very sensitive to thickness and remain virtually the same until further downstream. Figure 86 shows a similar plot but with constantan as the solid. Because of its lower thermal conductivity, interface temperature shows a somewhat higher sensitivity to disk thickness. Figure 87 combines both solids in one plot. Note that the temperature values for copper appear almost constant compared with those of constantan.

Figure 88 plots the local heat transfer coefficient at the interface against radial distance for the same configuration with three different disk thicknesses. The disk with a thickness of 2mm gives the highest overall variance of local heat transfer coefficient along the interface ( $2.5 \text{ kW/m}^2\text{K}$ ). As with the temperature plot, there is negligible difference between the local heat transfer coefficient values for the disks with thicknesses of 3mm and 4mm. Figure 89 plots the interface temperature against radial distance for three different solid materials (silicon, copper, and constantan) all with the same thickness (2mm) and with the same fluid flow parameters. It is interesting to note the cross-over effect that is predominant in all three temperature curves. Constantan gives the lowest temperature at the stagnation point but has by far the highest temperature at the disk edge. Copper has essentially the same profile but with a much milder overall temperature rise across the interface (5K) while silicon lies somewhere in between. This is compatible with their various thermal conductivities, with constantan having the lowest,  $22.7 \text{ W/mK}$ , copper the highest,  $386 \text{ W/mK}$ , and silicon in the middle at  $135 \text{ W/mK}$ . Figure 90 plots the local heat transfer coefficient at the interface against radial distance for the same three materials. Constantan expectedly has the largest variation in local heat transfer coefficient, dropping from  $55 \text{ kW/m}^2\text{K}$  at the disk center to  $14 \text{ kW/m}^2\text{K}$  at the disk edge. Thus, we can see that the effect of diffusion is quite as important as convection because the heat transfer characteristics are as strongly affected by the thermal conductivity of the solid material as by fluid inlet Reynolds number.

Figure 91 shows interface temperature against radial distance for five different impingement heights. Inlet Reynolds number is maintained at 1400 in all cases while disk material and thickness are kept constant. For the two submerged nozzle models, the jet at a height of 0.6mm gives much lower interface temperatures than that at an impingement height of 0.4mm, indicating that the optimum height lies somewhere in between. This is a curious effect that deserves further investigation in the study of submerged free surface jets because it implies that after a certain point, decreasing the height has no positive effects on the cooling properties of the system. For the three unsubmerged nozzles, ( $H_n = 6.7\text{mm}$ ,  $4.6\text{mm}$  and  $1.75\text{mm}$ ) interface temperatures are inversely proportional to impingement height, with the lowest interface temperatures being exhibited by the lowest height of 1.75mm. All plots have the same general profile with the lowest temperatures being at the stagnation point and increasing gradually towards the edge of the disk. Figure 92 shows the corresponding plot of heat transfer coefficient against radial distance for the same model. The results are complementary with the highest values of heat transfer coefficient corresponding to the lowest temperatures and vice-versa.



Figures 93 to 96 show the temperature contours within the solid disk for different simulation conditions. The maximum temperature inside the solid always occurs at the outer edge of the disk ( $r = r_o$ ) adjacent to the heat source ( $z = 0$ ). The control of the magnitude of this temperature is crucial in the design of electronic packages. Figure 93 compares temperature contours for the three different solids with thickness maintained constant at 2mm. Constantan gives lowest temperature values at the stagnation region but highest values at the outer edge of the solid. This is because it has much lower thermal conductivity which drastically reduces the effect of diffusion heat transfer within the solid. It has the highest overall temperature difference of 82K. Copper, which has the highest thermal conductivity, has the highest overall temperatures but also gives the lowest temperature variance of 8.65K. Figure 94 shows the temperature contours at three different Reynolds numbers using a 2mm thick copper wafer as the solid in all cases. Overall temperatures are inversely proportional to Reynolds number which is to be expected. Temperature variance is also proportional to Reynolds number with the highest variance of 8.65K occurring at the highest Reynolds number of 1400. Figure 95 shows contours for three different solid thicknesses, (2mm, 3mm, and 4mm) with copper as the solid and flow parameters maintained constant. There is no appreciable difference in the highest value of temperature within the solid for all three cases. The total deviation is only 0.20K between the 2mm and 4mm extremes. It is somewhat interesting to note though that the lowest temperature and lowest temperature variance occurs for the 3mm solid (379.40K and 8.37K). Figure 96 shows the temperature contours for three different impingement heights, 4.6mm, 1.75mm and 0.4mm. In all three cases, copper has been used as the solid with all flow parameters maintained constant. The maximum temperatures within the solid are found with the largest of the three impingement heights, (4.6mm). The largest deviation in temperature (8.65K) are found in the submerged case with an impingement height of 0.4mm. It is interesting to note that the lowest solid temperatures as well as lowest temperature deviations occur with an impingement height of 1.75mm which indicates that this height is the optimum for the geometries considered. The temperature contours are also markedly different from the other two cases, being less perpendicular to the interface.

## NOMENCLATURE

$b$	Thickness of the disk [m]
$c_p$	Specific heat at constant pressure [kJ / kg K]
$d$	Inlet nozzle diameter [m]
$g$	Acceleration due to gravity [ $\text{m} / \text{s}^2$ ]
$h$	Heat transfer coefficient [ $\text{W} / \text{m}^2 \text{ K}$ ]
$h_{av}$	Average heat transfer coefficient [ $\text{W} / \text{m}^2 \text{ K}$ ]
$H_n$	Height of the nozzle from the disk [m]
$k$	Thermal conductivity [ $\text{W} / \text{m K}$ ]
$n$	Coordinate normal to the free surface [m]
$Nu$	Nusselt number, $2 h r_o / k_f$
$p$	Pressure [Pa]
$Pr$	Prandtl number, $m c_p / k_f$

$q$	Heat flux [ $\text{W} / \text{m}^2$ ]
$r$	Radial coordinate [m]
$r_n$	Radius of the nozzle [m]
$r_o$	Radius of the disk [m]
Re	Reynolds number, $2r_n v_j / \nu_f$
$T$	Temperature [K]
$\bar{T}$	Average temperature [K]
$T_j$	Jet temperature [K]
$v_j$	Jet velocity [m / s]
$v_r$	Radial velocity [m / s]
$v_t$	Velocity along the free surface [m / s]
$v_z$	Axial velocity [m / s]
$z$	Axial coordinate [m]

#### **Greek Symbols**

$\delta$	Liquid film thickness [m]
$\mu$	Dynamic viscosity of fluid [ $\text{kg} / \text{m s}$ ]
$\nu$	Kinematic viscosity [ $\text{m}^2 / \text{s}$ ]
$\Theta$	Dimensionless temperature, $(T - T_j)k_f / q r_n$
$\rho$	Density [ $\text{kg} / \text{m}^3$ ]
$\sigma$	Surface tension coefficient [ $\text{N} / \text{m}$ ]

#### **Subscripts**

atm	Atmospheric condition
av	Average
f	Fluid
int	Solid - fluid interface
max	Maximum
s	Solid

## **CONCLUSIONS**

A numerical model of conjugate heat transfer process where heat is transmitted through a solid body from a heat source located on one side to a free fluid jet impinging on the opposite side has been solved. The variation of fluid properties with temperature has been taken into account. The effects of submerging the free surface jet was investigated. It was found that the film thickness decreases as the impingement velocity increases. The heat transfer coefficient showed a strong dependence on the impingement velocity; increasing in value as the velocity increased. The temperature at the solid-fluid interface decreased as the velocity increased. As the thickness of the disk was varied, the interface temperatures and heat transfer coefficients varied. The thermal conductivity of the disk material strongly affected the magnitude of maximum temperature in the solid, temperature difference at the interface, and heat transfer coefficient. It was found that a lower thermal conductivity in the solid results in slightly higher heat transfer coefficient, whereas a higher thermal conductivity material will maintain the disk at a lower temperature. Impingement height was found to be inversely proportional to

interface temperature for the submerged free surface jet , while for the unsubmerged jets, higher interface temperatures were generally observed for higher impingement heights. A crossover effect was observed in the case of different disk materials with thermal conductivity playing a critical role in controlling the interface temperature and heat transfer coefficient.

Table 4. Comparison of average heat transfer coefficient with experimental data of Leland [63]

Re	Heat Flux kW /m <sup>2</sup>	Average Heat Transfer Coefficient (Numerical) kW /m <sup>2</sup> K	Average Heat Transfer Coefficient (Experimental) kW /m <sup>2</sup> K	Percent Difference %
550	63	4.26	3.93	8.4
1100	63	7.28	6.74	8.1
Material : Copper, b=0.005m, H <sub>n</sub> = 0.0085m, r <sub>n</sub> =0.00085m				
550	63	10.27	9.68	5.74
1100	63	13.58	12.75	6.12
Material : Copper, b=0.005m, H <sub>n</sub> = 0.0001m, r <sub>n</sub> =0.00085m				

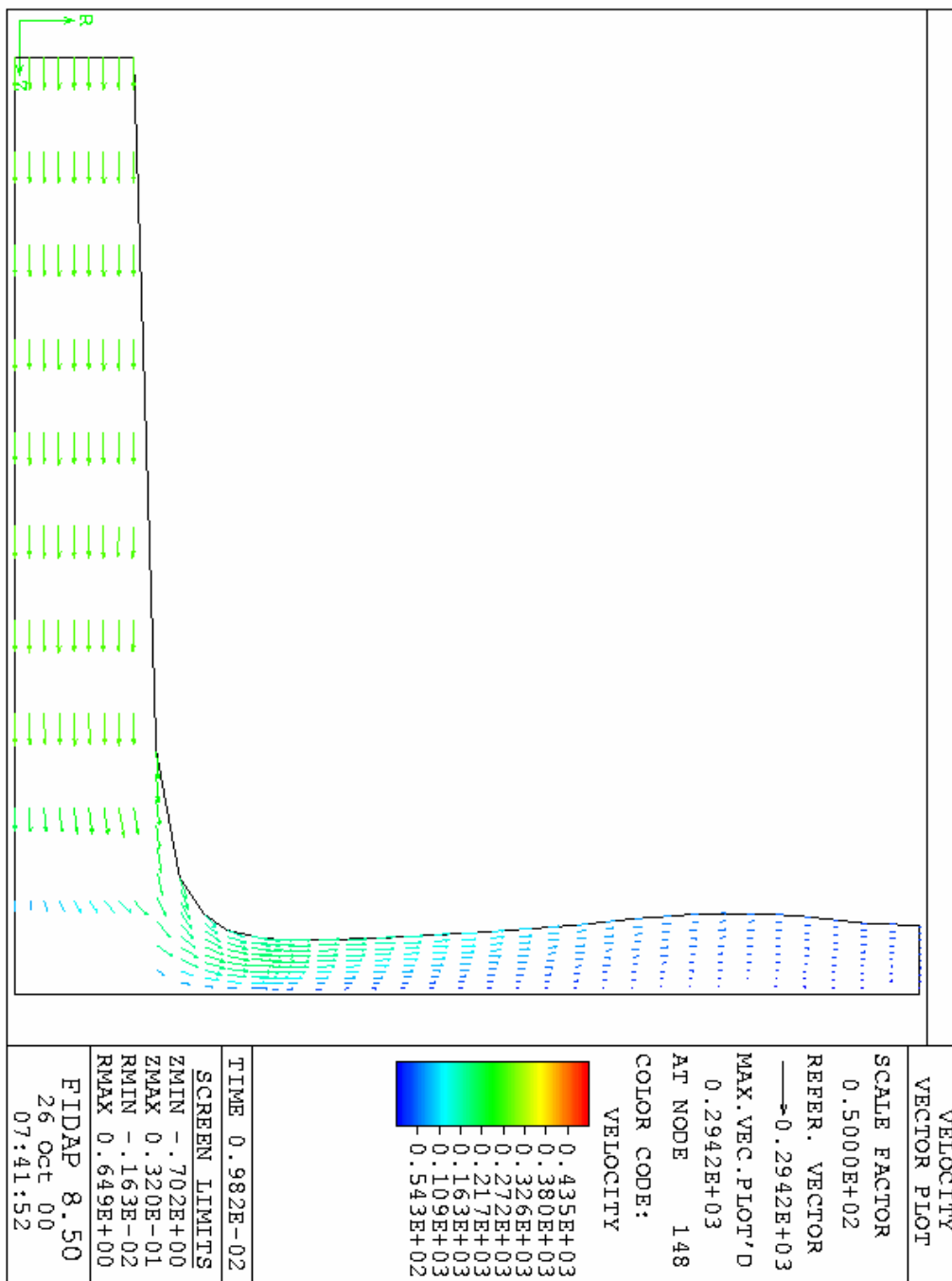


Figure 74. Converged free surface shape  
( $Re = 1400$ ,  $H_n = 0.0067m$ )

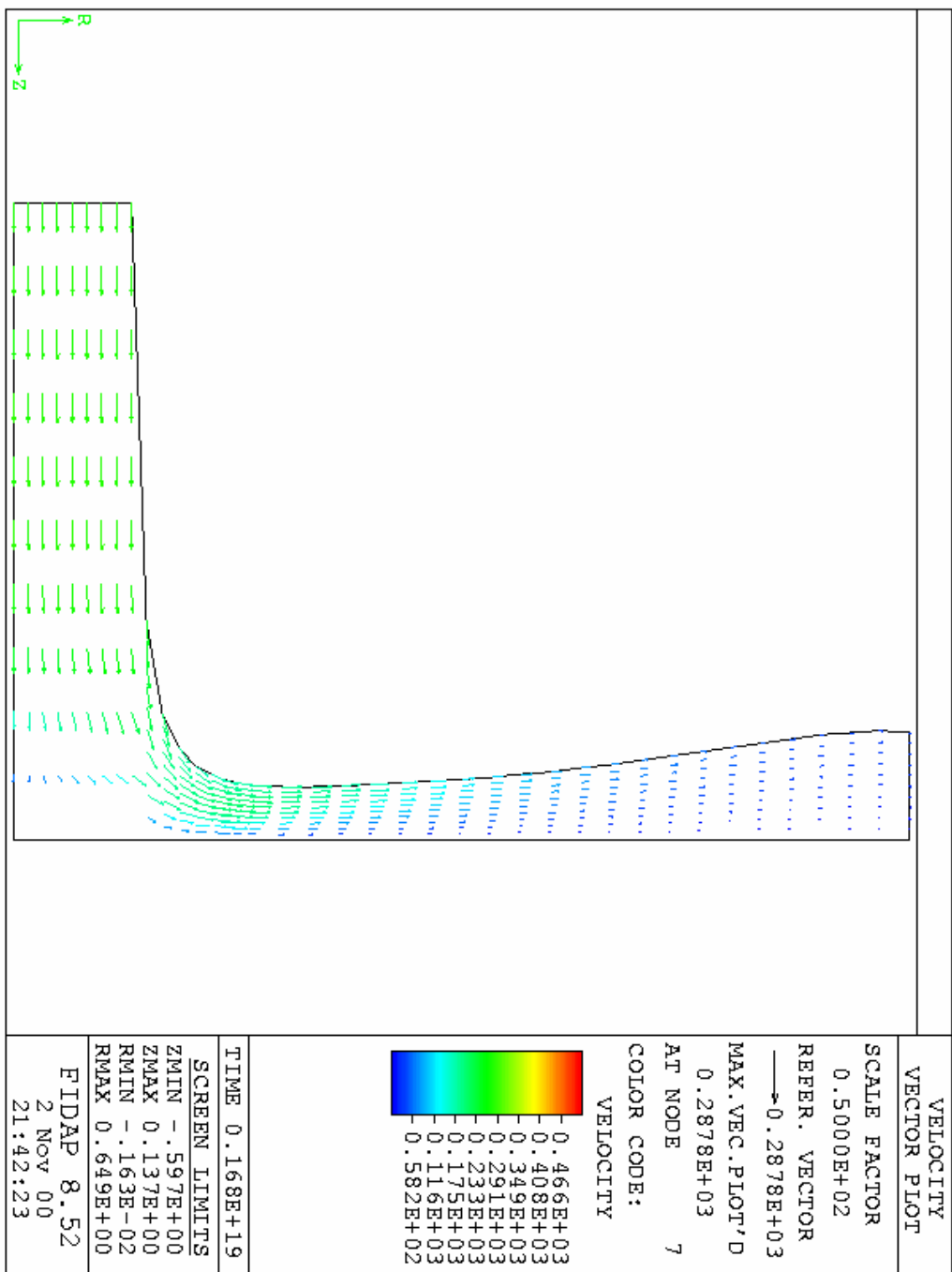


Figure 75. Converged free surface shape  
( $Re = 1400$ ,  $H_n = 0.0046m$ )

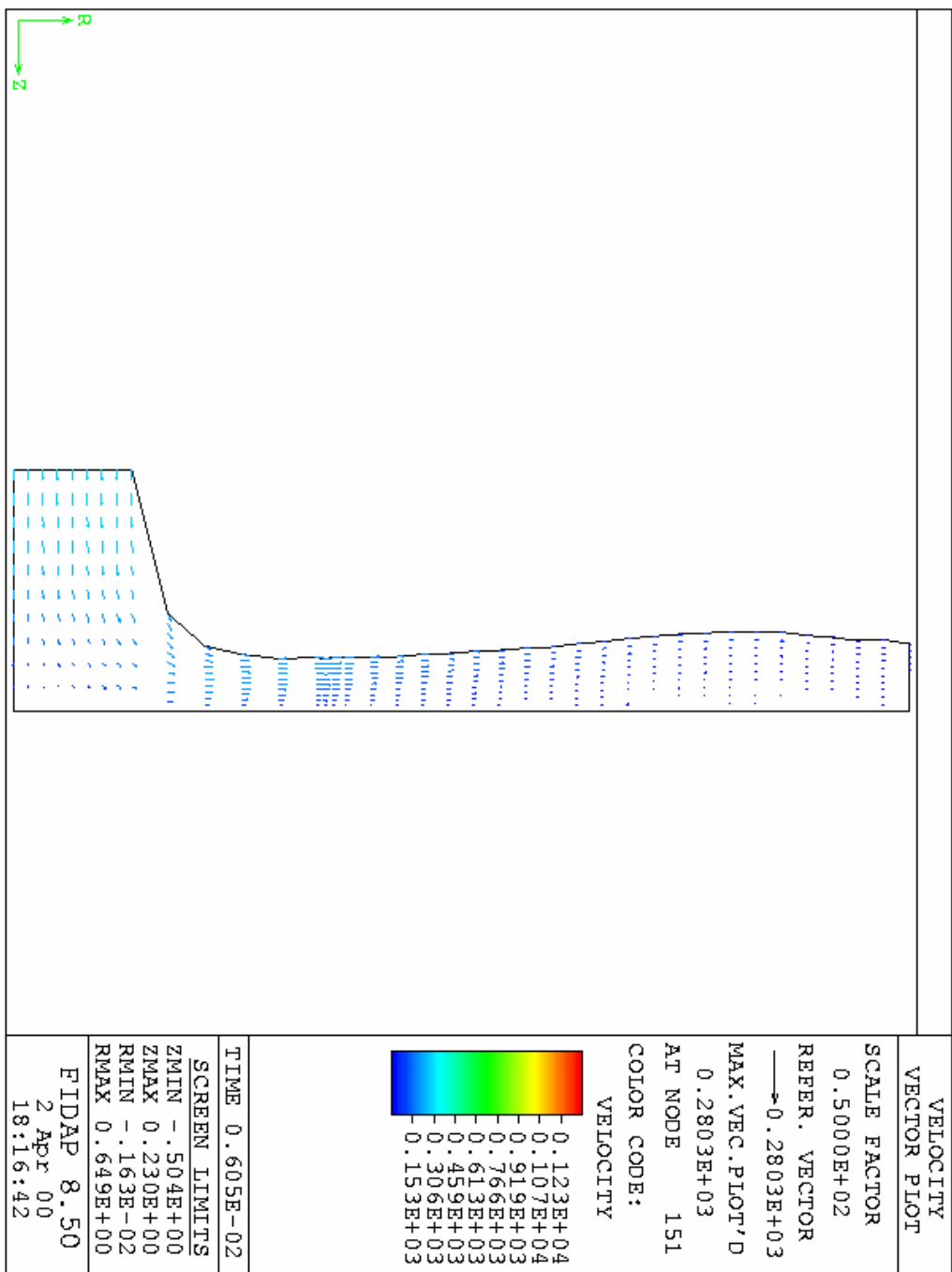


Figure 76. Converged free surface shape  
( $Re = 1400$ ,  $H_n = 0.00175m$ )

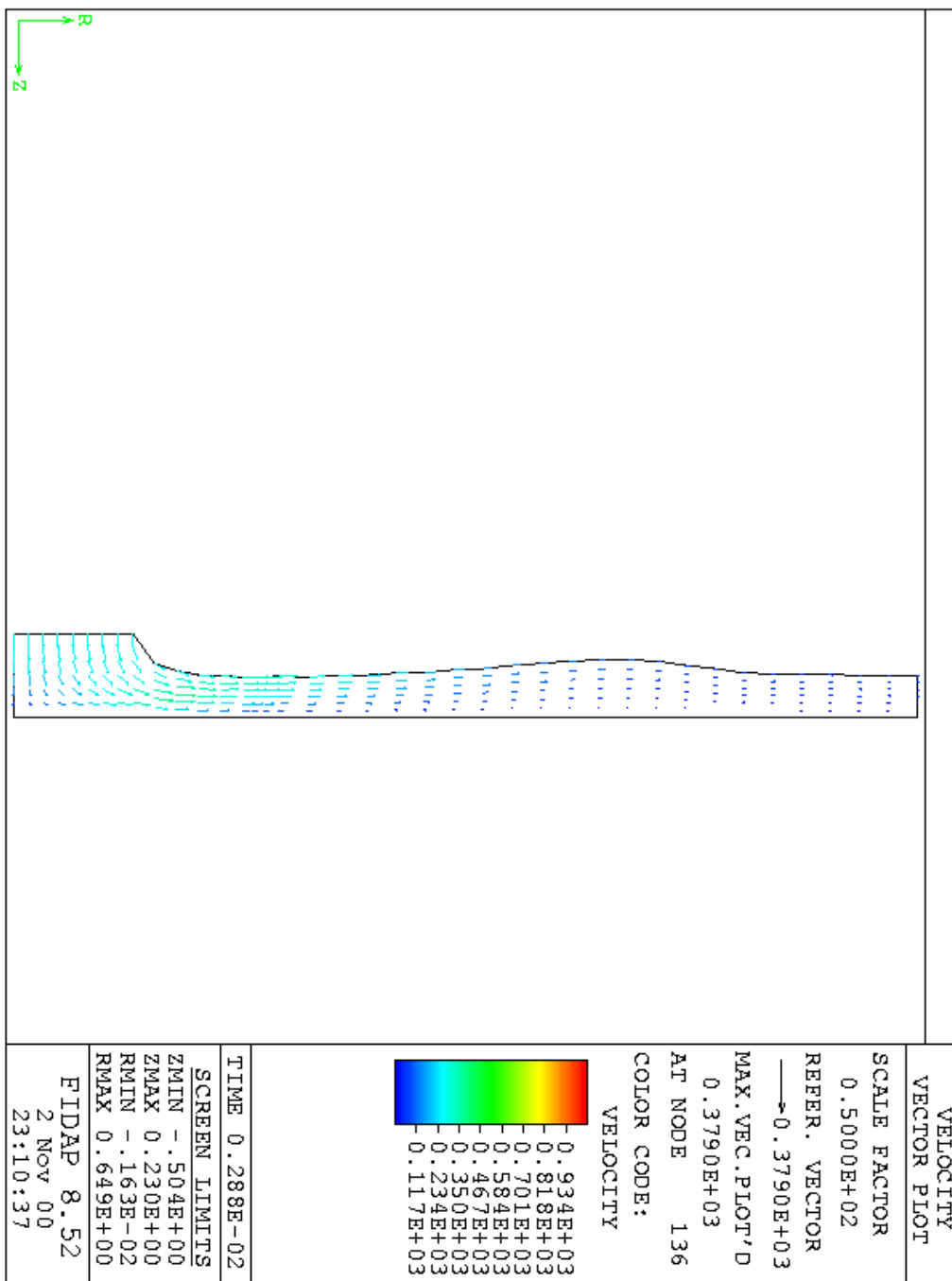


Figure 77. Converged free surface shape  
( $Re = 1400$ ,  $H_n = 0.0006m$ )

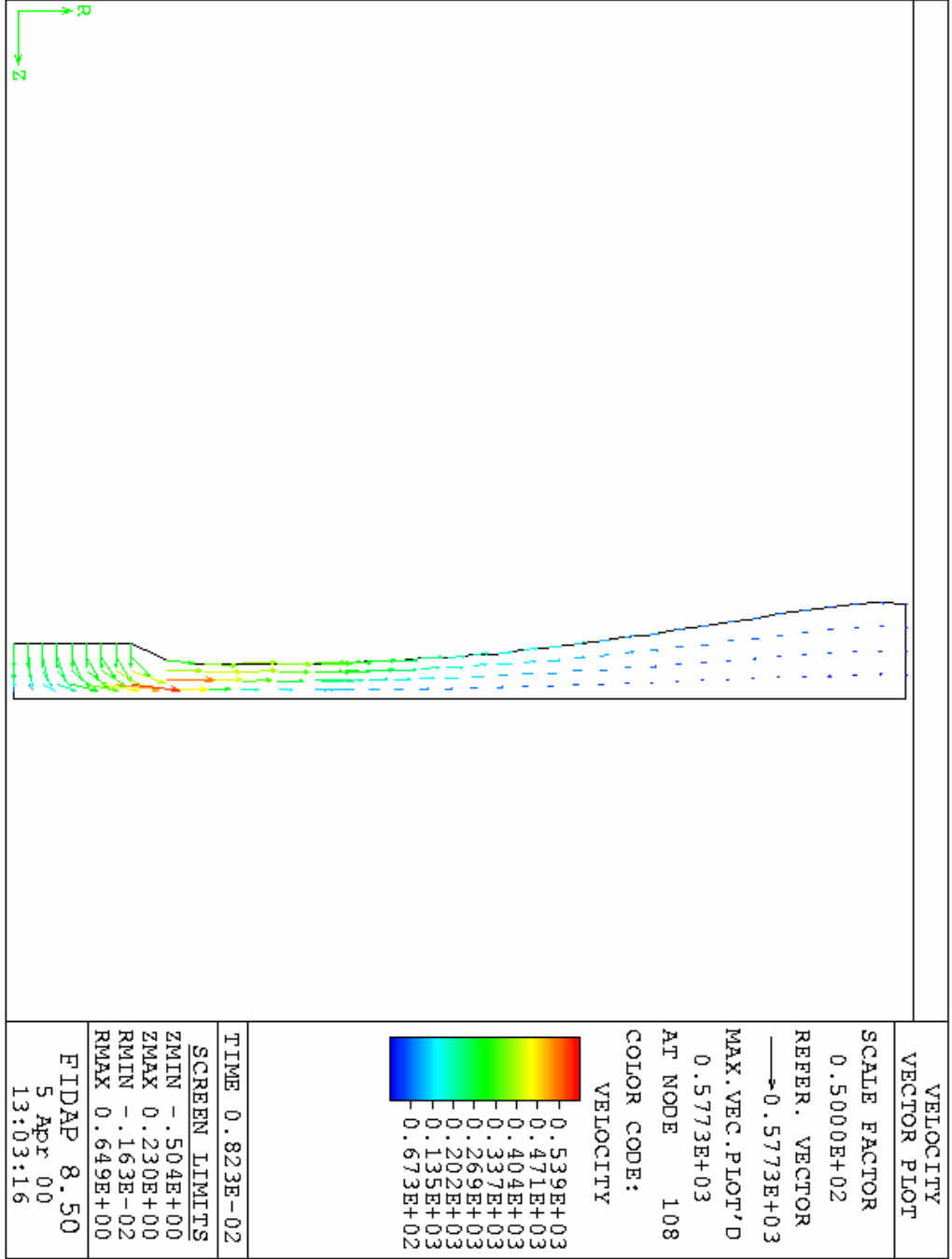


Figure 78. Converged free surface shape  
( $Re = 1400$ ,  $H_n = 0.0004m$ )



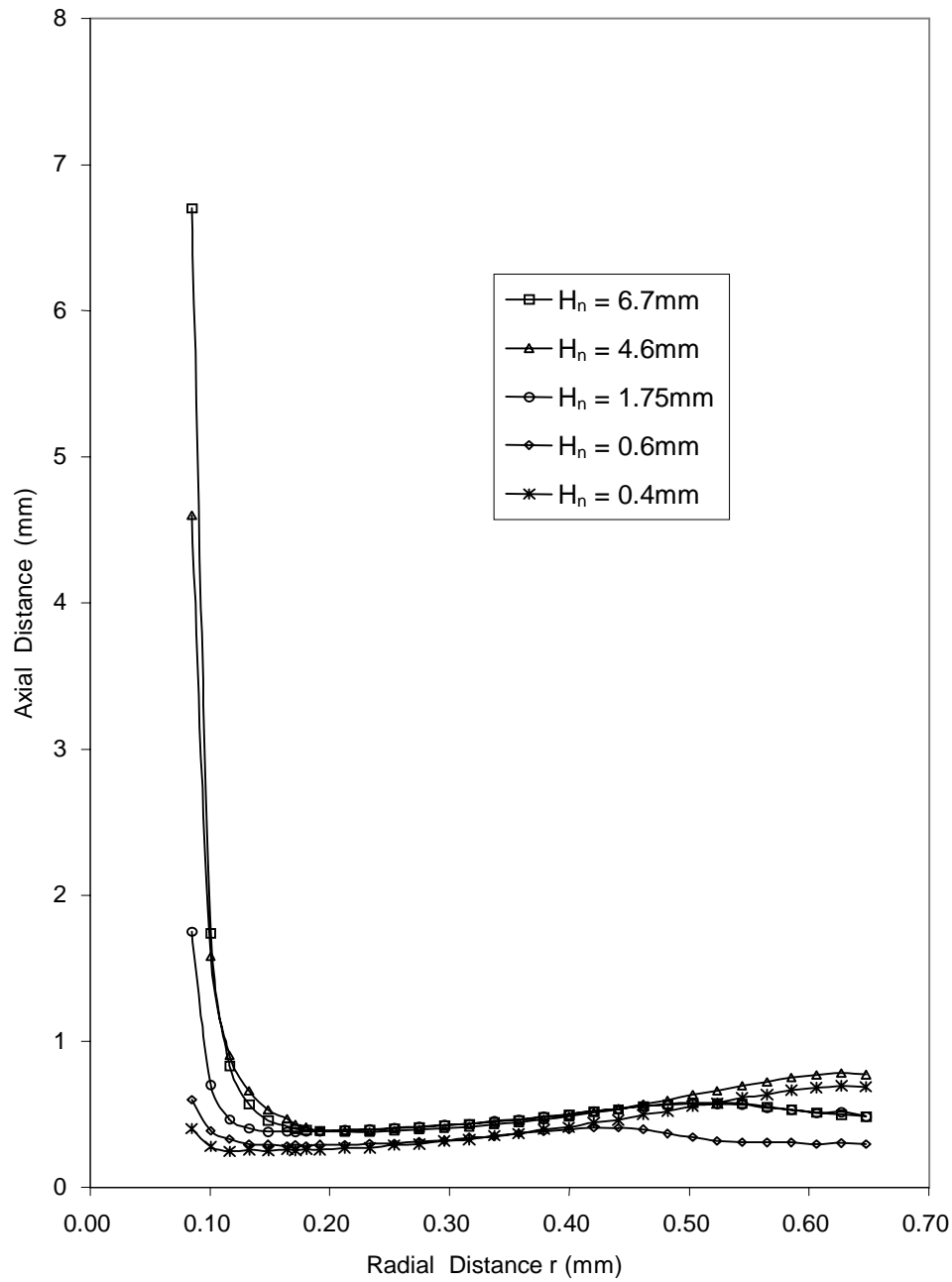


Figure 79. Converged free surface for different nozzle to plate impingement heights ( $Re = 1400$ )

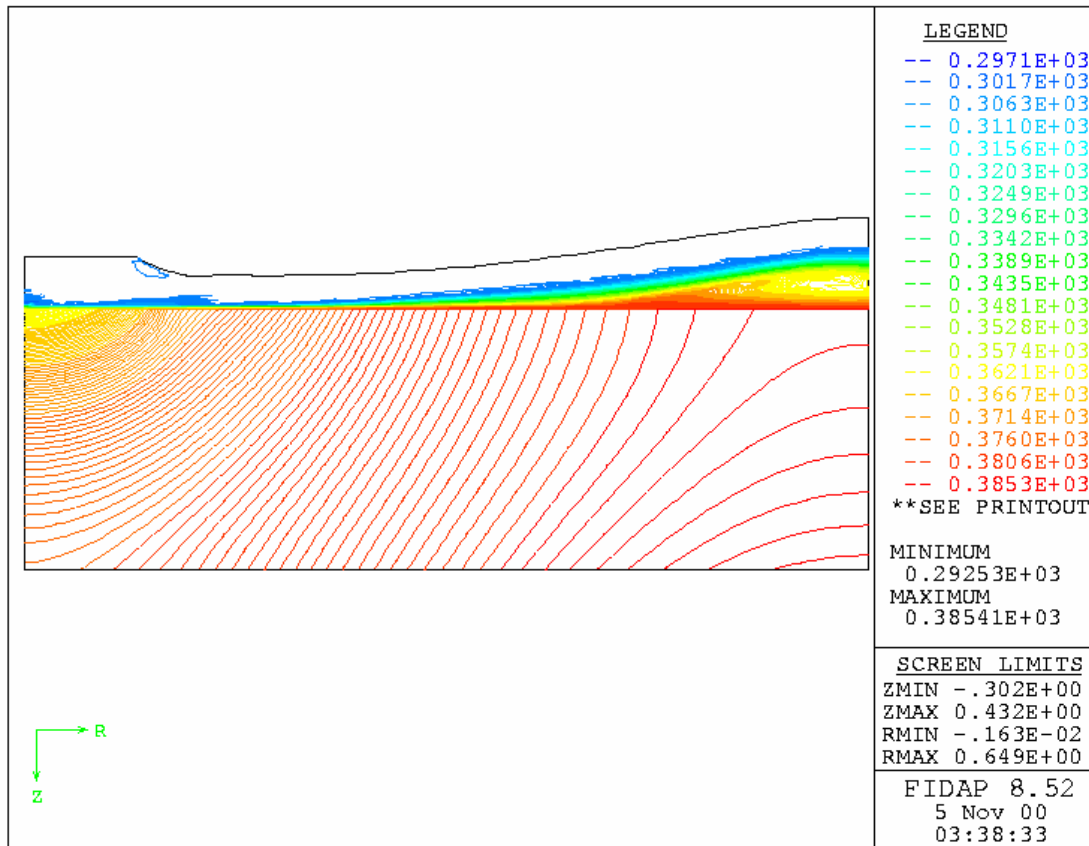


Figure 80. Temperature contour plot over the whole conjugate domain  
( $Re = 1400$ ,  $H_n = 0.0004\text{m}$ ,  $b = 2\text{mm}$ , fluid = Mil-7808, solid = silicon )

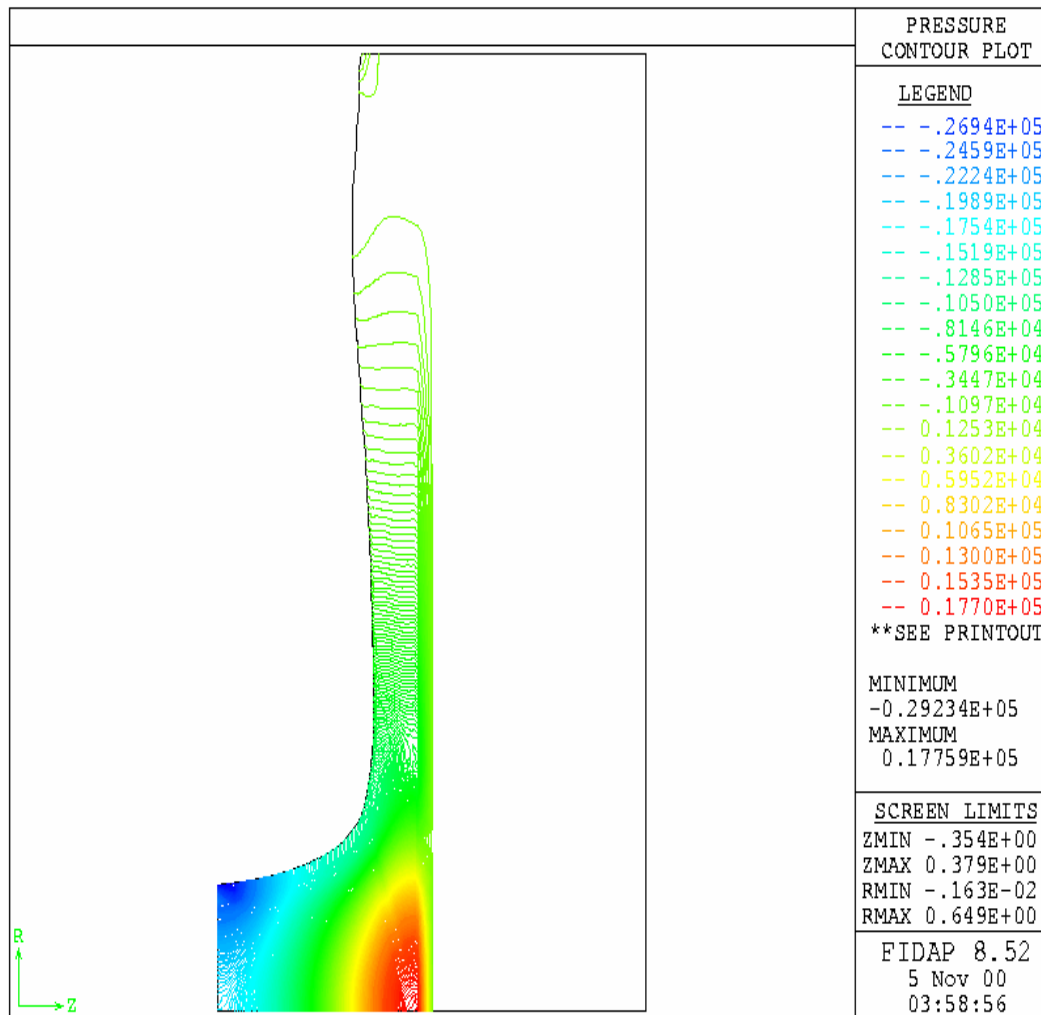


Figure 81. Pressure contour plot over the conjugate domain  
( $Re = 1400$ ,  $H_n = 0.00175m$ )

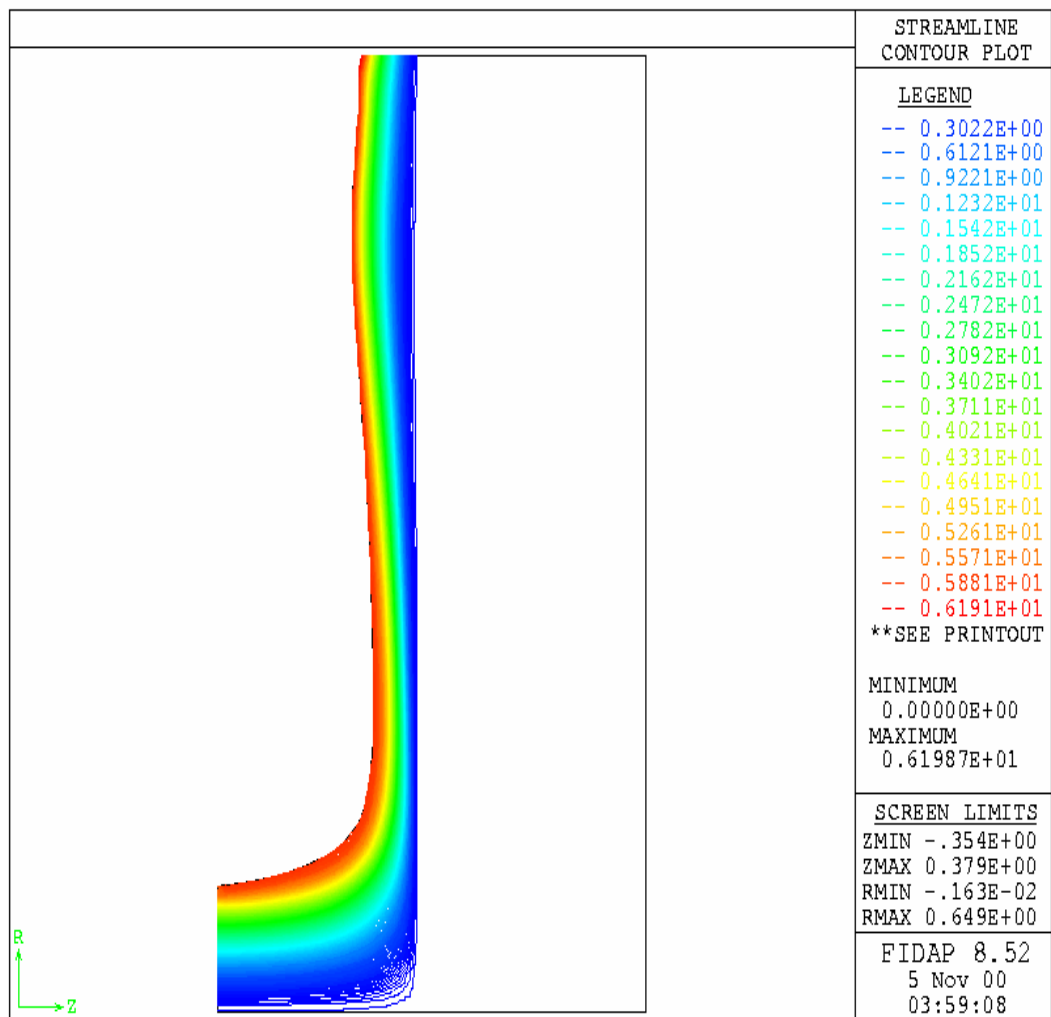


Figure 82. Streamline contour plot  
( $Re = 1400$ ,  $H_n = 0.00175m$ )

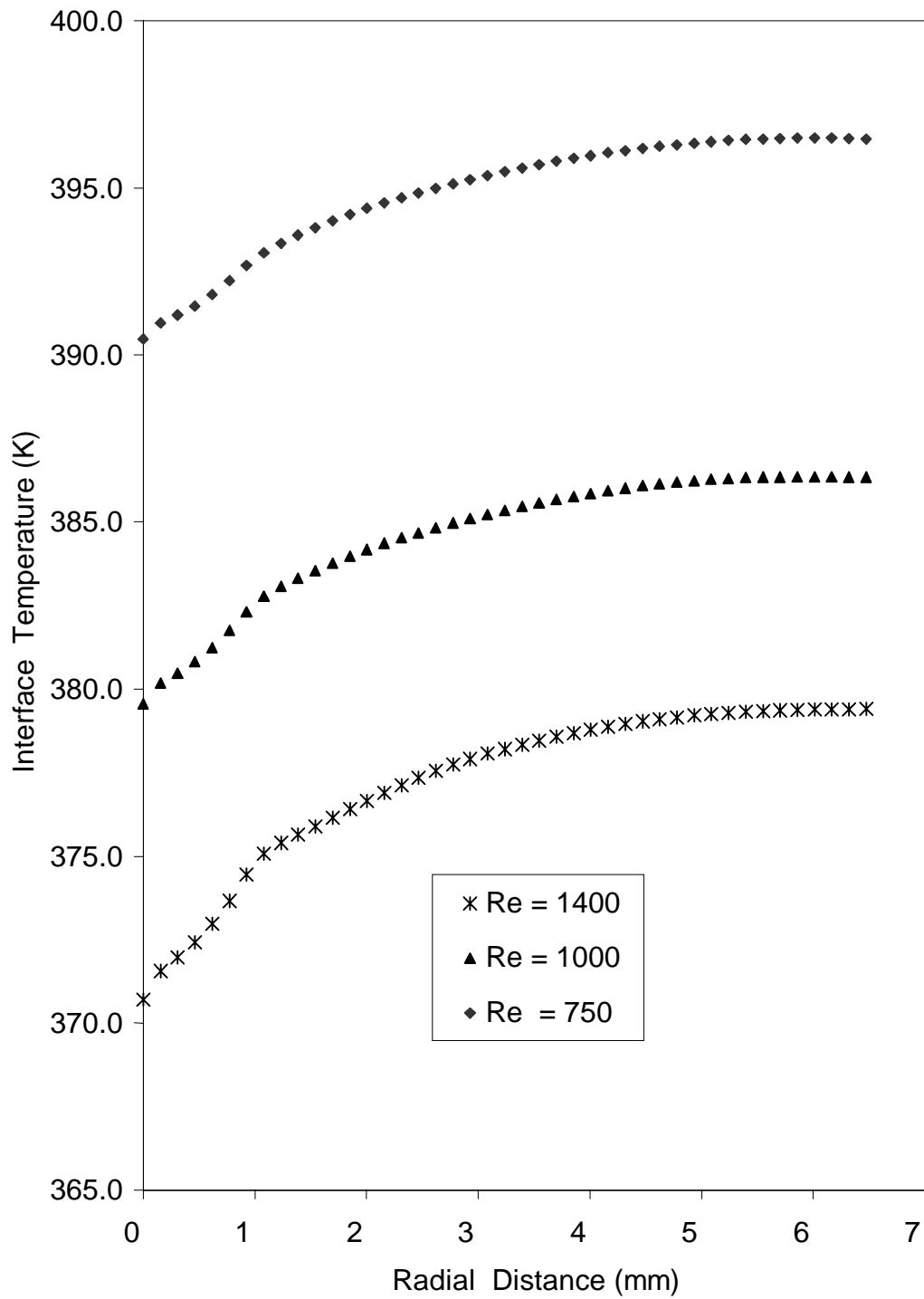


Figure 83. Temperature distribution at the solid-fluid interface for different Reynolds numbers ( $H_n = 0.0004$  m, solid = copper,  $b = 2$  mm)

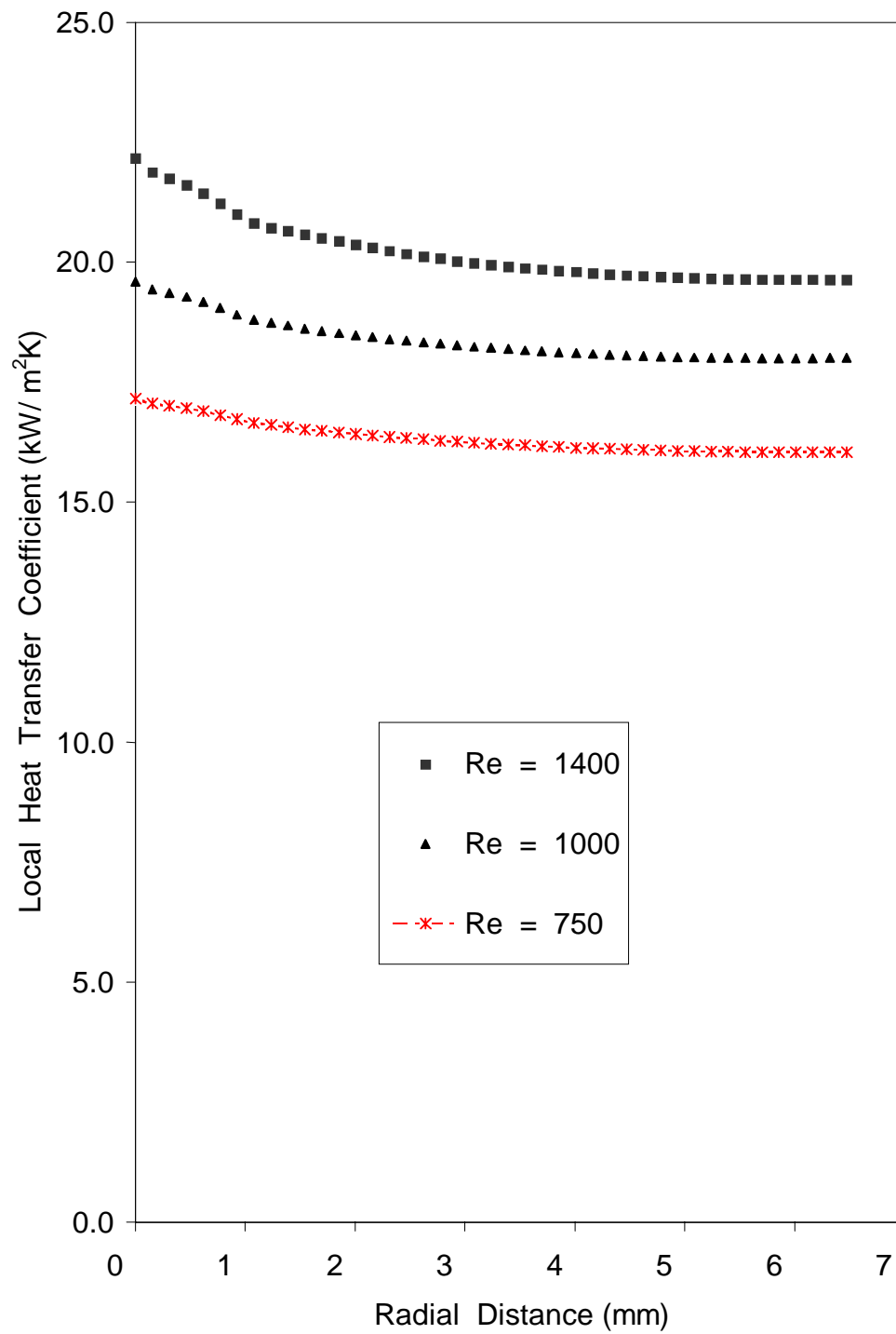


Figure 84. Local heat transfer coefficient at the solid-fluid interface for different Reynolds numbers ( $H_n = 0.0004$  m, solid = copper,  $b = 2$  mm)

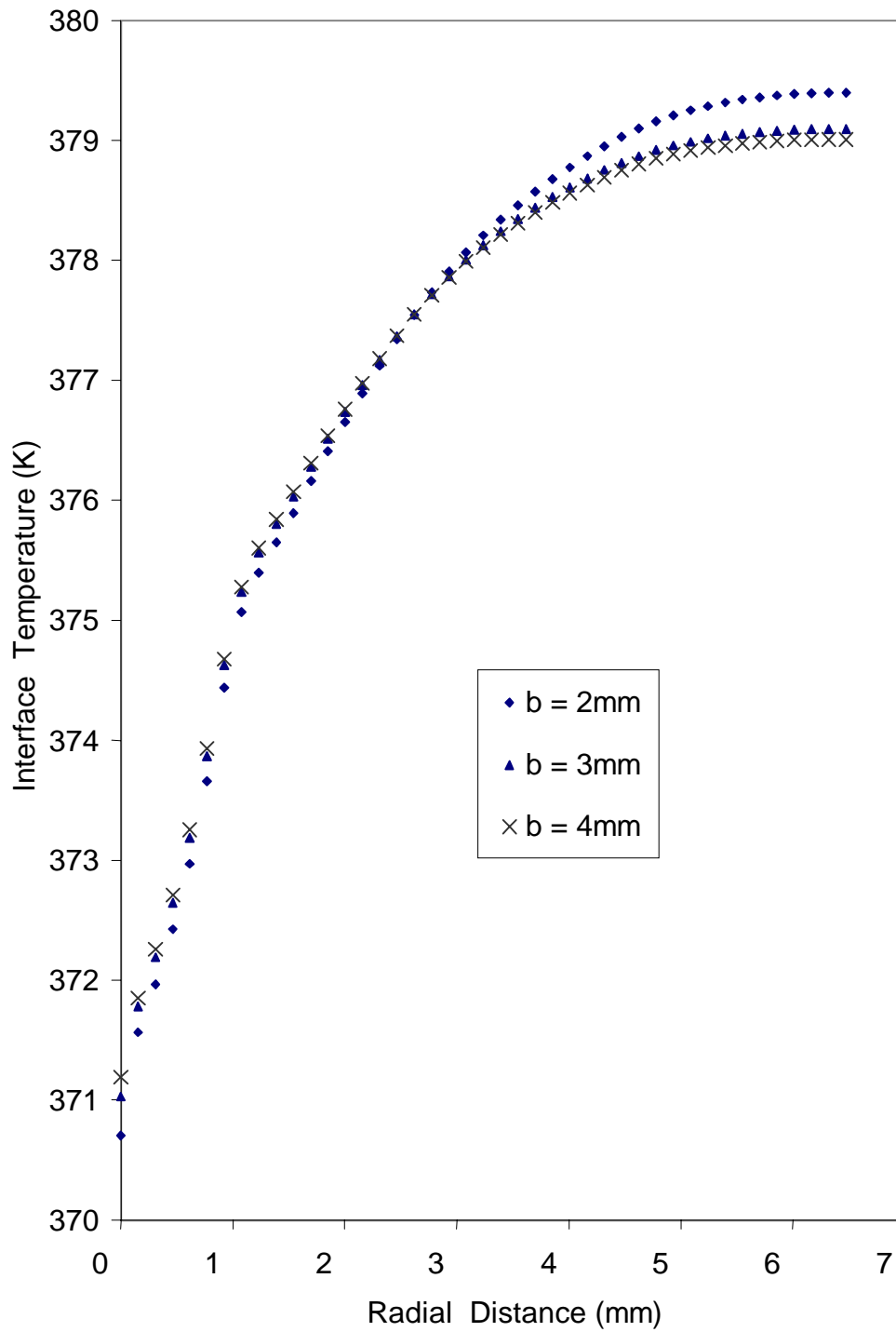


Figure 85. Temperature distribution at the fluid-solid interface for different solid thicknesses  
( $Re = 1400$ ,  $H_n = 0.0004\text{m}$ , solid material = copper)

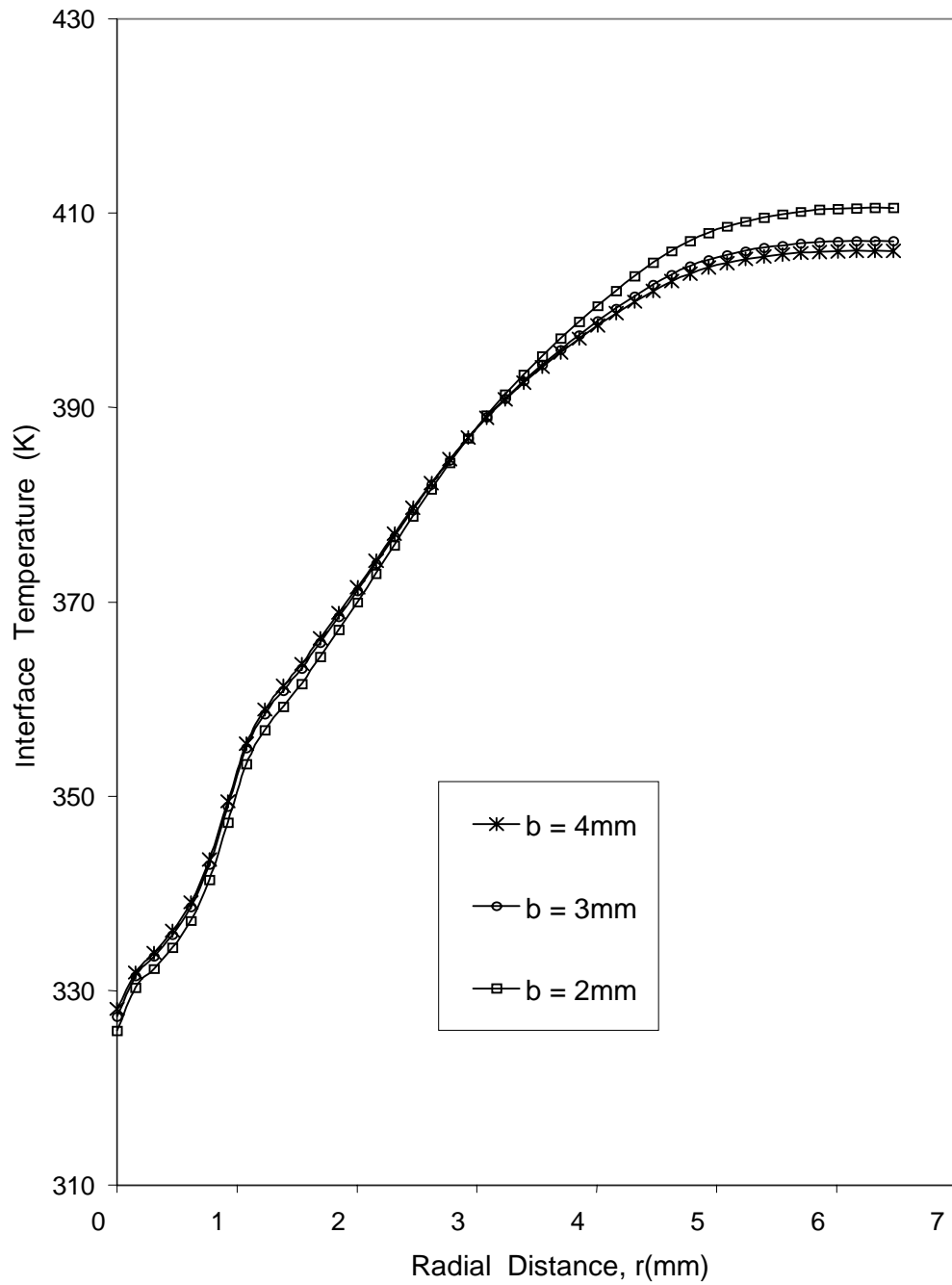


Figure 86. Temperature distribution at the solid-fluid interface for different thicknesses  
( $Re = 1400$ ,  $H_n = 0.0004\text{m}$ , solid material = constantan)



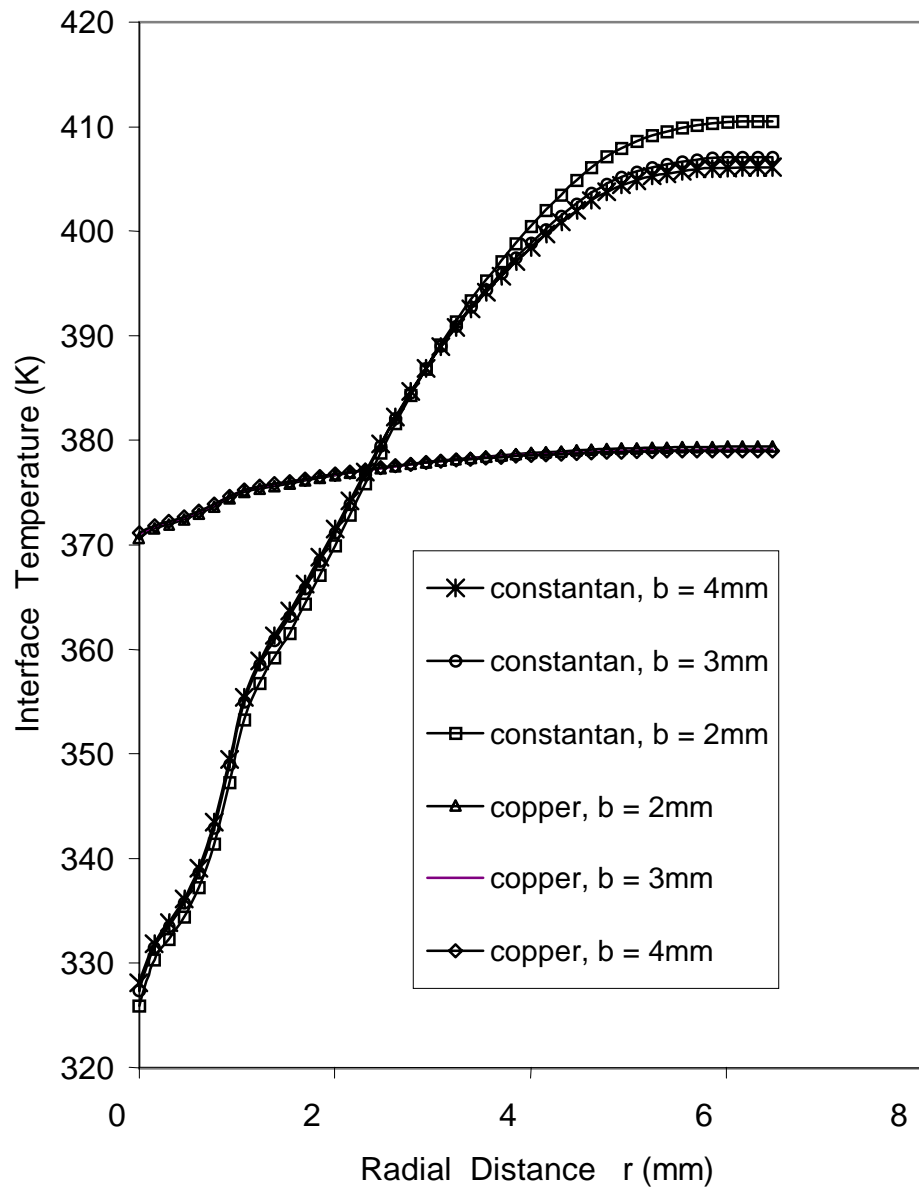


Figure 87. Comparison of temperature distribution at the solid-fluid interface for different thicknesses ( $Re = 1400$ ,  $H_n = 0.0004\text{m}$ ,  $q = 62\text{ kW/m}^2$ )

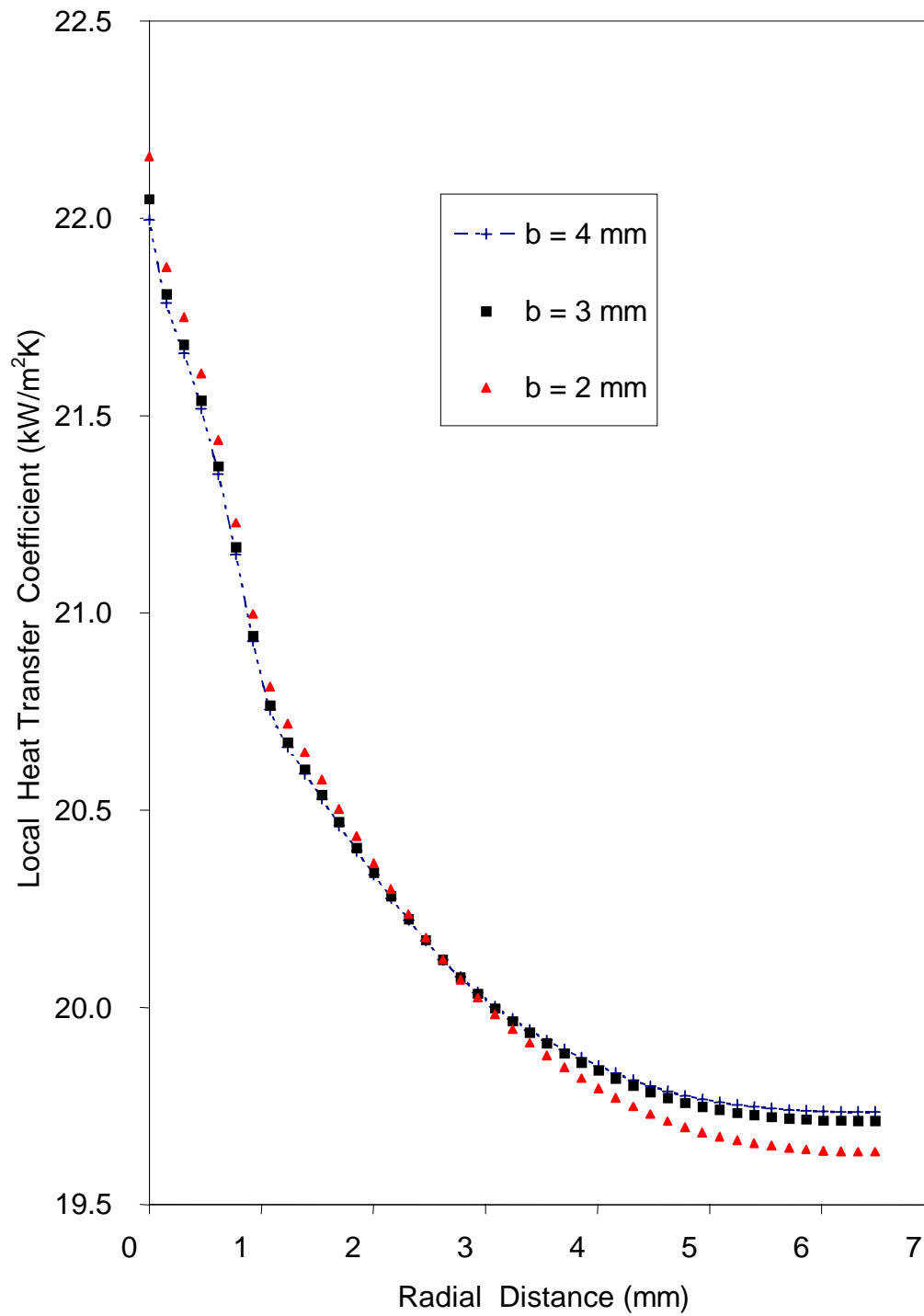


Figure 88. Local heat transfer coefficient at the solid-fluid interface for different thicknesses  
(  $Re = 1400$ ,  $H_n = 0.0004$ m, solid material = copper )

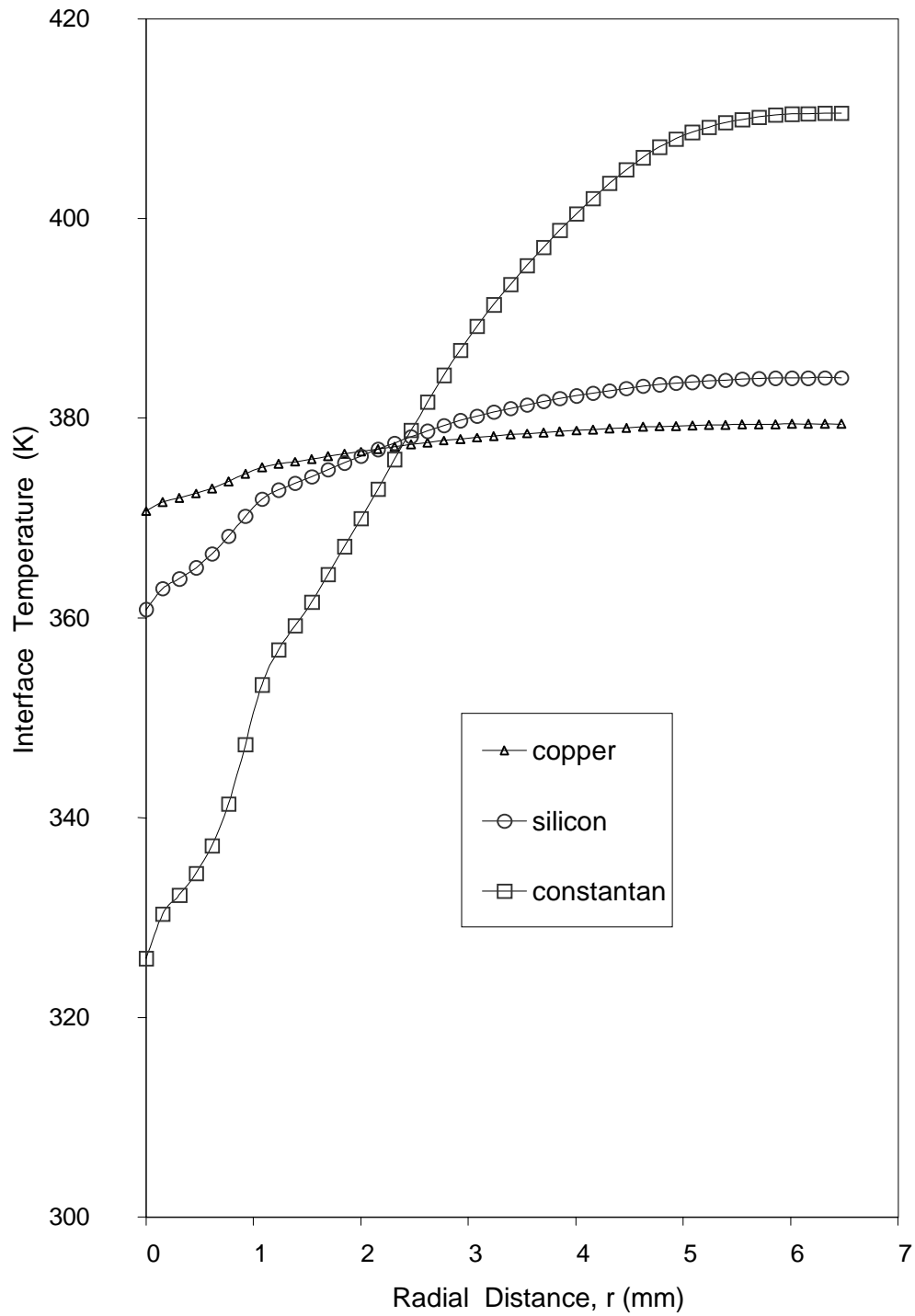


Figure 89. Local temperature distribution at the solid-fluid interface for different solid materials  
 (  $Re = 1400$ ,  $H_n = 0.0004$  m,  $b = 2$  mm)

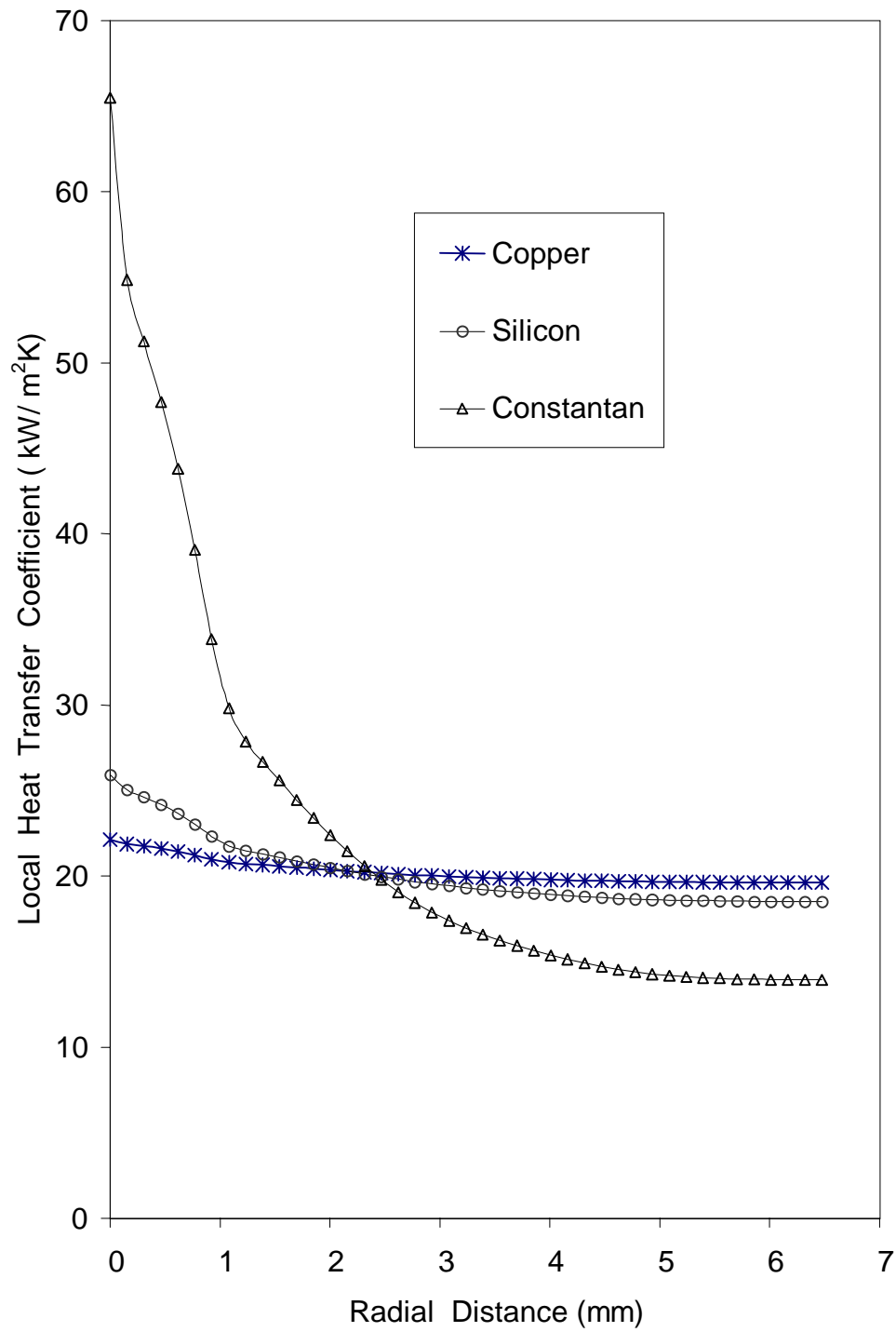


Figure 90. Local heat transfer coefficient at the solid-fluid interface for different solid materials  
 (  $Re = 1400$ ,  $H_n = 0.0004$  m,  $b = 2$  mm)

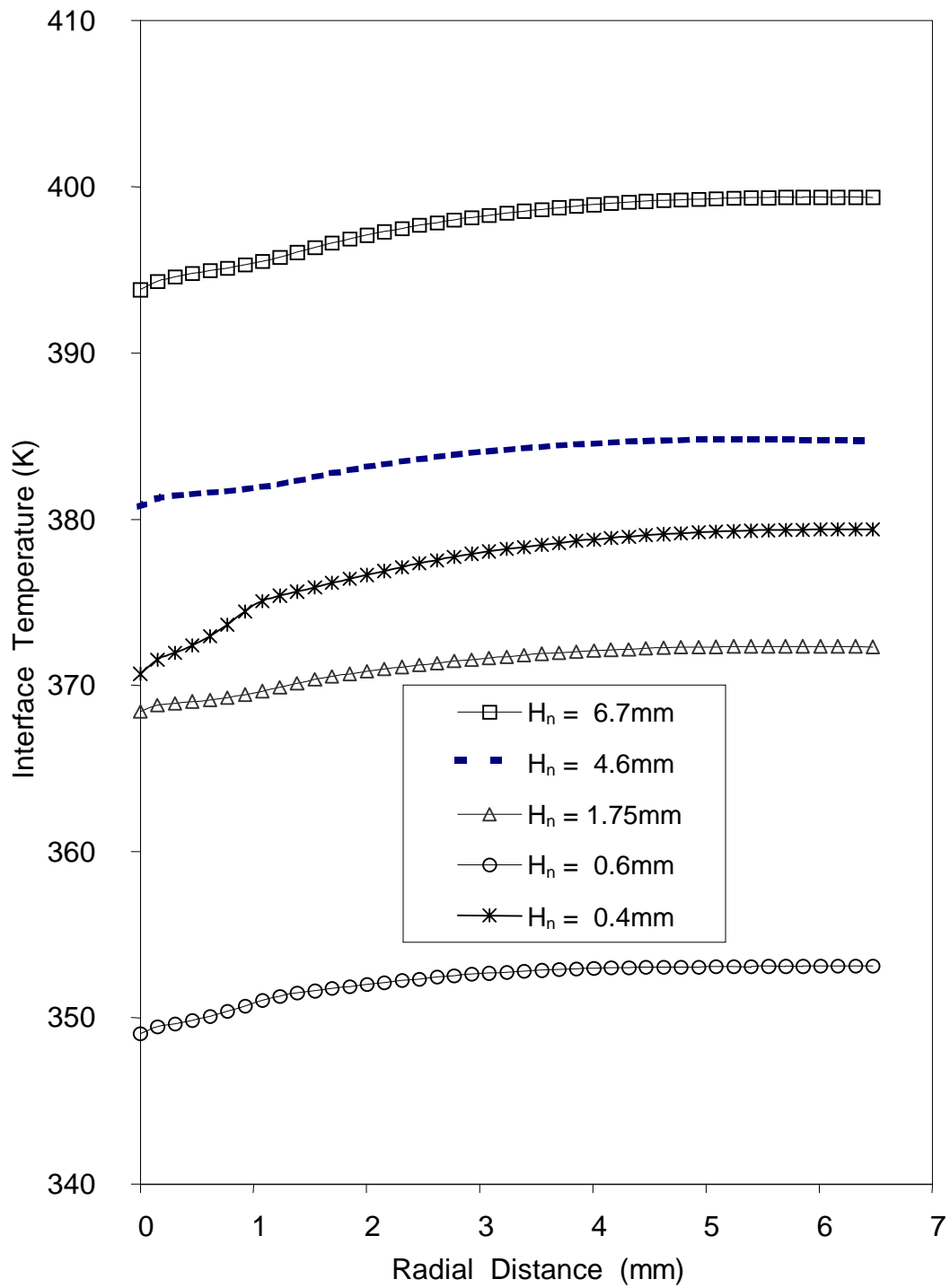


Figure 91. Local temperature distribution at the solid-fluid interface for five different impingement heights (Re = 1400, b = 2 mm, solid material = copper)

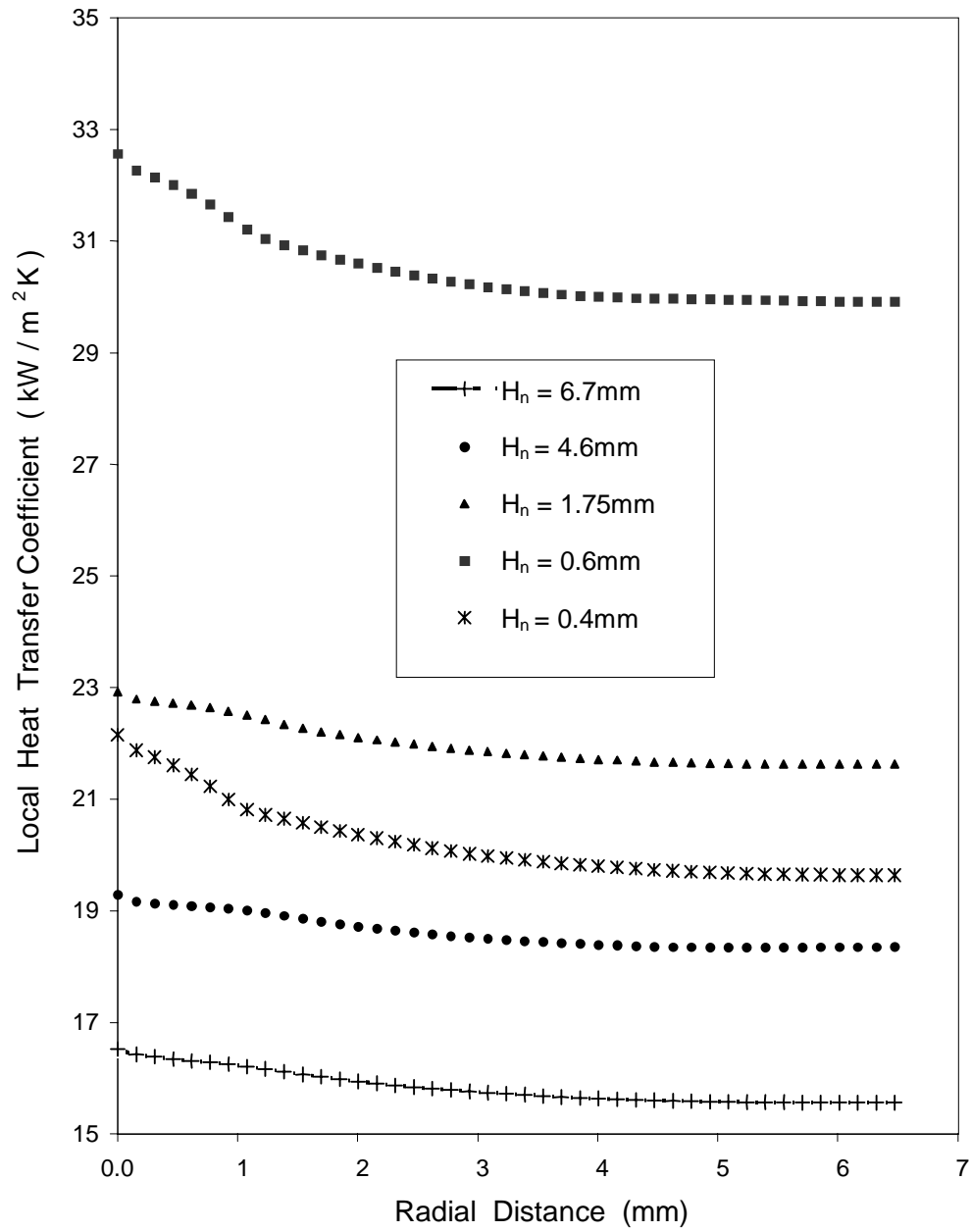
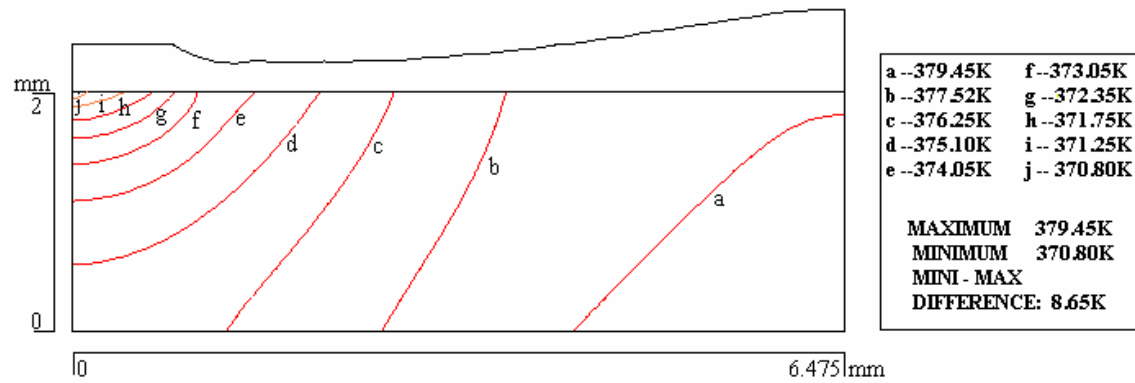
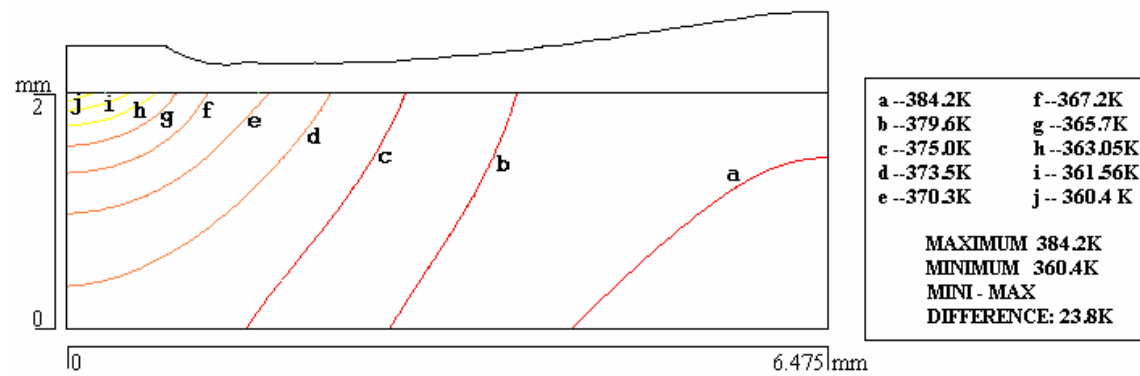


Figure 92. Local heat transfer coefficient at the solid-fluid interface for five different impingement heights (Re = 1400, b = 2 mm, solid material = copper)

### copper



### silicon



### constantan

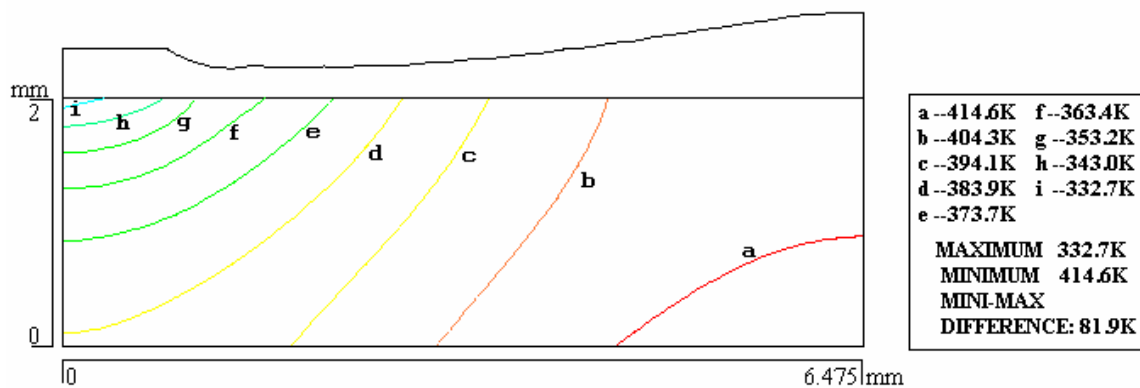
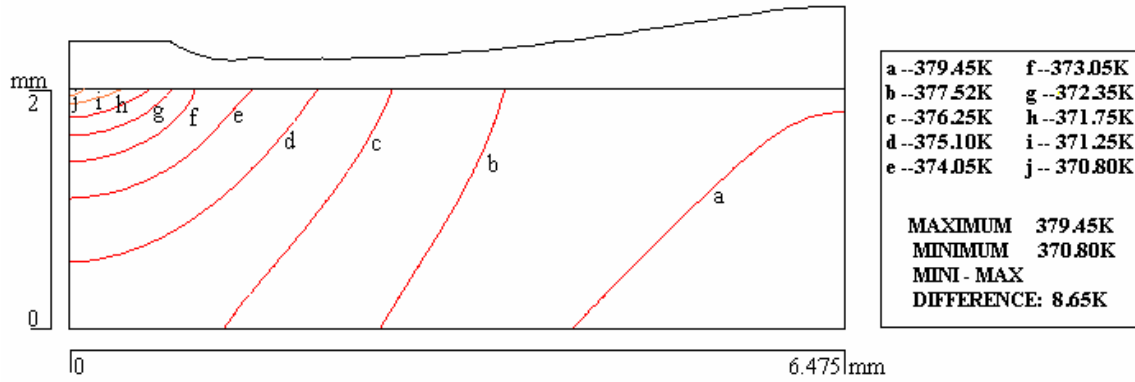
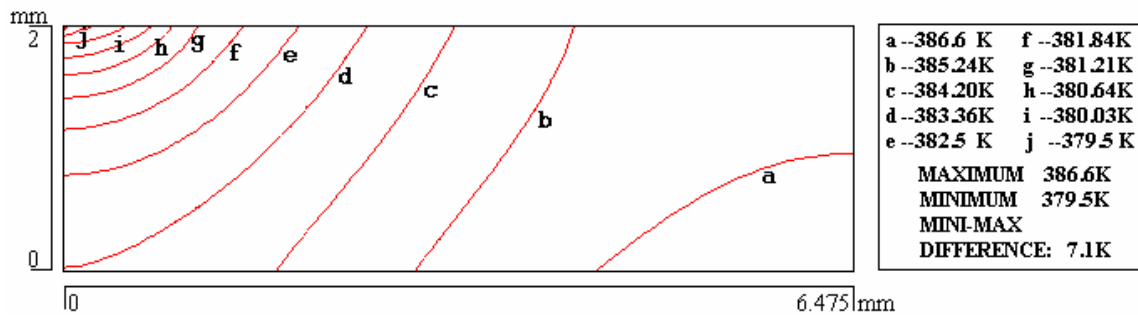


Figure 93. Solid temperature contours for three different materials  
( $H_n = 0.4$  mm,  $b = 2$  mm,  $Re = 1400$ )

Re = 1400



Re = 1000



Re = 750

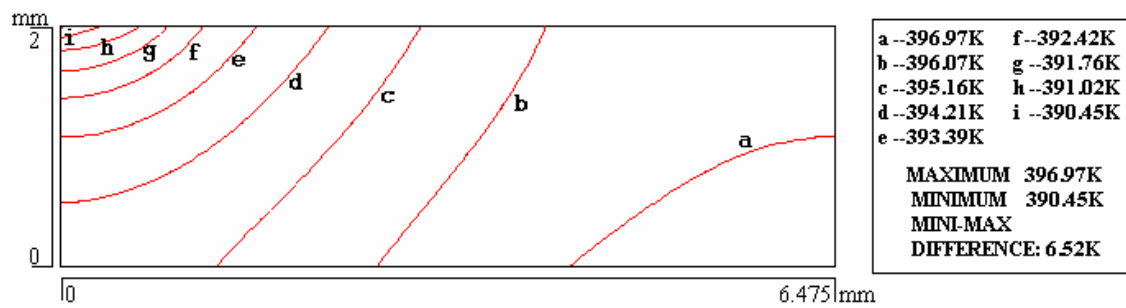


Figure 94. Solid temperature contours for three different Reynolds number ( $H_n = 0.4$  mm,  $b = 2$  mm, material = copper)



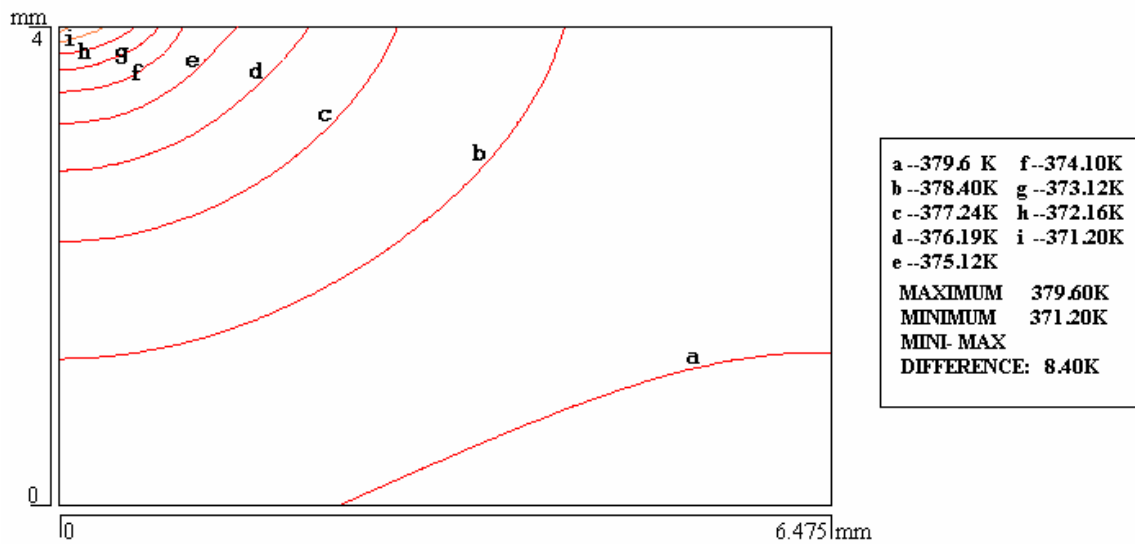
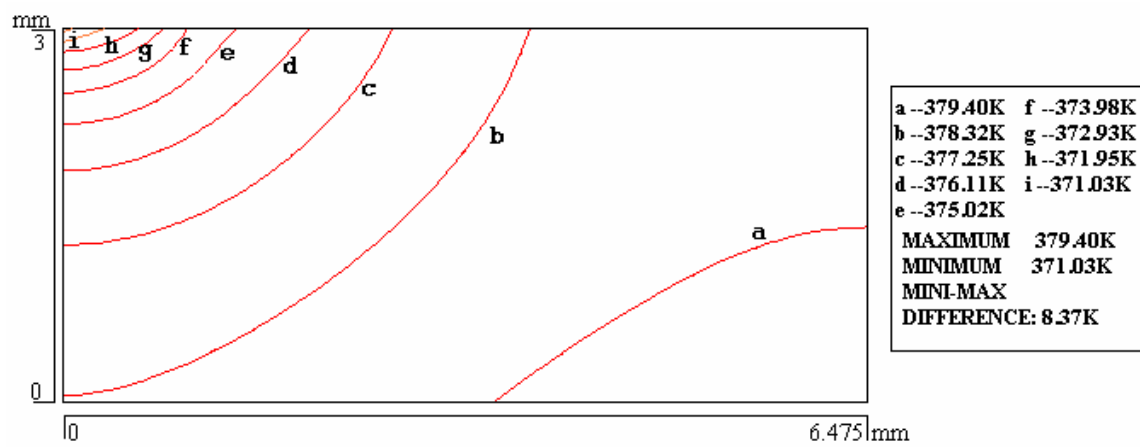
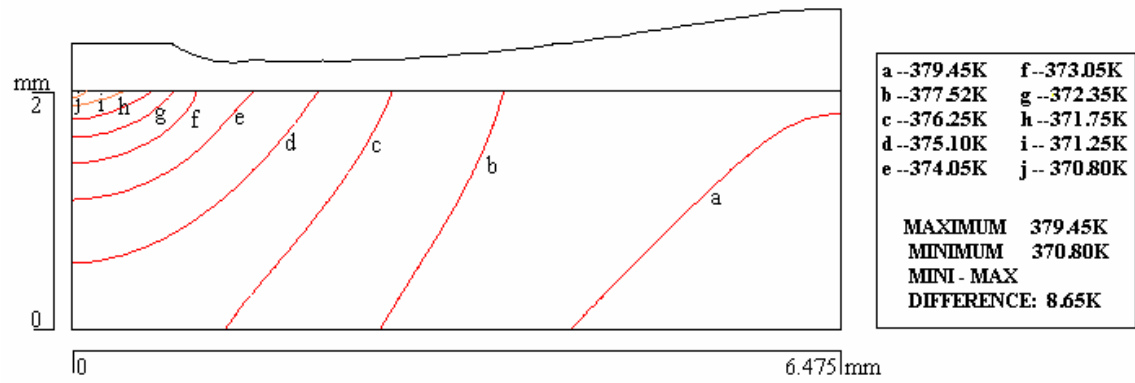
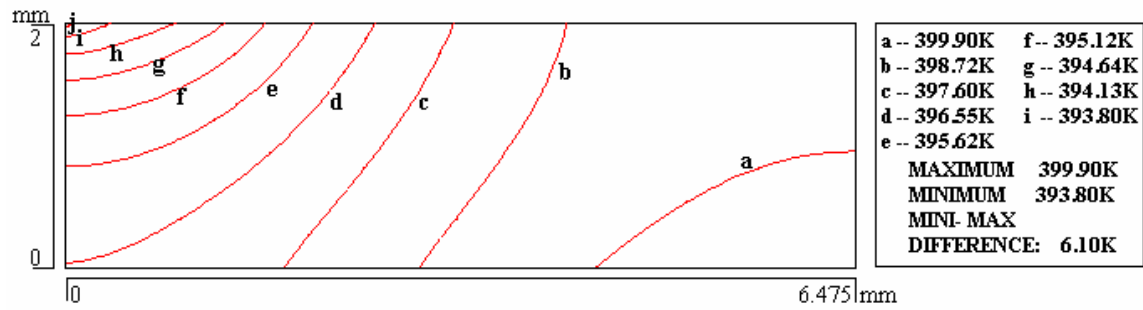
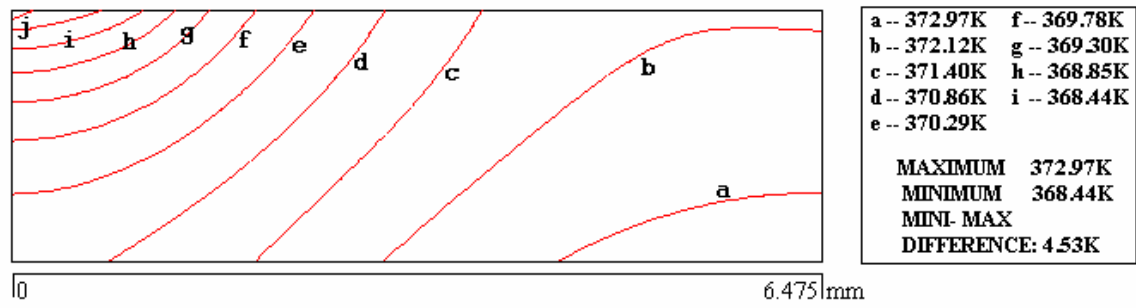


Figure 95. solid temperature contours for three different disk thicknesses  
( $Re = 1400$ , solid material = copper,  $H_n = 0.0004$  m)

$H_n = 4.6 \text{ mm}$



$H_n = 1.75 \text{ mm}$



$H_n = 0.4 \text{ mm}$

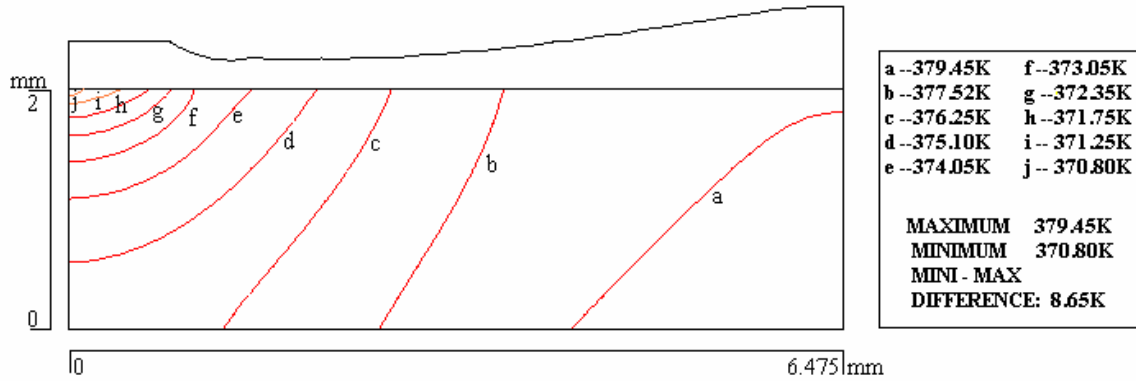


Figure 96. Solid temperature contours for three impingement heights  
( $Re = 1400$ , solid material = copper,  $b = 2 \text{ mm}$ )

# **RADIAL FREE JET IMPINGING ON A UNIFORMLY HEATED DISK: STEADY STATE**

## **INTRODUCTION**

For its relatively high heat transfer coefficient, impinging jets are becoming of great interest in many industrial applications such as paper drying process and electronics cooling. Jet impingement can be classified into several groups based on the flow Reynolds number, nozzle geometry, and the direction at which the flow impinges on the plate. Based on the Reynolds number, jets are classified into laminar and turbulent jets. The nozzle geometry determines whether a jet is rectangular (slot) or circular (round). In addition, a circular jet can be an axially impinging jet or a radially impinging jet. Any of these jets can be designed with submerged, confined, or free impingement configuration.

Extensive experimental, analytical, and numerical work has been carried out to characterize the fluid flow and heat transfer process in the submerged and confined impinging jets. A much fewer number of studies has been done on the free liquid jet and it was mainly experimental and for the axial impinging jet. Azuma and Hoshino [64] used LDV to measure the depth of the liquid layer of the spreading flow when liquid is discharged from an axisymmetric axial nozzle placed very close to a flat surface. They found that the radial film flow begins with a laminar boundary layer and for a much larger Reynolds number it changes to a turbulent boundary layer flow. Rao and Arakeri [65] derived integral equations for the conservation of momentum and energy from the respective governing equations for the general axisymmetric flow of a thin liquid film.

Radially impinging free liquid jets, however, has received almost no attention from numerical researchers because of its complicated flow characteristics. The primary difficulty appears to be the simulation of free surfaces in such a fluid flow configuration. There has been, however, a few studies on submerged radially impinging jet using air as the working fluid (for example, Sayed-Yagoobi et al. [66], Page et al. [67]). Laschefski et al. [68] used a numerical approach to investigate fluid flow and heat transfer for impinging laminar, semienclosed axial and vectored radial air jets. They concluded that the peak local heat transfer coefficient for the axial air jet is larger than that for the radial jet for the same flow rate and nozzle height. However, the average heat transfer for the radial jet is larger than that for the axial jet especially at around 60-degree angle of inclination of the radial jet. Peper et al. [69] studied the heat transfer and wall pressure distribution on a plane surface generated by single impinging in-line and radial air jets. Their experimental results showed that for the same volumetric flow rate, a radial jet with flow exit angle between 45 to 60 degrees generate up to 50% higher average Nusselt number compared with an in-line jet without any significant rise in pumping power.

From the aforementioned review, it appears that the radially impinging liquid jet has great potential for the application of thermal management of engineering equipment where a large overall heat transfer coefficient is required. The characterization of the flow field of an impinging free liquid jet is extremely important to understand the heat transfer process. So, this study is an attempt to go deeply into the fluid flow characteristics and heat transfer process by using computational fluid dynamics (CFD) tools, which has not yet been applied to the radially

impinging free liquid jets including free surfaces. This work is aiming at calculating the distribution of local Nusselt number over the heat transfer area of the plate and the average Nusselt number for different combinations of geometric and flow parameters.

## MATHEMATICAL MODEL

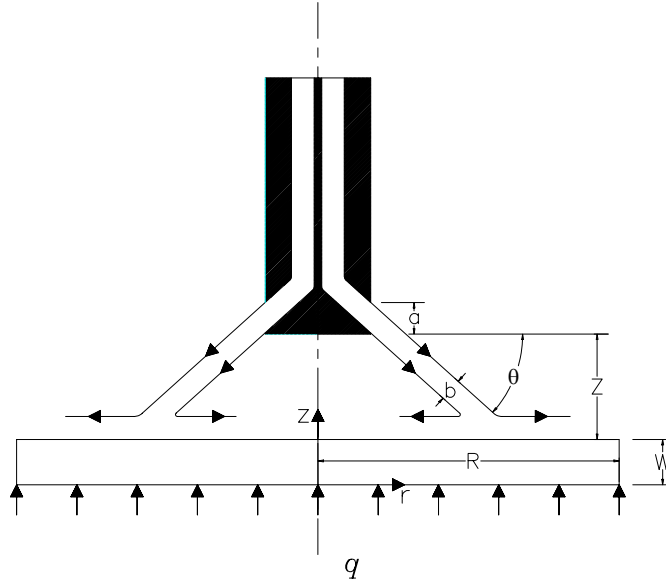


Figure 97. Schematic diagram of the radial jet impingement

Figure 97 presents the schematic diagram of the physical geometry of the jet under consideration. The fluid coming out from the nozzle exit impinges on the solid plate with a variable incidence angle ( $\theta$ ). After the impingement, the fluid spreads outward and inward on the plate cooling it off and then collected back to the reservoir. Three incidence angles ( $\theta = 45, 60$ , and  $75$  degrees) measured from the horizontal (radial direction) downward were studied. Three normal distances ( $Z = 5, 10$ , and  $15$  mm) between the jet exit and the hot plate along with three thicknesses ( $W = 1, 3$ , and  $5$  mm) of the hot plate were considered. With these variable incidence angles, the mass flow rate and fluid Reynolds number were kept constant. That has been done by adjusting the jet exit height ( $a$ ) in figure 97 to keep the cross sectional area of the flow constant which is represented by length normal to the flow ( $b$ ). The Reynolds number is estimated based on the characteristic length,  $d$ , which is the hydraulic diameter of the jet and is equal to  $2b$ . The plate was subjected to a uniform heat flux ( $q$ ) at the bottom surface.

Equations representing the conservation of mass, momentum, and energy (equations 1-5) were solved for laminar, axi-symmetric flow and steady-state conditions and the fluid properties were considered to be constants. These equations were solved using the appropriate boundary conditions. A symmetric condition was used at the axis of the nozzle and the plate ( $r=0$ ). The jet exiting the nozzle was assumed to have a uniform velocity ( $V_j$ ) directed at an angle  $\theta$  from the horizontal plane and a uniform temperature ( $T_j$ ). An uniform heat flux ( $q$ ) was applied at the bottom surface of the disk. The outer edge of the disk was assumed to be insulated. An outflow condition ( $p=0, \frac{\partial T_f}{\partial r}=0$ ) was imposed at locations where liquid exited the computational

domain, namely at the outer periphery of the disk and at its center. At the solid-fluid interface, equations (11) were satisfied. At the free surface (liquid-gas interface), equations (13) were satisfied.

## RESULTS AND DISCUSSION

Computations were performed for three different Reynolds numbers (1500, 2000, 2500). The jet Reynolds number was calculated using its hydraulic diameter (2b) as the length scale. Three jet inclination angles (45, 60, 75 degrees) and three jet elevations, Z, from the plate (5, 10, 15 mm) as well as three plate thicknesses (5, 3, 1 mm) were selected as parameters for this study. The local Nusselt number was calculated from the general formula:

$$Nu_{local} = \frac{q^* d}{k_f (T_w - T_j)} \quad (70)$$

The maximum normalized plate radius w.r.t. the jet characteristic length, 2b, was taken to be  $R/d=10$  where  $d=2b$ .

Figure 98 shows the variation of the local Nusselt number as a function of the flow Reynolds number. It can be seen that the maximum local Nusselt number occurs at the stagnation point at which the flow impinges on the plate. The heat transfer coefficient gradually decreases downstream as the flow moves outward and inward on the surface of the disk. The decrease of local heat transfer coefficient with distance from the impingement location is due to the development of thermal boundary layers as the flow moves downstream. A larger decrease is seen in the outward direction because a much larger amount of heat has to be carried away by the outward moving fluid because of much larger disk surface area in that region. The Nusselt number increases with Reynolds number because a larger velocity of the jet is expected to provide larger temperature gradient at the solid-fluid interface and enhance the rate of heat dissipation.

The variation in the local Nusselt number on the disk for different incidence angles of the jet is shown in figure 99. The maximum local Nu slightly increases as the inclination angle increases (the jet becomes more axial). This is quite expected because the normal component of the velocity at the incidence becomes higher which results in smaller thickness of the liquid film at the impingement location and larger local fluid velocity. The normal incidence (an axial jet) is expected to produce the highest local heat transfer coefficient for a given flow rate. But as we will see later in the paper the average Nusselt number over the plate is larger in the region between 45 and 60 degree inclination angle. This is due to the fact that the heat transfer area where the local Nu is higher at 45 degree is larger than the area where the local Nu is higher at the other smaller angles as the impingement area increases with radius.

The effect of the distance between the jet exit and the hot plate on the local Nusselt number is shown in figure 100. It can be noticed that the local heat transfer coefficient increases quite significantly with the height of impingement. This trend is opposite to that seen in submerged air jets [69] where it is advantageous to position the nozzle close to the plate for better thermal performance. This may be attributed to the gravity effect which is much stronger

for a liquid medium (higher density) that results in an increase in the flow momentum and the fluid velocity at the impingement location. It may be also interesting to observe that local Nusselt number outward from the impingement location stays higher for a higher nozzle height whereas for locations inward from the impingement location it tends to approach an asymptotic line. A similar trend was seen at other values of impingement angle and Reynolds number.

The effect of changing the thickness of the plate is demonstrated in figure 101. As the plate thickness decreases, the maximum local Nu increases. The lower thickness apparently results in smaller amount of thermal resistance between the heat source at the bottom of the disk and the heat sink (liquid medium) at the top of the disk. It may be also noticed that the local Nusselt number decreases more rapidly downstream when the thickness is smaller. A thicker disk allows for more uniform distribution of temperature within the disk due to lateral conduction and results in more uniform temperature at the solid-fluid interface. This results in more uniform distribution of local heat transfer coefficient.

The average Nusselt number is calculated based on the average distribution of the temperature along the interface between the plate and the fluid. Temperature is averaged over the heat transfer area which is represented by circles with increasing diameter away from the impinging ring.

$$Nu_{ave} = \frac{q^* d}{k_f (T_{ave} - T_j)} \quad (71)$$

where

$$T_{ave} = \frac{\sum T_i ((r/d)^2_i - (r/d)^2_{i-1})}{(R/d)^2} \quad (72)$$

The contour lines of the average Nu are shown in figure 102. The average Nu is generally higher in the region of 45 to 60 degree angle of inclination. Not only the maximum local Nu increases as the spacing between the jet and the plate increases but also the average Nu does the same thing as can be seen in this figure. This figure shows that for a given jet elevation, the average Nusselt number is highest at an inclination angle of 45 degrees. The effect of the plate thickness on the average Nu at different incidence angles is shown in figure 103. At 45 degree the effect is minimum. As the inclination angle increases (the jet becomes more axial) the average Nu is strongly affected and reduced as shown in the figure.

## NOMENCLATURE

d	Hydraulic diameter of the jet [m]
g	Acceleration due to gravity [m/s <sup>2</sup> ]
k	Thermal conductivity [W/m.K]
n	Coordinate normal to the free surface [m]
Nu	Nusselt number
p	Pressure [Pa]
q	Heat Flux [W/m <sup>2</sup> ]
r	Radial coordinate [m]

R	Radius of the disk [m]
Re	Reynolds number
T	Temperature [K]
V	Velocity [m/s]
W	Plate thickness [m]
z	Axial coordinate [m]
Z	Nozzle height [m]

#### **Greek Symbols**

$\alpha$	Thermal diffusivity [ $\text{m}^2/\text{s}$ ]
$\delta$	Film height [m]
$\mu$	Dynamic viscosity [ $\text{kg/m} \cdot \text{s}$ ]
$\theta$	Angle of incidence
$\rho$	Density [ $\text{kg/m}^3$ ]
$\sigma$	Surface tension coefficient [N/m]

#### **Subscripts**

atm	Ambient
ave	Average
f	Fluid
j	Jet
local	Local
O	Maximum local condition
r	Radial
s	Solid
t	Tangent to the free surface
w	solid-fluid interface
z	Axial

## **CONCLUSIONS**

CFD computation based on the finite element method was used to analyze the flow and heat transfer characteristics of a radially impinging free liquid laminar jet. The analysis includes the simulation of the free surface flow and heat transfer process for both the spreading forward flow and the circulating backward flow. A parametric study was made for different Reynolds number, different jet incidence angles, different jet height from the impingement plate and different plate thicknesses. A 45 to 60 degree incidence angle was found to give higher local heat transfer coefficient and consequently higher average Nusselt number. For liquid jet it is preferable to increase the spacing between the jet and the impingement plate. Plate thickness has minimum effect on the average Nu at 45 degree angle while it has a pronounced effect as the angle increases. A reasonable qualitative agreement was obtained between the current CFD analysis and previous experimental and analytical investigations.

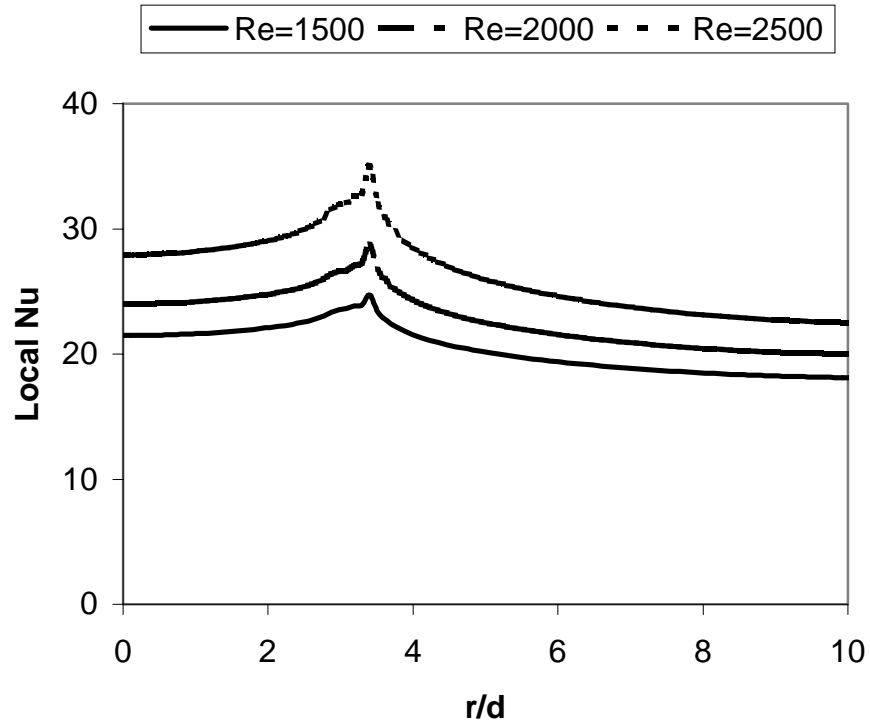


Figure 98. Local Nusselt number variation at different Reynolds number of the jet flow( $\theta=45$  deg,  $Z=5$ mm,  $W=5$ mm)

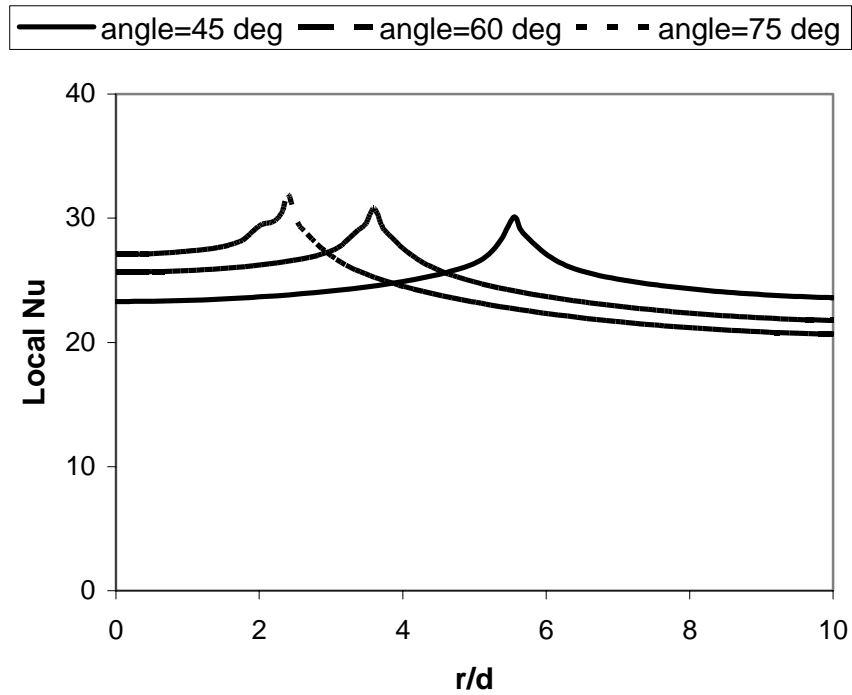


Figure 99. Local Nu at different incidence angles of the jet (Re=2000,  $Z=10$  mm,  $W=5$ mm)



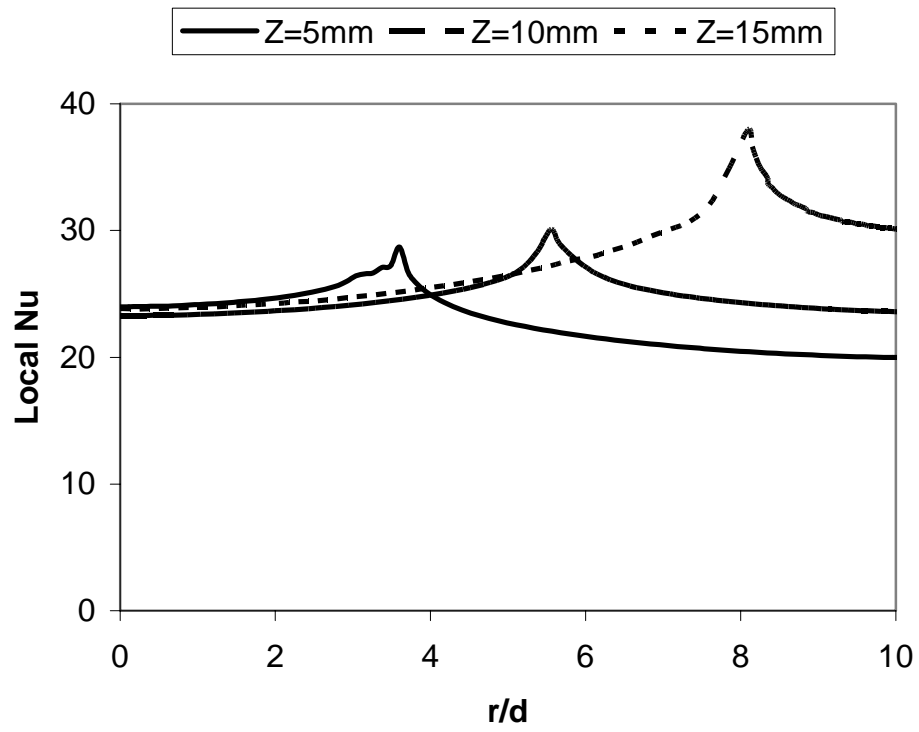


Figure 100. Local Nu at different distance of the jet from the disk ( $\theta=45$ ,  $Re=2000$ ,  $W=5mm$ )

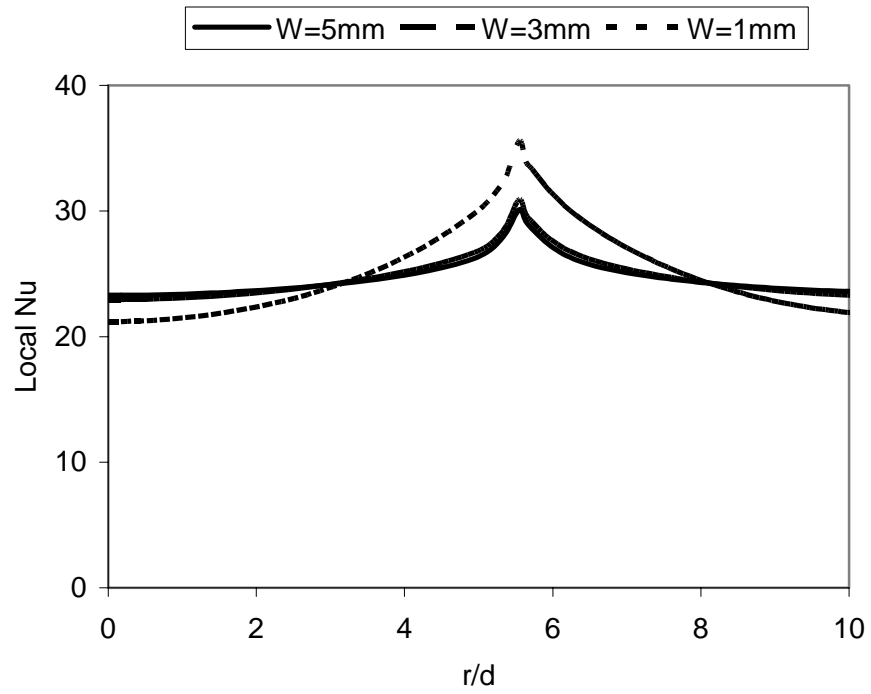


Figure 101. Local Nu distribution at different thickness of Impingement plate ( $\theta=45$ ,  $Re=2000$ ,  $Z=10mm$ )

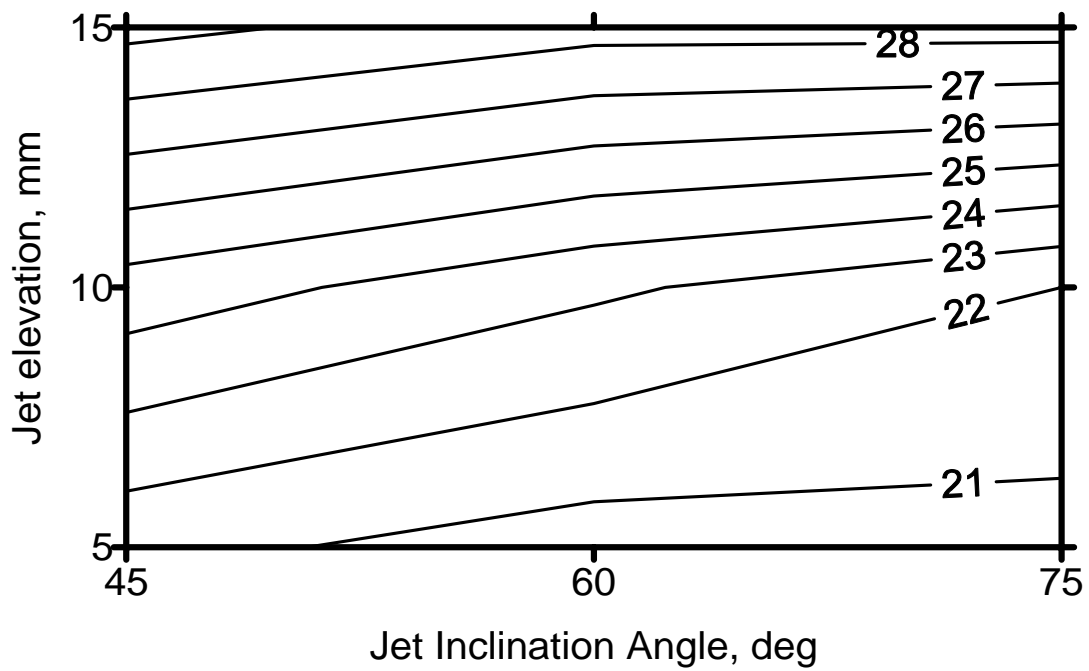


Figure 102. Contour lines of the average Nu at different jet incidence angle and jet height from the plate ( $Re=2000$ ,  $W=5mm$ ).

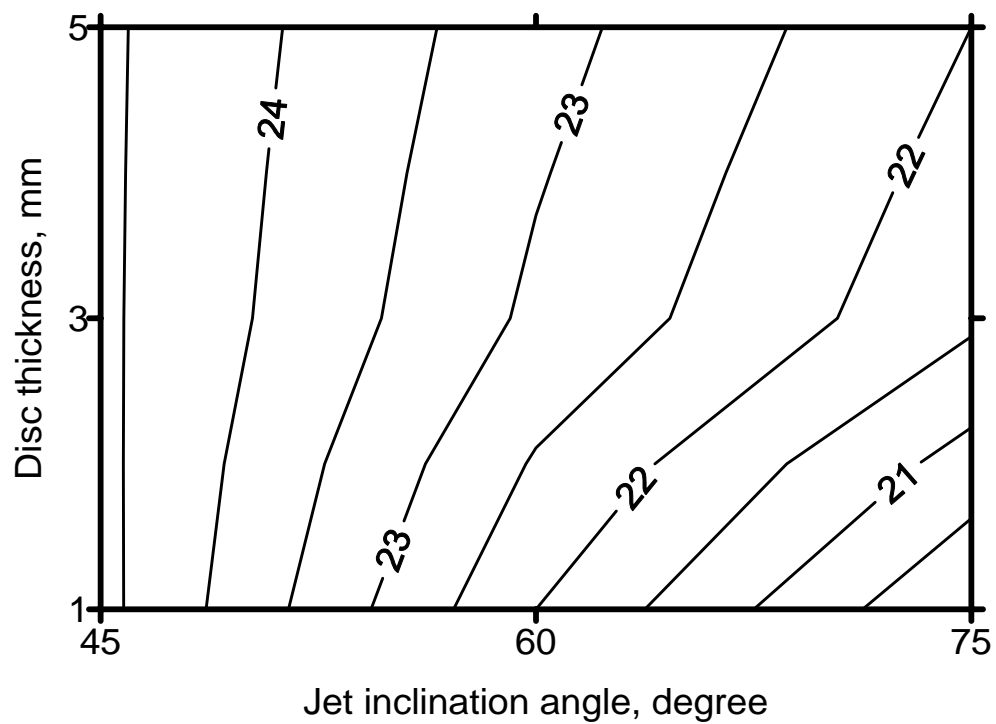


Figure 103. Contour lines of the average Nu at different jet incidence angle and different plate thickness ( $Re=2000$ ,  $Z=10mm$ )

# **CONFINED JET OF AMMONIA FROM A SLOT NOZZLE IMPINGING ON A UNIFORMLY HEATED PLATE: STEADY STATE**

## **INTRODUCTION**

Jet impingement heat transfer (JIHT) has received considerable research attention due to its potential application in the area of thermal heating and cooling processes. As computers and sundry electronic products such as cellular telephones have become more sophisticated and smaller in size, the logistics of heat elimination have also become more difficult. Traditional methods such as the use of fans because of their bulk size and noise are inadequate and difficult to use.

This two-part study presents the numerical simulation of heat transfer to a two-dimensional (slot) submerged confined jet of ammonia impinging vertically on a solid plate. The first part solves a non-conjugate problem (plate thickness = 0) where only the fluid region is considered. The second part extended it into a conjugate problem in which the heat conduction in the solid plate was included in the numerical simulation model. Equations for the conservation of mass, momentum, and energy were solved in the fluid region. In the solid region, only the energy equation, which reduced to the heat conduction equation, had to be solved.

A detailed parametric study was performed to explore the heat transfer characteristics. Computations using Ammonia as the working fluid were carried out for five different flow rates (or jet Reynolds number), two different disk materials, namely, constantan and silicon, six different disk thickness ranging from 0.001 m to 0.01 m, and four different nozzle widths, and three different impingement heights. Results were compared with previous studies using FC-77 and Mil-7808 as working fluids.

Submerged liquid jets find use in both axisymmetric and planar configurations. Both configurations share the common feature of a very small stagnation zone at the impingement surface whose size is of the order of the jet dimension, with the subsequent formation of a wall jet region. Both are affected by viscous shear in the submerged configuration. Both may be configured in arrays in an attempt to achieve higher transport characteristics of the stagnation zone over a larger area. Both may also be oriented normal or oblique to the impingement plate. Oblique impingement obviously affects the hydrodynamics of the flow and consequently the heat and/or mass transfer. Abou-Ziyan and Hassan [70] made an experimental study of forced convection due to impingement of confined, submerged and fully turbulent jets in relation to the cooling of engine cylinder heads by water. They concluded that jet impingement can save between 50% and 92% of required cooling water compared to simple forced convection. Morris et al. [71] made an analytical investigation of flow fields in the orifice and confinement regions of a normally impinging confined and submerged liquid jet. Predicted characteristics of the separation region at the orifice entrance agreed with published experimental values for different orifice diameters and orifice to target plate spacing. The pressure drop across the orifice was predicted to be within 5% of their proposed empirical correlations based on published experimental data. They also found that computed flow patterns in the confinement region were in good qualitative agreement with experimental flow

visualizations. Dinu et al. [72] made a numerical study of convective heat transfer from a confined submerged jet impinging on a moving surface. They considered both constant temperature as well as constant heat flux boundary conditions on the moving surface. With a constant temperature boundary condition, heat transfer distributions were found to be sensitive to the speed of the heat transfer surface and to the jet inlet Reynolds number. For a uniform heat flux boundary condition, Nusselt number on the moving plate was more uniform than for a constant temperature boundary condition.

## MATHEMATICAL MODEL

We consider an axisymmetric jet discharging from a nozzle and impinging perpendicularly at the center of a solid plate subjected to a constant heat flux. If the fluid is considered to be incompressible and have constant properties, equations describing the conservation of mass, momentum, and energy in Cartesian coordinates can be written as [23]:

$$\frac{\partial v_x}{\partial x} + \frac{\partial v_z}{\partial z} = 0 \quad (73)$$

$$v_x \frac{\partial v_x}{\partial x} + v_z \frac{\partial v_x}{\partial z} = -\frac{1}{\rho_f} \frac{\partial p}{\partial x} + \nu_f \left( \frac{\partial^2 v_x}{\partial x^2} + \frac{\partial^2 v_x}{\partial z^2} \right) \quad (74)$$

$$v_x \frac{\partial v_z}{\partial x} + v_z \frac{\partial v_z}{\partial z} = -g - \frac{1}{\rho_f} \frac{\partial p}{\partial z} + \nu_f \left( \frac{\partial^2 v_z}{\partial x^2} + \frac{\partial^2 v_z}{\partial z^2} \right) \quad (75)$$

$$v_x \frac{\partial T_f}{\partial x} + v_z \frac{\partial T_f}{\partial z} = \alpha_f \left( \frac{\partial^2 T_f}{\partial x^2} + \frac{\partial^2 T_f}{\partial z^2} \right) \quad (76)$$

The equation describing the conservation of energy inside the solid can be written as:

$$\frac{\partial^2 T_s}{\partial x^2} + \frac{\partial^2 T_s}{\partial z^2} = 0 \quad (77)$$

To complete the physical model, equations (73) to (77) are subjected to the boundary conditions described by equations (46-51). In addition, the following two boundary conditions are needed.

$$\text{At } z = 0 : -k_s \frac{\partial T_s}{\partial z} = q \quad (78)$$

$$\text{At } z = b + H_n, W/2 \leq x \leq L : v_x = 0, v_z = 0, \frac{\partial T_f}{\partial z} = 0 \quad (79)$$

## DISCUSSION OF RESULTS

Figure 104 shows the simulated geometry. The simulation was carried out for two different materials, namely constantan and silicon. The length of the plate ( $L = 0.008$  m) and the temperature of the jet at the nozzle exit ( $T_j = 293$  K) were kept constant during the simulation. Ammonia was used as the primary working fluid for the simulation, which is an emerging coolant for space based thermal management systems. In order to determine the number of elements for accurate numerical solution, computations were performed for several combinations of number of elements in the x and z directions covering the solid and fluid regions. The solid-fluid interface temperature for these simulations are plotted in figure 105. It was observed that

the numerical solution becomes grid independent when the number of divisions in the x and z directions are increased over 80. Computations with 80x80 grids gave almost identical results when compared to those obtained using 160x160 grids. In order to save computer time while retaining accuracy, 80 x 80 divisions was chosen for all final computations

Figure 106 presents the solid-fluid interface temperature distribution for different Reynolds number. It can be observed that the minimum temperature is present at the stagnation point and the maximum at the edge of the plate. As expected, the interface temperature, as well as the minimum-to-maximum temperature difference at the interface decreases with Reynolds number because of more fluid flow rate to carry away the heat. Figures 107 and 108 show the variations in local heat transfer coefficient and Nusselt number respectively along the solid-fluid interface for different Reynolds numbers. In these simulations, a constant nozzle slot width of 3.2 mm and  $H_n/W$  ratio of 1 have been used. Also, for figure 108, the distance from the axis of the nozzle has been non-dimensionalised as  $x/W$  to conform with the non-dimensional Nusselt number. The overall values of the local heat transfer coefficient and hence the local Nusselt number increases with jet inlet Reynolds number over the entire solid-fluid interface. The usual bell shaped profile typical for impinging jets with a peak at the stagnation line is obtained in the numerical study. The heat transfer coefficient increases with Reynolds number because of higher velocity of the fluid impinging on the plate.

Figures 109 and 110 show streamline contours and velocity vectors respectively for the simulation with Reynolds number of 890 and heat flux of  $250 \text{ kW/m}^2$ . The streamlines indicate that the flow after leaving the slot nozzle moves vertically downward and turns by an angle of 90 degrees as it approaches the plate. The jet expands as it moves down towards the plate. The streamlines show clearly that the flow is strongly governed by forced convection due to the incoming fluid. After the flow changes direction along the solid plate towards the outflow region, the streamlines within the parallel flow zone reflect the hydrodynamic boundary layer. Above the boundary layer all the way to the confinement plate, the streamline pattern indicates a recirculation zone. This recirculating flow is in line with experimental observations by Garimella and Rice [36]. The extent of the recirculation region depends on the fluid velocity and the impingement height. At smaller nozzle height, due to the growth of the hydrodynamic boundary layer and the consequent expansion of wall jet, the mainstream flow may encompass the entire region all the way to the confinement plate. The velocity vector plot (figure 110) shows that the velocity decreases gradually until the fluid strikes the solid surface at which point there is a rapid deceleration while the flow changes direction parallel to the solid plate. There is a brief acceleration along this so called parallel flow zone for a distance of about two times the slot opening after which the fluid decelerates gradually all the way to the outflow. The development of the hydrodynamic boundary layer topped by a rapidly moving fluid as wall jet is apparent in the velocity vector pattern. It can be also seen that the magnitude of fluid velocity in the recirculation zone is an order of magnitude smaller compared to the mainstream flow.

Figures 111, 112, and 113 show the variations of solid-fluid interface temperature, heat transfer coefficient, and Nusselt number, respectively with radial distance for various slot widths maintaining a constant Reynolds number of 890. It may be noted that the flow rate is directly proportional to Reynolds number and therefore the flow rate is also the same in

these simulations. The nozzle slot widths considered are 0.8mm, 1.6mm, 3.2mm and 6.4mm. For the local heat transfer coefficient and Nusselt number, the same half bell shaped curves (considering only one axisymmetric half) are present. The interface temperature increases outwardly with radial distance and the lowest temperature is found at the stagnation line underneath the center of the slot opening. It may be observed in figure 111 that the interface temperature decreases with decrease in the slot opening all along the plate. The lower interface temperature is the result of larger convective heat transfer rate caused by higher jet velocity. When the flow rate (or Reynolds number) is kept constant, a smaller slot opening results in larger impingement velocity which consequently contributes to larger velocity of fluid moving along the plate (within the boundary layer as well as in the wall jet). From figures 112 and 113, it can be noticed that the heat transfer rate at the impingement region can be augmented by a great extent if the nozzle width is reduced. For an eight-fold reduction in slot opening width, the peak value of local heat transfer coefficient as well as the Nusselt number increases by almost 4 times. Due to more rapid decrease from the peak in the case of smaller opening, the average heat transfer coefficient does not increase as much, but still of the order of 2.5 times for the length of the plate considered in the present investigation. The average values of heat transfer coefficient and Nusselt number for these cases are listed in Table 5. The above observation suggests that a smaller slot opening is more desirable in nozzle design because of larger convective heat transfer rate at the solid-fluid interface for any given fluid flow rate. However, further study including the pressure drop characteristics may be needed to arrive at the optimum slot opening.

Figures 114, 115, and 116 show the variations of solid-fluid interface temperature, heat transfer coefficient, and Nusselt number, respectively with radial distance for various slot widths for a constant jet velocity. Since the slot width is used as the length scale for Reynolds number, the Reynolds number also varied in these runs. There is a cross-over of local distributions of temperature as well as the heat transfer coefficient as the nozzle width is varied. The minimum temperature and highest local values of heat transfer coefficient and Nusselt number are still obtained for a nozzle width of 0.08 cm, the lowest width considered in the present investigation. However, this run also results in the lowest heat transfer coefficient at the exit end of the plate. The local values of Nusselt number at the downstream locations increase with nozzle width because of larger impingement region as well as larger flow rate to carry away the heat. It can be also noticed that when the nozzle width is increased from 0.32 cm to 0.64 cm, the heat transfer performance improves everywhere in the plate. Looking at the average values of heat transfer coefficient and Nusselt number listed in Table 5, it can be observed that the lowest values are for  $W=0.16$  cm and it increases in both directions. A more significant increase is seen when the width is increased, even though that increase is at the expense of a larger flow rate.

Figures 117 and 118 show plots of temperature at the solid-fluid interface against distance from the axis of impingement for silicon and constantan respectively and for six different solid thicknesses. In all three cases, it is evident that the interface temperature is sensitive to the solid thickness especially at the stagnation point where rather significantly lower temperatures are observed as the solid wafer reduces to 1 mm thickness ( $b/W = 0.3125$ ). At higher thicknesses in the region of 4 to 12 mm ( $b/W = 1.25-3.75$ ), the changes in stagnation point temperature are relatively lower. Also apparent is the fact that when stagnation temperatures are lower, the outflow temperature tends to be relatively higher which is quite expected because both flow rate and heat flux at the bottom surface of

the disk were kept constant. This phenomenon has been documented by Lachefski et al. [68] and is the main drawback of axially impinging jets as opposed to radial jets which gives better uniformity of temperature. It can also be noted that a thicker plate provides more uniform interface temperature because of radial distribution of heat within the solid due to conduction. Figures 119-120 show the plots for the distribution of local heat transfer coefficient for different disk thicknesses and the corresponding plots for local Nusselt number are shown in figures 121-122. A higher variation is seen for a disk with smaller thickness. As the thickness increases, the distribution of local heat transfer coefficient becomes more uniform. Analogous to the interface temperature plot, beyond the disk thickness of 4 mm ( $b/W=1.25$ ), the distribution does not change very significantly indicating that the overall transport is dominated by convection at the solid-fluid interface and not by conduction within the solid. The values of average heat transfer coefficient and average Nusselt number for these cases are also listed in Table 5. It may be noticed that for all three materials, the average Nusselt number increases with plate thickness. The increment, however, is small in magnitude and practically disappears at large thickness.

Figures 123 and 124 show isotherm contour plots within the solid for Constantan at thicknesses of 5mm and 1mm respectively. The minimum temperature in both cases occurs at the stagnation point while the maximum occurs at the outer end of the bottom surface of the plate (heat flux surface). For the thicker solid, the isotherms exhibit better uniformity as indicated by the fact that they are more parallel to the interface and disk bottom surfaces. This fact is also borne out by the fact that the maximum temperature difference within the thicker solid (21.72 K) is lesser than for the thinner one (27.44 K). The heat transfer at the solid-fluid interface becomes more uniform as the thickness increases.

## NOMENCLATURE

$b$	Thickness of the disk [m]
$c_p$	Specific heat at constant pressure [kJ / kg K]
$g$	Acceleration due to gravity [ $\text{m} / \text{s}^2$ ]
$h$	Heat transfer coefficient [ $\text{W} / \text{m}^2 \text{K}$ ], $q_{int}/(T_{int} - T_j)$
$H_n$	Height of the nozzle from the plate [m]
$k$	Thermal conductivity [ $\text{W} / \text{m K}$ ]
$L$	Length of the plate [m]
$W$	Width of the nozzle [m]
$n$	Coordinate normal to the free surface [m]
$Nu$	Nusselt number, $hW / k_f$
$p$	Pressure [Pa]
$q$	Heat flux [ $\text{W} / \text{m}^2$ ]
$Re$	Reynolds number, $Wv_j / \nu_f$
$T$	Temperature [K]
$T_j$	Jet temperature [K]
$v_j$	Jet velocity [ $\text{m} / \text{s}$ ]
$v_x$	Velocity component in the x-direction [m/s]

$v_z$	Velocity component in the z-direction [m/s]
W	Width of the slot nozzle [m]
x	Coordinate parallel to the plate [m]
z	Coordinate perpendicular to the plate [m]

#### **Greek Symbols**

$\alpha$	Thermal diffusivity [ $\text{m}^2/\text{s}$ ]
$\nu$	Kinematic viscosity [ $\text{m}^2/\text{s}$ ]
$\rho$	Density [ $\text{kg} / \text{m}^3$ ]

#### **Subscripts**

av	Average
f	Fluid
int	Solid - fluid interface
max	Maximum
s	Solid

## **CONCLUSIONS**

The solid-fluid interface temperature as well as the heat transfer coefficient shows a strong dependence on several geometric, fluid flow, and heat transfer parameters such as jet Reynolds number, nozzle slot width, impingement height, plate thickness, plate material, and fluid properties. The inlet Reynolds number was kept at values where laminar flow could be obtained. The heat transfer coefficient increased with Reynolds number. It decreased with slot width for a given flowrate. At the stagnation line, local values of heat transfer coefficient was highest because of the pronounced convective effects. Heat transfer then reduced gradually towards the outflow boundary. A lower impingement height resulted in higher heat transfer coefficient. A higher heat transfer coefficient at the impingement location was seen at a smaller thickness, whereas a thicker plate provided a more uniform distribution of heat transfer coefficient. Plate materials with a higher thermal conductivity provided a more uniform distribution of interface temperature as well as the heat transfer coefficient.



Table 5 Average heat transfer coefficient and average Nusselt number for an uniformly heated plate

Material	fluid	Re	W(cm)	b(cm)	V <sub>in</sub> (cm/sec)	H <sub>n</sub> (cm)	h <sub>av</sub> (w/m <sup>2</sup> K)	Nu <sub>av</sub>
-	ammonia	445	0.32	-	4.836	0.32	2286.18	14.104
-	ammonia	668	0.32	-	7.259	0.32	2803.08	17.296
-	ammonia	890	0.32	-	9.672	0.32	3234.69	19.963
-	ammonia	1115	0.32	-	12.117	0.32	3619.00	22.338
-	ammonia	222.5	0.08	-	9.672	0.32	3121.73	19.903
-	ammonia	445	0.16	-	9.672	0.32	3103.78	19.789
-	ammonia	890	0.32	-	9.672	0.32	3234.19	20.452
-	ammonia	1780	0.64	-	9.672	0.32	3903.54	24.888
-	ammonia	890	0.64	-	4.836	0.32	2740.50	17.128
-	ammonia	890	0.32	-	9.672	0.32	3239.97	20.312
-	ammonia	890	0.16	-	19.344	0.32	4419.09	27.780
-	ammonia	890	0.08	-	38.688	0.32	6606.43	40.489
Silicon	ammonia	1545	0.32	0.1	16.78	0.32	3865.35	24.043
Silicon	ammonia	1545	0.32	0.2	16.78	0.32	3836.06	23.860
Silicon	ammonia	1545	0.32	0.4	16.78	0.32	3824.45	23.788
Silicon	ammonia	1545	0.32	0.6	16.78	0.32	3822.48	23.776
Silicon	ammonia	1545	0.32	0.9	16.78	0.32	3822.01	23.773
Silicon	ammonia	1545	0.32	1.2	16.78	0.32	3821.92	23.772
Constantan	ammonia	1545	0.32	0.1	16.78	0.32	4076.98	25.360
Constantan	ammonia	1545	0.32	0.2	16.78	0.32	3994.18	24.844
Constantan	ammonia	1545	0.32	0.4	16.78	0.32	3950.23	24.571
Constantan	ammonia	1545	0.32	0.6	16.78	0.32	3941.99	24.520
Constantan	ammonia	1545	0.32	0.9	16.78	0.32	3939.96	24.507
Constantan	ammonia	1545	0.32	1.2	16.78	0.32	3939.61	24.505

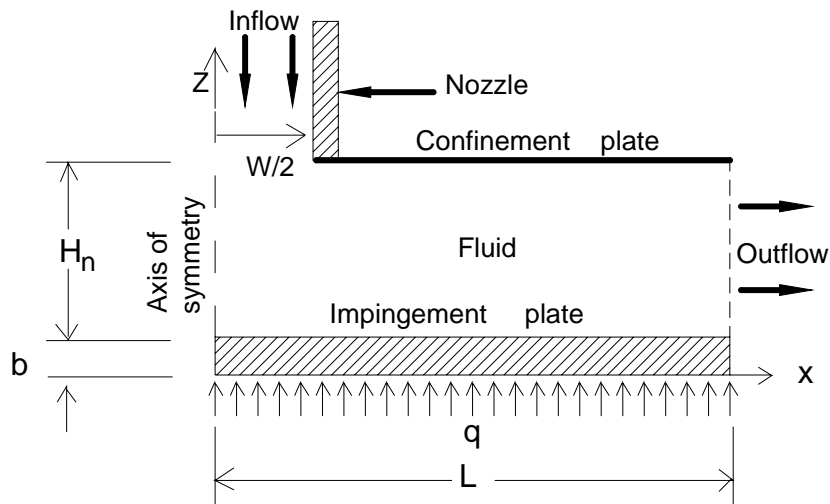


Figure 104. Schematic of a confined slot jet impinging on a uniformly heated solid plate

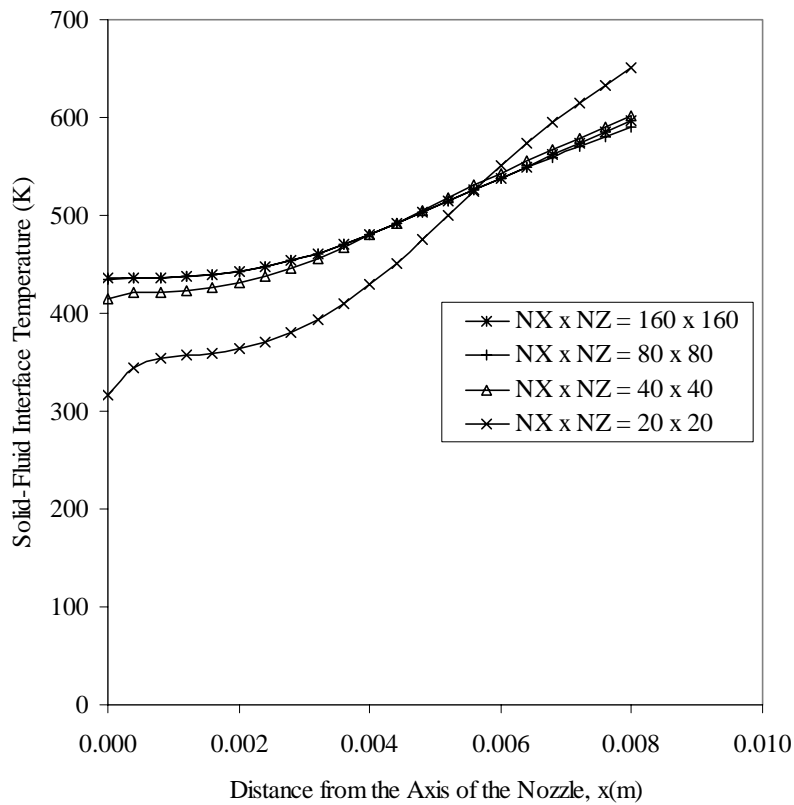


Figure 105. Local interface temperature for different number of elements in x and z directions.  
(  $Re = 1645$ ,  $b = 0$ ,  $H_n/W = 1$ ,  $q = 250 \text{ kW/m}^2$ )

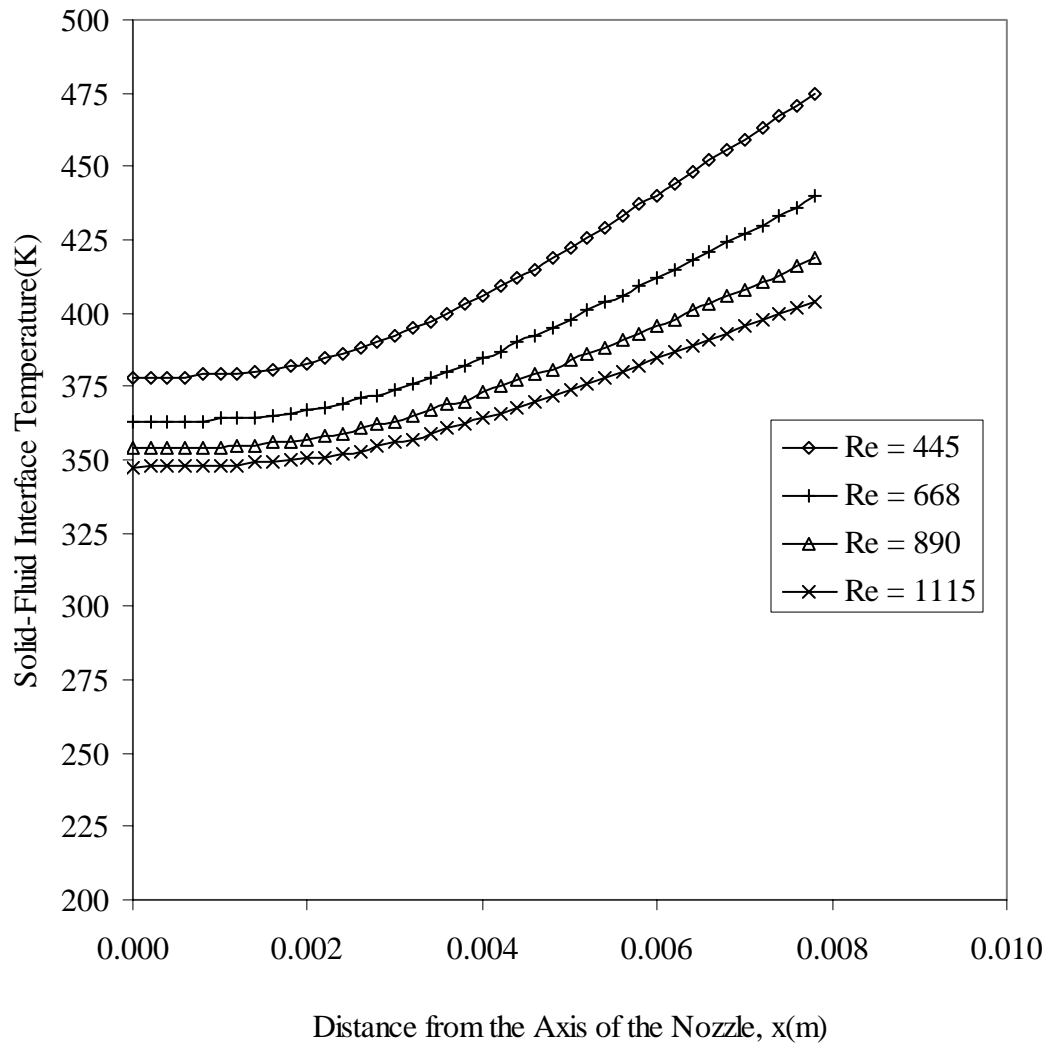


Figure 106. Temperature at the solid-fluid interface  
for varying Reynolds number  
( $W = 3.2 \text{ mm}$ ,  $H_n = 3.2 \text{ mm}$ ,  $b = 0$ ,  $q = 250 \text{ kW/m}^2$ )

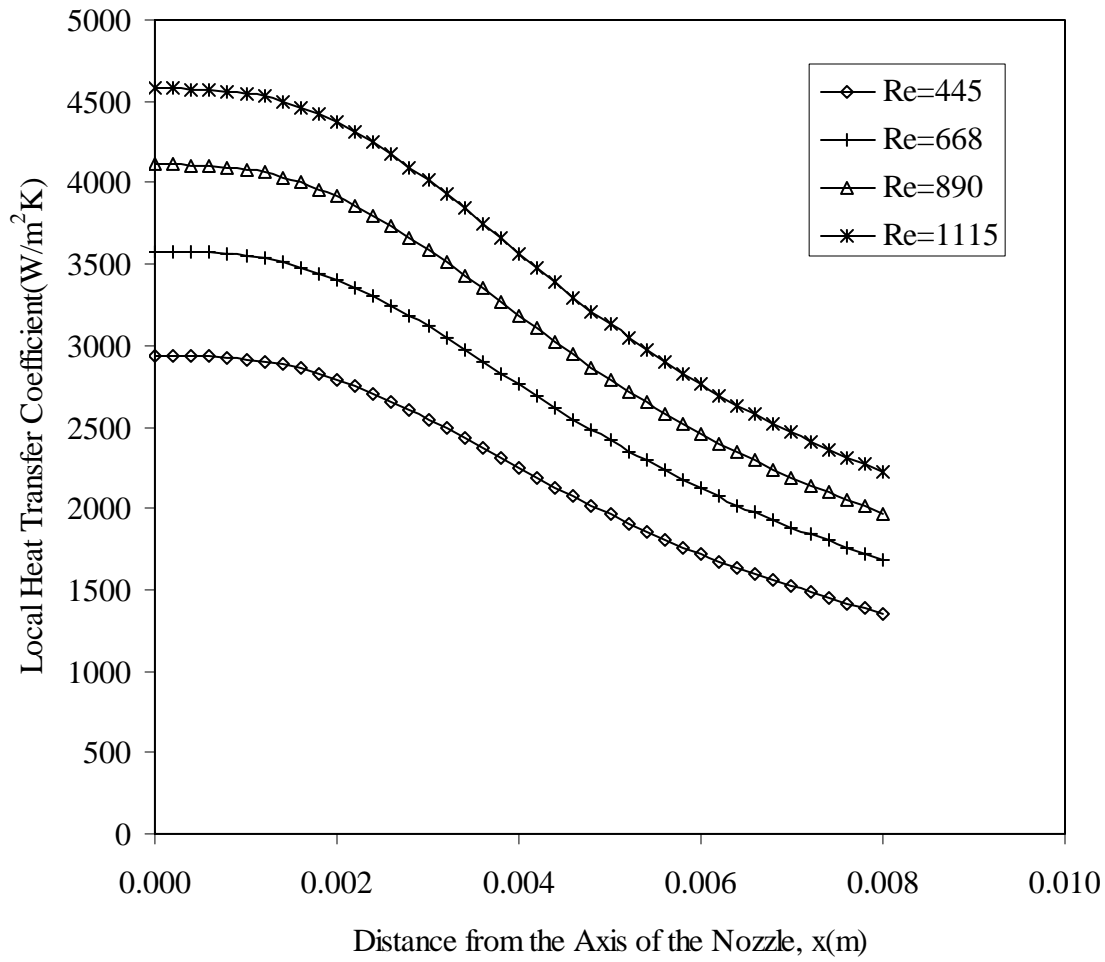


Figure 107. Heat transfer coefficient at the solid-fluid interface  
for varying Reynolds number  
( $H_n/W = 1$ ,  $b/W = 0$ ,  $q = 250 \text{ kW/m}^2$ )

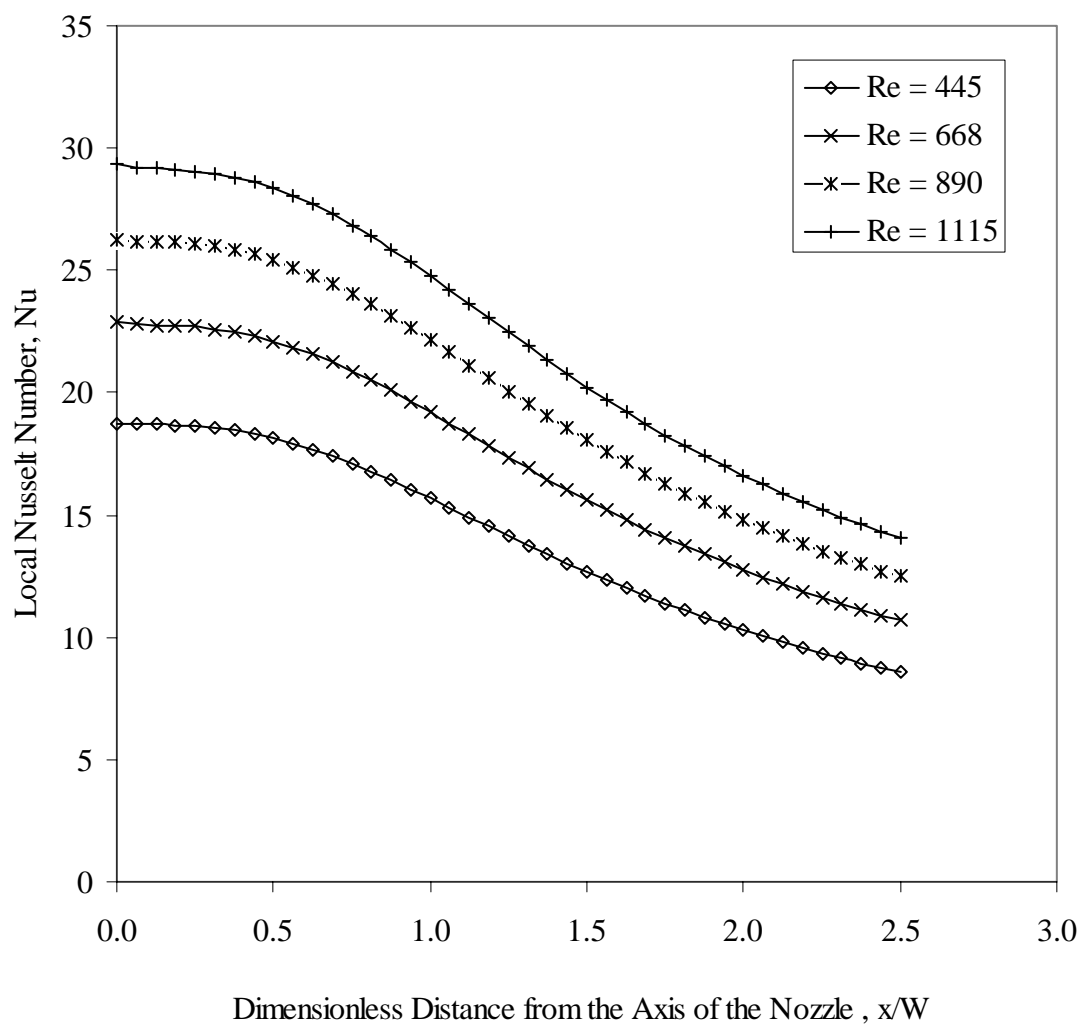


Figure 108. Nusselt number at the solid-fluid interface  
for varying Reynolds number  
( $H_n/W = 1$ ,  $b/W = 0$ ,  $q = 250 \text{ kW/m}^2$ )

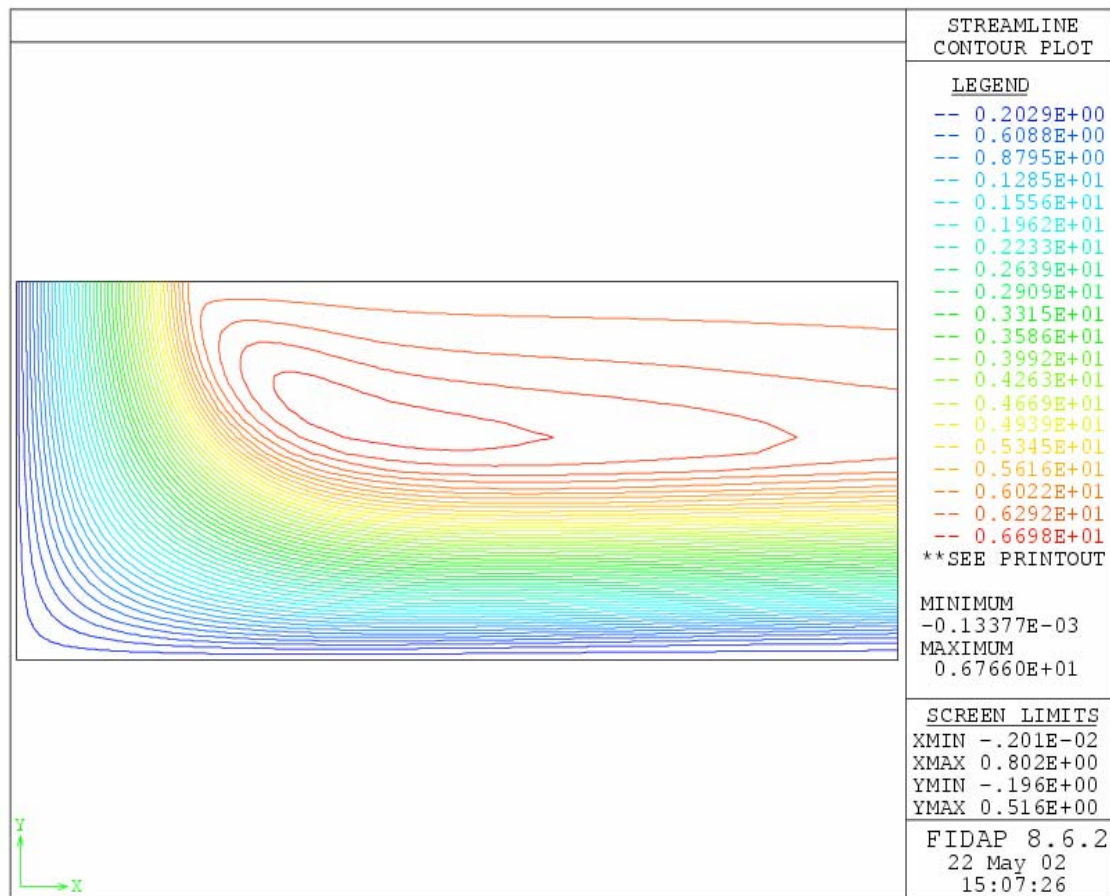


Figure 109. Streamline plot for confined jet impingement  
(Re = 890,  $q = 250 \text{ kW/m}^2$ ,  $W = 3.2 \text{ mm}$ ,  $H_n/W = 1$ ,  $b/W = 0$ , )

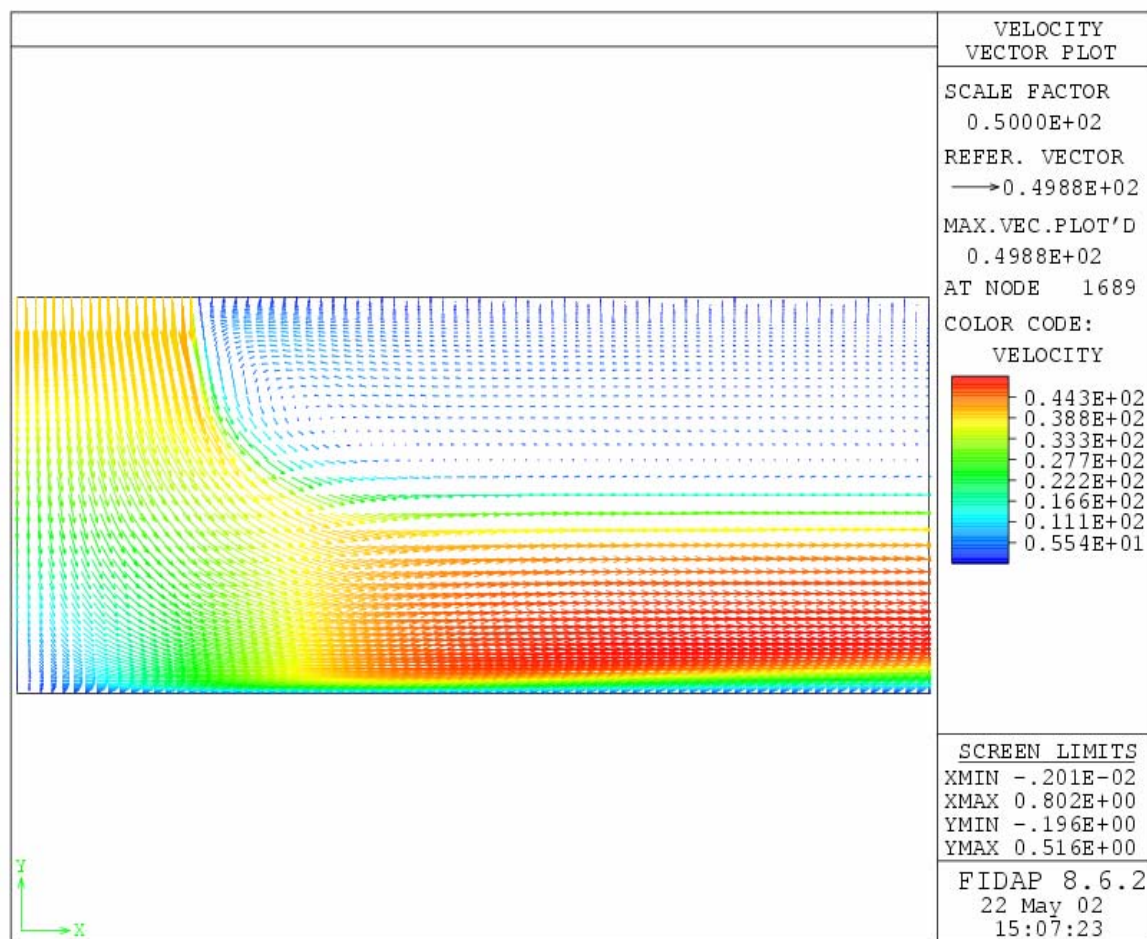


Figure 110. Streamline plot for confined jet impingement  
( $Re = 890$ ,  $q = 250 \text{ kW/m}^2$ ,  $W = 3.2 \text{ mm}$ ,  $H_n/W = 1$ ,  $b/W = 0$ )

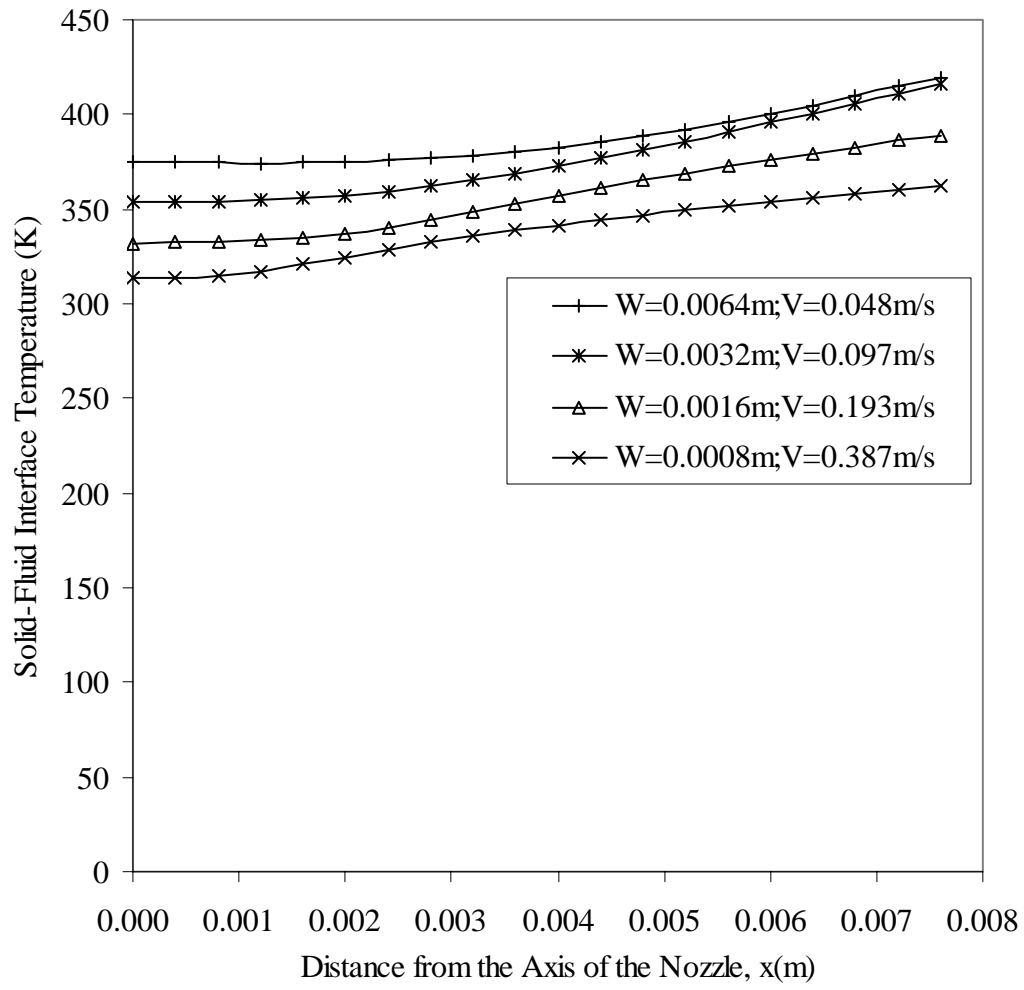


Figure 111. Temperature at the solid-fluid interface  
for constant flow rate  
(  $H_n = 3.2 \text{ mm}$ ,  $Q = 3.1 \times 10^{-4} \text{ m}^2/\text{s}$ ,  $b = 0$  )



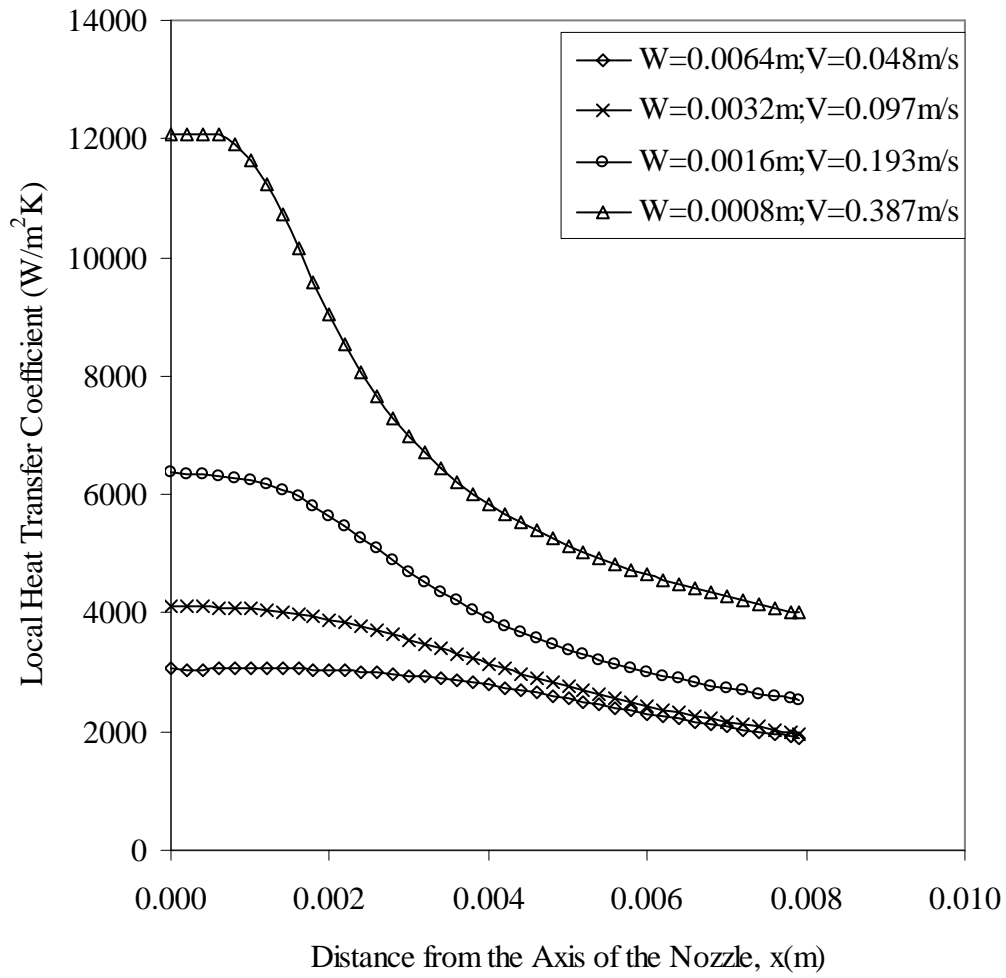


Figure 112. Heat transfer coefficient at solid-fluid interface  
for constant flow rate  
(  $H_n = 3.2 \text{ mm}$ ,  $Q = 3.1 \times 10^{-4} \text{ m}^2/s$ ,  $b = 0$  )

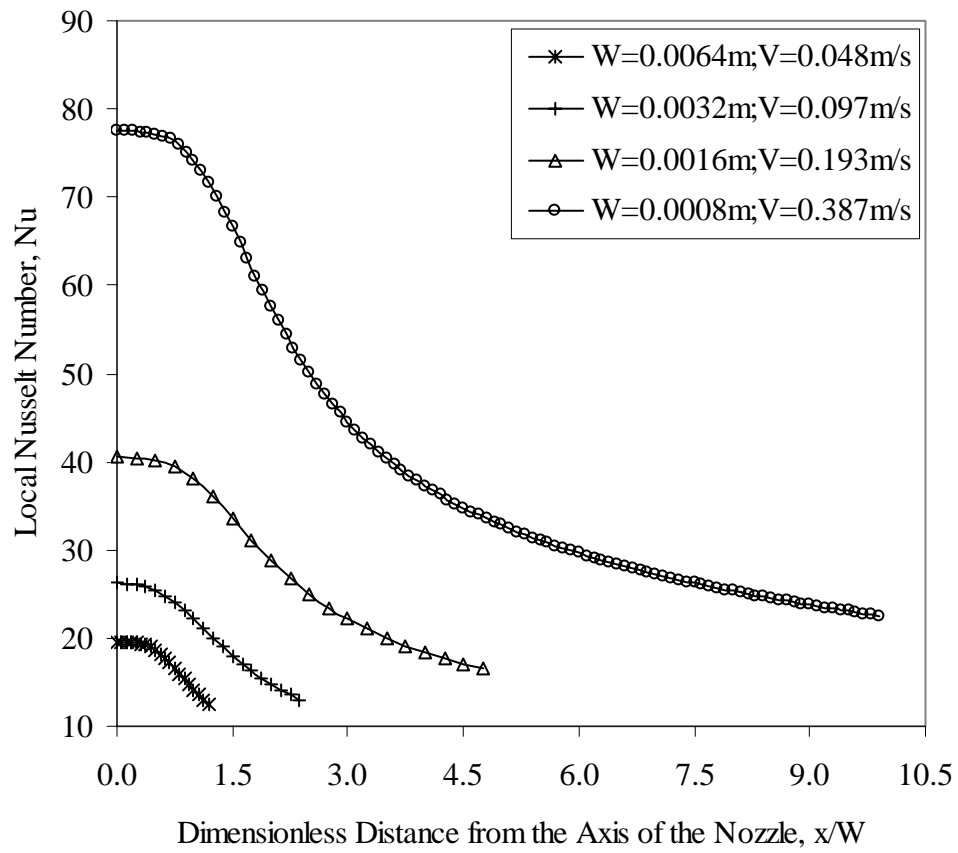


Figure 113. Nusselt number at solid-fluid interface  
for constant flow rate  
(  $H_n = 3.2 \text{ mm}$ ,  $b = 0$ ,  $Q = 3.1 \times 10^{-4} \text{ m}^2/\text{s}$  )

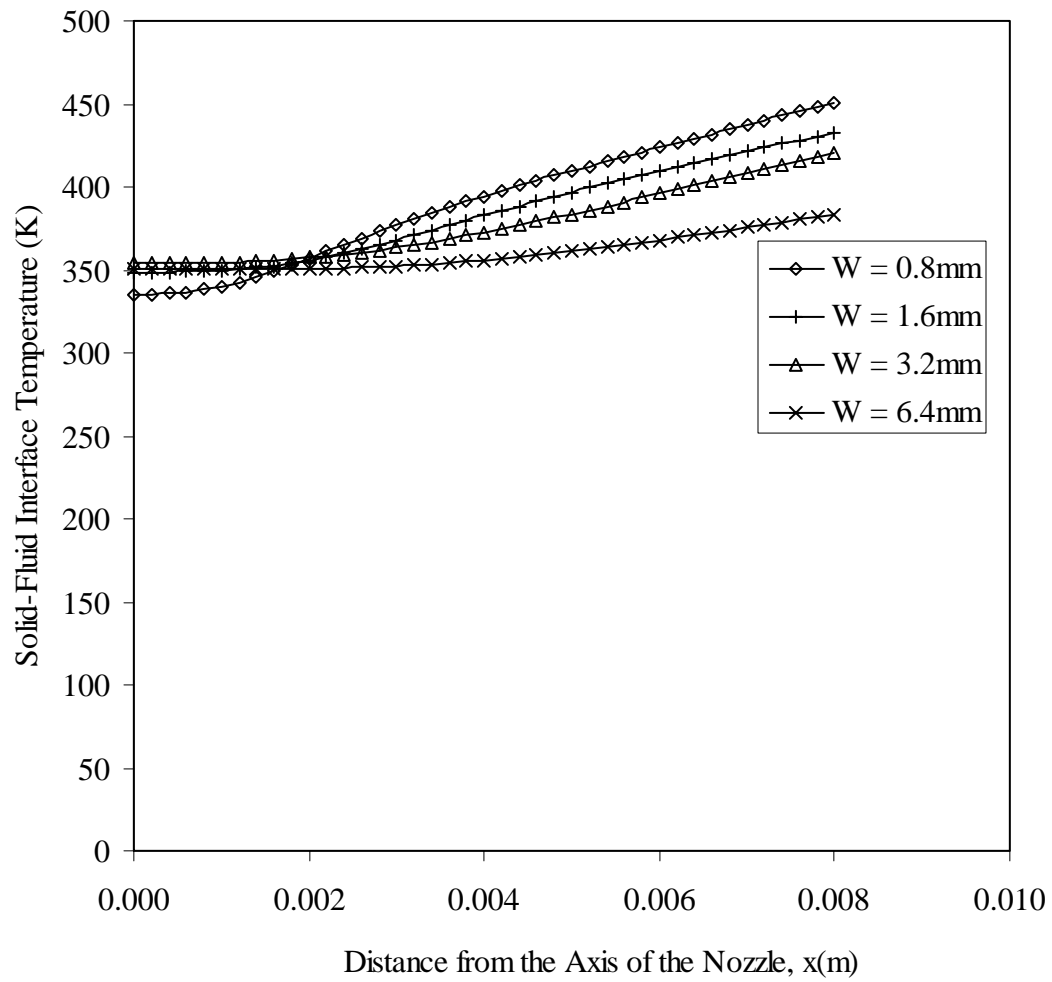


Figure 114. Local temperature distribution at the solid-fluid interface for different nozzle widths  
 (  $H_n = 3.2$  mm,  $b = 0$ ,  $q = 250$  kW/m<sup>2</sup> )

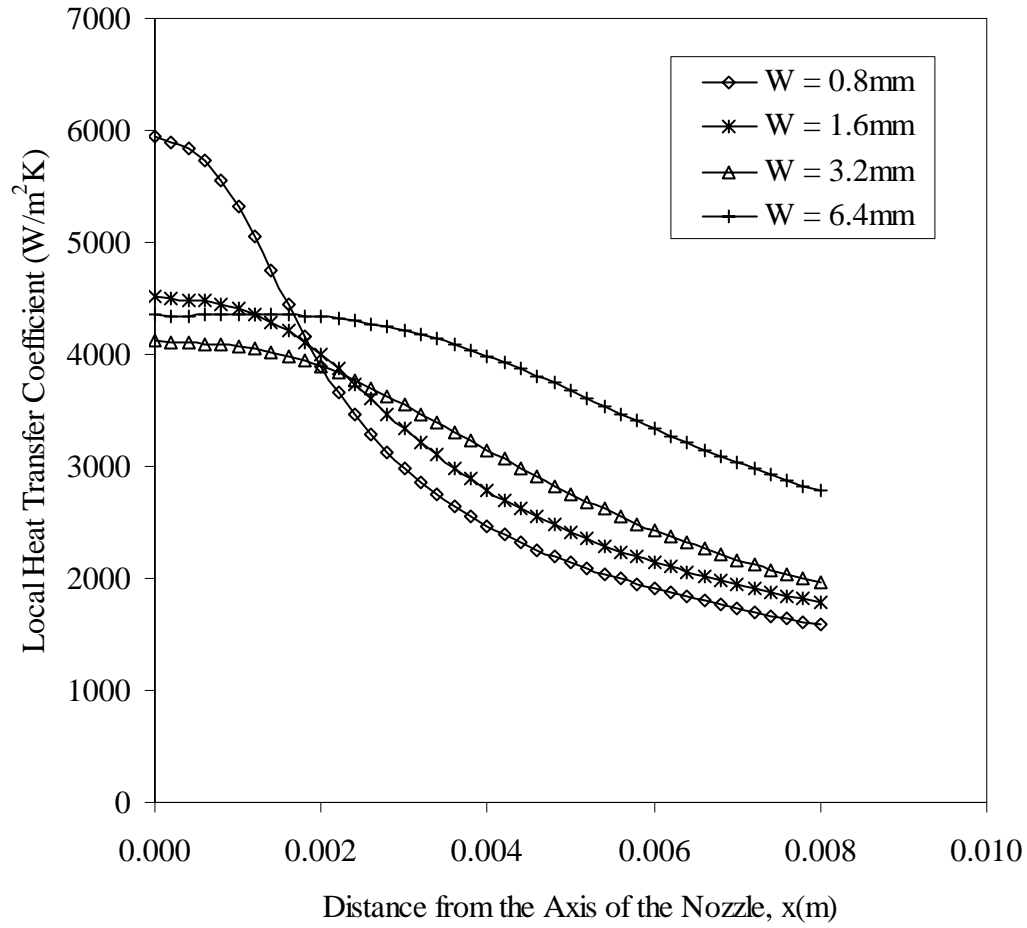


Figure 115. Local heat transfer coefficient distribution at the solid-fluid interface for different nozzle widths ( $H_n = 3.2\text{ mm}$ ,  $b = 0$ ,  $q = 250\text{ kW/m}^2$ )

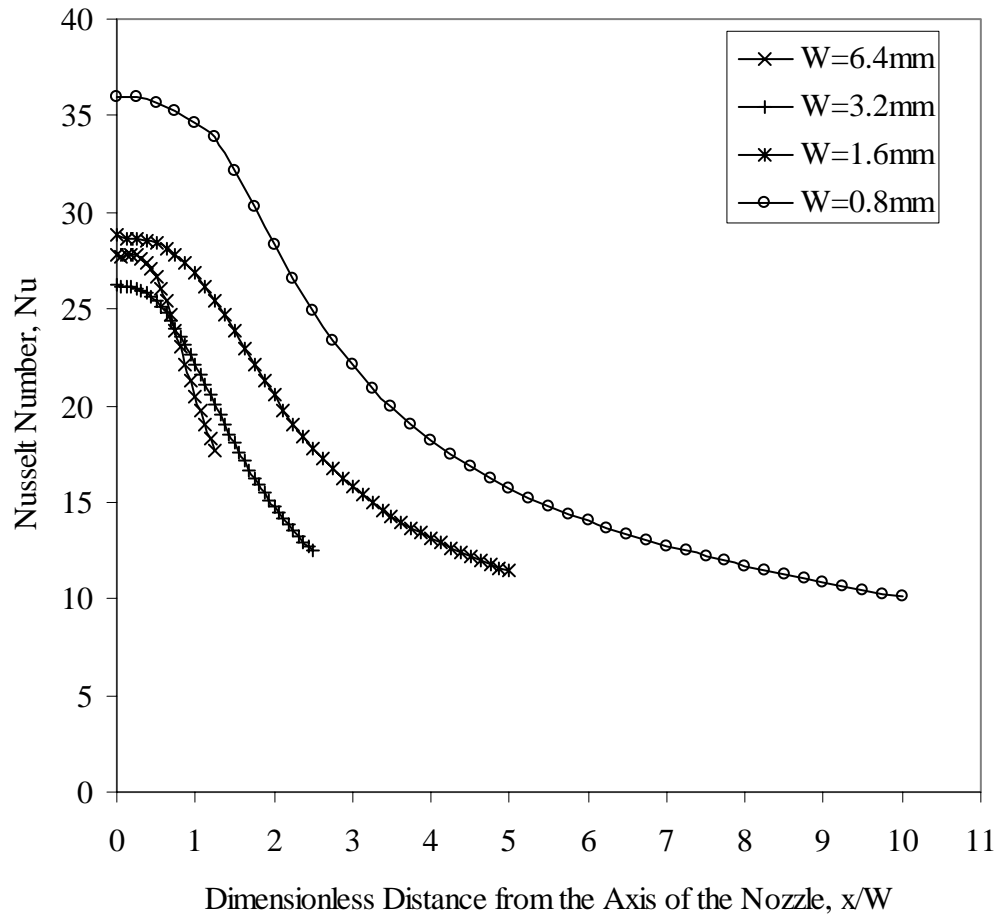


Figure 116. Local Nusselt number at the solid-fluid interface  
for different nozzle widths  
(  $H_n = 3.2\text{ mm}$ ,  $b = 0$ ,  $q = 250\text{ kW/m}^2$  )

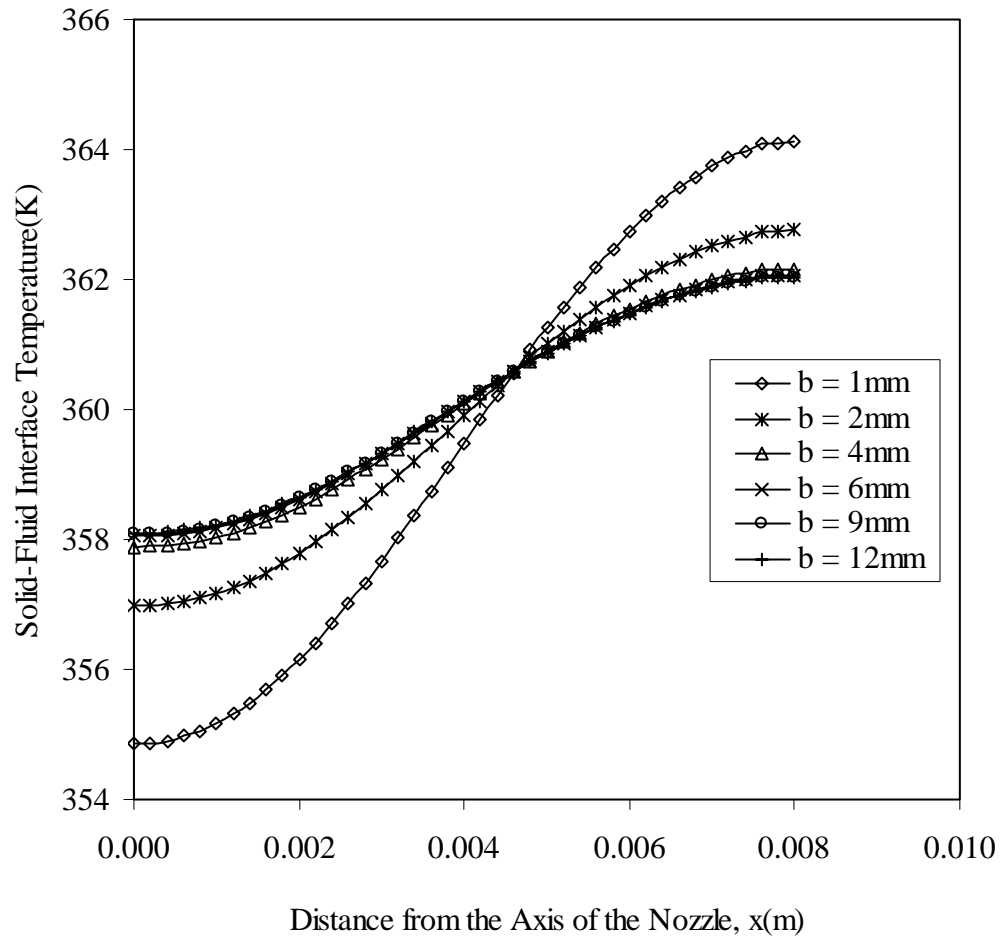


Figure 117. Local interface temperatures for six different plate thicknesses  
 (  $Re = 1545$ ,  $H_n/W = 1$ ,  $q = 250\text{ kW/m}^2$ , solid material = silicon)

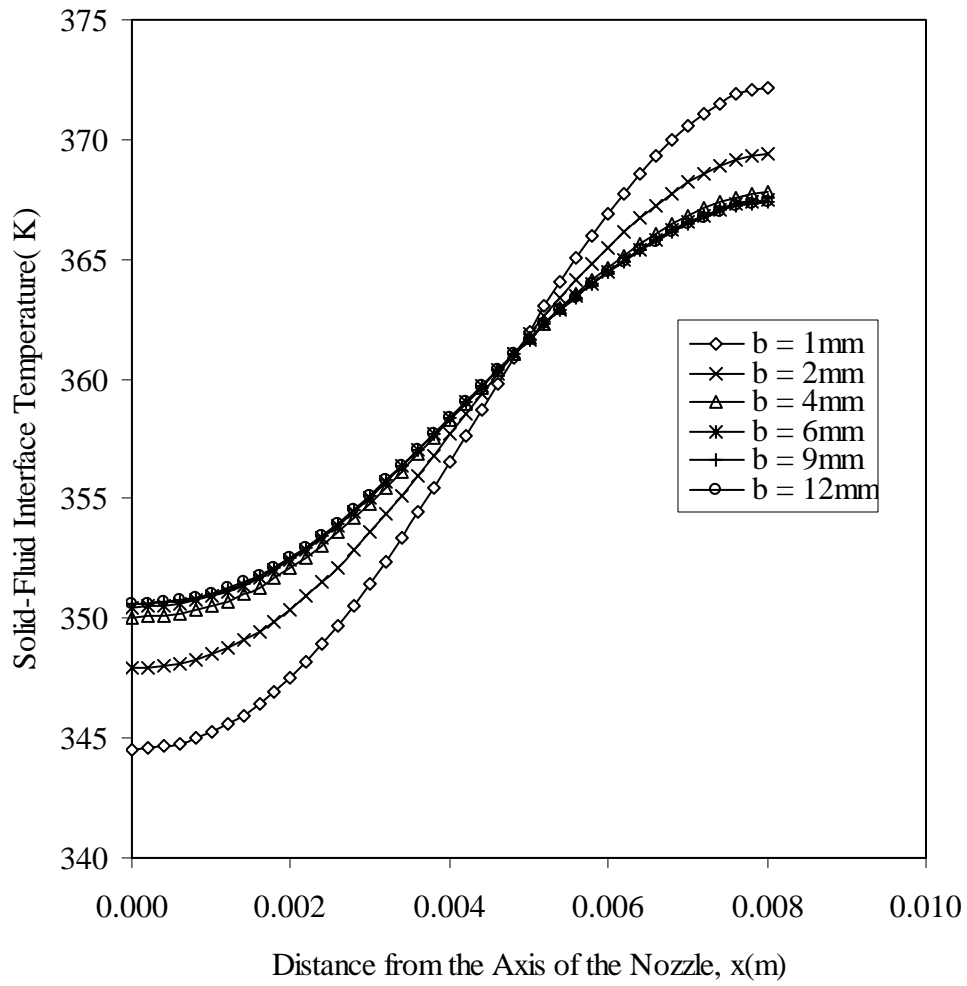


Figure 118. Local interface temperatures for six different plate thicknesses  
 ( $q = 250 \text{ kW/m}^2$ ,  $H_n/W = 1$ ,  $Re = 1545$ , solid material = Constantan)

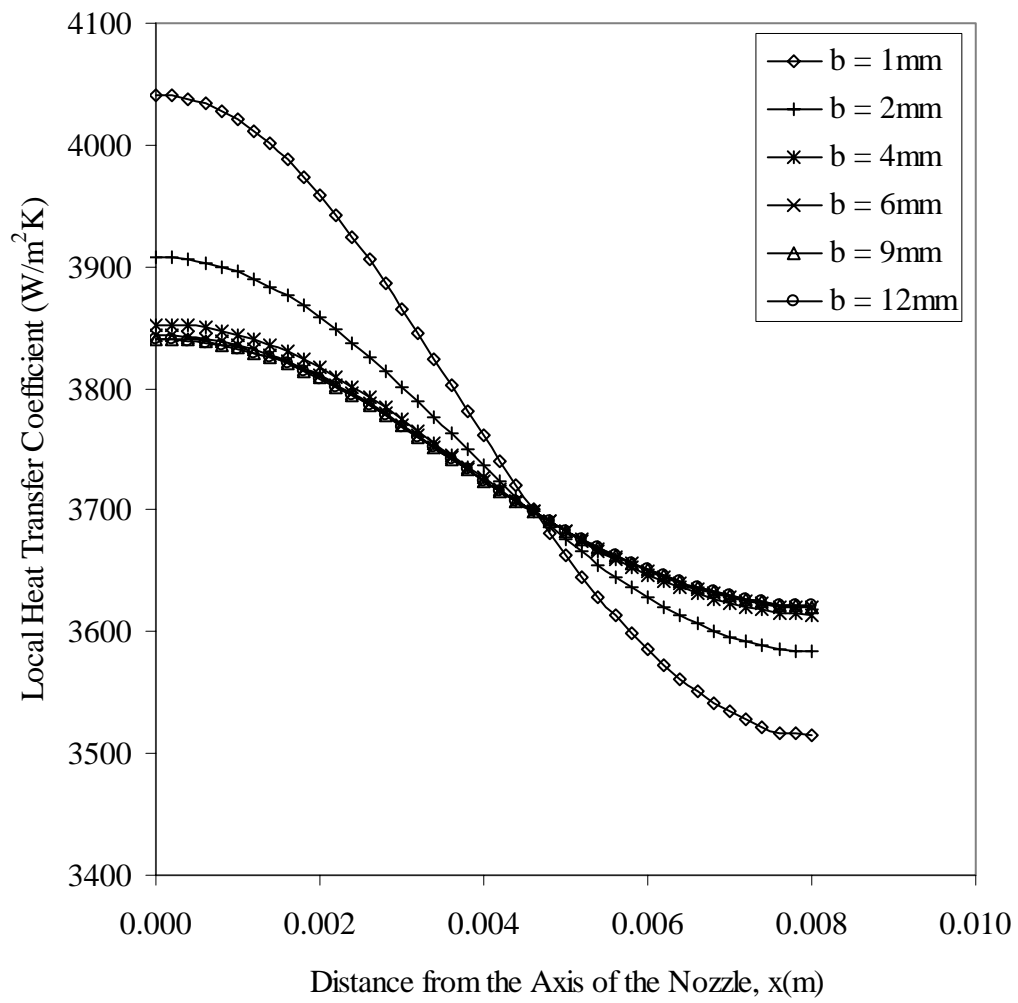


Figure 119. Heat transfer coefficient at the solid-fluid interface  
for different plate thicknesses  
(  $q = 250 \text{ kW/m}^2$ ,  $H_n/W = 1$ ,  $Re = 1545$ , solid material = Silicon )



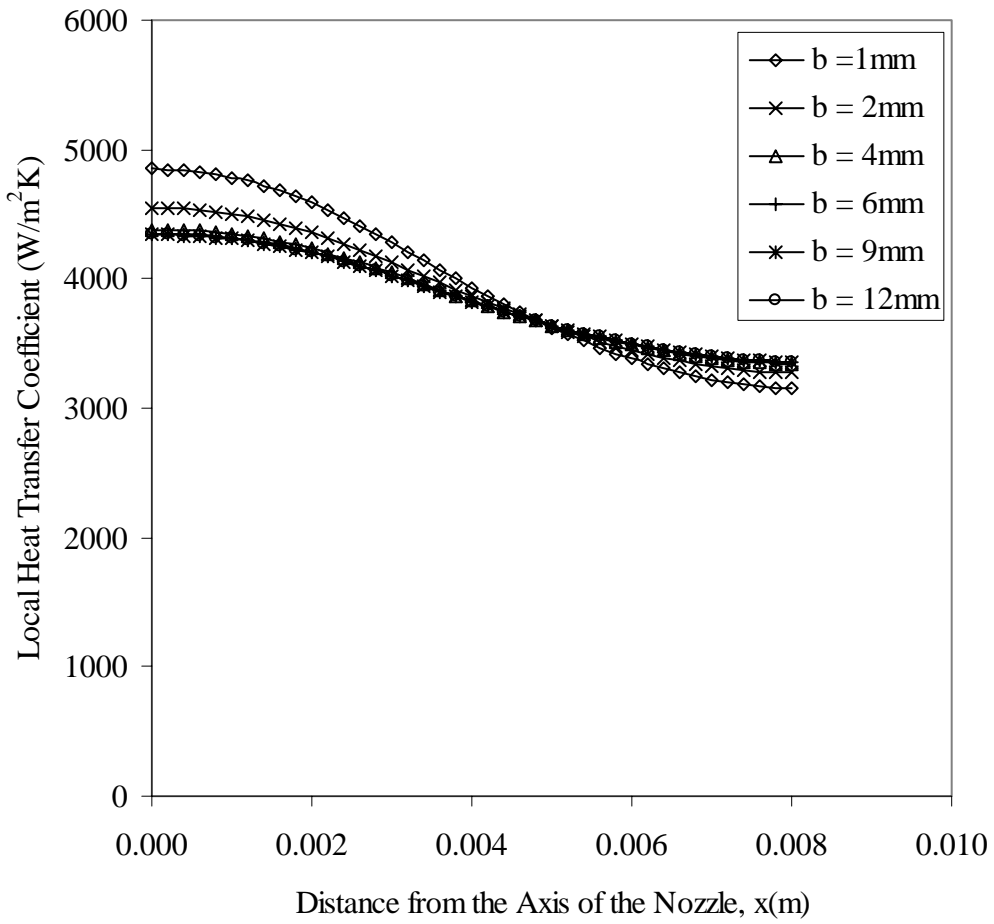


Figure 120. Heat transfer coefficient at the solid-fluid interface  
for different plate thicknesses  
( $q = 250 \text{ kW/m}^2$ ,  $H_n/W = 1$ ,  $Re = 1545$ , solid material = Constantan)

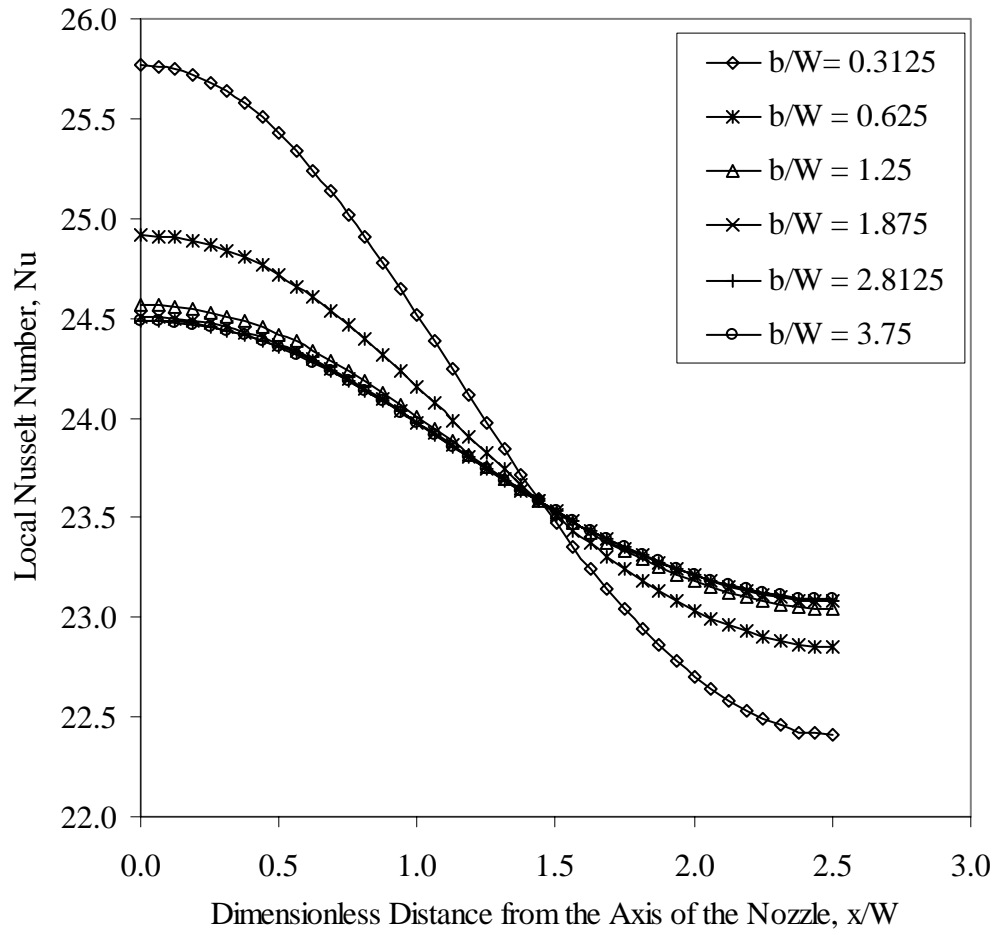


Figure 121. Local Nusselt number at the solid-fluid interface for different plate thicknesses.  
 $(q = 250 \text{ kW/m}^2, H_n/W = 1, \text{Re} = 1545, \text{solid-material} = \text{Silicon})$

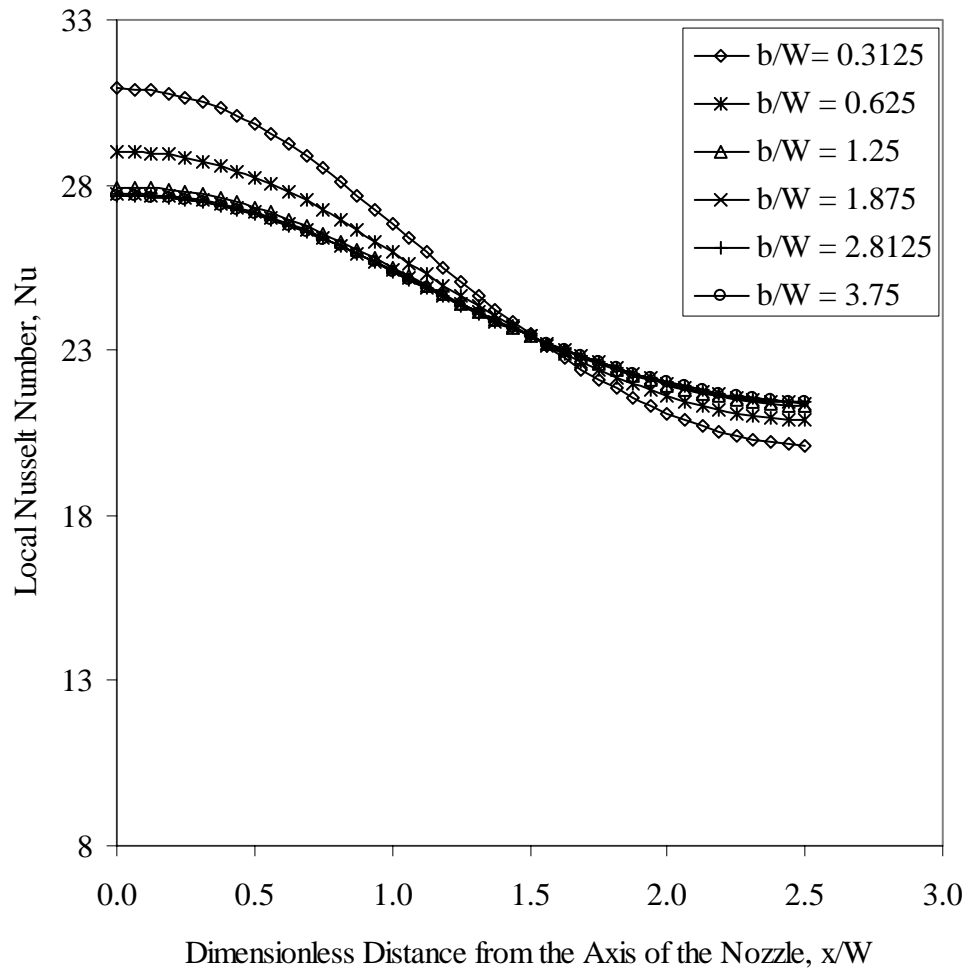


Figure 122. Local Nusselt number at solid-fluid interface  
for different plate thicknesses  
( $q = 250 \text{ kW/m}^2$ ,  $H_n/W = 1$ ,  $Re = 1545$ , solid material = Constantan)

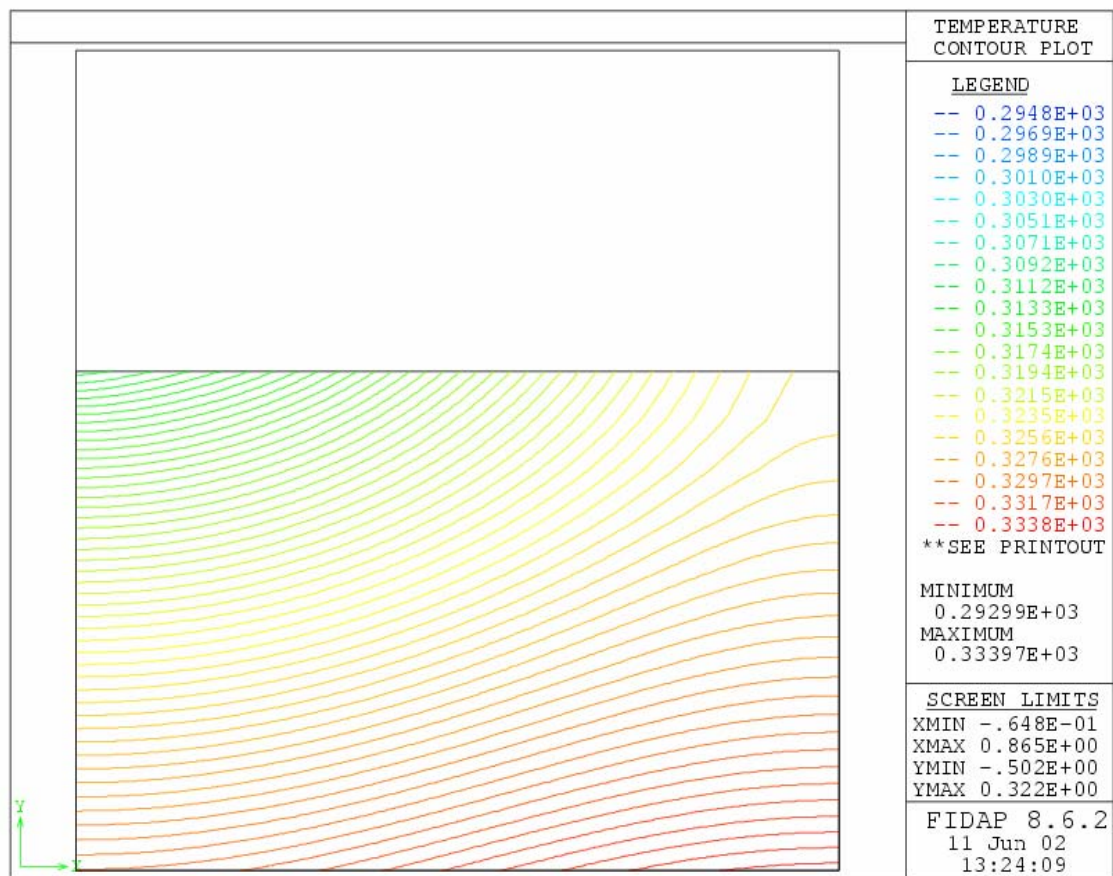


Figure 123. Isotherms in solid plate  
 (  $b = 5$  mm,  $W = 3.2$  mm,  $q = 63$  kW/m<sup>2</sup>,  $Re = 890$ ,  $H_n/W = 1$ ,  
 solid = Constantan )

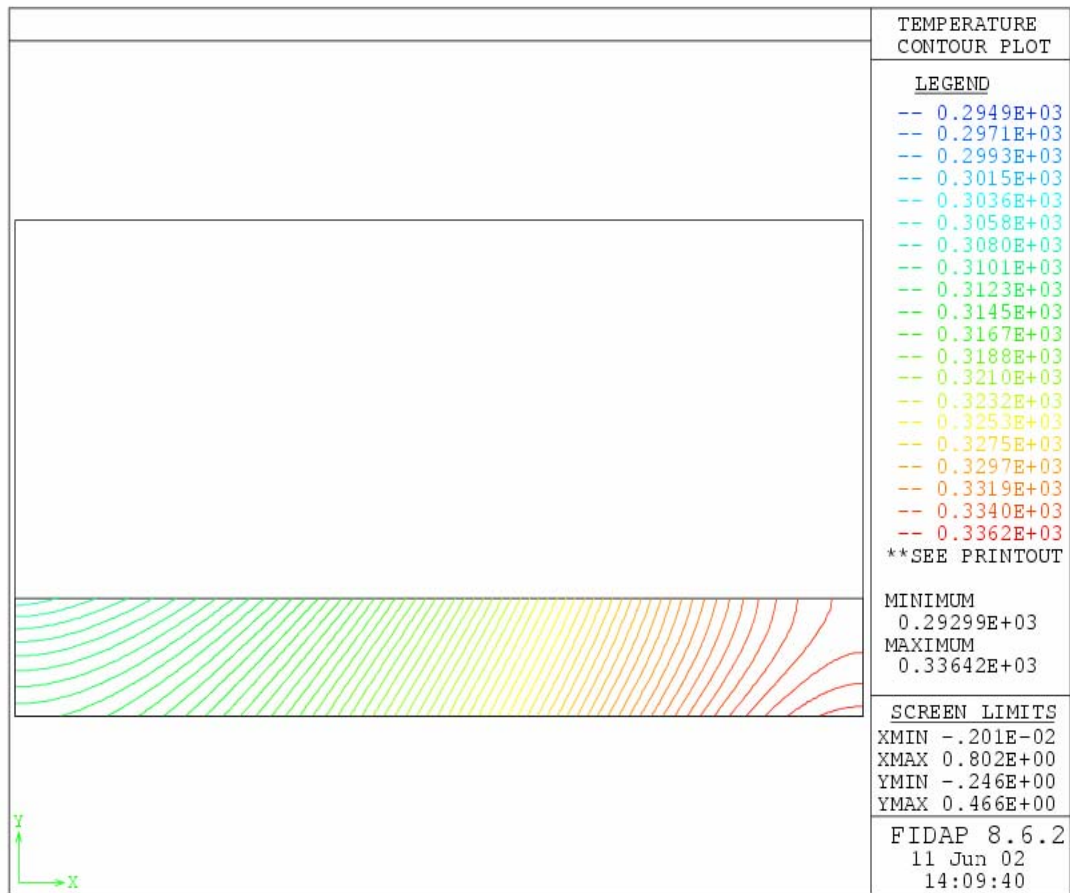


Figure 124. Isotherms in solid plate  
 (  $b = 1$  mm,  $W = 3.2$  mm,  $q = 63$  kW/m<sup>2</sup>,  $Re = 890$ ,  $H_n/W = 1$ ,  
 solid = Constantan )

# **CONFINED JET OF AMMONIA FROM A SLOT NOZZLE IMPINGING ON A PLATE WITH DISCRETE HEAT SOURCES: STEADY STATE**

## **INTRODUCTION**

In cooling electronic components, increased power densities per device and smaller spacing between the devices have necessitated the search for innovative techniques of heat dissipation. Jet impingement from a slot or axial nozzle is widely employed in industries for highly localized heating or cooling. In recent years, the demand for compactness and higher operational processors has led to high power density in electronic packages. An enhanced heat transfer method such as jet impingement will be required to provide the desired thermal environment in electronic equipment.

Impinging jets can be classified into various groups such as gas and liquid jets, and circular (also known as axisymmetric) and planar (also known as slot) jets. This work focuses only on liquid jets in slot configuration impinging on the heated plate perpendicularly. Liquid jets can be further classified into submerged and free surface jets. In the submerged configuration, the fluid exits a nozzle or orifice into a body of surrounding fluid that is the same as the jet itself. Submerged jets thus entrain surrounding fluid which may be at a different temperature. Vertical confinement of the submerged jet may also be important and influence the heat transfer if the jet is formed by an orifice plate which bounds the flow. Gravitational effects are generally smaller in submerged jets. Free surface jets result when a liquid issues from a nozzle or orifice into a gas environment. Entrainment of surrounding fluid is therefore negligible. The shape of the free surface is governed by a balance of gravity, surface tension, and pressure forces. Gravity effects are obviously very dominant in this configuration.

This study presents the numerical simulation of heat transfer to a two-dimensional (slot) submerged confined jet of ammonia impinging vertically on a solid plate heated with discrete heat sources. Ammonia was chosen as the working fluid for the simulation, because of its possible application in space based thermal management systems. All material properties ( $\rho$ ,  $\mu$ ,  $c_p$ ,  $k$ ) were allowed to vary as a function of local temperature. A conjugate model in which the heat conduction in the solid plate was included in the numerical simulation was used. A non-conjugate model (plate thickness = 0) was solved to compare the results with that of a conjugate model. Equations for the conservation of mass, momentum, and energy were solved in the fluid region. In the solid region, only the energy equation, which reduced to the heat conduction equation, had to be solved. Computations using Ammonia as the working fluid and Constantan as the plate material were carried out for four different number of heat sources, three different locations of heat sources at the bottom of the solid plate, and four different magnitudes of the heat energy.

Teuscher et al. [73] investigated FC-77 impingement on an array of discrete heat sources with pin fins and parallel plate fins used as surface modifications. The former showed an increase in heat transfer coefficient by three times while the parallel plate fins resulted in a three to five times increase. The heat transfer from discrete heat sources to single and multiple confined air jets was studied by Schroeder and Garimella [74]. The results are compared to

those previously obtained for single air jets. A reduction in orifice-to-target spacing was found to increase the heat transfer coefficient in multiple jets, with this effect being stronger at higher Reynolds numbers. With a nine-jet arrangement, the heat transfer to the central jet was higher than for a corresponding single jet. The effectiveness of single and multiple jets in removing heat from a given heat source was compared at a fixed total flow rate. El-Sheikh and Gaimella [75] experimentally investigated the enhancement of heat transfer from a discrete heat source in confined air jet impingement. The enhancement in heat transfer was found to be a strong function of nozzle diameter and heat sink footprint area; at a given flow rate, the effectiveness decreased with decreasing nozzle diameter.

We consider an axisymmetric jet discharging from a nozzle and impinging perpendicularly at the center of a solid plate subjected to heating by discrete heat sources on the opposite surface of the plate as shown in figure 125. If the fluid is considered to be incompressible and its properties (density, viscosity, thermal conductivity, and specific heat) are dependent on temperature, the equations describing the conservation of mass, momentum, and energy in Cartesian coordinates can be written as equations (41-44). Considering variable thermal conductivity, the equation describing the conservation of energy inside the solid can be written as equation (45). Equations (41-45) are subjected to the boundary conditions described by equations (46-51), (53-57), and (79).

## DISCUSSION OF RESULTS

Figure 125 shows the simulated geometry. The length of the plate ( $L = 0.008$  m) and the temperature of the jet at the nozzle exit ( $T_j = 293$  K) were kept constant during the simulation. Ammonia was used as the working fluid for the simulation, which is an emerging coolant for space based thermal management systems. The properties of ammonia are temperature dependent and for any given temperature, conductivity, viscosity, specific heat, and density can be calculated using equations (80) to (83).

$$k = 69912.953 - 1026.449T + 6.0828125T^2 - 0.018005208T^3 + 2.65625E-05T^4 - 1.5625E-08T^5 \quad (80)$$

$$\mu = -78411.526 + 1209.4674T - 7.3773828T^2 + 0.022323698T^3 - 3.3554687E-05T^4 + 2.00652083E-08T^5 \quad (81)$$

$$c_p = -14633.163 + 222.04991T - 1.345077T^2 + 0.0040670703T^3 - 6.1386719E-06T^4 + 3.7005208E-09T^5 \quad (82)$$

$$\rho = 161497.37 - 2416.6952T + 14.514766T^2 - 0.043544271T^3 + 6.5234375E-05T^4 - 3.90625E-08T^5 \quad (83)$$

Here 'T' is the absolute temperature in K. These equations were developed by fitting tabulated data for ammonia for the temperature range of 290 – 370 K as presented by Carey [76].

In order to determine the number of elements for accurate numerical solution, computations were performed for several combinations of number of elements in the x and z directions covering the solid and fluid regions. It was observed that the numerical solution becomes grid independent when the number of divisions in the x and z directions are increased over 80. Computations with 80x80 grids gave almost identical results when compared to those obtained using 160x160 grids. In order to save computer time while retaining accuracy, 80 x 80 divisions was chosen for all final computations. The error in the numerical solution can be estimated by using equation (84).

$$T = A + \frac{B}{N^e} \quad (84)$$

where A, B, and e are constants to be evaluated. N is number of divisions along an axis. T is the interface temperature at a given x-location of the plate. Equation (84) has 3 unknowns. Substituting 3 sets of temperatures taken at 3 different grid sizes results in a set of non-linear equations with three variables. Initially assuming the value of e and doing a number of iterations, the solution for e was obtained. At  $x = 0.0012$  m, the value of e obtained in the above example calculation was 8.456. The value of e should be greater than 1. Substituting e in the equations, A and B values were obtained to be 437.2701142 and -4.963956E14. The percentage error can be calculated using the following equation.

$$\left| \frac{T - A}{A} \right| \times 100 \quad (85)$$

The error at  $x = 0.0012$  m was found to be 2.612E-05% for 160 x 160 grids and 9.17E-03% for 80 x 80 grids.

Figure 126 presents the interface temperature distribution for different number of heat sources when the solid thickness is negligible ( $b = 0$ ). In this case, the total applied heat energy was kept constant. The heat flux was obtained by dividing the total energy by the total heated area of the plate. For continuous heating (one heat source), the value of heat flux was  $250 \text{ kW/m}^2$ . The value of heat flux for three heat sources was  $450 \text{ kW/m}^2$ . Similarly for four heat sources and seven heat sources cases, the heat fluxes applied were  $464 \text{ kW/m}^2$  and  $480 \text{ kW/m}^2$ , respectively. It can be observed that for a single heat source case, the minimum temperature is present at the stagnation point. For multiple heat sources case, the temperature increased as the fluid moved downstream along the heater. The temperature dropped in the region where heat is not applied. The drastic change in temperature throughout the interface for multiple sources of heat is because of the mixing of low density hot fluid near the plate with high density cold fluid away from the plate (outside the thermal boundary layer). It is observed that the temperature at the stagnation point is highest for the seven heat sources because of the application of larger amount of heat flux when compared to other three cases. As the number of heat sources reduced, the temperature at the stagnation point also decreased. The discrete heating resulted in periodic rise and fall of interface temperature along the heated and unheated regions of the plate. For all different cases, the temperature varied around the curve for continuous heating (heat sources = 1) because the total thermal energy input was kept constant. Figure 127 shows the bulk temperature of the fluid (Ammonia). The bulk temperature of the fluid increased gradually for a single heat source case because of the uniform application of heat flux. In case of discrete heating, the bulk temperature increases linearly in the region where the heat source is present because of the addition of heat by uniform heat flux. The fluid bulk temperature remains unchanged throughout the area where heat flux is zero. Since the total energy applied is the same for both uniform



heating and discrete heating, the fluid bulk temperature at the exit end of the plate is the same for all the cases. Figure 128 shows the heat transfer coefficient along the interface. It may be noted that unlike continuous heating, the discrete heating does not give the highest heat transfer coefficient at the stagnation point. Because of the absence of heat flux in certain regions during discrete heating, the heat transfer coefficient in those regions is zero. In each heated region, the local heat transfer coefficient is highest at the leading edge of the heat source, and it gradually decreases as the flow moves downstream. This behavior is expected because of repeated growth of thermal boundary layer in the fluid adjacent to the heater. As the number of heat sources increased, the value of maximum local heat transfer coefficient increased. A similar behavior is observed in figure 129 where the variation of Nusselt number at the solid-fluid interface has been plotted. Average values of heat transfer coefficient and Nusselt number are shown in Table 6. It can be observed in the table that the average heat transfer coefficient value is highest for uniform heating case. For discrete heating, the average heat transfer coefficient value and the average Nusselt number value increased with increase in number of heat sources.

Figure 130 presents the solid-fluid interface temperature distribution for different number of heat sources with solid (Constantan). Total heat energy applied was kept constant. Figures 131, 132, and 133 present the variations of fluid bulk temperature, local heat transfer coefficient, and Nusselt number. Because of the poor thermal conductivity of Constantan, we can clearly see that the temperature distribution inside the solid is periodic for the cases of three sources and four sources. The solid-fluid interface temperature is minimum at the stagnation point and the maximum at the edge of the plate. This is due to the development of the thermal boundary layer. The interface temperature at the axis of impingement ( $x = 0$ ) is highest for uniformly heated plate (one heat source). This is opposite to that seen in the non-conjugate model (figure 126). This is because of the distribution of heat by conduction within the solid. It may be noticed that for heat sources = 1 or 7, the bulk temperature increases more or less uniformly along the plate whereas for 3 or 4 heat sources, less increase in unheated regions is clearly observed. This is because of larger spacing between the heat sources in these cases. As the total energy applied is constant, the fluid bulk temperature at the exit end of the plate is the same for all cases considered here. The local heat transfer coefficient and local Nusselt number are highest at the stagnation point. A gradual decrease downstream is seen for both 1 and 7 heat sources. In the case of 3 and 4 heat sources, the heat transfer coefficient tend to remain constant or increase slightly in the unheated region. Due to larger spacing of heat sources in these two cases, the interfacial heat flux as well as temperature distribution in that region play a more significant role in the overall distribution of heat transfer coefficient. The average heat transfer coefficient value is highest for uniform heating case. We can clearly see that for discrete heating, with the increase in number of heat sources, there is increase in both average heat transfer coefficient value as well as the average Nusselt number value. It is expected that for large number of heat sources, these will become equivalent to those for single heat source (uniformly heated plate) case.

Figures 134-137 show the variations of temperature at the solid-fluid interface, fluid bulk temperature, heat transfer coefficient and Nusselt number respectively for different number of heat sources when the heat flux at the sources were kept at a constant value. As we have applied same heat flux, it can be observed from figure 134 that the temperature at the stagnation point is same for all single and multiple heat source cases. But for multiple heat source cases, because of the absence of heat at particular regions and also because of the mixing of hot fluid with the cold

fluid, the temperature gradually decreased, reached minimum and then increased to a maximum value where heat is applied. Figure 135 shows the variation of fluid bulk temperature along the interface. Since the total energy applied is not the same for all the cases, the fluid bulk temperature at the exit end of the plate is not the same for all cases. Analogous to figure 127, there is no increase in bulk fluid temperature in the unheated region when the plate thickness is zero. High variation in fluid bulk temperature along the length of the plate is observed for uniformly heated plate because of the highest energy applied here when compared to other cases. As the number of heat sources increased, the total energy applied decreased and the variation of the fluid bulk temperature along the interface is less. In figure 136, for multiple heat sources case, it can be clearly seen that wherever heat is not applied the heat transfer coefficient dropped to zero, raised to a value at the beginning of the heated region and then gradually decreased throughout the heated region due to the development of thermal boundary layer. A similar trend can be seen with Nusselt number in figure 137. The highest local Nusselt number is obtained for seven heat sources, the maximum number of sources used in this investigation. The average values of heat transfer coefficient and Nusselt number for these cases is listed in the Table 6. Because of the application of constant heat flux, the variation in average values of heat transfer coefficient and Nusselt number for multiple heat sources is very significant. Highest average heat transfer coefficient value is observed for uniform heating. The Nusselt number for continuous heating is about 1.5 times that of Nusselt number for three heat sources case. There is not much variation in the value of average Nusselt number in all discrete heating cases.

Figure 138 shows the variation of solid-fluid interface temperature with solid (Constantan). Since the heat flux at the sources was kept at a constant value, the temperature at the stagnation point is higher when the plate is uniformly heated. As the number of heat sources increased, the temperature at the stagnation point decreased. A periodic distribution of solid-fluid interface temperature can be observed from figure 138 for three and four heat source cases. But as the number of heat sources increases, the distribution of heat becomes more and more uniform because of the reduced distance between the heat sources. Figure 139 shows the fluid bulk temperature along the length of the plate. Since the total energy applied is highest in uniform heating, the variation of the fluid bulk temperature is high here. As the number of heat sources increased, the variation of the fluid bulk temperature has decreased and has shown lowest in the case of seven heat sources because of the least energy applied in the present investigation. But the overall variation is low in multiple heat sources cases because of the lower total energy applied when compared to uniform heating. And also there is not a significant difference in fluid bulk temperature variation in multiple heat source cases because there is not a significant difference in the total energies applied in multiple heat sources cases. Figures 140 and 141 show the variation of local heat transfer coefficient and local Nusselt number. The local heat transfer coefficient and Nusselt number are maximum for the uniformly distributed heat case and decreased with number of heat sources. But the difference is negligible in case of multiple heat sources cases. Average values of heat transfer coefficient and Nusselt number are listed in Table 6. We can clearly see the decrease in average values with the increase in number of heat sources. However, the difference is not that significant between different multiple heat source cases. This trend can be related to total heat energy applied to the plate. There is only a very small difference between total energy for different cases of discrete heating considered here, whereas the total energy for continuous heating (heat source = 1) is significantly higher. The value of  $E$  for the cases of 1, 3, 4, and 7 sources were 2000 W/m, 1111 W/m, 1077 W/m, 1040 W/m, respectively.

## NOMENCLATURE

$b$	Thickness of the disk [m]
$c_p$	Specific heat at constant pressure [kJ / kg K]
$E$	Total applied thermal energy [kW/m]
$g$	Acceleration due to gravity [ $\text{m} / \text{s}^2$ ]
$h$	Heat transfer coefficient using bulk temperature [ $\text{W} / \text{m}^2 \text{ K}$ ], $q_{int}/(T_{int} - T_b)$
$H_n$	Height of the nozzle from the plate [m]
$k$	Thermal conductivity [ $\text{W} / \text{m K}$ ]
$L$	Length of the plate [m]
$Nu$	Nusselt number using bulk temperature, $hW / k_f$
$p$	Pressure [Pa]
$q$	Heat flux [ $\text{W} / \text{m}^2$ ]
$q_{int}$	Interface heat flux, $k_f (T_{int} - T_1)/\Delta z$
$Re$	Reynolds number, $Wv_j / \nu_f$
$T$	Temperature [K]
$T_j$	Jet temperature [K]
$T_1$	Temperature in the fluid at $\Delta z$ above the interface [K]
$v_j$	Jet velocity [ $\text{m} / \text{s}$ ]
$v_x$	Velocity component in the x-direction [m/s]
$v_z$	Velocity component in the z-direction [m/s]
$W$	Width of the slot nozzle [m]
$x$	Coordinate parallel to the plate [m]
$z$	Coordinate perpendicular to the plate [m]
$\Delta z$	Distance between the interface and the node just above the interface [m]

### Greek Symbols

$\mu$	Dynamic viscosity of fluid [ $\text{m}^2 / \text{s}$ ]
$\rho$	Density [ $\text{kg} / \text{m}^3$ ]

### Subscripts

av	Average
b	Bulk or mixed mean
f	Fluid
int	Solid - fluid interface
s	Solid
w	Bottom surface of the plate

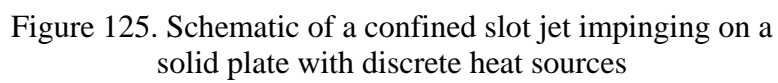
## CONCLUSIONS

The solid-fluid interface temperature as well as the heat transfer coefficient (or Nusselt number) shows a strong dependence on the number of heat sources, their magnitudes and location, and plate material properties. For a given constant total heat energy, the following conclusions can be drawn from the numerical results: (1) The temperature at the stagnation point

reduced with the decrease in number of heat sources. (2) The average heat transfer coefficient and the average Nusselt number values increased with increase in number of heat sources in both conjugate and non-conjugate models. (3) The effect of number of heat sources is negligible when the solid conductivity is high. (4) The average heat transfer coefficient is highest for uniform heating when compared to discrete heating. (5) The isothermal lines inside the solid showed that beyond a critical thickness, the plate presented a one dimensional heat conduction in regions away from the impingement plane and the heated surface, and therefore did not exert much influence in convection heat transfer process. When the heat flux at the sources were kept at a constant value, the highest average heat transfer coefficient was observed for uniform heating in both conjugate and non-conjugate models. For discrete heating, the magnitude and the geometric location of heat sources influenced the maximum temperature as well as local distribution of heat transfer coefficient.

Table 6. Average heat transfer coefficient and Nusselt number for a discretely heated plate

Material	Fluid	Re	W (cm)	b (cm)	$V_j$ (cm/s)	Number of Heat Sources	Heat source Type	Position/ Magnitude of heat sources	$H_n$ (cm)	$h_{av}$ (W/m <sup>2</sup> K)	$Nu_{av}$
-	Ammonia	890	0.32	0	9.672	1	Constant power	a/M	0.32	3525.58	22.48
-	Ammonia	890	0.32	0	9.672	3	Constant power	a/M	0.32	1289.46	8.26
-	Ammonia	890	0.32	0	9.672	4	Constant power	a/M	0.32	1305.53	8.32
-	Ammonia	890	0.32	0	9.672	7	Constant power	a/M	0.32	1314.29	8.38
Constantan	Ammonia	890	0.32	0.1	9.672	1	Constant power	a/M	0.32	4784.47	30.50
Constantan	Ammonia	890	0.32	0.1	9.672	3	Constant power	a/M	0.32	3656.74	23.31
Constantan	Ammonia	890	0.32	0.1	9.672	4	Constant power	a/M	0.32	3861.78	24.62
Constantan	Ammonia	890	0.32	0.1	9.672	7	Constant power	a/M	0.32	4270.98	27.23
-	Ammonia	890	0.32	0	9.672	3	Constant heat flux	a/M	0.32	2423.27	15.45
-	Ammonia	890	0.32	0	9.672	4	Constant heat flux	a/M	0.32	2377.81	15.16
-	Ammonia	890	0.32	0	9.672	7	Constant heat flux	a/M	0.32	2445.87	15.59
Constantan	Ammonia	890	0.32	0.1	9.672	3	Constant heat flux	a/M	0.32	4321.68	27.55
Constantan	Ammonia	890	0.32	0.1	9.672	4	Constant heat flux	a/M	0.32	4268.17	27.21
Constantan	Ammonia	890	0.32	0.1	9.672	7	Constant heat flux	a/M	0.32	4203.56	26.80



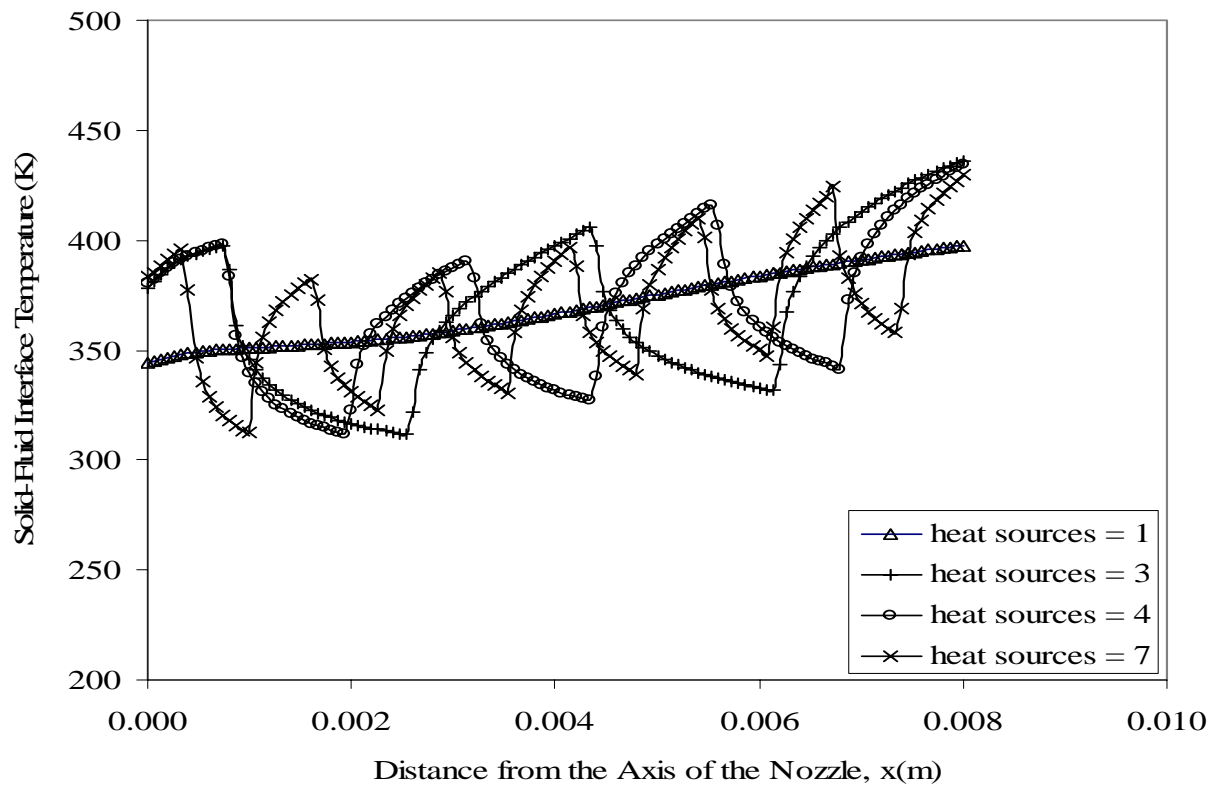


Figure 126. Temperature at the interface for different discrete heat sources with constant total power ( $W = 3.2$  mm,  $E = 2$  kW/m,  $H_n/W = 1$ ,  $b = 0$ ,  $Re = 890$ )

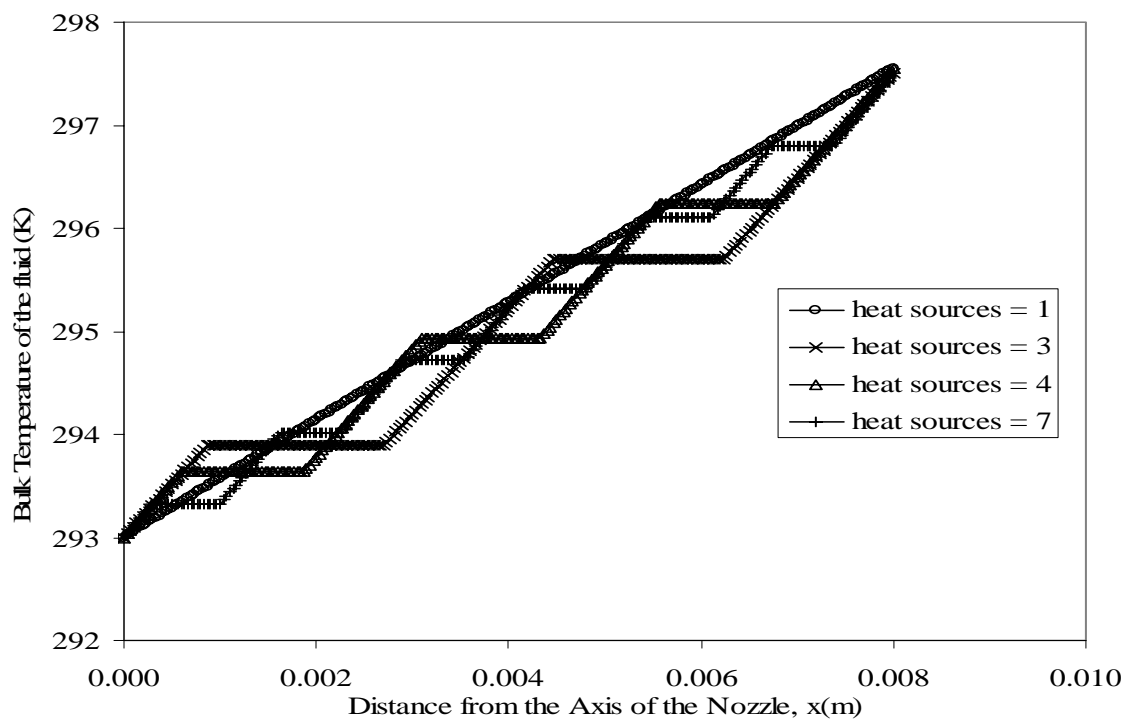


Figure 127. Bulk temperature of the fluid for different discrete heat sources with constant total power ( $W = 3.2$  mm,  $E = 2$  kW/m,  $H_n/W = 1$ ,  $b = 0$ ,  $Re = 890$ )

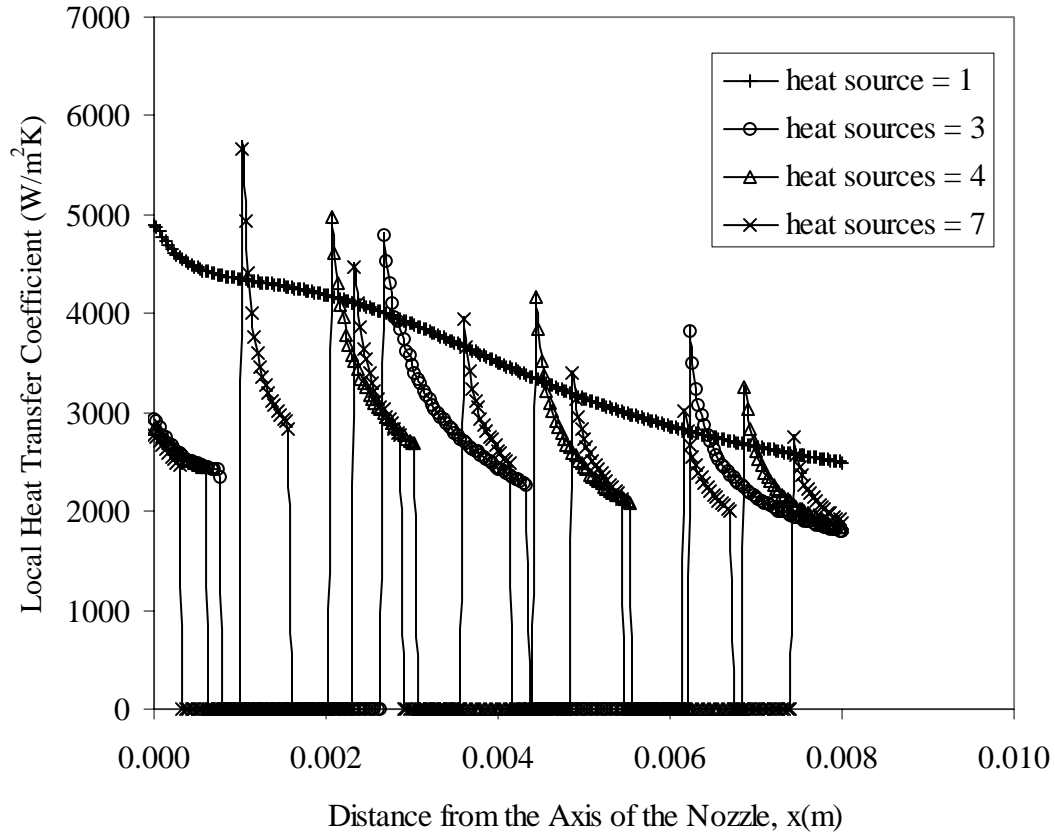


Figure 128. Heat transfer coefficient at the interface using bulk temperature for different discrete heat sources with total power constant ( $W = 3.2 \text{ mm}$ ,  $E = 2 \text{ kW/m}$ ,  $H_n/W = 1$ ,  $b = 0$ ,  $Re = 890$  )



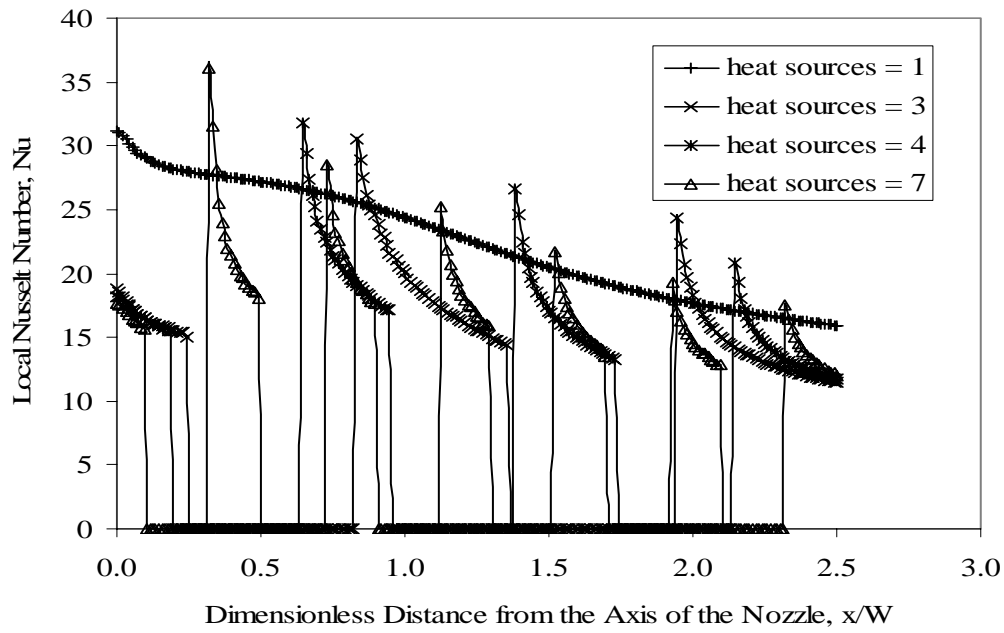


Figure 129. Nusselt number at the interface using bulk temperature for different discrete heat sources with total power constant ( $W = 3.2$  mm,  $b = 0$ ,  $E = 2$  kW/m,  $Re = 890$ ,  $H_n/W = 1$ )

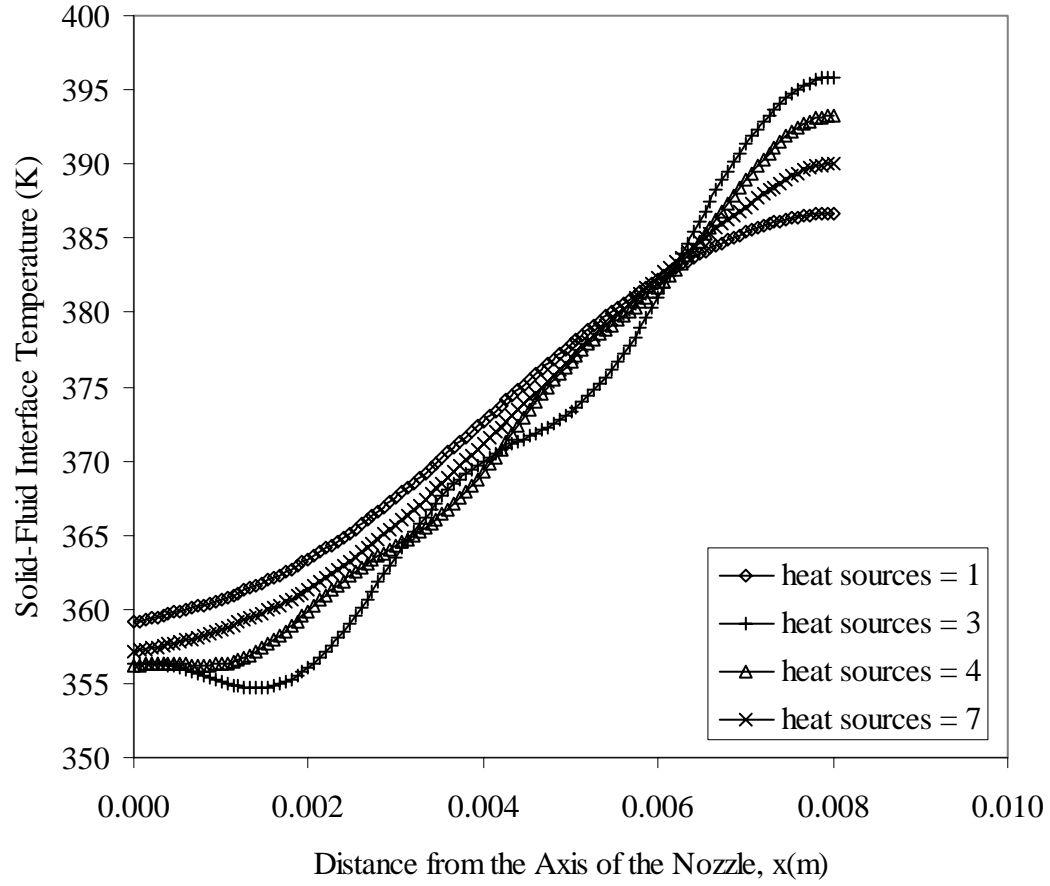


Figure 130. Temperature at the interface for different discrete heat sources with total power constant ( $b = 1$  mm,  $W = 3.2$  mm,  $H_n/W = 1$ ,  $E = 2$  kW/m,  $Re = 890$ , solid = Constantan )

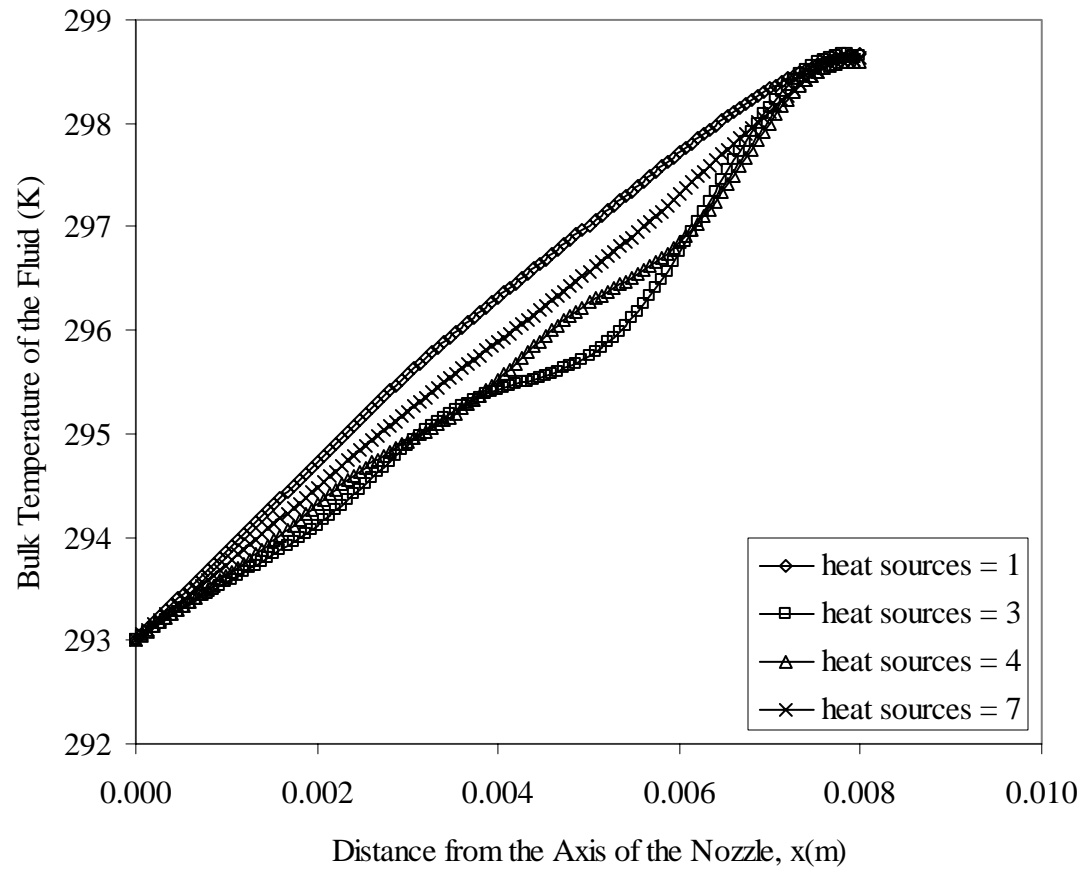


Figure 131. Bulk temperature of the fluid for different discrete heat sources with total power constant ( $b = 1$  mm,  $W = 3.2$  mm,  $H_n/W = 1$ ,  $E = 2$  kW/m,  $Re = 890$ , solid = Constantan )

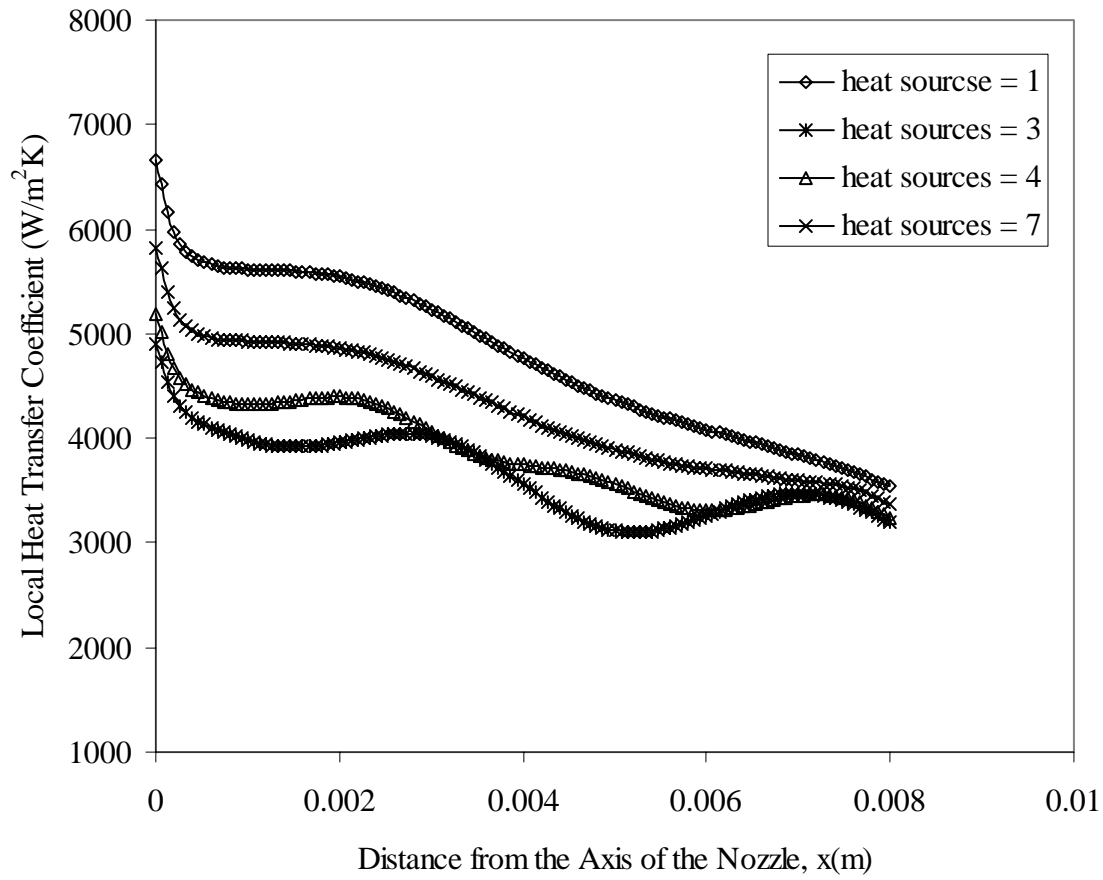


Figure 132. Heat transfer coefficient at the interface using bulk temperature for different discrete heat sources with total power constant ( $b = 1$  mm,  $W = 3.2$  mm,  $H_n/W = 1$ ,  $E = 2$  kW/m,  $Re = 890$ , solid = Constantan)

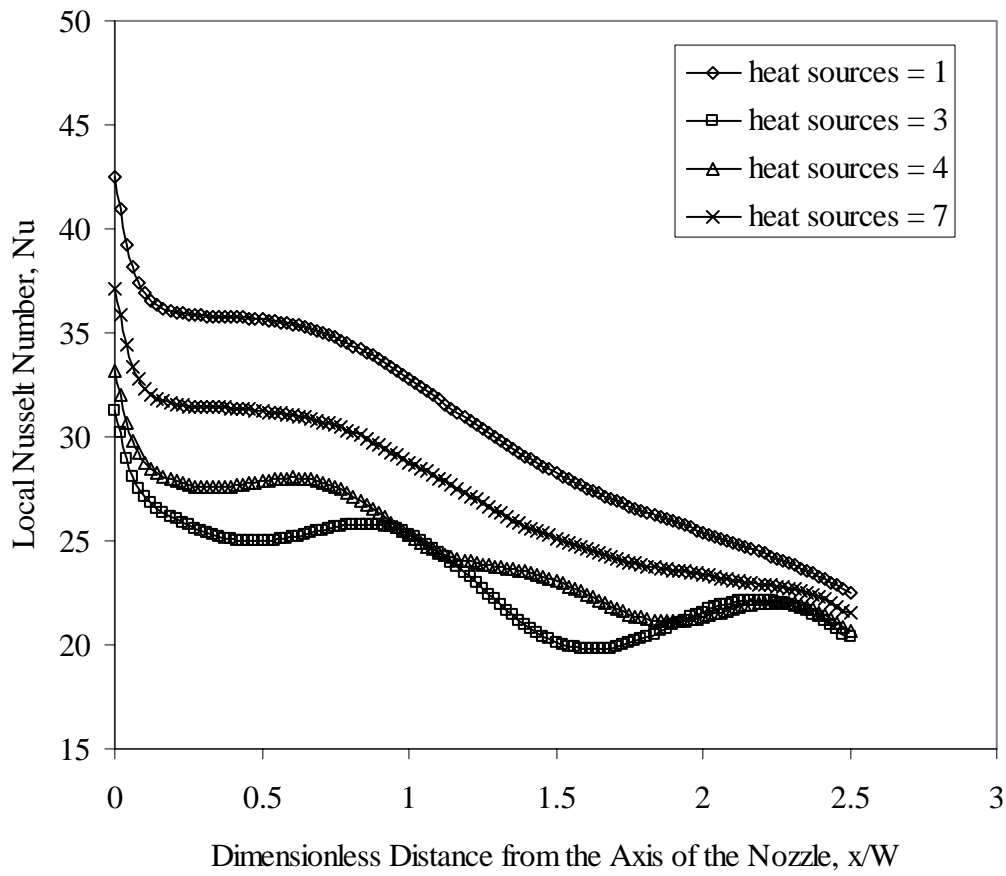


Figure 133. Nusselt number at the interface using bulk temperature for different discrete heat sources with total power constant ( $W = 3.2$  mm,  $b = 1$  mm,  $E = 2$  kW/m,  $Re = 890$ ,  $H_n/W = 1$ , solid = Constantan)

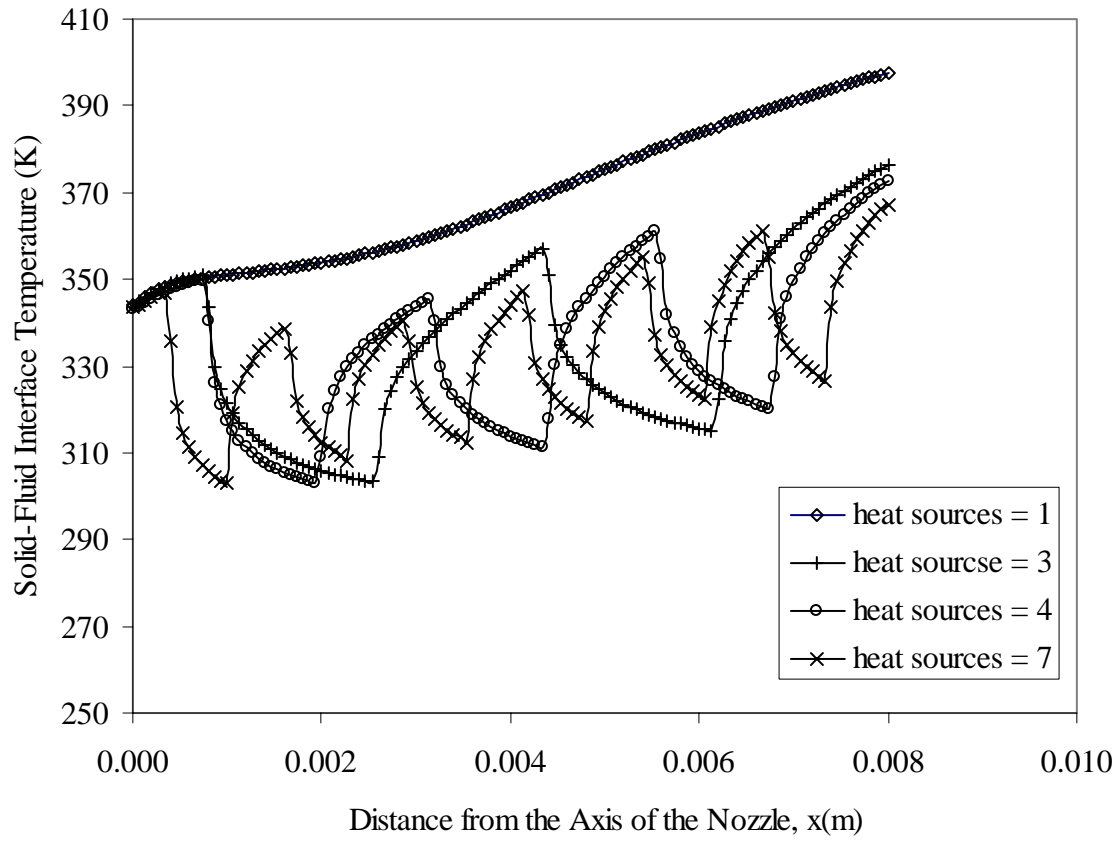


Figure 134. Temperature at the solid-fluid interface for different discrete heat sources with constant heat flux ( $W = 3.2 \text{ mm}$ ,  $q = 250 \text{ kW/m}^2$ ,  $Re = 890$ ,  $b = 0$ ,  $H_n/W = 1$ )

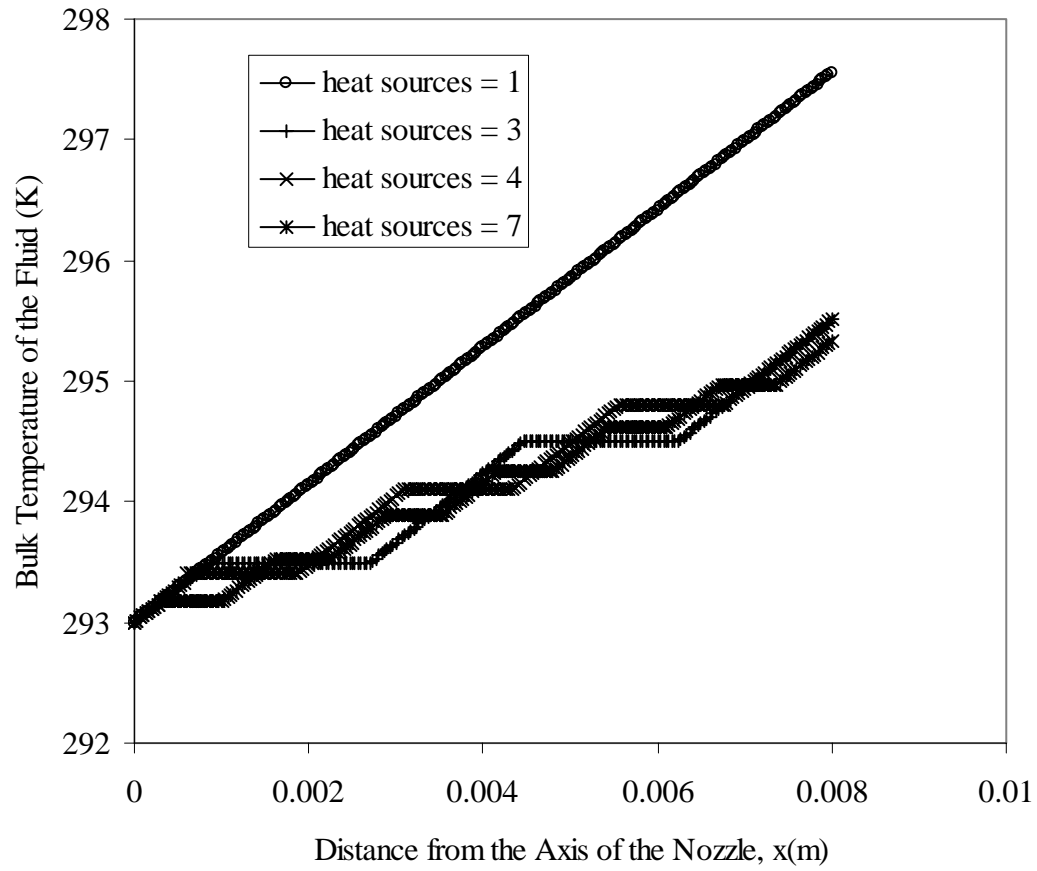


Figure 135. Bulk temperature at the solid-fluid interface for different discrete heat sources with constant heat flux ( $W = 3.2 \text{ mm}$ ,  $q = 250 \text{ kW/m}^2$ ,  $Re = 890$ ,  $b = 0$ ,  $H_n/W = 1$ )

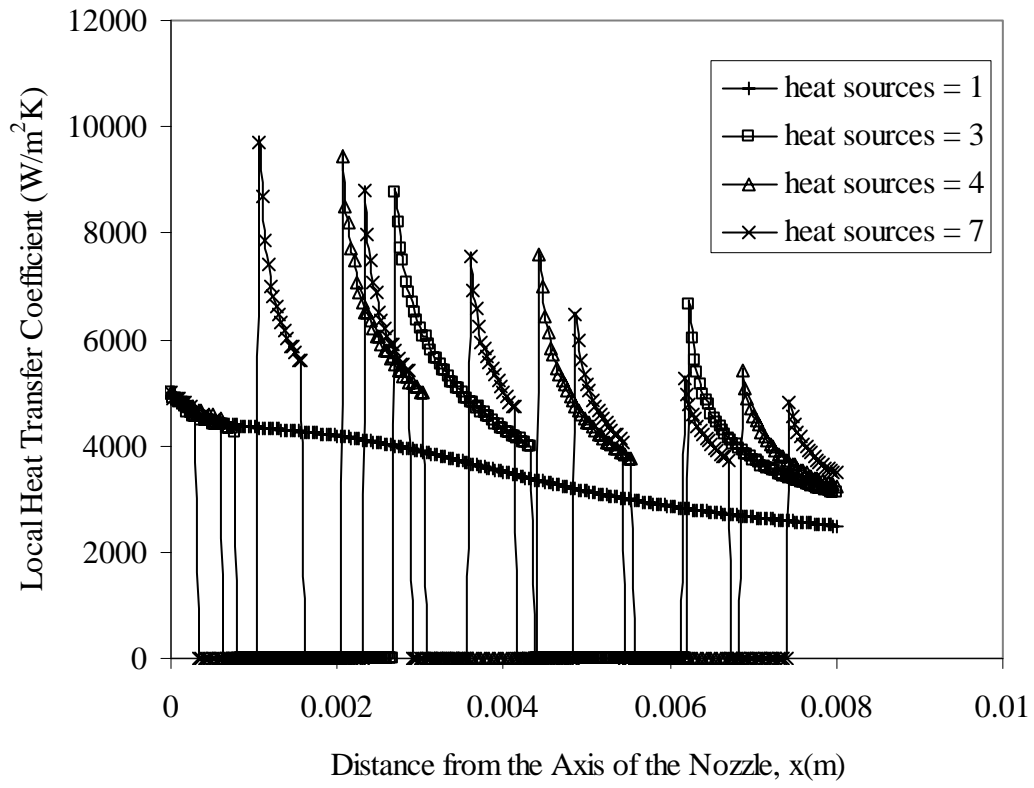


Figure 136. Heat transfer coefficient at the solid-fluid interface using bulk temperature for different discrete heat sources with constant heat flux ( $W = 3.2$  mm,  $q = 250$  kW/m<sup>2</sup>,  $Re = 890$ ,  $b = 0$ ,  $H_n/W = 1$ )



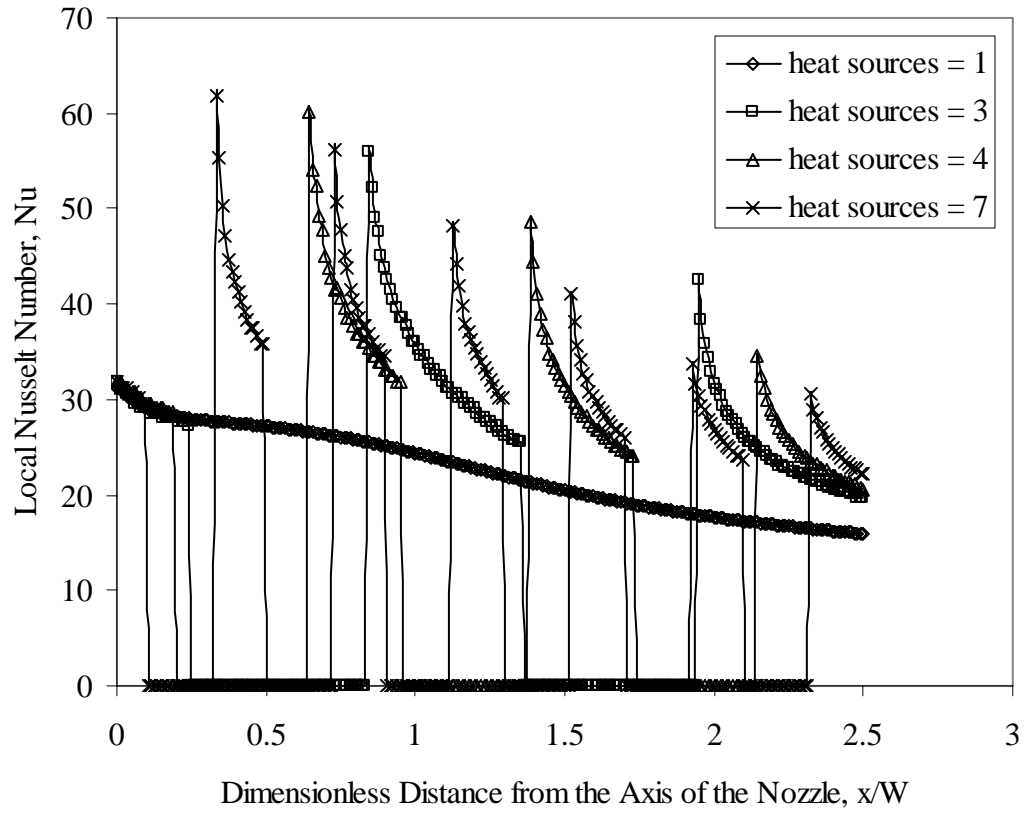


Figure 137. Nusselt number at the solid-fluid interface using bulk temperature for different discrete heat sources with constant heat flux ( $W = 3.2$  mm,  $q = 250$  kW/m<sup>2</sup>,  $Re = 890$ ,  $b = 0$ ,  $H_n/W = 1$ )

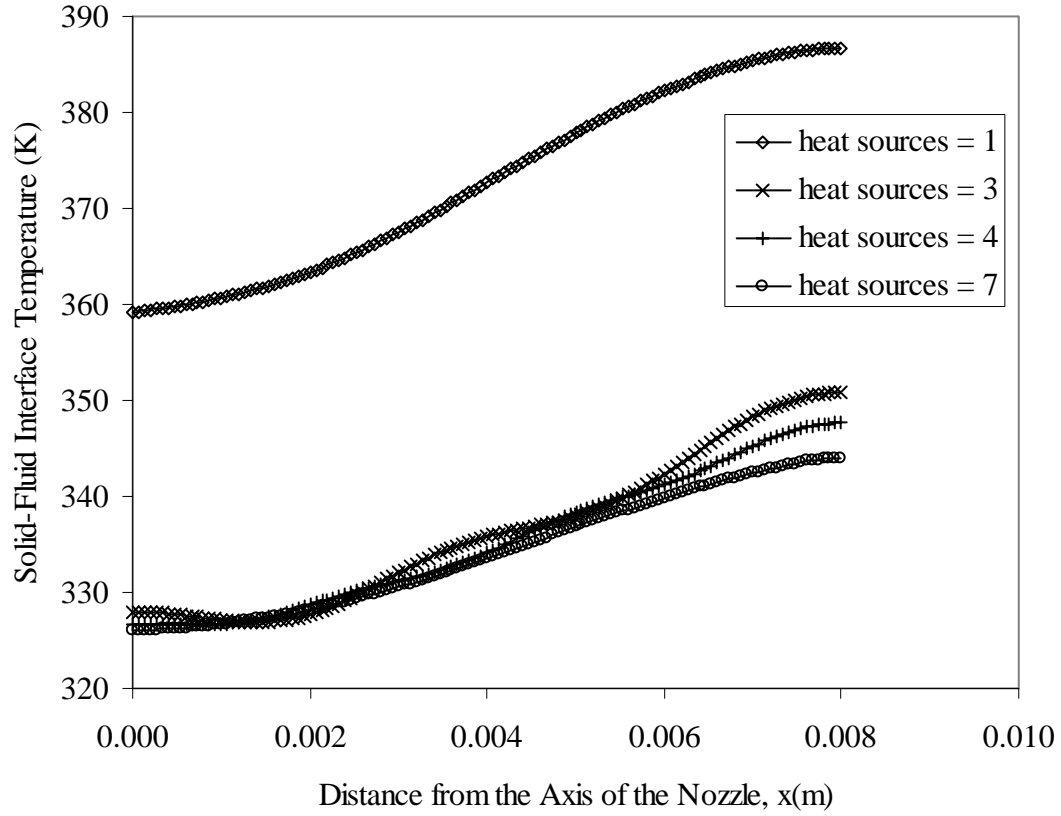


Figure 138. Temperature at the solid-fluid interface for different discrete heat sources with heat flux constant ( $W = 3.2$  mm,  $b = 1$  mm,  $q = 250$  kW/m<sup>2</sup>,  $Re = 890$ ,  $H_n/W = 1$ , solid = Constantan)

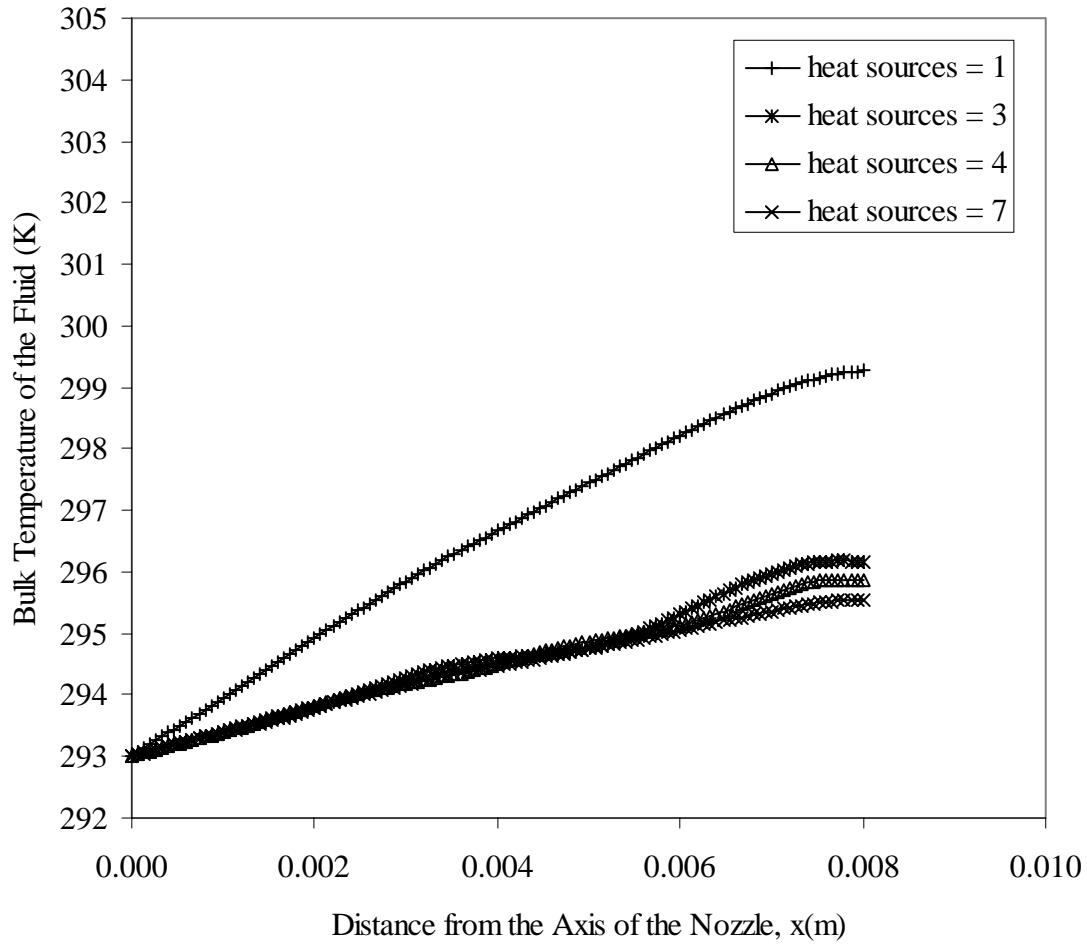


Figure 139. Bulk temperature of the fluid for different discrete heat sources with heat flux constant ( $W = 3.2$  mm,  $b = 1$  mm,  $q = 250$  kW/m<sup>2</sup>,  $Re = 890$ ,  $H_n/W = 1$ , solid = Constantan)

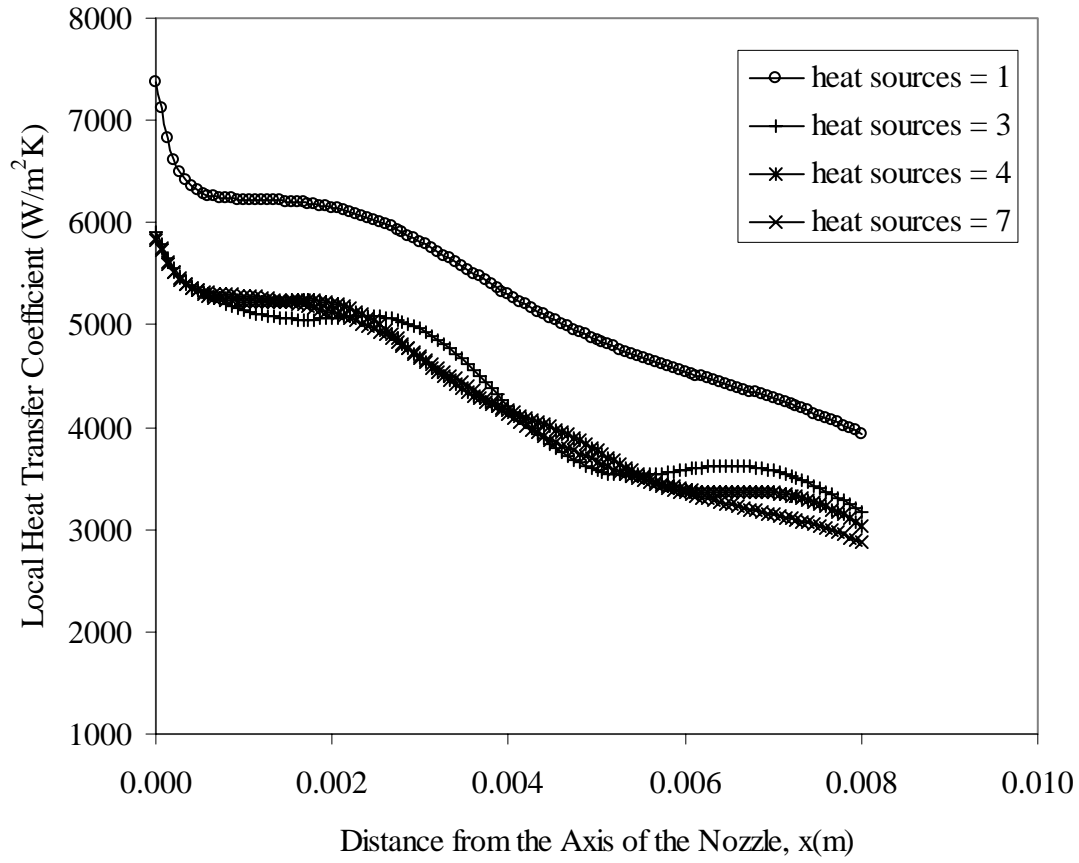


Figure 140. Heat transfer coefficient at the solid-fluid interface using bulk temperature for different discrete heat sources with heat flux constant ( $W = 3.2$  mm,  $b = 1$  mm,  $q = 250$  kW/m<sup>2</sup>,  $Re = 890$ ,  $H_n/W = 1$ , solid = Constantan)

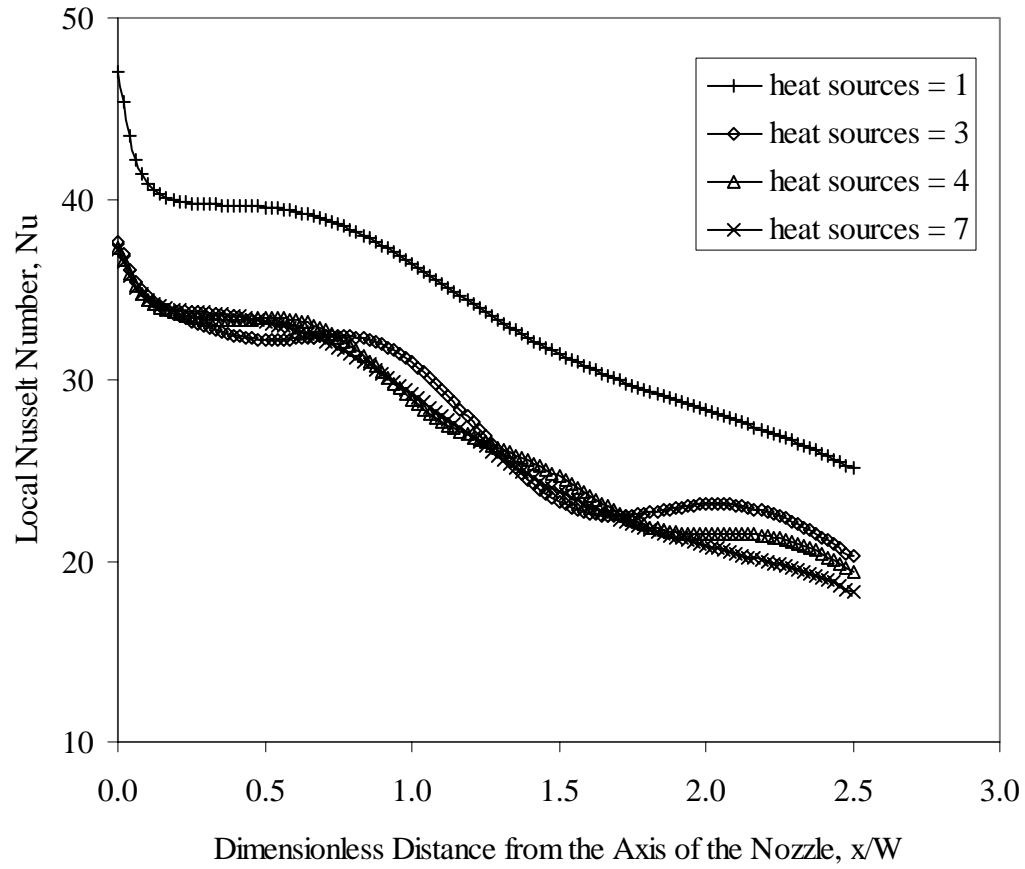


Figure 141. Nusselt number at the solid-fluid interface using bulk temperature for different discrete heat sources with heat flux constant ( $W = 3.2$  mm,  $b = 1$  mm,  $q = 250$  kW/m<sup>2</sup>,  $Re = 890$ ,  $H_n/W = 1$ , solid = Constantan)

# **CONFINED AXIAL JET OF AMMONIA IMPINGING ON A UNIFORMLY HEATED DISK: STEADY STATE**

## **INTRODUCTION**

This study presents the steady state analysis of heat transfer to an axi-symmetric, confined, submerged fluid jet impinging vertically on a flat disk as shown in figure 142. The jet impinges perpendicularly on the impingement disk (solid disk placed under the nozzle, also called as the target disk) of finite thickness and spreads out radially. The radial fluid flow is confined in a narrow channel bounded by the confinement disk and the impingement disk. Confinement disk is placed at the same level as the exit of the jet nozzle. Confinement of jet might be important and affect the transfer process. A number of different regions can be identified in the flow resulting from the impingement of the fluid jet on the target disk. They are: stagnation region, transition region, wall jet region, flow separation region, and developing channel flow region. Confinement disk is well insulated and hence there is no heat transfer along that wall. Ammonia is used as the primary working fluid. The diameter of the impingement disk is kept constant throughout the study. Steady state analysis was performed in two stages. The first stage involves a non-conjugate problem (zero disk thickness) where only the fluid region is considered and in the second stage, a conjugate problem in which the heat conduction in the solid disk was included in the numerical simulation model was considered.

The jet discharges from a nozzle and impinges perpendicularly at the center of a solid disk subject to constant heat flux. Equations describing the conservation of mass, momentum, and energy in cylindrical coordinates can be written as equation (1-5). The boundary conditions can be described by equations (6-12) and the following equation.

$$\text{At } z = b + H, \quad \frac{d}{2} \leq r \leq r_d: \quad v_r = 0, \quad v_z = 0, \quad \frac{\partial T_f}{\partial z} = 0 \quad (86)$$

The local and average heat transfer coefficients can be defined as

$$h = \frac{q}{(T_{\text{int}} - T_j)} \quad (87)$$

$$h_{av} = \frac{2}{r_d^2} \int_0^{r_d} h r dr \quad (88)$$

## **DISCUSSION OF RESULTS**

Figure 142 shows the simulated geometry. Ammonia is used as the primary working fluid and Silicon as the disk material. During some of the runs, the fluid was changed to FC-77 or Mil-7808 to explore the affects of fluid properties. Temperature of the jet at the nozzle ( $T_j = 293 \text{ K}$ ) and the radius of the solid disk ( $r_d = 0.008\text{m}$ ) were kept constant during the simulation. In order to determine the number of elements for accurate numerical solution, computations were performed for several combinations of number of elements in the r and z directions covering the solid and the fluid regions. The solid-fluid interface temperature for these simulations is plotted in figure 143. It can be observed that the numerical solution becomes grid independent when the number of divisions in the r and z directions is increased over 80. Results obtained for 80 x 80

and 160 x 160 grids were almost identical. In order to reduce the computational time while retaining the accuracy, 80 x 80 grid was chosen for all final computations.

Figure 144 presents the solid-fluid interface temperature distribution for different Reynolds number. It is observed that the minimum temperature is obtained at the stagnation point and the maximum at the edge of the disk. As expected, the interface temperature as well as the minimum to maximum temperature difference at the interface decreases with Reynolds number because of more fluid flow rate to carry away the heat. Figures 145 and 146 show the variations in local heat transfer coefficient and Nusselt number. In these simulations constant nozzle diameters of 3.2mm and  $H / d$  ratio of 1 have been used. Also, in figure 146, dimensionless distance ( $r / d$ ) was used to match with the dimensionless Nusselt number. The overall values of the local heat transfer coefficient and hence the local Nusselt number increases with jet inlet Reynolds number over the entire solid-fluid interface. This is because of the higher velocity of the fluid impinging on the disk. Figures 147 and 148 show the streamline contours and the velocity vectors respectively with Reynolds number of 668 and heat flux of  $250 \text{ kW/m}^2$ . The streamlines indicate that the flow after leaving the nozzle moves vertically downward and turns by an angle of  $90^\circ$  as it reaches the disk. The jet expands as it moves down towards the disk. The streamlines show clearly that the flow changes direction along the solid disk towards the outflow region, the streamlines within the parallel flow zone reflect the hydrodynamic boundary layer. Above the hydrodynamic boundary layer and towards the outflow, the streamline pattern indicates a recirculation zone. This recirculation region depends on the fluid velocity and the impingement height. At smaller nozzle height, due the growth of the hydrodynamic boundary layer and the consequent expansion of wall jet, the mainstream flow may encompass the entire region all the way to the confinement disk.

Figure 148, the velocity plot, shows that the velocity decreases gradually until the fluid strikes the solid surface at which point there is a rapid deceleration while the flow changes direction parallel to the solid disk. There is a brief acceleration along this so called parallel flow zone for a distance of about half the nozzle diameter after which the fluid decelerates gradually all the way to the outflow. The development of the hydrodynamic boundary layer topped by a rapidly moving fluid as a wall jet is apparent in the velocity pattern. It can be also seen that the magnitude of the fluid velocity in the recirculation zone is an order of magnitude smaller compared to the mainstream flow.

Figures 149, 150, 151 show the variations of solid-fluid interface temperature, heat transfer coefficient, and the Nusselt number, respectively with radial distance for various nozzle diameters maintaining a constant flow rate. The interface temperature increases outwardly with radial distance and the lowest temperature is found at the stagnation point located at the center of the disk. It may be noted that near the stagnation point, temperature is lower for a smaller jet diameter. The lower interface temperature is the result of larger convective heat transfer rate caused by higher jet velocity. When the flow rate is kept constant, a smaller nozzle opening results in larger impingement velocity that consequently contributes to larger velocity of fluid moving along the disk (within the boundary layer as well as in the wall jet). As the fluid moves downstream, the larger momentum caused by high velocity in smaller diameter nozzle dies down and the interface temperature curves cross each other resulting in the highest interface temperature for the smallest diameter nozzle at the outer edge of the disk.

From figures 150 and 151, it can be noticed that the heat transfer rate at the impingement region can be augmented by a great extent if the nozzle diameter is reduced. For an eight-fold reduction in nozzle opening diameter, the peak value of local heat transfer coefficient increases by almost 5 times. Due to more rapid decrease from the peak in the case of smaller opening, the average values of heat transfer coefficient does not increase much, but still of the order of 2 times for the radius of the disk considered in the present investigation. The above observation suggests that a smaller nozzle diameter is more desirable in nozzle design because of larger convective heat transfer rate at the solid-fluid interface for any given fluid flow rate.

Figures 152, 153, and 154 show the variations in interface temperature, heat transfer coefficient, and Nusselt number, respectively with radial distance for various nozzle diameters. Inlet jet velocity was kept constant in these simulations. Since the jet diameter is used as the length scale for Reynolds number, the Reynolds number varies in these runs. In addition, the flow rate increases with increase in nozzle diameter. There is a crossover over of local distributions of temperature as well as the heat transfer coefficient as the nozzle diameter is varied. The minimum temperature and the highest local values of heat transfer coefficient are still obtained for the nozzle diameter of 0.008m, the lowest diameter considered in the present investigation. However, this run also results in the lowest heat transfer coefficient at the exit end of the disk. The local values of the Nusselt number increase with nozzle diameter because of the larger impingement region as well as larger flow rate to carry away the heat.

Computations were also done to explore the effects of impingement height on the solid-fluid interface temperature. Four different nozzle to disk heights of  $H/d = 1, 2, 4$ , and 5 were modeled using ammonia as the working fluid and silicon of 5mm thickness as the solid. Figures 155-157 show the results for interface temperature, local heat transfer coefficient, and Nusselt number.  $H/d = 5$  gives the lowest interface temperature and consequently the highest heat transfer coefficient and Nusselt number. As  $H/d$  is decreased to 4, local interface temperature increases and the heat transfer coefficient and the Nusselt number decrease. The results for  $H/d = 2$  and  $H/d = 4$  are almost identical. However, as the  $H/d$  is further decreased to 1, local interface temperature decreases and the heat transfer coefficient and the Nusselt number increase.

Figures 158 and 159 show plots of temperature at the solid-fluid interface against the distance from the axis of impingement for silicon and Constantan respectively and for different solid thicknesses. In all cases, it is evident that the interface temperature is sensitive to the solid thickness especially at the stagnation point where rather significantly lower temperatures are observed as the solid wafer reduces to 1mm thickness ( $b/d = 0.3125$ ). At higher thickness in the region of 4-12mm, the changes in stagnation point temperatures are relatively lower. It may be noticed that there is a larger range of interface temperature for smaller disk thickness. As the thickness increases, the interface temperature becomes more uniform due to distribution of heat within the solid by conduction. For a given heat flux, the magnitude of interface temperature is controlled by the thermal conductivity of the disk material. Since Constantan has a smaller thermal conductivity compared to silicon, its range of temperature variation is also larger.

Figures 160 and 161 show the steady state distribution of local heat transfer coefficient for different disk thicknesses and the corresponding plots for local Nusselt number are shown in



figures 162 and 163. A higher variation is seen for a disk with smaller thickness. As the thickness increases, the distribution of local heat transfer coefficient becomes more uniform. Analogous to the interface temperature plot, beyond the disk thickness of 4mm, the distribution does not change very significantly indicating that the overall transport is dominated by convection at the interface and not by conduction within the solid. Figure 164 shows the variation of temperature at the solid-fluid interface for two different solid materials at the same thickness of 3.2 mm. The temperature values are found to be sensitive to thermal conductivity of the solids with Constantan giving the lower temperature at the stagnation point and the higher temperature at the outlet. This is consistent with the fact that it has the lower thermal conductivity when compared with silicon, implying that silicon has higher stagnation point temperature and lower outlet temperature. This shows that a larger thermal conductivity allows a better distribution of heat within the solid. It follows trivially that a plot of the local heat transfer coefficient would simply give the diametrically opposite effect with Constantan having the higher local heat transfer coefficient at the stagnation point and the lower at the outlet. This is shown in figure 165. Figure 166 shows the variation of Nusselt number for these materials. As expected, the Nusselt number is highest at the stagnation point and decreases gradually downstream. The crossover of the curves for both materials, seen in figures 164-166 is also expected because the fluid flow rate and the heat flux at the bottom of the disk remain constant.

Figures 167-169 compare the results of present working fluid (ammonia) with two other coolants that have been considered in previous thermal management studies, namely FC-77 and Mil-7808. It may be noticed that ammonia gives much lower interface temperature and much higher heat transfer coefficient compared to both FC-77 and Mil-7808. The Nusselt number, however, is highest for FC-77, primarily because of its lower thermal conductivity compared to the other two fluids. The superior thermal performance of ammonia may be useful for its applications as a working fluid in thermal management systems for aircraft and spacecraft.

## NOMENCLATURE

$b$	Thickness of the disk [m]
$c_p$	Specific heat at constant pressure [kJ / kg K]
$d$	Inlet nozzle diameter [m]
$g$	Acceleration due to gravity [m / s <sup>2</sup> ]
$h$	Heat transfer coefficient [W / m <sup>2</sup> K]
$H$	Height of the nozzle from the target disk [m]
$k$	Thermal conductivity [W / m K]
$Nu$	Nusselt number, [ $h d / k_f$ ]
$p$	Pressure [Pa]
$r_d$	Radius of the impingement disk [m]
$Re$	Reynolds number, [ $d v_j / \nu_f$ ]
$T_{int}$	Interface temperature [K]
$T_j$	Temperature of the jet [K]
$q$	Heat flux [kW / m <sup>2</sup> ]
$v_j$	Jet velocity [m / s]

### **Greek Symbols**

$\mu$	Dynamic viscosity of fluid [kg / m s]
$\nu$	Kinematic viscosity [m <sup>2</sup> /s]
$\rho$	Density [kg / m <sup>3</sup> ]

### **Subscripts**

av	Average
f	Fluid
int	Solid – fluid interface
max	Maximum
s	Solid

## **CONCLUSIONS**

The following specific conclusions could be drawn from the numerical results:

1. Local heat transfer coefficient at the solid-fluid interface was found to be sensitive to nozzle inlet Reynolds number with higher overall values for higher Reynolds number.
2. Local heat transfer coefficient at the solid-fluid interface was sensitive to distance from the axis of impingement. At the stagnation point, local values of heat transfer coefficient was highest because of the pronounced convective effects. Heat transfer then reduced gradually towards the outflow boundary.
3. Local heat transfer coefficient at the solid-fluid interface was sensitive to the nozzle diameter. For a given flow rate, a higher heat transfer coefficient was obtained with smaller diameter.
4. Local heat transfer coefficient was sensitive to the distance of the disk from the nozzle (impingement height).
5. The distribution of local heat transfer coefficient was found to be sensitive to the thickness of the disk. A higher heat transfer coefficient at the impingement location was seen at a smaller thickness, whereas a thicker plate provided a more uniform distribution of heat transfer coefficient.
6. The values of the local heat transfer coefficient at the solid-fluid interface also depended on disk material properties. Materials with a higher thermal conductivity provided more uniform distribution of interface temperature as well as the heat transfer coefficient.
7. Compared to Mil-7808 and FC-77, ammonia provided much smaller solid-fluid interface temperature and higher heat transfer coefficient.

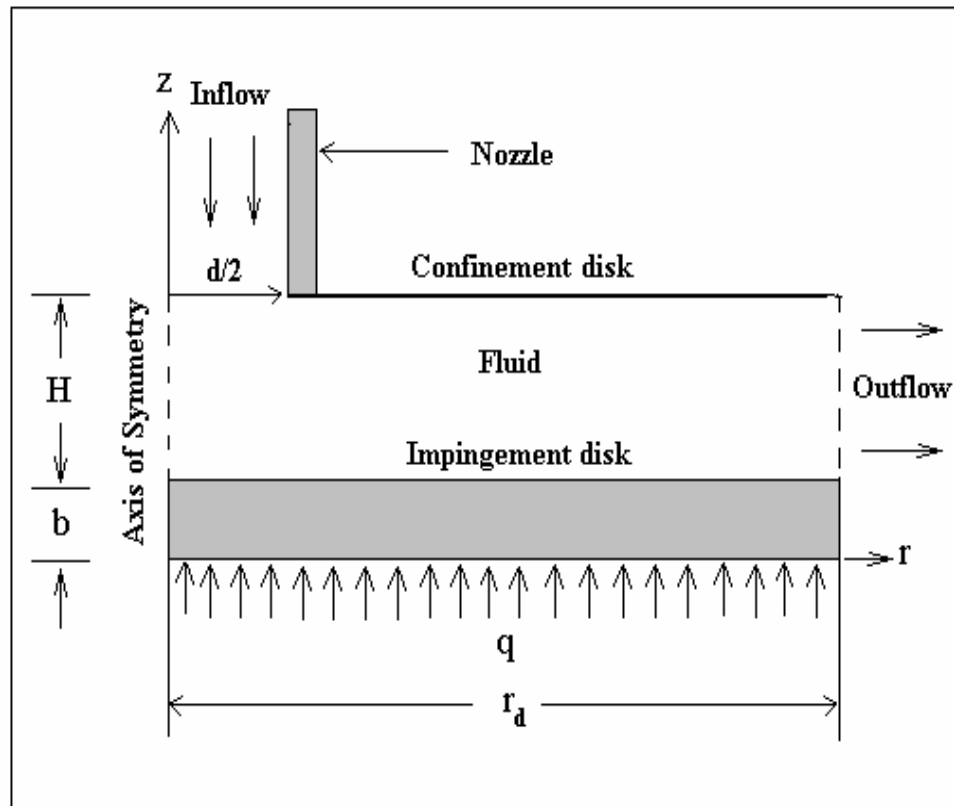


Figure 142. Schematic of a confined jet impinging on a uniformly heated disk

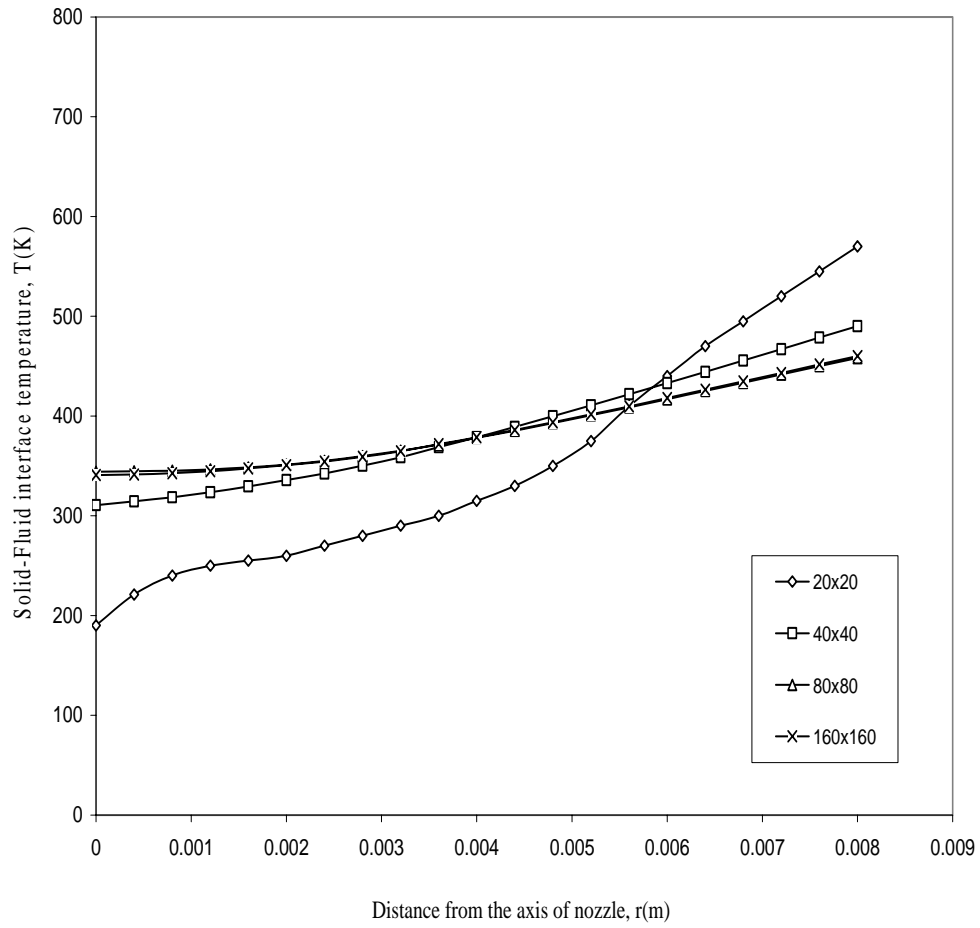


Figure 143. Local interface temperature for different number of elements in  $r$  and  $z$  directions (  $Re = 890$ ,  $b = 0$ ,  $H = d = 3.2\text{mm}$ ,  $q = 250\text{kW/m}^2$ )

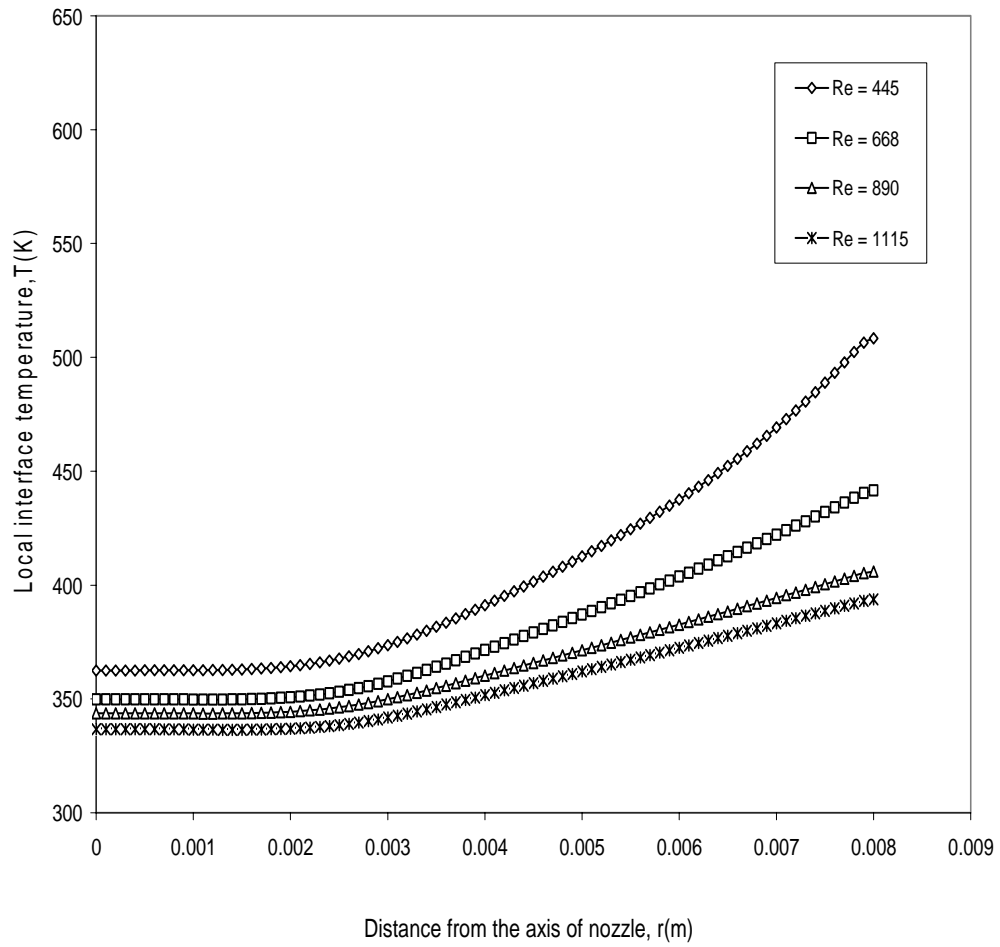


Figure 144. Local interface temperature for varying Reynolds number  
 (  $H = d = 3.2\text{mm}$ ,  $b = 0$ ,  $q = 250\text{kW/m}^2$  )

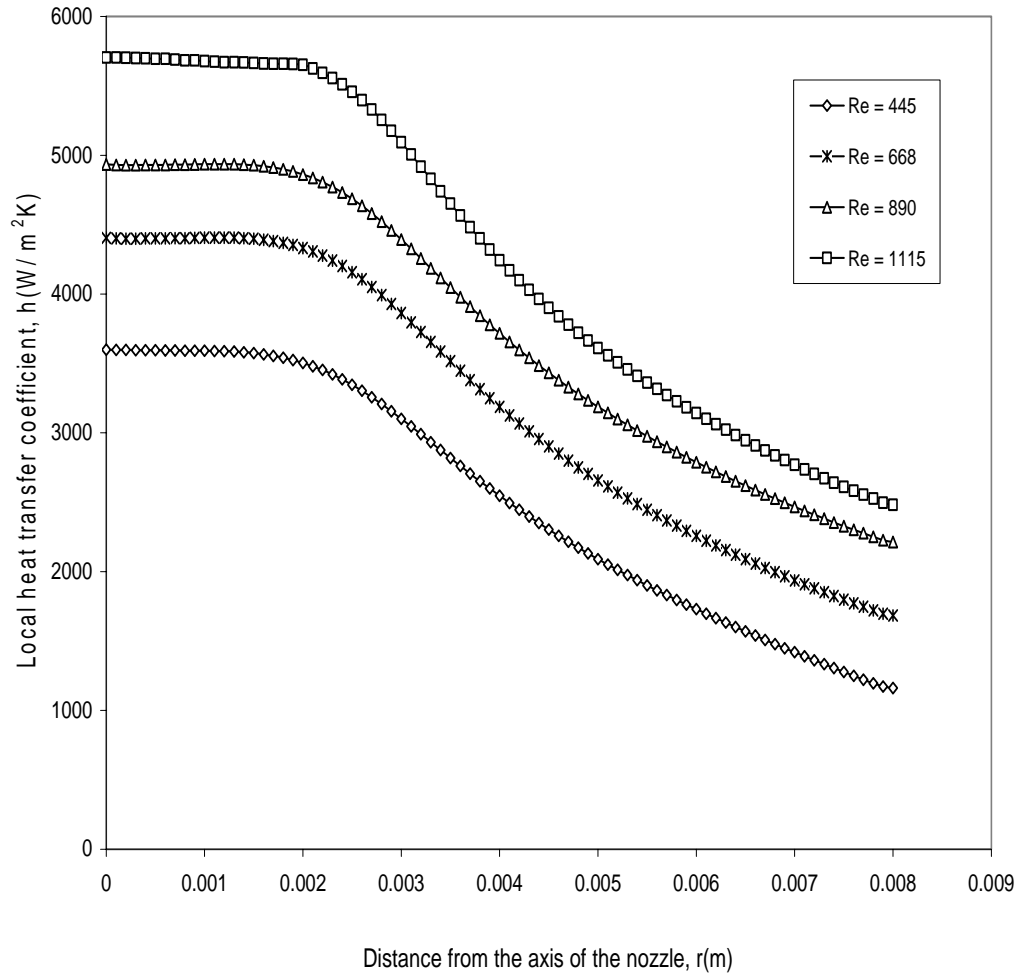


Figure 145. Local heat transfer coefficient at the interface for varying Reynolds number (  $H = d = 3.2\text{mm}$ ,  $b = 0$ ,  $q = 250 \text{ kW/m}^2$  )

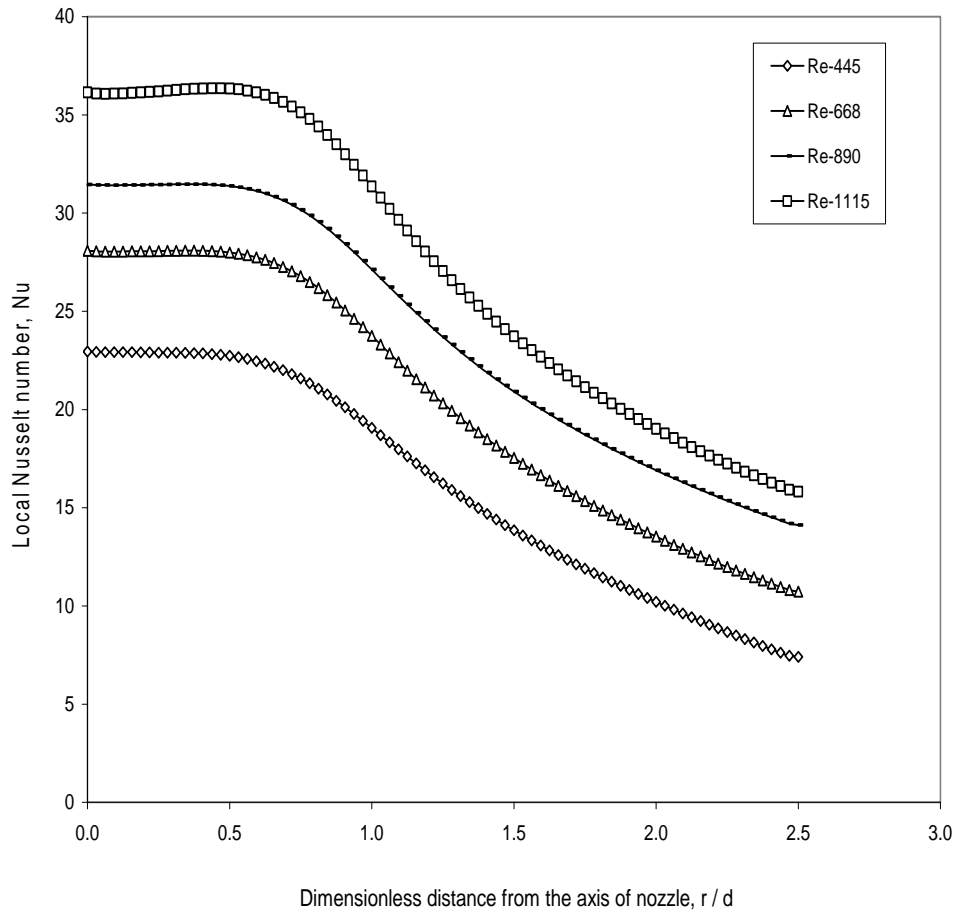


Figure 146. Local Nusselt number at the solid-fluid interface for varying Reynolds number (  $H = d = 3.2\text{mm}$ ,  $b = 0$ ,  $q = 250 \text{ kW/m}^2$ )

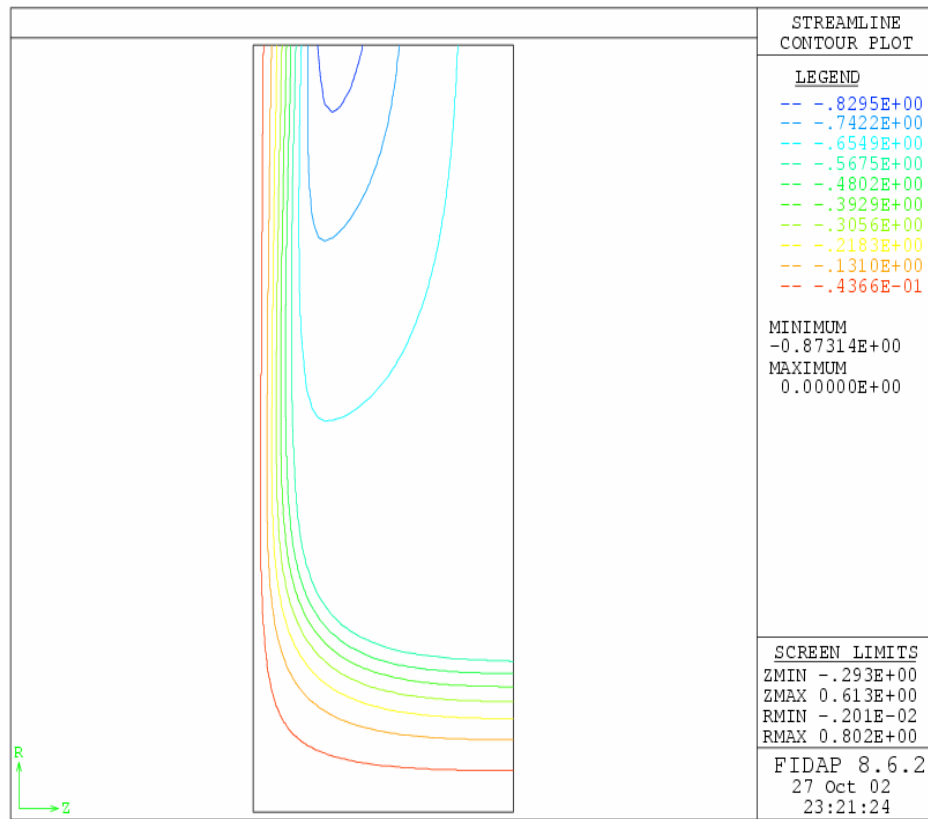


Figure 147. Streamline plot for confined jet impingement  
(  $Re = 668$ ,  $q = 250 \text{ kW/m}^2$ ,  $d = 3.2\text{mm}$ ,  $H = 3.2\text{mm}$ ,  $b = 0$  )



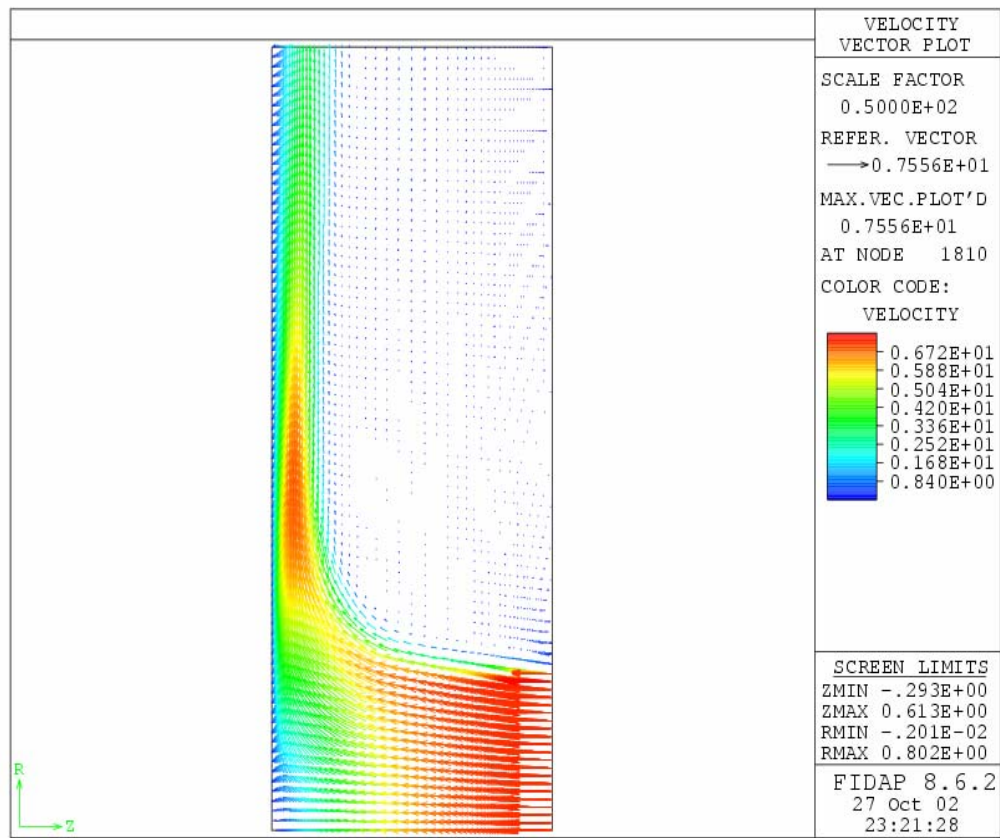


Figure 148. Velocity plot for confined jet impingement  
 (  $Re = 668$ ,  $q = 250 \text{ kW/m}^2$ ,  $d = 3.2\text{mm}$ ,  $H = 3.2\text{mm}$ ,  $b = 0$  )

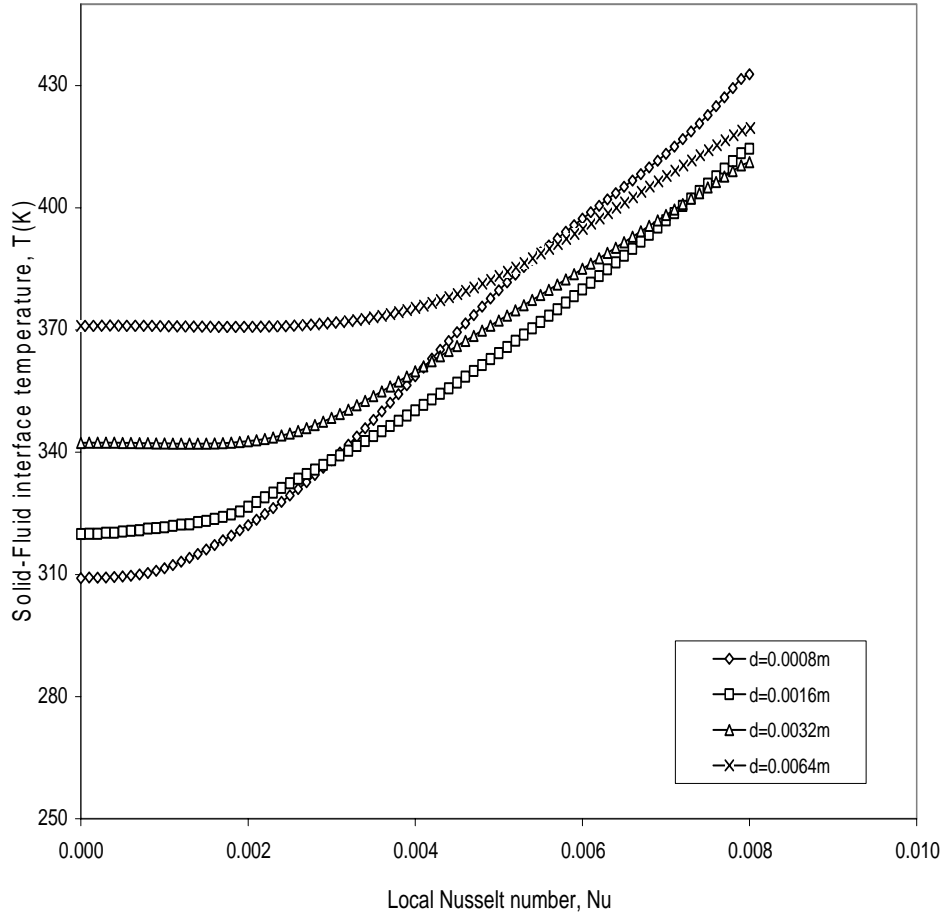


Figure 149. Local interface temperature for different nozzle diameters  
at constant flow rate  
(  $b = 0$ ,  $H = 3.2mm$ ,  $q = 250 \text{ kW/m}^2$ ,  $Q = 3.9 \times 10^{-3} \text{ m}^3/s$  )

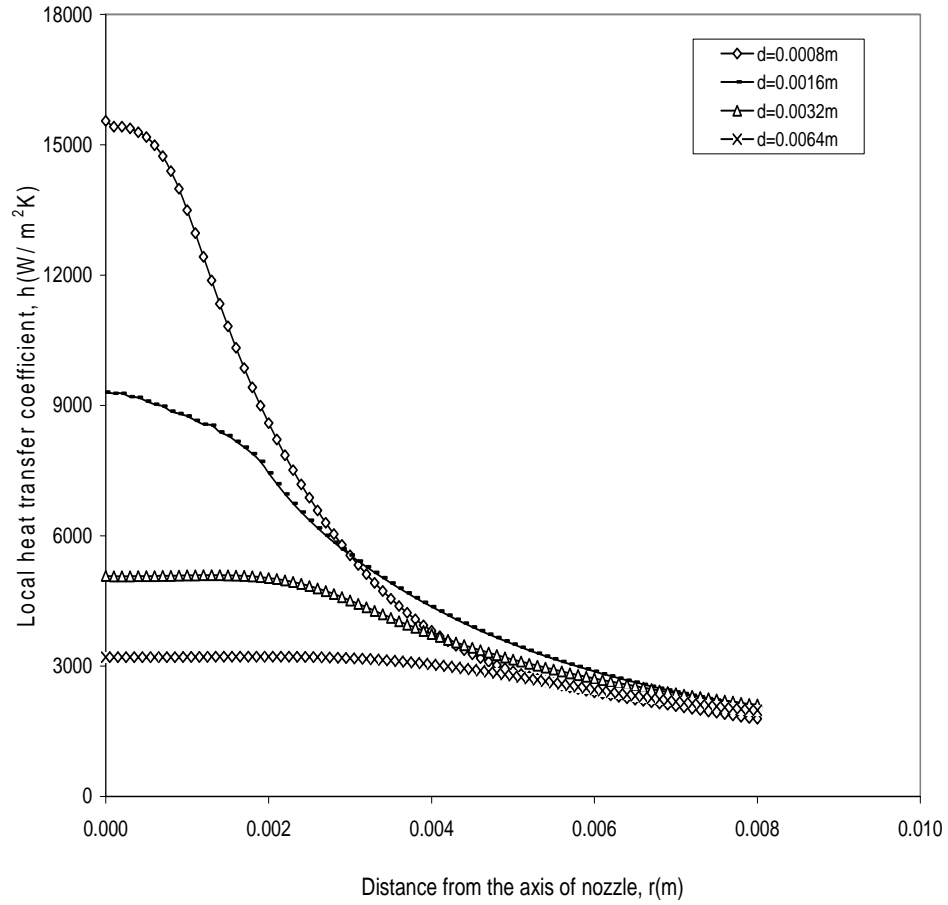


Figure 150. Local heat transfer coefficient at the interface for different nozzle diameters at constant flow rate  
 (  $b = 0$ ,  $H = 3.2\text{mm}$ ,  $q = 250 \text{ kW/m}^2$ ,  $Q = 3.9 \times 10^{-3} \text{ m}^3/\text{s}$  )

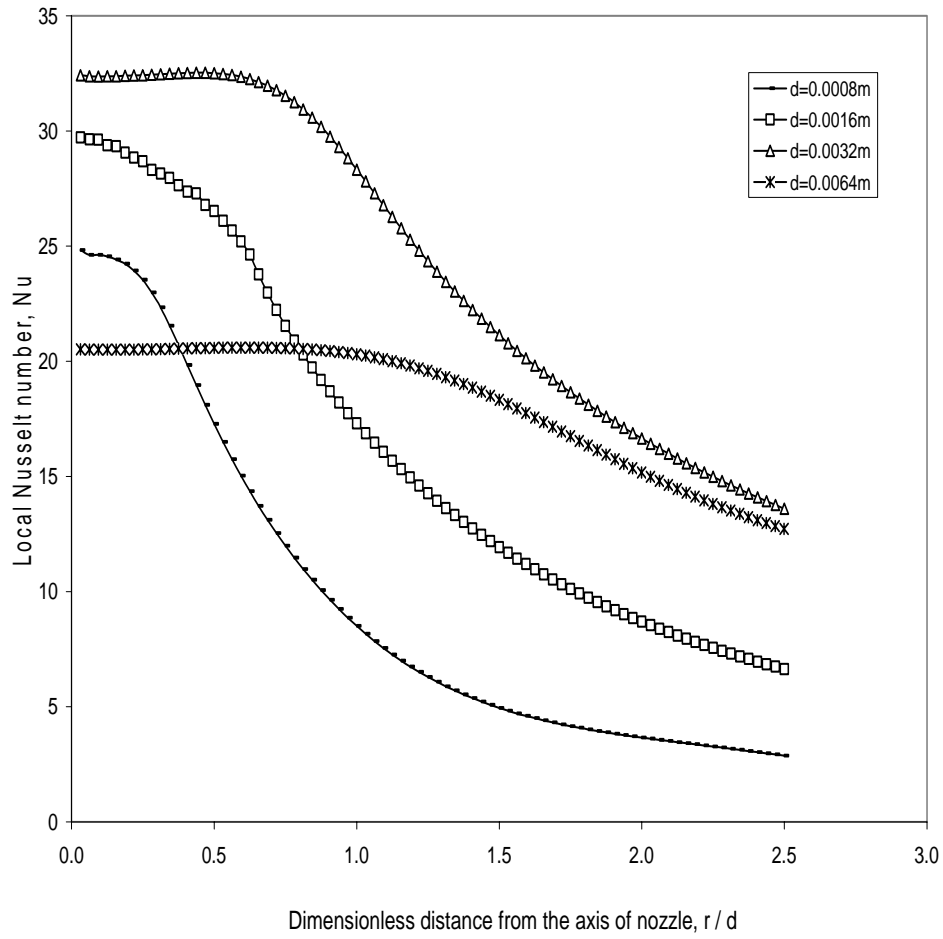


Figure 151. Local Nusselt number at the interface for different nozzle diameters at constant flow rate  
 (  $b = 0$ ,  $H = 3.2\text{mm}$ ,  $q = 250 \text{ kW/m}^2$ ,  $Q = 3.9 \times 10^{-3} \text{ m}^3/\text{s}$  )

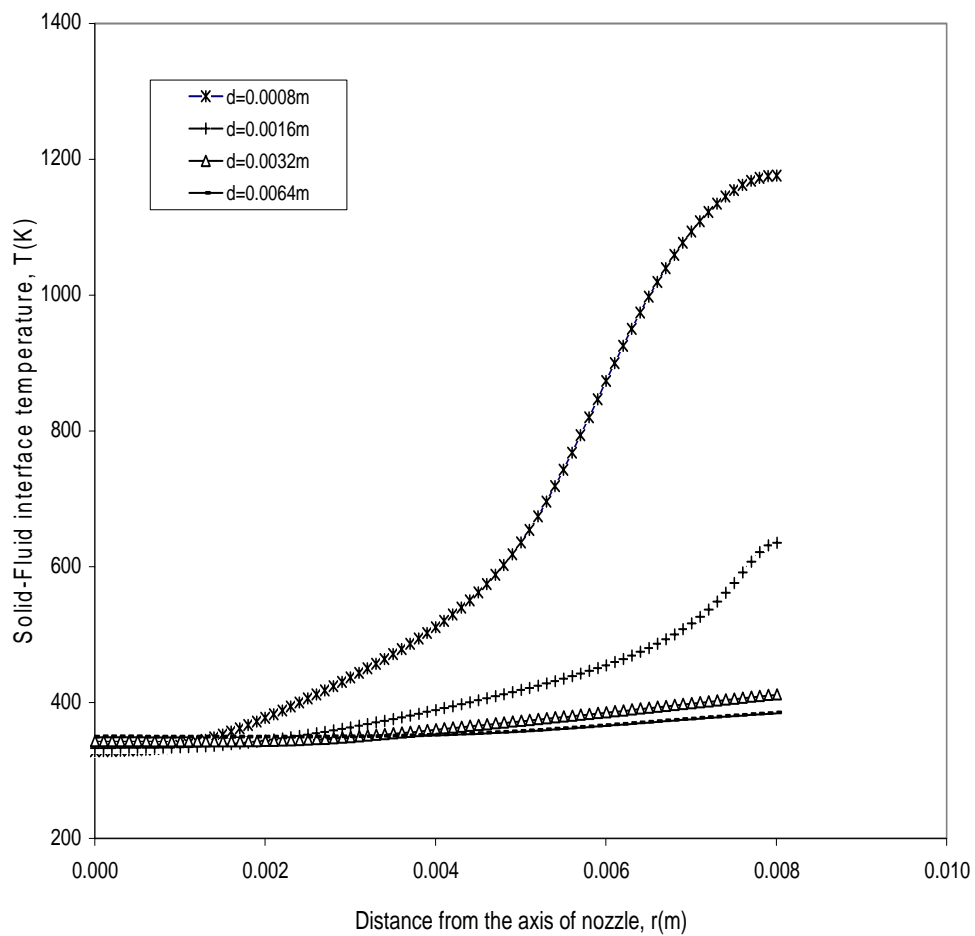


Figure 152. Local interface temperature for different nozzle diameters  
 (  $b = 0$ ,  $H = 3.2mm$ ,  $q = 250 \text{ kW/ m}^2$ ,  $V_j = 9.672cm/s$  )

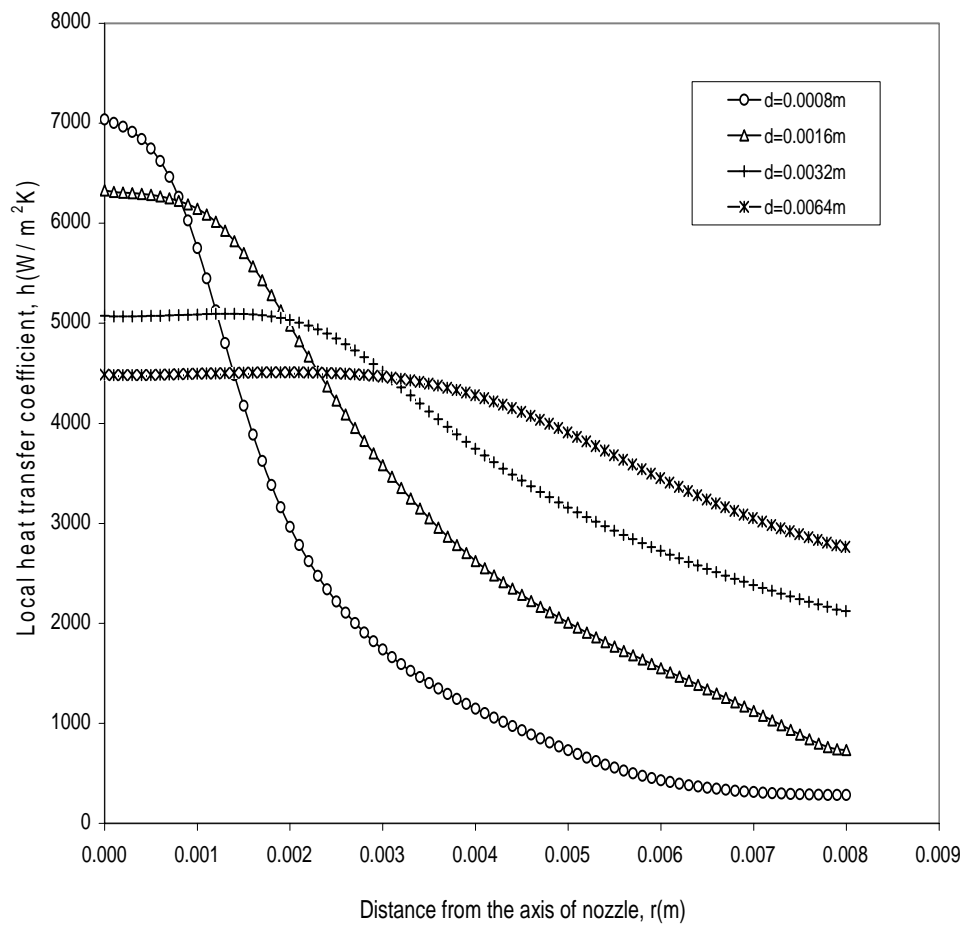


Figure 153. Local heat transfer coefficient at the interface for different nozzle diameters ( $b = 0$ ,  $H = 3.2\text{mm}$ ,  $q = 250\text{kW/m}^2$ ,  $V_j = 9.672\text{cm/s}$ )

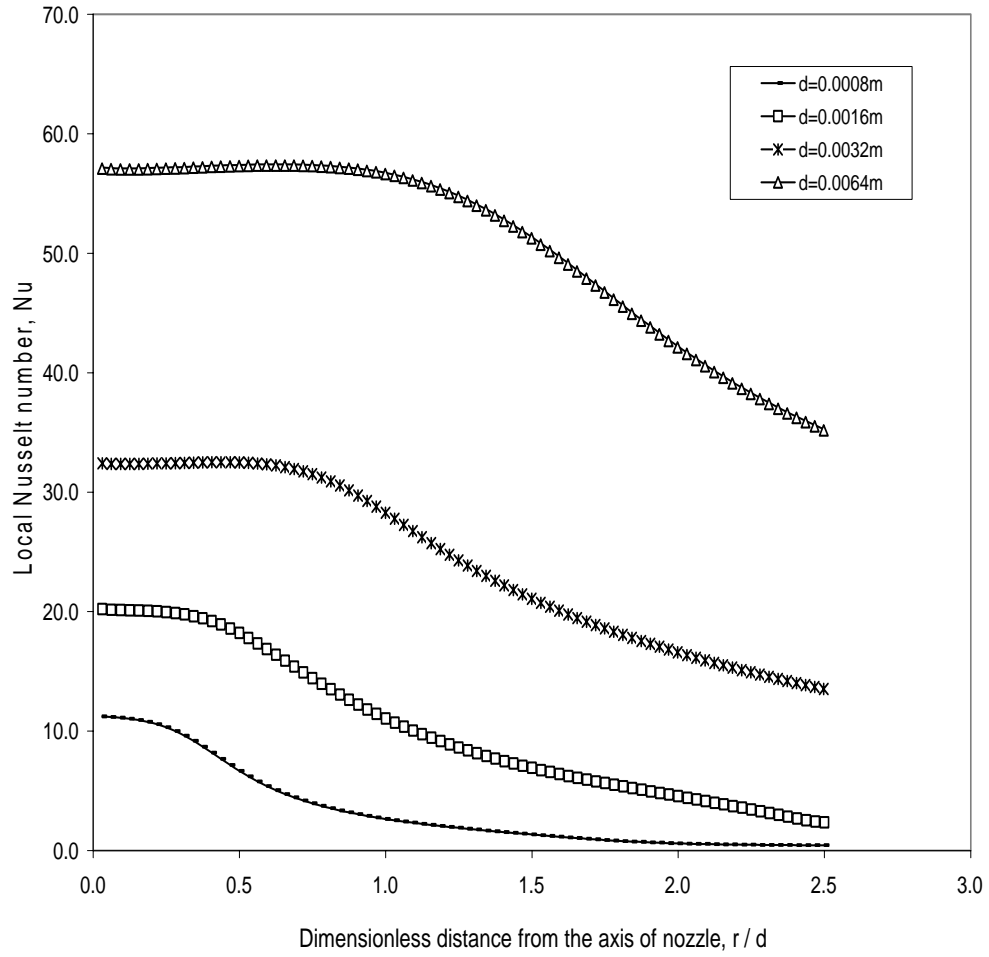


Figure 154. Local Nusselt number at the interface for different nozzle diameters (  $b = 0$ ,  $H = 3.2\text{mm}$ ,  $q = 250\text{kW/m}^2$ ,  $V_j = 9.672\text{cm/s}$  )

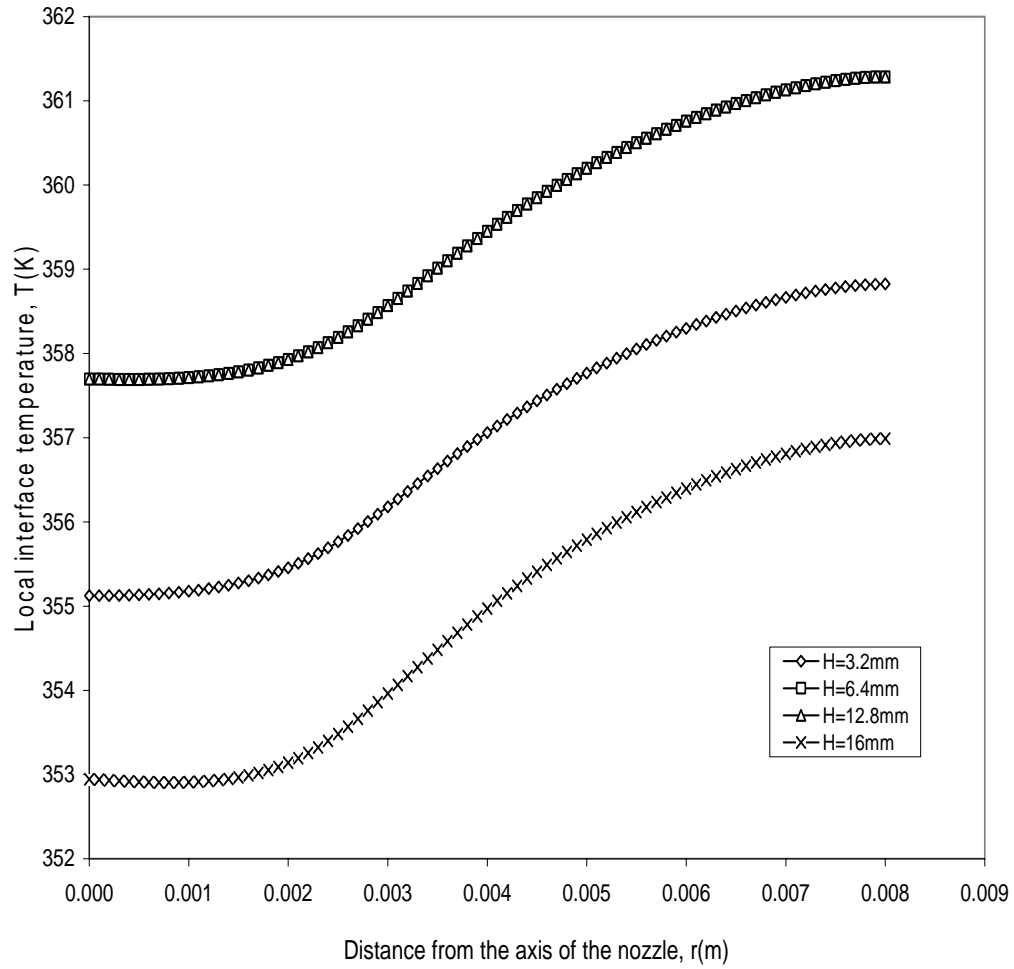


Figure 155. Local interface temperature for different impingement heights (  $b = 5mm$ ,  $q = 250 \text{ kW/ m}^2$ ,  $H = d = 3.2mm$ ,  $Re = 1545$ , solid = silicon )



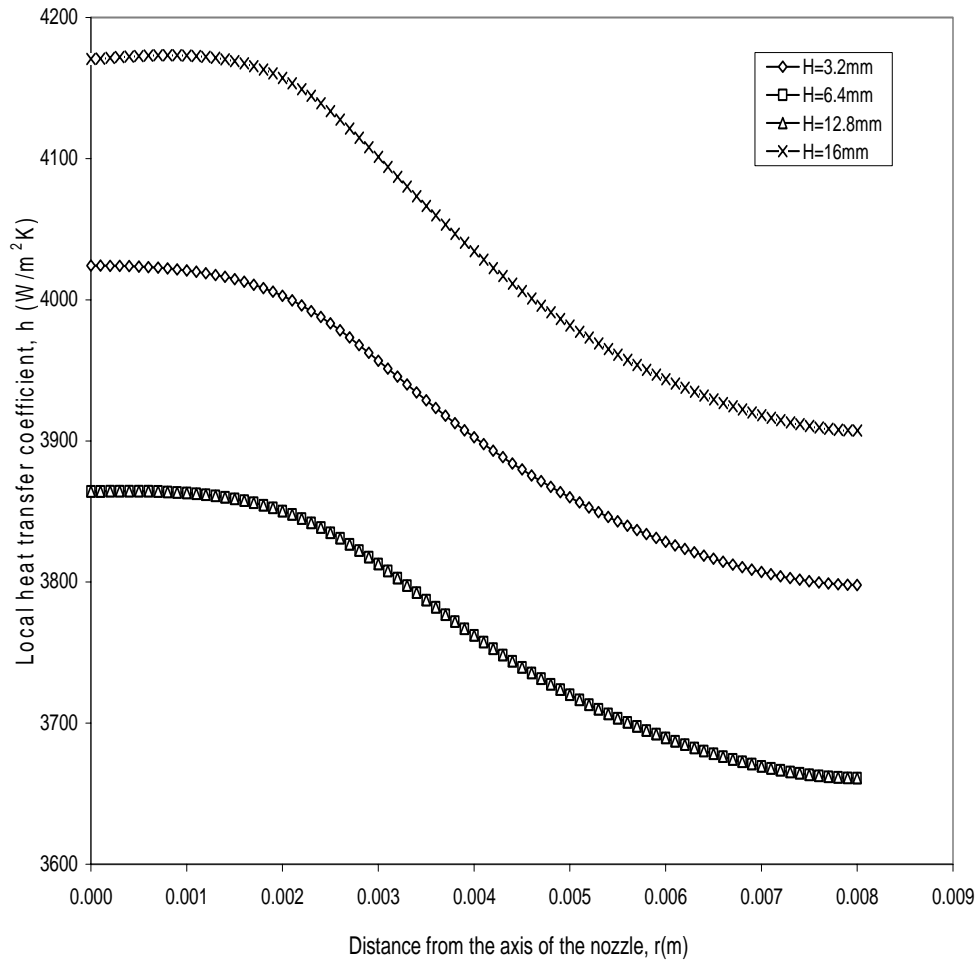


Figure 156. Local heat transfer coefficient at the interface for different impingement heights  
(  $b = 5\text{mm}$ ,  $q = 250 \text{ kW/ m}^2$ ,  $H = d = 3.2\text{mm}$ ,  $Re = 1545$ , solid = silicon )

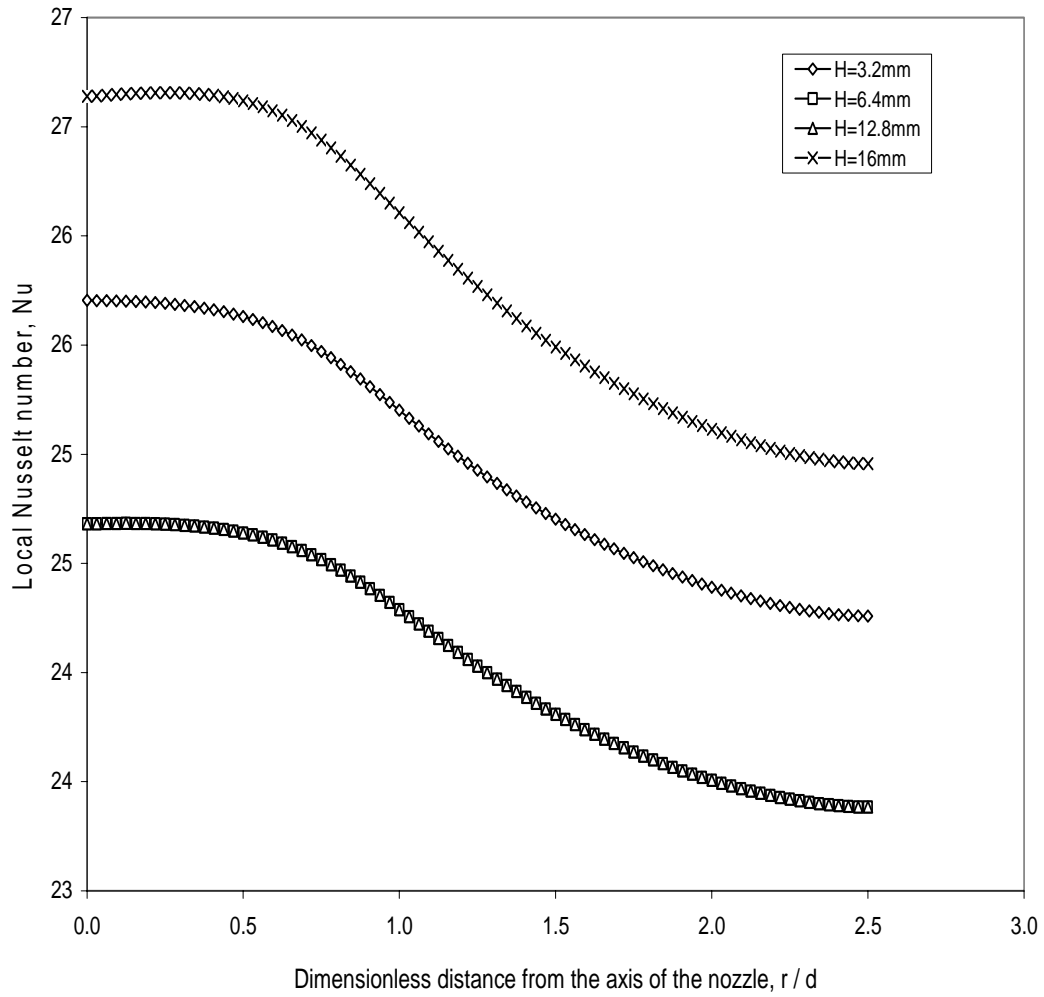


Figure 157. Local Nusselt number at the interface for different impingement heights  
(  $b = 5\text{mm}$ ,  $q = 250\text{ kW/m}^2$ ,  $H = d = 3.2\text{mm}$ ,  $Re = 1545$ , solid = silicon )

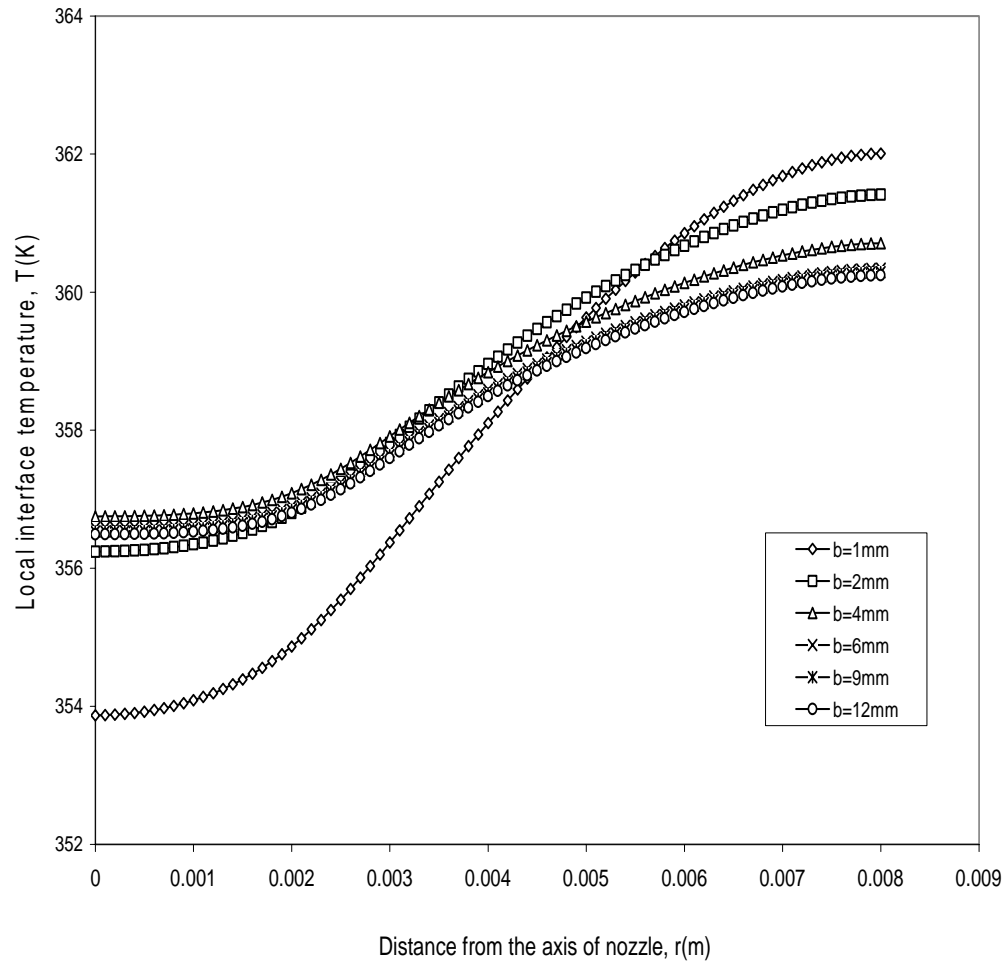


Figure 158. Local interface temperature for different plate thicknesses  
 $(q = 250 \text{ kW/m}^2, \text{Re} = 1545, H = d = 3.2\text{mm}, \text{solid} = \text{silicon})$

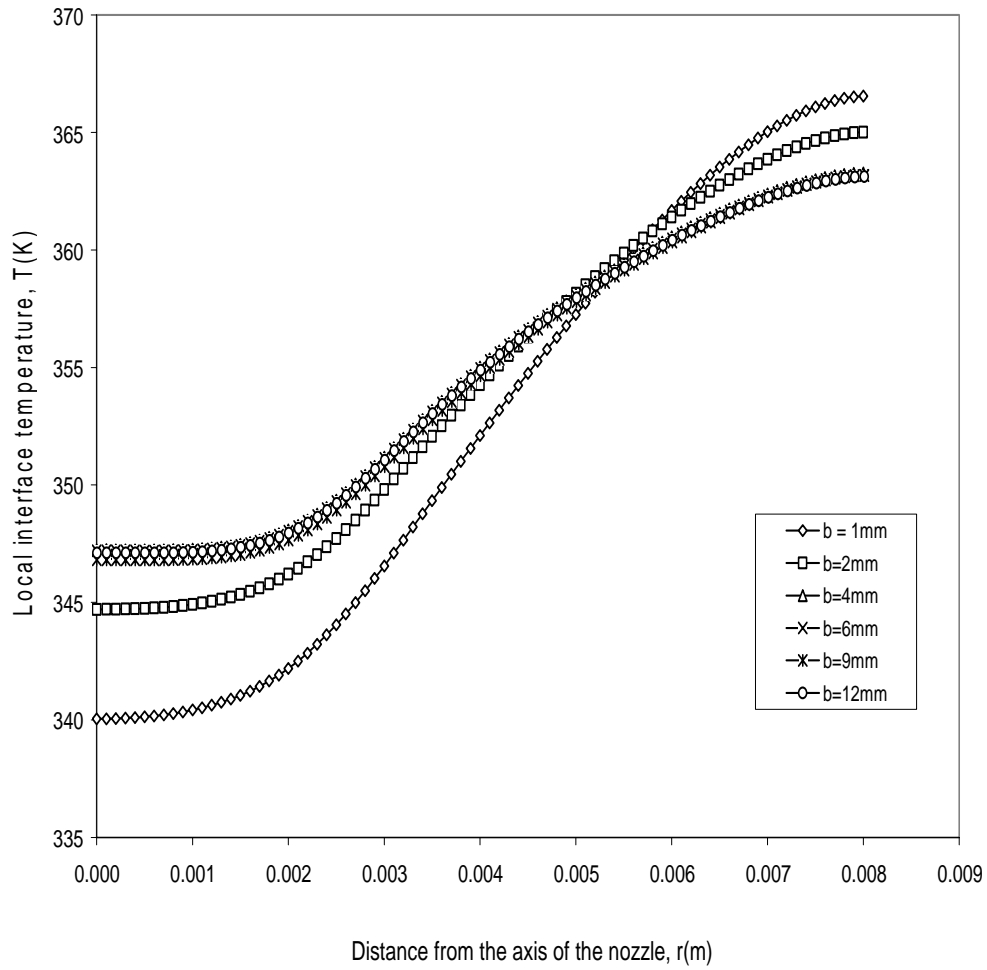


Figure 159. Local interface temperature for different plate thicknesses  
 $(q = 250 \text{ kW/m}^2, \text{Re} = 1545, H = d = 3.2\text{mm}, \text{solid} = \text{Constantan})$

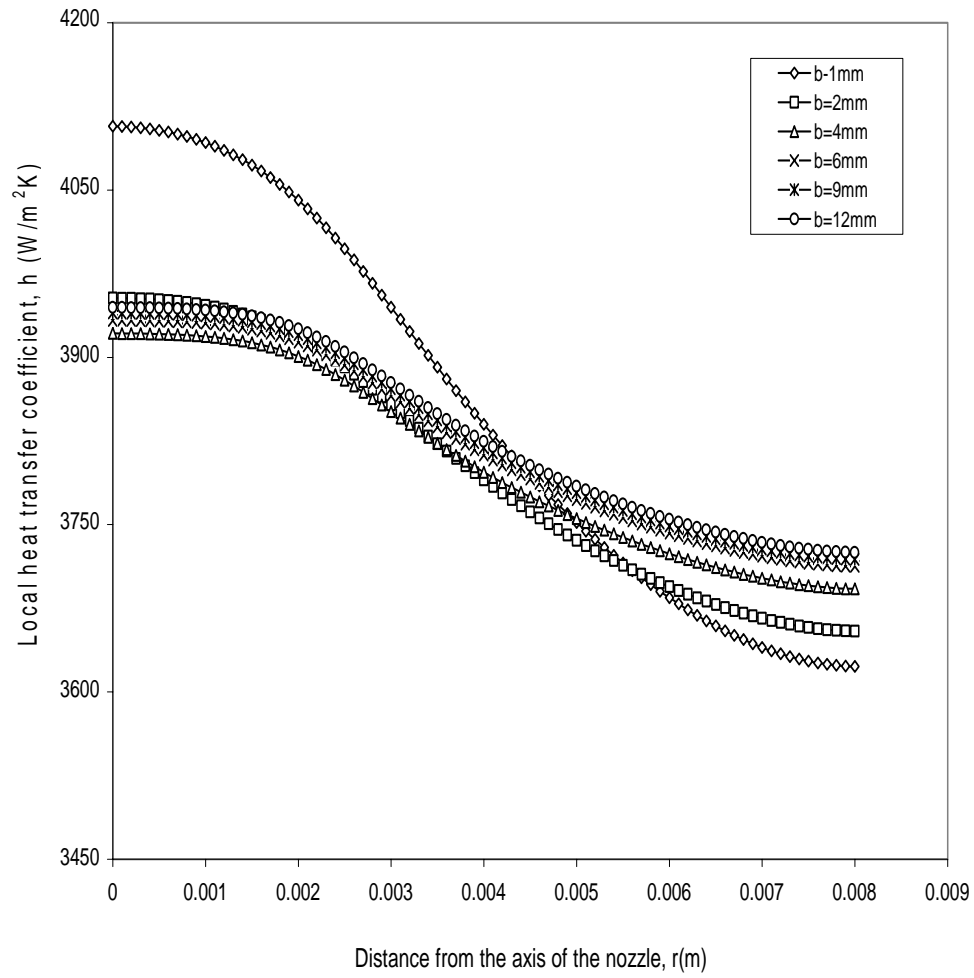


Figure 160. Local heat transfer coefficient at the interface for different plate thicknesses ( $q = 250\text{kW/m}^2$ ,  $H = d = 3.2\text{mm}$ ,  $\text{Re} = 1545$ , solid = silicon)

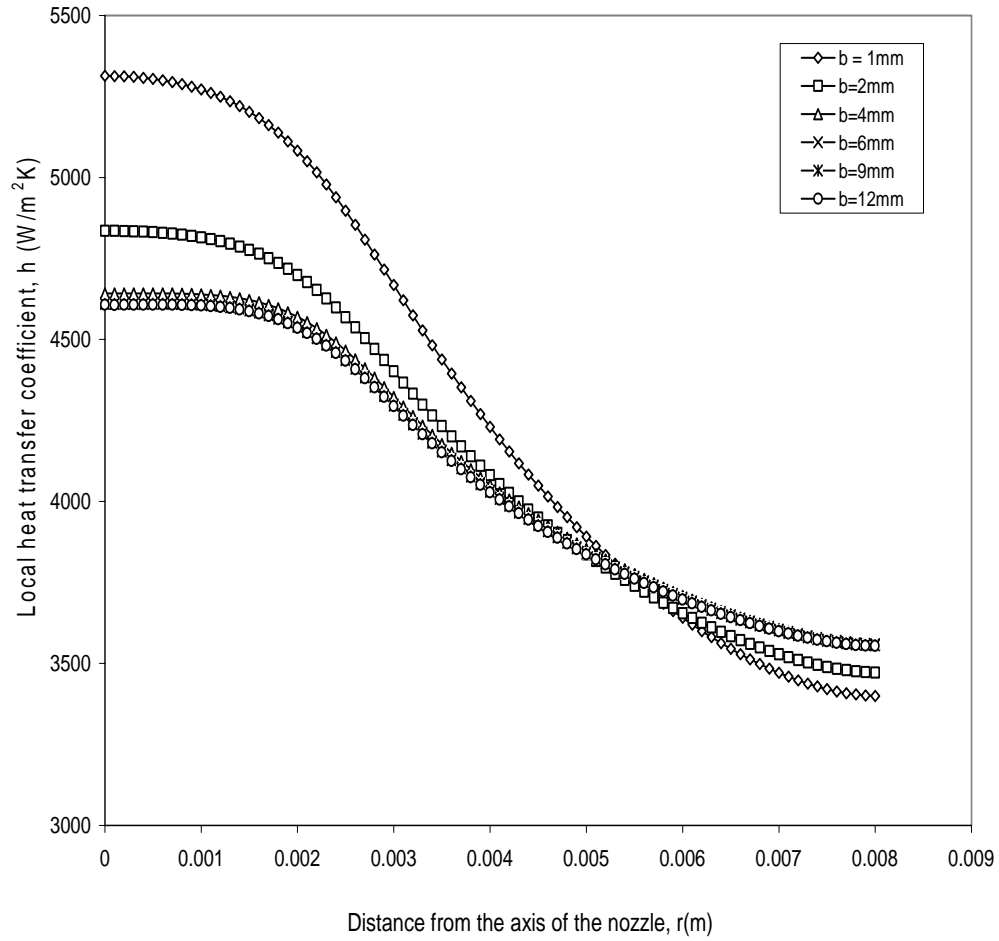


Figure 161. Local heat transfer coefficient at the interface for the different plate thicknesses  
 $(q = 250\text{kW/m}^2, H = d = 3.2\text{mm}, \text{Re} = 1545, \text{solid} = \text{Constantan})$

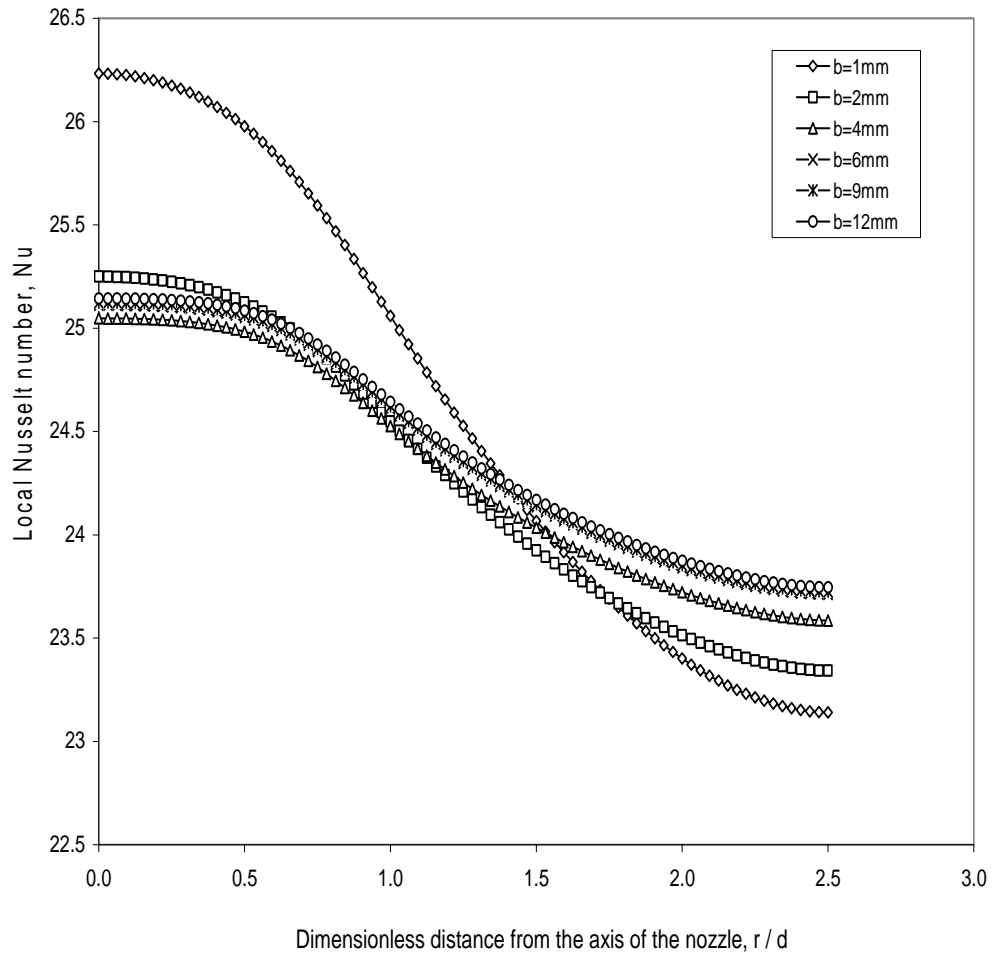


Figure 162. Local Nusselt number at the interface for different plate thicknesses.  
 $(q = 250\text{kW/m}^2, H = d = 3.2\text{mm}, \text{Re} = 1545, \text{solid} = \text{silicon})$

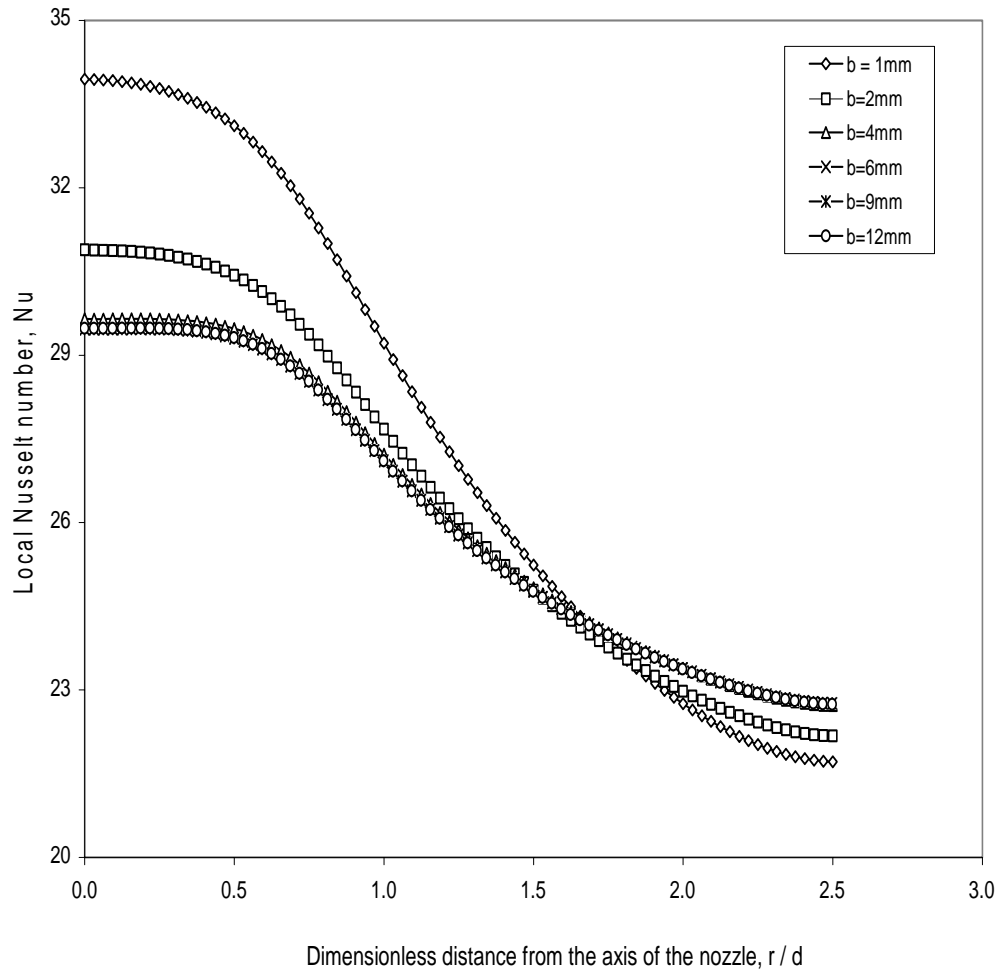


Figure 163. Local Nusselt number at the interface for different plate thicknesses ( $q = 250\text{kW}/\text{m}^2$ ,  $H = d = 3.2\text{mm}$ ,  $Re = 1545$ , solid = Constantan)



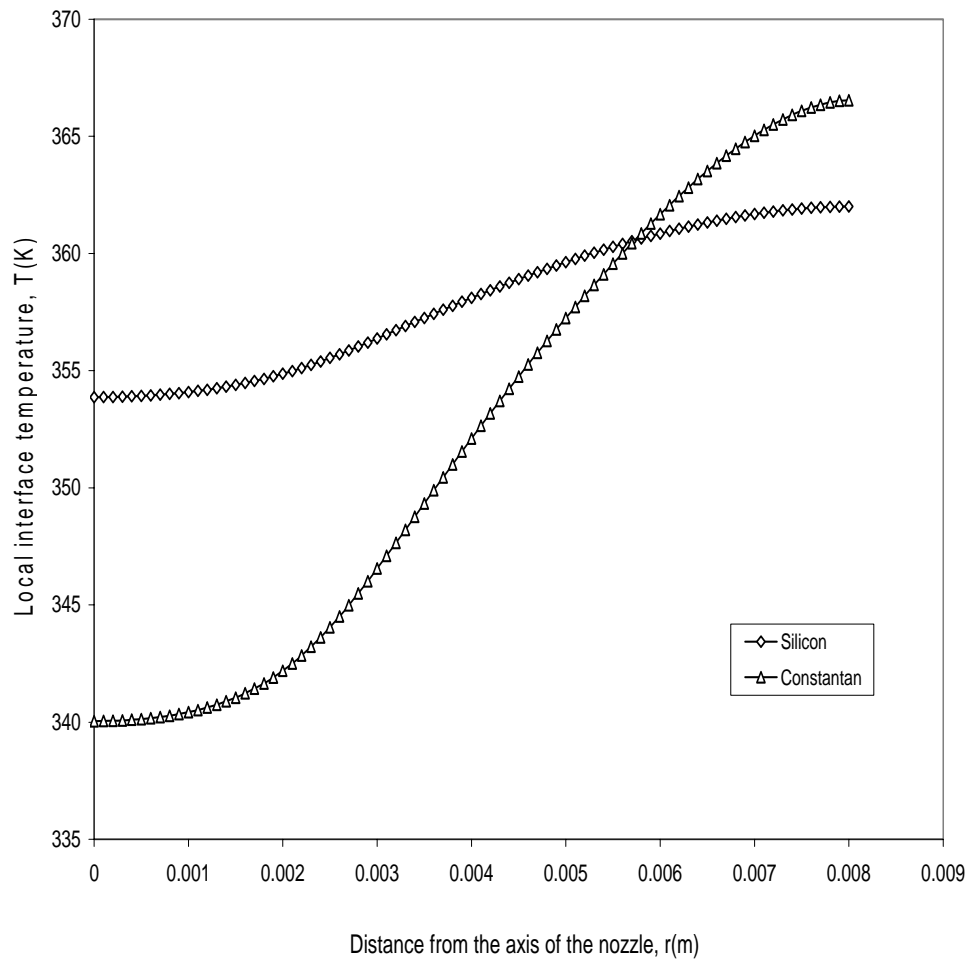


Figure 164. Local interface temperature for two different solids  
 $(q = 250 \text{ kW/m}^2, b = 1\text{mm}, \text{Re} = 1545, H = d = 3.2\text{mm})$

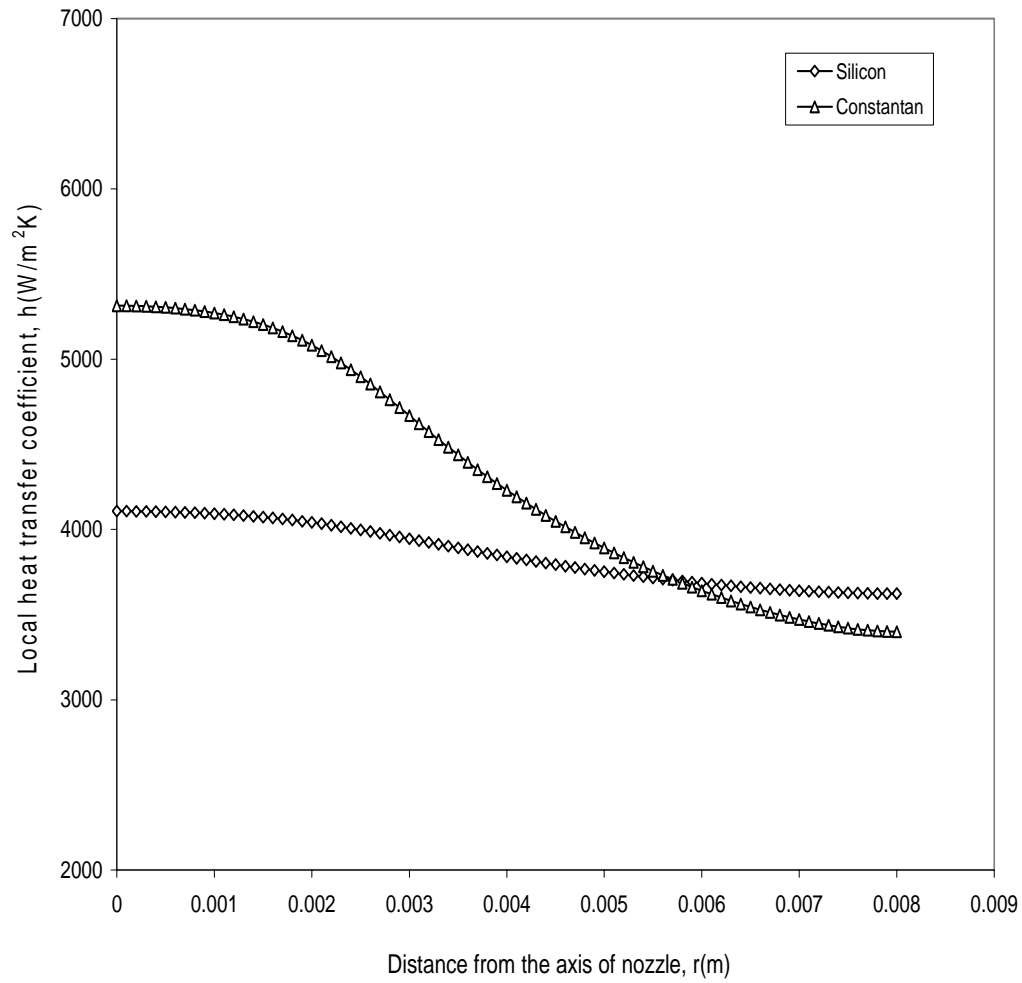


Figure 165. Local heat transfer coefficient at the interface for two different solids  
 ( $b = 1\text{mm}$ ,  $q = 250\text{kW/m}^2$ ,  $H = d = 3.2\text{mm}$ ,  $Re = 1545$ )

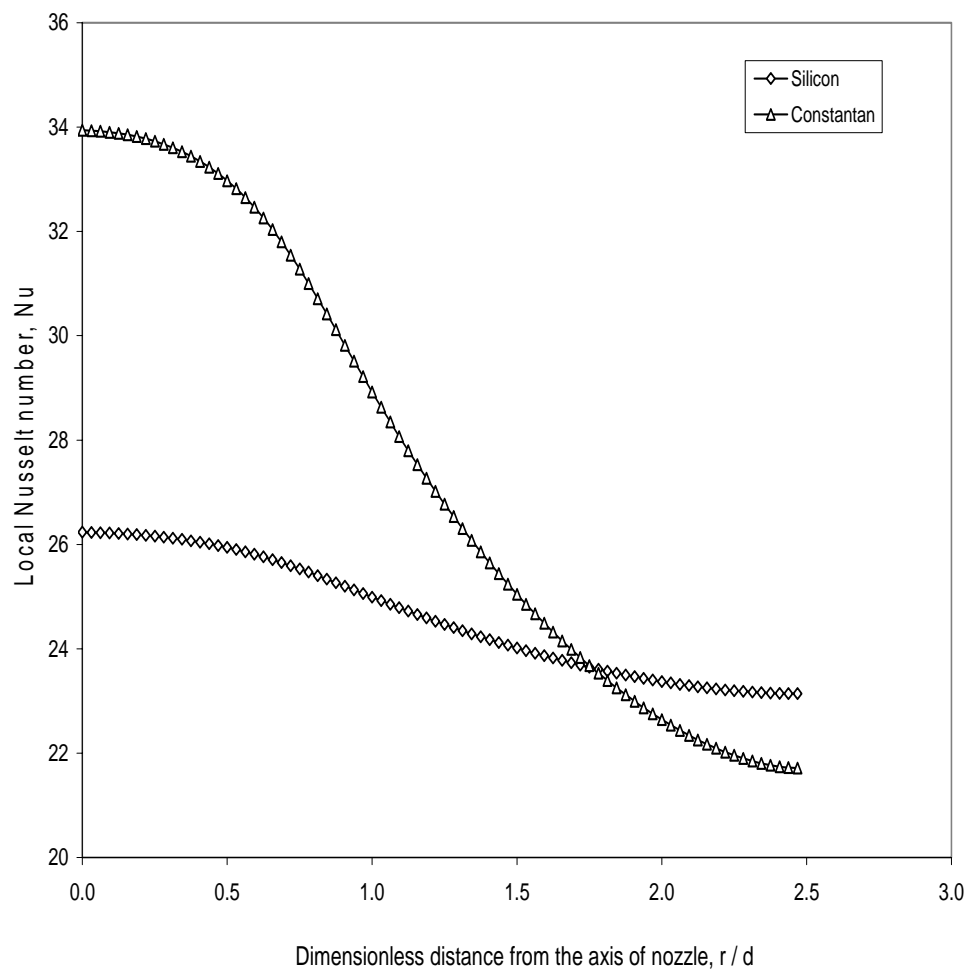


Figure 166. Local Nusselt number at the interface for two different solids  
 ( $b = 1\text{mm}$ ,  $q = 250 \text{ kW/ m}^2$ ,  $H = d = 3.2\text{mm}$ ,  $Re = 1545$ )

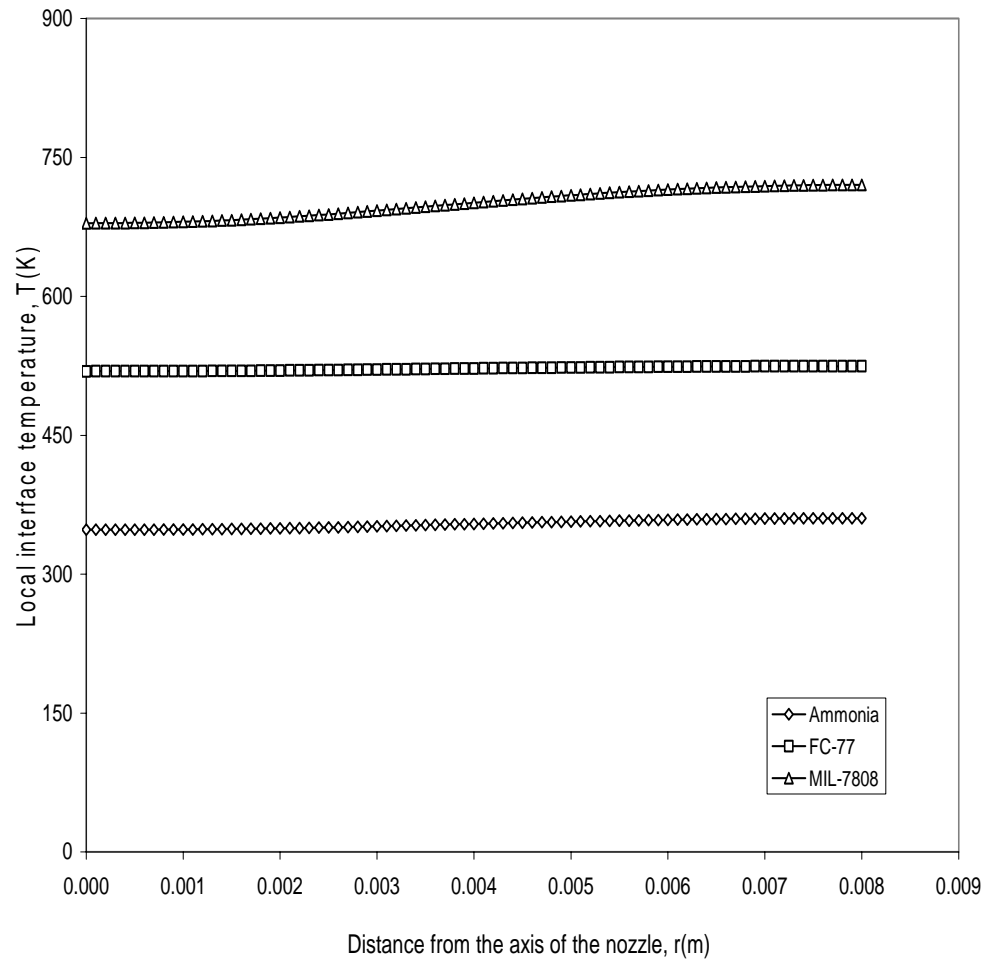


Figure 167. Local interface temperature for three different fluids  
 (  $b = 0.5\text{mm}$ ,  $q = 250\text{ kW/ m}^2$ ,  $H = d = 3.2\text{mm}$ ,  $Re = 1545$ , solid = silicon )

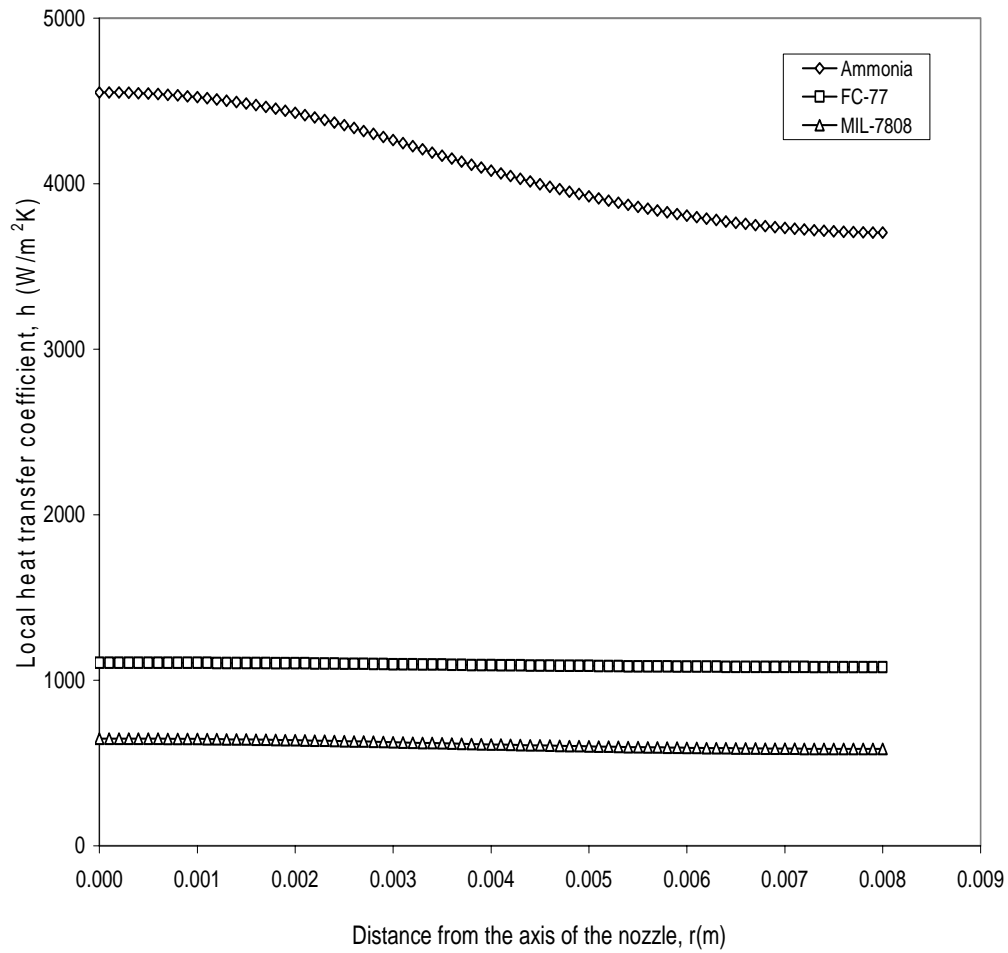


Figure 168. Local heat transfer coefficient at the interface for different fluids (  $b = 0.5\text{mm}$ ,  $q = 250\text{ kW/ m}^2$ ,  $H = d = 3.2\text{mm}$ ,  $Re = 1545$ , solid = silicon )

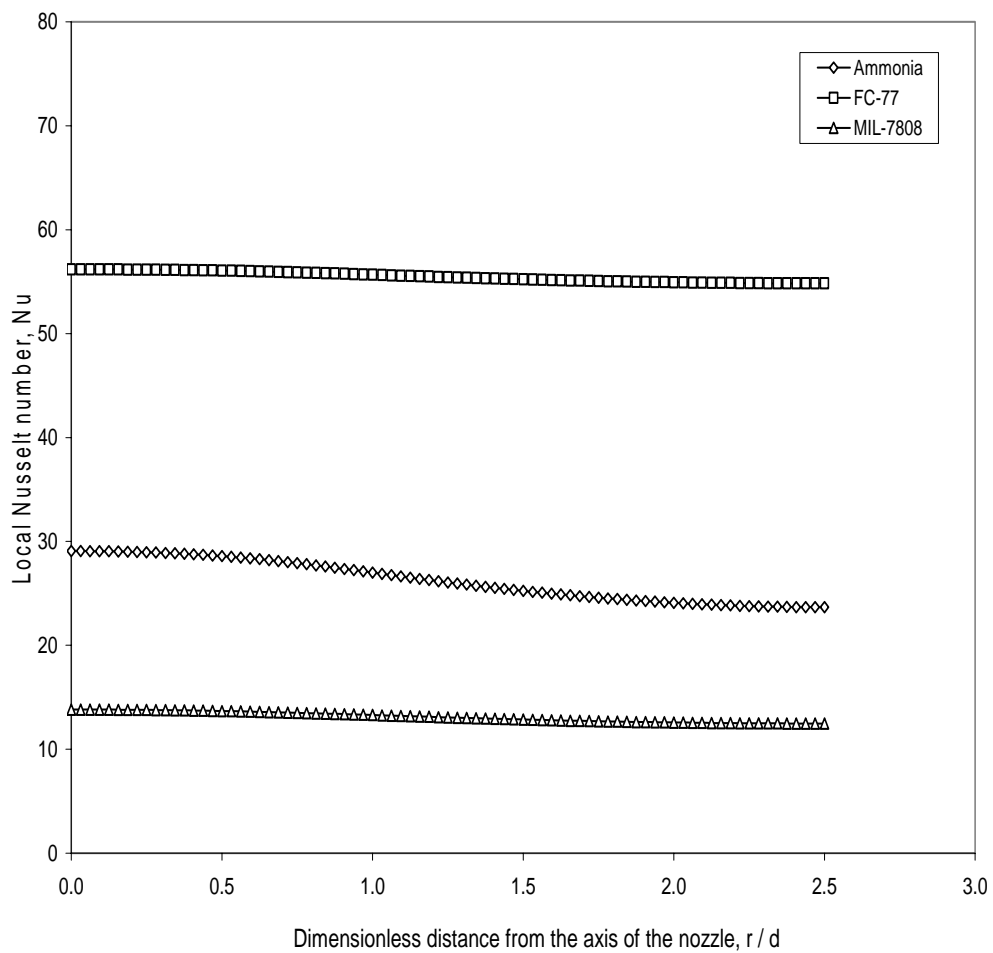


Figure 169. Local Nusselt number at the interface for different fluids  
 (  $b = 0.5\text{mm}$ ,  $q = 250 \text{ kW/ m}^2$ ,  $H = d = 3.2\text{mm}$ ,  $Re = 1545$ , solid = silicon )

## REFERENCES

1. M.B. Glauert, The Wall Jet, *Journal of Fluid Mechanics*, vol. 1, no. 6, pp. 625-643, 1956.
2. R.G. Olson and E. T. Turkdogan, Radial Spread of a Liquid Stream on a Horizontal Plate, *Nature*, vol. 221, no. 5051, pp. 813-816, 1966.
3. D. E. Metzger, K. N. Cummings, and W. A. Ruby, Effects of Prandtl Number on Heat Transfer Characteristics of Impinging Liquid Jets, *Proceedings of the 5<sup>th</sup> International Heat Transfer Conference*, vol. 2, pp. 20-24, 1974.
4. V. E. Nakoryakov, B. G. Pokusaev, and E. N. Troyan, Impingement of an Axisymmetric Liquid Jet on a Barrier, *International Journal of Heat and Mass Transfer*, vol. 21, pp. 1175-1184, 1978.
5. P. Hrycak, Heat Transfer from Round impinging Jets to a Flat Plate, *International Journal of Heat and Mass Transfer*, vol. 26, no. 12, pp. 1857-1865, 1983.
6. X. Liu and J. H. Lienhard, Liquid Jet Impingement Heat Transfer on a Uniform Flux Surface, *Heat Transfer Phenomena in Radiation, Combustion, and Fires*, ASME HTD/vol. 106, pp. 523-530, 1989.
7. X. S. Wang, Z. Dagan, and L. M. Jiji, Heat Transfer between a Circular Free Impinging Jet and Solid Surface with Non-Uniform Wall Temperature or Wall Heat Flux – 1. Solution for the Stagnation Region, *International Journal of Heat and Mass Transfer*, vol. 32, no. 7, pp. 1351-1360, 1989.
8. X. S. Wang, Z. Dagan, and L. M. Jiji, Heat Transfer between a Circular Free Impinging Jet and a Solid Surface with Non-Uniform Wall Temperature or Wall Heat Flux – 2. Solution for the Boundary Layer Region, *International Journal of Heat and Mass Transfer*, vol. 32, no. 7, pp. 1361-1371, 1989.
9. X. S. Wang, Z. Dagan, and L. M. Jiji, Conjugate Heat Transfer between a Laminar Impinging Liquid Jet and a Solid Disk, *International Journal of Heat and Mass Transfer*, vol. 32, no. 11, pp. 2189-2197, 1989.
10. X. S. Wang, Z. Dagan, and L. M. Jiji, Prediction of Surface Temperature and Heat Flux of a Microelectronic Chip with Jet Impingement Cooling, *Journal of Electronic Packaging*, vol. 112, pp. 57-62, 1990.
11. D. H. Wolf, R. Viskanta, and F. P. Incropera, Local Convective Heat Transfer from a Heated Surface to a Planar Jet of Water with Nonuniform Velocity Profile, *Journal of Heat Transfer*, vol. 112, pp. 899-905, 1990.

12. D. T. Vader, F. P. Incropera, and R. Viskanta, Local Convective Heat Transfer from a Heated Surface to an Impinging, Planar Jet of Water, *International Journal of Heat and Mass Transfer*, vol. 34, no. 3, pp. 611-623, 1991.
13. J. Stevens and B. W. Webb, Local Heat Transfer Coefficients Under an Axisymmetric, Single-Phase Liquid Jet, *Journal of Heat Transfer*, vol. 113, pp. 71-78, 1991.
14. X. Liu, J. H. Lienhard, and J. S. Lombara, Convective Transfer by Impingement of Circular Liquid Jets, *Journal of Heat Transfer*, vol. 113, pp. 571-582, 1991.
15. Y. Pan, J. Stevens, and B. W. Webb, Effect of Nozzle Configuration on Transport in the Stagnation Zone of Axisymmetric, Impinging Free-Surface Liquid Jets : Part 2 – Local Heat Transfer, *Journal of Heat Transfer*, vol. 114, pp. 880-886, 1992.
16. B. Elison and B. W. Webb, Local Heat Transfer to Impinging Liquid Jets in the Initially Laminar, Transitional, and Turbulent Regimes, *International Journal of Heat and Mass Transfer*, vol. 37, no. 8, pp. 1207-1216, 1994.
17. C. F. Ma, Q. Zheng, H. Sun, K. Wu, T. Gomi, and B. W. Webb, Local Characteristics of Impingement Heat Transfer with oblique Round Free Surface Jets of Large Prandtl number Liquid, *International Journal of Heat and Mass Transfer*, vol. 40, no. 10, pp. 2249-2259, 1997.
18. C. F. Ma, Q. Zheng, S. C. Lee, and T. Gomi, Impingement Heat Transfer and Recovery Effect with Submerged Jets of Large Prandtl number Liquid – I. Unconfined Circular Jets, *International Journal of Heat and Mass Transfer*, vol. 40, no. 6, pp. 1481-1490, 1997.
19. C. F. Ma, Q. Zheng, S. C. Lee, and T. Gomi, Impingement Heat Transfer and Recovery Effect with Submerged Jets of Large Prandtl number Liquid – II. Initially Laminar Confined Slot Jets, *International Journal of Heat and Mass Transfer*, vol. 40, no. 6, pp. 1491-1500, 1997.
20. X. C. Lee, C. F. Ma, Q. Zheng, Y. Zhuang, and Y. Q. Tian, Numerical Study of Recovery Effect and Impingement Heat Transfer with Submerged Circular Jets of Large Prandtl number Liquid, *International Journal of Heat and Mass Transfer*, vol. 40, no. 11, pp. 2647-2653, 1997.
21. C. F. Ma, Q. Zheng, and S.Y. Ko, Local Heat Transfer and Recovery Factor with Impinging Free Surface Circular Jets of Transformer Oil, *International Journal of Heat and Mass Transfer*, vol. 40, no. 18, pp. 4295-4308, 1997.
22. J. E. Leland and M. R. Pais, Free Jet Impingement Heat Transfer of a High Prandtl Number Fluid under Conditions of Highly Varying Properties, *Journal of Heat Transfer*, vol.121, pp. 592-597, 1999.



23. L. C. Burmeister, *Convective Heat Transfer*, Second Edition, Wiley, New York, 1993.
24. F.P. Incropera and D.P. DeWitt, *Fundamentals of Heat and Mass Transfer*, Fourth Edition, p.391, Wiley, New York, 1996.
25. N. Rajaratnam, *Turbulent Jets*, Elsevier, New York, 1976.
26. H. Martin, Heat and Mass Transfer Between Impinging Gas Jets and Solid Surfaces, *Advances in Heat Transfer*, vol. 13, pp. 1-60, 1977.
27. W. Rodi, *Turbulent Buoyant Jets and Plumes*, Pergamon, New York, 1982.
28. S. Polat, B. Huang, A.S. Majumdar, and W.J.M. Douglas, Numerical Flow and Heat Transfer under Impinging Jets: A Review, *Annual Review of Numerical Fluid Mechanics and Heat Transfer*, vol. 2, pp. 157-197, 1989.
29. D.C. Wadsworth and I. Mudawar, Cooling of a Multiple Electronic Module by Means of Confined Two-Dimensional Jets of Dielectric Liquid, *Journal of Heat Transfer*, vol. 112, pp. 891-898, 1990.
30. D. Schaffer, F.P. Incropera, and S. Ramadhyani, Planar Liquid Jet Impingement Cooling of Multiple Discrete Heat Sources, *Journal of Electronic Packaging*, vol. 113, pp. 359-366, 1991.
31. D.L. Besserman, S. Ramadhyani, and F.P. Incropera, Numerical Simulation of Laminar Flow and Heat Transfer for Liquid Jet Impingement Cooling of a Circular Heat Source with Annular Collection of the Spent Fluid, *Numerical Heat Transfer, Part A*, vol. 20, pp. 263-278, 1991.
32. D.J. Womac, S. Ramadhyani, and F.P. Incropera, Correlating Equations for Impingement Cooling of Small Heat Sources with Single Circular Liquid Jets, *Journal of Heat Transfer*, vol. 115, pp. 106-115, 1993.
33. D.J. Womac, F. Incropera, and S. Ramadhyani, Correlating Equations for Impingement Cooling of Small Heat Sources with Multiple Liquid Jets, *Journal of Heat Transfer*, vol. 116, pp. 482-486, 1994.
34. R.A. Rice and S.V. Garimella, Heat Transfer from Discrete Sources Using an Axisymmetric, Submerged and Confined Liquid Jet, *Proceedings of the 10<sup>th</sup> International Heat Transfer Conference*, Brighton, U.K., vol. 3, pp. 89-94, 1994.
35. D.E. Maddox and A. Bar-Cohen, Thermofluid Design of Single-Phase Submerged-Jet Impingement Cooling for Electronic Components, *Journal of Electronic Packaging*, vol. 116, pp. 237-240, 1994.

36. S.V. Garimella and R.A. Rice, Confined and Submerged Liquid Jet Impingement Heat Transfer, *Journal of Heat Transfer*, vol. 117, pp. 871-877, 1995.
37. F.M. White, *Fluid Mechanics*, Fourth Edition. WCB/McGraw-Hill, New York, 1999.
38. C.A.J. Fletcher, *Computational Galerkin Methods*, Springer-Verlag, New York, 1984.
39. M. Alkam and P.B. Butler, Transient Conjugate Heat Transfer Between a Laminar Stagnation Zone and a Solid Disk, *Journal of Thermophysics and Heat Transfer*, vol. 8, no. 4, pp. 664-669, 1994.
40. J. Stevens and B.W. Webb, Measurements of the Free Surface Flow Structure Under an Impinging Free Liquid Jet, *Journal of Heat Transfer*, vol. 114, pp. 79-84, 1992.
41. E.J. Watson, The Radial Spread of a Liquid Jet Over a Horizontal Plane, *Journal of Fluid Mechanics*, vol. 20, part 3, pp. 481-499, 1964.
42. X. Liu, L.A. Gabour, and J.H. Lienhard, Stagnation-Point Heat Transfer During Impingement of Laminar Liquid Jets: Analysis Including Surface Tension, *Journal of Heat Transfer*, vol. 115, pp. 99-105, 1993.
43. S. Inada, Y. Miyasaka, and R. Izumi, A Study on the Laminar Flow between a Two-dimensional Water Jet and a Flat Surface with Constant Heat Flux, *Bulletin of the JSME*, vol. 24, no. 196, pp. 1803-1810, 1981.
44. V.K. Garg and S. Jayaraj, Boundary Layer Analysis for Two-dimensional Slot Jet Impingement on Inclined Plates, *Journal of Heat Transfer*, vol. 110, pp. 577-582, 1988.
45. S. Polat, A.S. Mujumdar, and W.J.M. Douglas, Impingement Heat Transfer Under a Confined Slot Jet. Part I: Effect of Surface Throughflow, *Canadian Journal of Chemical Engineering*, vol. 69, pp. 266-273, 1991.
46. S. Polat, A.S. Mujumdar, and W.J.M. Douglas, Impingement Heat Transfer Under a Confined Slot Jet. Part II: Effect of Surface Motion and Throughflow, *Canadian Journal of Chemical Engineering*, vol. 69, pp. 274-280, 1991.
47. S. Al-Sanea, A Numerical Study of the Flow and Heat Transfer Characteristics of an Impinging Laminar Slot Jet Including Crossflow Effects, *International Journal of Heat and Mass Transfer*, vol. 35, no. 10, pp. 2501-2513, 1992.
48. Y.J. Chou and Y.H. Hung, Impingement Cooling of an Isothermally Heated Surface with a Confined Slot Jet, *Journal of Heat Transfer*, vol. 116, pp. 479-482, 1994.
49. Y.J. Chou and Y.H. Hung, Fluid Flow and Heat Transfer of an Extended Slot Jet Impingement, *Journal of Thermophysics and Heat Transfer*, vol. 8, no. 3, pp. 538-545, 1994.

50. S.H. Seyedein, M. Hasan, and A.S. Mujumdar, Modeling of a Single Confined Turbulent Slot Jet Impingement Using Various Turbulence Models, *Applied Mathematical Modeling*, vol. 18, pp. 526-537, 1994.
51. S.H. Seyedein, M. Hasan, and A.S. Mujumdar, Turbulent Flow and Heat Transfer from Confined Multiple Impinging Slot Jets, *Numerical Heat Transfer, Part A*, vol. 27, pp. 35-51, 1995.
52. H. Laschefski, T. Cziesla, G. Biswas, and N.K. Mitra, Numerical Investigation of Heat Transfer by Rows of Rectangular Impinging Jets, *Numerical Heat Transfer, Part A*, vol. 30, pp. 87-101, 1996.
53. T. Cziesla, E. Tandogan, and N.K. Mitra, Large Eddy Simulations of Heat Transfer from Impinging Slot Jets, *Numerical Heat Transfer, Part A*, vol. 32, pp. 1-17, 1997.
54. S. Ashforth-Frost, K. Jambunatham, and C.F. Whitney, Velocity and Turbulence Characteristics of a Semiconfined Orthogonally Impinging Slot Jet, *Experimental Thermal and Fluid Science*, vol. 14, pp. 60-67, 1997.
55. Z.H. Lin, Y.J. Chou, and Y.H. Hung, Heat Transfer Behaviors of a Confined Slot Jet Impingement, *International Journal of Heat and Mass Transfer*, vol. 40, no. 5, pp. 1095-1107, 1997.
56. R. Gordon and J.C. Akfirat, Heat Transfer Characteristics of Impinging Two-Dimensional Air Jets, *Journal of Heat Transfer*, vol. 88, pp. 101-108, 1966.
57. I. Sezai and A.A. Mohamad, Three-Dimensional Simulation of Laminar Rectangular Impinging Jets, *Journal of Heat Transfer*, vol. 121, pp. 50-56, 1999.
58. Q. Chen and V. Modi, Mass Transfer in Turbulent Impinging Slot Jets, *International Journal of Heat and Mass Transfer*, vol. 42, no. 5, pp. 873-887, 1999.
59. G. Yang, M. Choi, and J.S. Lee, An Experimental Study of Slot Jet Impingement Cooling on Concave Surface: Effects of Nozzle Configuration and Curvature, *International Journal of Heat and Mass Transfer*, vol. 42, no. 12, pp. 2199-2209, 1999.
60. R. B. Bird, W. E. Stewart, and E. N. Lightfoot, *Transport Phenomena*, Wiley, New York, 1992.
61. D.A. Zumbrunnen, F.P. Incropera, and R. Viskanta, Convective Heat Transfer Distributions on a Plate Cooled by Planar Water Jets, *Journal of Heat Transfer*, vol. 111, pp. 889-896, 1989.

62. S. Kumagai, S. Suzuki, Y. Sano, and M. Kawazoe, Transient Cooling of a Hot Metal Slab by Impinging Jet with Boiling Heat Transfer, *ASME/JSME Thermal Engineering Conference*, vol. 2, pp. 347-352, 1995.
63. J.E. Leland, Experimental Data on Submerged Free Liquid Jet Impingement, Personal Communications, Air Force Research Laboratory, Wright Patterson AFB, Ohio, 1999.
64. T. Azuma and T. Hoshino, LDV Measurement in Radial Flow of Thin Liquid Film, *Proceedings of the Osaka Symposium on Flow Measuring Techniques: The Application of LDV*, Association for the Study of Flow Measurements, Osaka, Japan, pp. 1-15, 1983.
65. A. Rao and J. Arakeri, Integral Analysis Applied to Radial Film Flows, *International Journal of Heat and Mass Transfer*, vol. 41, pp. 2757-2767, 1998.
66. J. Seyed-Yagoobi, V. Narayan, and R.H. Page, Comparison of Heat Transfer Characteristics of Radial Jet Reattachment Nozzle to In-Line Impinging Jet Nozzle, *Journal of Heat Transfer*, vol. 120, pp. 335-341, 1988.
67. R.H. Page, L.L. Hadden, and C. Ostovari, Theory for Radial Jet Reattachment Flow, *AIAA Journal*, vol. 27, pp. 1500-1505, 1989.
68. H. Laschefske, T. Cziesla, and N.K. Mitra, Influence of Exit Angle on Radial Jet Reattachment and Heat Transfer, *Journal of Thermophysics and Heat Transfer*, vol. 9, pp. 169-173, 1995.
69. F. Peper, W. Leiner, and M. Fiebig, Impinging Radial and Inline Jets: A Comparison with Regard to Heat Transfer, Wall Pressure Distribution, and Pressure Loss, *Experimental Thermal and Fluid Science*, vol. 14, pp. 194-204, 1997.
70. A.B. Abou-Ziyan and F. Hassan, Effect of Jet Characteristics on Heat Transfer by Impingement of Submerged Confined Water Jets, *Proc. ASME Heat Transfer Division*, vol. 361-1, pp. 211 – 218, 1998.
71. G.K. Morris, S. Garimella, and J.A. Fitzgerald, Improved Predictions of the Flow Field in Submerged and Confined Impinging Jets Using the Reynolds Stress Model, Thermomechanical Phenomena in Electronic Systems - Proceedings of the Intersociety Conference, IEEE, NJ 98CH36208, pp. 362 –370, 1998.
72. C.A. Dinu, D.E. Beasley, and J.A. Liburdy, Heat Transfer from a Moving Plate to a Confined Impinging Jet, *Proc. ASME Heat Transfer Division*, vol. 357-4, pp. 192 – 205, 1998.
73. K.L. Teucher, S. Ramadhyani, and F.P. Incropera, Jet Impingement Cooling of an Array of Discrete Heat Sources with Extended Surfaces, *Enhanced Cooling Techniques for Electronics Applications*, ASME /HTD-vol. 263, pp.1-10, 1993.

74. V.P. Schroeder and S.V. Garimella, Heat Transfer from a Discrete Heat Source in Confined Air Jet Impingement, *Proc. 11th Int. Heat Transfer Conference*, vol. 5, pp. 451-456, 1998.
75. H.A. El-Sheikh and S.V. Garimella, Enhancement of Air Jet Impingement Heat Transfer Using Pin-Fin Heat Sinks, *IEEE Transactions on Components and Packaging Technology*, vol. 23, no. 2, pp. 300-308, 2000.
76. V.P. Carey, *Liquid-Vapor Phase-Change Phenomena*, Taylor & Francis, Bristol, PA, 1992.